

High resolution resist-free lithography in the SEM

Hari, Sangeetha

DOI

[10.4233/uuid:e2f5a2d2-7e79-4049-9031-6924d7ec0f22](https://doi.org/10.4233/uuid:e2f5a2d2-7e79-4049-9031-6924d7ec0f22)

Publication date

2017

Document Version

Final published version

Citation (APA)

Hari, S. (2017). *High resolution resist-free lithography in the SEM*. [Dissertation (TU Delft), Delft University of Technology]. <https://doi.org/10.4233/uuid:e2f5a2d2-7e79-4049-9031-6924d7ec0f22>

Important note

To cite this publication, please use the final published version (if applicable).
Please check the document version above.

Copyright

Other than for strictly personal use, it is not permitted to download, forward or distribute the text or part of it, without the consent of the author(s) and/or copyright holder(s), unless the work is under an open content license such as Creative Commons.

Takedown policy

Please contact us and provide details if you believe this document breaches copyrights.
We will remove access to the work immediately and investigate your claim.

**High resolution resist-free lithography
in the SEM**



This work was financially supported by NanoNextNL

Printed by: Ridderprint BV, Ridderkerk, The Netherlands

Copyright © 2017 by Sangeetha Hari

ISBN 978-94-6299-752-3

An electronic version of this thesis is available at

<http://repository.tudelft.nl/>

High resolution resist-free lithography in the SEM

Proefschrift

ter verkrijging van de graad van doctor
aan de Technische Universiteit Delft,
op gezag van de Rector Magnificus Prof. Ir. K. C. A. M. Luyben;
voorzitter van het College voor Promoties,
in het openbaar te verdedigen op
dinsdag 17 Oktober 2017 om 15:00 uur

door

Sangeetha HARI
Master of Science (Physics),
University of Delhi, India
geboren te Chennai, India

This dissertation has been approved by the

promotor: Prof. Dr. Ir. P. Kruit

copromotor: Dr. C. W. Hagen

Composition of the doctoral committee:

Rector Magnificus Chairman

Prof. Dr. Ir. P. Kruit Delft University of Technology

Dr. C. W. Hagen Delft University of Technology

Independent members:

Prof. Dr. W. M. J. M. Coene Delft University of Technology

Prof. Dr. O. Ingolfsson University of Iceland, Iceland

Dr. L. Dinu-Gurtler Mapper Lithography B.V., The Netherlands

Dr. I. Utke EMPA, Switzerland

Prof. Dr. B. Rieger Delft University of Technology,
reserve member

Other member:

Dr. J. J. L. Mulders Thermo Fisher Scientific, The Netherlands

“ *For still there are so many things
that I have never seen:
in every wood in every spring
there is a different green*

”
J. R. R. Tolkien,

Contents

1	Introduction	1
2	EBID control for lithography	6
2.1	High Resolution EBID - state of the art	7
2.2	Current limited versus precursor limited regime	11
2.3	Experimental details	14
2.4	Results and Discussion	15
2.4.1	Conclusions	23
3	Reproducibility of EBID	25
3.1	Metrology of dense EBID lines	26
3.1.1	Edge Detection in dense EBID lines	31
3.1.2	Performance verification of edge detection technique	34
3.2	Experimental details	37
3.2.1	Patterning of dense EBID lines for measurement of reproducibility	37
3.2.2	Imaging of dense EBID lines for measurement of reproducibility	40
3.2.3	Characterisation of dense EBID lines for measurement of reproducibility	46
3.3	Results - Reproducibility of EBID lines	52
3.3.1	Power Spectral Density of EBID lines	54
3.3.2	EBID simulator including the effect of vibrations	54
3.3.3	Reproducibility	59
3.3.4	Comparison of LW of horizontal and vertical lines	60
3.3.5	Reproducibility over space and time	61
3.3.6	Comparison of line width measurement from ICD and MD images	63
3.4	Discussion	63
3.4.1	Line Edge Roughness of EBID lines	65
3.5	Conclusions and recommendations	65

4	Patterning of dense lines - EBID profile evolution and characterisation	69
4.1	Deposit growth in EBID	70
4.2	Imaging and characterisation of dense lines	77
4.2.1	Line Width determination by AFM	79
4.2.2	3D characterisation of dense EBID lines using AFM	81
4.3	Interpretation of contrast in SEM imaging	84
4.3.1	Combining SE, BSE and AFM imaging	85
4.4	Simulated EBID line profiles	90
4.5	Recipe development for the patterning of dense lines	95
4.5.1	Evolution of line width	97
4.6	Discussion	104
4.7	Conclusions and recommendations	106
5	Removal of interconnects in dense EBID lines	110
5.1	Experimental methods	113
5.1.1	Choice of precursor	113
5.1.2	Choice of substrate	115
5.1.3	Imaging	116
5.2	Removal of carbon halo	116
5.3	Removal of interconnects	121
5.4	Discussion	126
5.5	Conclusions	127
6	3D shape control - sidewall angle tuning in FEBIP	130
6.1	Sidewall slope modification by EBIE - proof of principle simulation	132
6.2	Electron beam induced etching of carbon with water	136
6.3	Experimental details	137
6.3.1	Influence of electron current	139
6.3.2	Influence of gas flux	140
6.4	Sidewall slope evolution under EBIE	141
6.5	Modelling of sidewall modification by EBIE	148
6.5.1	Sidewall evolution with electron dose	159
6.5.2	Sidewall evolution with etch position	160
6.5.3	Discussion	160
6.6	In situ monitoring of sidewall evolution	163
6.7	Repeatability	164

6.8 Sidewall modification in high resolution dense lines	167
6.9 Interesting observations during EBIE of EBID patterns	168
6.10 Conclusions	172
6.11 Recommendations	173
7 Conclusions	174
Summary	180
Samenvatting	183
Appendix A Fabrication of calibration standards for super-resolution microscopy	187
A.1 Experimental details	189
A.1.1 Control experiment	192
A.1.2 Patterning and biofunctionalisation	192
A.1.3 Influence of electron dose on resolution	194
A.2 Fabrication of high resolution dense fluorescent patterns . .	199
A.2.1 Quantitative dimensional analysis using SEM	202
A.3 Discussion	209
A.4 Conclusions	210
Appendix B EBID simulator including the effect of vibrations	212
Bibliography	213
Acknowledgements	225

Chapter 1

Introduction

“ *All that is gold does not glitter,
Not all those who wander are lost;* ”

J. R. R. Tolkien,

Autumn of 1958 saw the demonstration of the world’s first integrated circuit (IC) by Jack Kilby at Texas Instruments, U.S.A [1]. It was a compact solution to the problem of making complex electronic circuits, achieved by fabricating all the components and the chip out of one slab of germanium (therefore referred to as lithography). Specialised metallization techniques were since developed which could be used to form connections between the devices as desired. This eliminated the need for using wires, which created a significant probability of device failure at every soldered joint, and made it possible to fabricate reliable miniature electronic circuits. Recognised immediately as “an idea whose time had come” [2], it went on to spawn a host of others and has revolutionised the field of modern electronics. From the hand-held calculator that first brought it into prominence to sensors, computers and mobile phones, today IC’s are responsible for reliable, low-cost, low-power, easy-to-replace electronics in virtually every field imaginable. Over the years, the number of IC’s on a chip has steadily increased, following Moore’s law, and has led to the fabrication of smaller and smaller chips.

The driving force, as well as the limiting factor, in chip manufacturing is the device fabrication technology. The minimum feature size and the packing density are together determined by the lithography technique used in printing the chip. The state-of-the-art commercial technique is Extreme Ultra Violet (EUV) lithography. Developed by ASML, it involves coating the chip with a layer of resist and illuminating it with EUV light. Giant machines with intricate lens systems currently provide a resolution of 18 nm and efforts are continually underway to achieve higher resolution by

using increasingly smaller wavelengths of EUV light. However, it is not known how far it can be pushed and competing technologies, collectively called Next Generation Lithography (NGL) remain under consideration. These include electron beam lithography (EBL), scanning probe lithography, nanoimprint lithography (NIL), X-ray and ion beam lithography. While EUV lithography is a high throughput technique where the resist exposure takes place in one shot, EBL involves scanning the electron beam to expose the patterns one pixel at a time and is therefore very slow. Both techniques involve the use of resist and the interaction of photons/electrons with the resist is crucial for understanding and controlling the process. The resolution in EBL is limited by the spread of the electrons in the resist and the smallest features patterned are of the order of several nanometres. In the case of EUV, the resolution is currently limited by the wavelength of the light used (13.5 nm). On approaching 5 nm resolution, however, the processes induced in the resist would once again limit the feature size. Scanning probe techniques such as those used to fabricate the quantum coral [3] and the atomic hard drive [4] provide the highest possible resolution as individual atoms can be manipulated to form patterns. But severe restrictions such as the need for liquid nitrogen temperatures and the low speed of the process have prevented it from becoming a commercially viable technique. NIL is a promising lithography technique in which a stamp patterned with the features of interest is pressed into a resist/polymer that is applied on the surface of the chip, transferring the pattern onto it. It is then exposed to UV radiation, causing the polymer to solidify, after which the stamp is removed. An etching step then transfers the pattern to the underlying substrate. Although it involves multiple steps, it has a high throughput as the UV exposure and etching are performed over the entire chip in one shot. The resolution in NIL is determined by the size of the features on the mask, so a high resolution technique is needed to fabricate it. High resolution capability is no doubt essential for application as a nanolithography technique. In order to be viable as a large scale commercial manufacturing process, there are several other considerations as well. The use of a resist, multiple exposure steps, the use of a mask, manipulation of atoms, pixel patterning and single shot exposure all provide advantages and disadvantages for the accompanying technique. The highest resolution, for example, comes at the cost of throughput. So, on comparing the different technologies in terms of resolution, throughput and ease of use/maintenance, the above mentioned

techniques all have advantages and disadvantages. It is evident that no clear winner emerges. There is room to develop a new lithography technique.

This thesis approaches the challenge by looking for a nanofabrication technique that is inherently high resolution, investigating its potential for the patterning of dense lines and developing it for lithography. Focussed Electron Beam Induced Processing (FEBIP) is a sub-10 nm direct-write patterning technique comprising two complementary techniques - Electron Beam Induced Deposition (EBID) and Etching (EBIE). EBID can be carried out in a Scanning Electron Microscope (SEM) by focussing the primary electron beam onto the substrate in the presence of adsorbed precursor gas molecules which have been let in through a nozzle close to the sample surface. The electrons interact with the substrate generating high energy backscattered and low energy (< 50 eV) secondary electrons, all of which interact with the molecules causing them to dissociate. The non-volatile dissociation fragment forms a deposit on the substrate and in this manner patterning can be carried out by simply scanning the beam. EBIE is essentially similar: adsorbed precursor molecules are dissociated by the electron beam, leading to the formation of reactive fragments which in turn react with the substrate to locally volatilize it. Although analogous to gas assisted etching by ions, it is in fact a chemically selective technique, complementary to EBID in that it is top down, with a significant advantage over ion milling due to the absence of sputtering. It therefore has wide applications, including being suitable for use on samples that cannot withstand ion exposure.

The main advantage of FEBIP is the high resolution achievable by the use of focused electron beams. It has an even higher resolution than that of EBL and does not require a development step. It is low maintenance, implementable in a standard SEM with a simple gas injection nozzle, therefore affordable for low end applications as well. Another great advantage is in the inherent ease of use and flexibility when compared to NGL techniques. A variety of materials can be deposited/etched by the use of appropriate precursors [5] and being an inherently 3D technique, it enables the growth of structures in height. It requires no resist or sample preparation. In addition, there are few restrictions on the substrate to be patterned, accommodating in principle everything from flat wafers to spherical and

uneven surfaces. Extensive reviews of EBID and EBIE can be found in [5], [6], [7], [8]. Due to the versatility of FEBIP, it has been used for several applications such as the fabrication of electrodes, etch masks, nanorods, 3-dimensional, plasmonic and even superconducting nanostructures [9], [10] using EBID, and EUV mask repair [11], cutting of nanotubes [12] and etching of holes in thin films using EBIE. One of the issues in this technique is the deposit composition. The precursor molecules used in EBID come from the field of Chemical Vapour Deposition and are therefore not necessarily ideal for dissociation by electrons; in fact they are most often not. This results in an EBID deposit that is not purely metallic, instead often containing a large amount of carbonaceous material as well. If the goal is the direct fabrication of conducting deposits, this is a serious disadvantage. However, a different application such as the fabrication of masks for NIL, for instance, would not suffer from this problem. In that case, the deposit shape and dimensions would become critical. Another issue is of course the throughput which is low on account of scanning the beam. This can be compensated by the use of multiple beams, but it is also possible to envisage a different route. There exist well developed lithography techniques for large area patterning. FEBIP can be used for selective modification of patterned wafers by adding or removing connections at very high resolution in a non contaminating (resist-free) manner. In fact, FEBIP is already being used in some commercial applications that make use of the high resolution and 3D nature of the process. It has been developed as a mask repair tool by Zeiss (Zeiss MeRiT neXT) for the modification of and defect removal in photomasks, including EUV masks using EBID and EBIE. It has also led to the founding of Nanotools GmbH, specialising in the fabrication of custom-made high aspect ratio AFM tips for scanning probe microscopy. The high resolution and versatility of FEBIP demonstrate significant potential for next generation lithography.

So how is a nanofabrication technique to be developed into a technology for lithography? This work presents an experimental study of FEBIP in terms of the various aspects of patterning that have been shown to be critical in state-of-the-art technologies. The goal is to determine how FEBIP measures up to existing techniques and to develop the aspects that are not satisfactory. Reproducibility is a basic requirement for a lithography technique. As a result of the complexity of the process and the wide range of applications that are being pursued with FEBIP, this has not been inves-

tigated in literature. Chapter 2 describes the parameters involved in EBID, the wide range of which contributes to the problem of reproducibility, and makes a prediction regarding a preferred patterning regime. Sub-20 nm dense lines are patterned in this regime and the results are compared with reports in literature. A preliminary technique is presented for the measurement of line width and line edge roughness, two of the most important aspects in lithography. In Chapter 3, the challenges in the characterisation of EBID lines are demonstrated and an improved technique for imaging and dimensional metrology is described, especially tailored for the Gaussian line profiles obtained with EBID. This is used to perform quantitative measurements of the critical dimension/feature size and to systematically investigate the reproducibility of patterning. Chapter 4 studies electron dose-controlled growth of high resolution lines and the evolution of the EBID line profile with height and width is investigated. While patterning in resist can achieve lines with vertical sidewalls, the profile of as-deposited EBID lines is quite different. This difference comes about due to the fact that EBL requires two steps: exposure and development. A minimum dose is needed for the resist to subsequently be developed. This is not the case in EBID. Exposure of the adsorbed precursor to the electron beam immediately results in lateral and vertical growth, and increasing the dose causes both the width and the height to increase. The increase in line width as a result of increase in dose is non-linear in EBL, whereas this doesn't seem to be the case in EBID, and the line profiles are Gaussian. The resulting challenges to the resolution, such as the creation of interconnecting material, are addressed in Chapter 5. Subsequent to the study of 2D growth, imaging techniques and characterisation of lines, the 3D shape of EBID lines is studied in Chapter 6 with a view to achieving the desired line profiles using FEBIP.

Experiments towards reproducibility and control also paved the way for some novel applications of FEBIP. In Appendix A electron beam induced modification of a polymer coated substrate has been used for selective functionalisation of the surface with fluorescent biomolecules. These samples have been developed for applications in the field of optical superresolution microscopy.

Chapter 2

EBID control for lithography

“ *Just as the words came up to me
I sang it under the wild wood tree.* ”

Walter de la Mare,

Nanopatterning using Electron Induced Deposition (EBID) involves the direct deposition of material in a scanning electron microscope (SEM) by scanning the beam in the presence of adsorbed precursor gas molecules. With SEM offering spot sizes of about a nanometre, EBID is a versatile, high resolution technique. As discussed in Chapter 1, it has several advantages over conventional lithography techniques like EBL and EUV for high resolution work. However, while a lot of research has already been performed in these fields resulting in a high degree of process control, EBID is largely unexplored. The literature contains reports of a myriad of shapes, dimensions, profiles, chemical composition as well as applications that are a result of EBID, but there is a lack of understanding of the fundamentals of the process. So although the input parameters may be known for patterning a certain structure, the processes responsible for deposition at the molecular level are so poorly understood that these parameters may not be sufficient or appropriate for repeating it successfully. In other words, the real input parameters are often unknown and there are no models accurately explaining EBID growth at the nanoscale.

In addition, there is a wide parameter space in EBID patterning. This can be divided broadly into five categories:

1. Electron beam parameters: electron flux, electron energy
2. Precursor related parameters: precursor flux from nozzle, nozzle geometry and position, adsorption/desorption of precursor molecules, electron stimulated desorption, electron-induced dissociation cross section, electron beam induced heating

3. Substrate related parameters: substrate material, energy dependent electron scattering cross section in the material, surface composition, surface diffusion, exit area of scattered electrons
4. SEM related parameters: temperature, base vacuum, residual gas composition
5. Patterning parameters: pixel overlap, pixel dwell time, number of passes, wait time between passes, patterning strategy, proximity of patterns

and others, possibly unknown. Many of these parameters are not very well known or vary between experiments and between labs. In the literature, many interesting EBID structures can be found, but the circumstances under which they were made are not well known. This uncertainty exists even in experiments where some, but not all, of the parameters listed above have been measured. Most often, the parameters reported are the beam current, energy, pixel dwell time and number of passes. But these are not sufficient to determine the deposit growth rate as this is determined by a combination of several factors: the local gas flux at the sample, in turn determined by the nozzle position and geometry, the residual gas pressure, the distribution of current in the beam and the pixel overlap during patterning. However, EBID reports typically do not contain these measurements as they are much harder to make and in their absence the results are difficult to reproduce. The purpose of this work is to find a set of parameters where reproducible patterning can be carried out and to then demonstrate the fabrication of sub-30 nm dense lines in this regime. As a further step towards reproducibility, we measure the line widths and line edge roughness using a recently developed technique, providing the first quantitative report of the characterisation of high resolution EBID lines.

2.1 High Resolution EBID - state of the art

Since the darkening due to decomposition of hydrocarbon contamination was first observed while imaging in the SEM, this process was exploited to deposit insulating thin films [13] and sub-micron patterns [14] of a range of materials in a controlled manner by scanning the electron beam. The high resolution of this technique was demonstrated as early on as 1976 by

Broers et al. [15] who patterned EBID lines on a gold-palladium film coated on a carbon membrane using hydrocarbon contamination in the SEM chamber. Using this as an etch mask, the "unprotected" gold-palladium was removed, resulting in 8 nm wide conducting lines. But structures grown using EBID were most often of sizes larger than 20 nm, and it was Cividjian et al. [16] who realized that structures as small as 2 nm could be fabricated in the initial stage of the growth process. Van Dorp et al. [17] pushed the spatial resolution limit even further and deposited dots of 0.7 nm diameter on thin carbon membranes in a STEM with a 0.3 nm electron probe. It was then discovered that the placement accuracy of the deposits at the few nanometre-scale was prone to the Poisson statistics of the dissociation process ([18]).

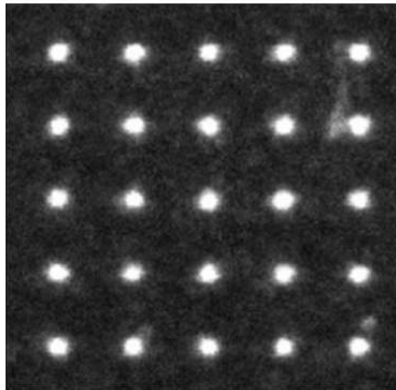


Figure 2.1: Annular dark field (ADF) image of an array of 4 nm diameter carbon dots, at 11 nm pitch, deposited on a carbon membrane in a 200 keV scanning transmission electron microscope.

At a somewhat larger scale, but still sub-10 nm, good control over the deposition process was obtained as is illustrated in Fig. 2.1 (from W. F. van dorp, unpublished). The next challenge was to achieve similar spatial resolution in the much more user-friendly SEM. Van Kouwen et al. [19] succeeded in depositing arrays of dots as small as 2.8 nm on carbon membranes, using methyl cyclopentadienyl trimethyl platinum (MeCpPtMe_3 , CAS: 94442-22-5) as a precursor gas. These were imaged in annular dark field (ADF) mode using a Scanning Tunnelling Electron Microscope (STEM) detector in the SEM. For applications, however, it is necessary to move away from membrane substrates and use silicon wafers. But that introduces two difficulties: (i) one can no longer rely on the superb ADF imaging, but use secondary electron (SE) or backscattered

electron (BSE) imaging instead and (ii) in addition to the PE's and SE's, the electrons backscattered from the bulk substrate will also contribute to the deposition process. The latter difficulty, fortunately, is not a serious problem in the fabrication of sub-30 nm structures. Assume, for simplicity, that the number of BSE's is equal to the sum of the SEs and PEs, that the BSE exit area has a diameter of typically 1 μm , and that the BSE's are as effective in dissociating precursor molecules as the SE's and PE's. Then, during the growth of a 5 x 5 x 5 nm³ deposit, i.e., ≈ 4600 atoms, 4600 atoms are also deposited in the 1 μm diameter circular area which is the BSE range. But this is an area that can contain 7 million atoms in a monolayer, so the concentration of deposited atoms due to the BSE's is extremely low when growing nanostructures. This has also been exploited by Van Oven et al. [20] who succeeded in depositing 3 nm dense lines and spaces on a bulk silicon wafer and imaged the structures using SE detection (Fig.2.2).

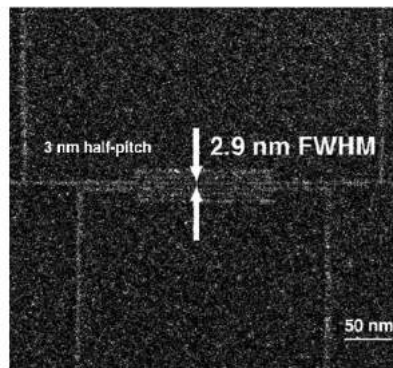


Figure 2.2: Secondary electron (SE) image of 3 nm dense lines and spaces deposited in an SEM on a bulk Si wafer, using MeCpPtMe₃ as a precursor (30 kV beam, spot 4, 40 ms/nm linear dwell time, 0.96 pC/nm total line dose, beam step size 0.12 nm, 3 mm working distance, 500 passes, synchronized with the power line, and with a 100 ms pause after each pass). [Reprinted with permission from J.C. van Oven et al., *Journal of Vacuum Science & Technology B*29, 06F305 (2011), 2011, American Vacuum Society.]

During EBID, the precursor is usually let in using a gas injection system fitted with a needle that can be inserted such that the distance between the sample and the needle is about 150 μm . Fig. 2.3 from [5] shows a cartoon representation of the process. This geometry ensures a high molecular flux locally while maintaining low pressure in the chamber for continued working of the turbo pump.

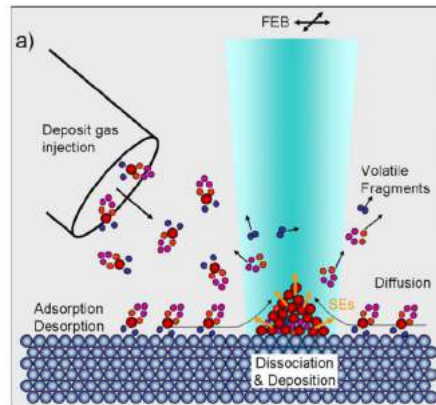


Figure 2.3: Cartoon representation of EBID from [5] showing the geometry of the system which includes a GIS nozzle maintained at a fixed distance from the sample surface. This ensures a high molecular flux locally while maintaining low pressure in the chamber for continued operation of the turbo pump.

However, to achieve a high spatial resolution, a very small working distance was chosen in the SEM and the precursor supply nozzle could no longer be inserted between the pole piece of the objective lens and the substrate. Therefore, the nozzle was retracted, and the experiments were done by filling the SEM chamber with the gas, resulting in a rather low gas pressure. When depositing lines consisting of overlapping neighbouring pixels and exposing each pixel only once, the growth rate of the resulting lines showed an increase over time (the beam step size between pixels was 0.12 nm compared to a probe size of about 2.6 nm). This is due to a proximity effect that arises when the next pixel is deposited partly on top of the sloped sidewall of the previous deposit, thereby emitting more SE's due to the angular dependence of the SE-yield, and thus dissociating more precursor molecules. A second type of proximity effect occurred when dense lines and spaces were deposited. SEs, emitted from a growing line, dissociate precursor molecules on a previously deposited neighbouring line and make it grow further. Both proximity effects could be countered by changing the writing strategy such that the entire pattern is written in multiple passes, keeping the total dose the same. This way, flatter deposits are obtained and neighbouring lines are of the same height during the entire growth process. In addition to the proximity problems, the inner area of the array of dense lines was observed to become depleted of precursor molecules, evidenced by the fact that less mass was deposited in the inner

lines than in the outer lines. This problem could be resolved by inserting a waiting time between passes to allow for replenishment of precursor molecules. A combination of low beam current, low working distance and multiple pass patterning synchronised with the 50 Hz disturbances resulted in the successful fabrication of 3 nm Pt/C lines and spaces on bulk silicon. While this is a significant result demonstrating single nanometre fabrication using EBID, it is only a proof of concept. Here, as well as in the majority of EBID work reported in literature, it would appear that the patterning parameters have been chosen by trial and error to yield the desired result. But since several parameters of importance such as SE profile, pixel overlap, local precursor flux, diffusion rates, etc. are either unknown or not reported, such an approach makes it difficult to extend the results - to go from patterning lines of a certain width to those of twice the width, for example, and limits the use of EBID for lithography. A better understanding of the patterning parameters and their influence is therefore needed to advance the technique. In the following section, we present an analysis of this problem and an intelligent choice of parameters for reproducible patterning.

2.2 Current limited versus precursor limited regime

In EBID the deposit growth is governed by the dissociation of adsorbed precursor molecules by PE's, SE's and BSE's. The electrons involved in the process therefore have a range of energies, initiating deposition by four distinct mechanisms of electron induced fragmentation of the respective precursor molecules, i.e., Dissociative Electron Attachment (DEA) and Dissociative Ionisation (DI), and Neutral and Dipolar Dissociation (ND and DD respectively) subsequent to electronic excitation. The nature of these processes and their potential role in EBID is described in [21] and references therein. The steady state growth rate in EBID, in its simplest form, is given by [14]:

$$R = V_0 N_0 \frac{\left(\frac{qF}{N_0}\right) \sigma f}{\left(\frac{qF}{N_0}\right) + \frac{1}{\tau} + \sigma f} \quad (2.1)$$

where

R is the growth rate [m/s], f [electrons/m²/s] is the electron flux, F

[molecules/m²/s] is the molecular flux at the surface, σ [m²] is the dissociation cross section, g is the sticking coefficient, τ [s] is the residence time of adsorbed molecule, V_0 [m³] is the volume of a deposit molecule or fragment and N_0 [molecules/m²] is the density of molecules in a monolayer.

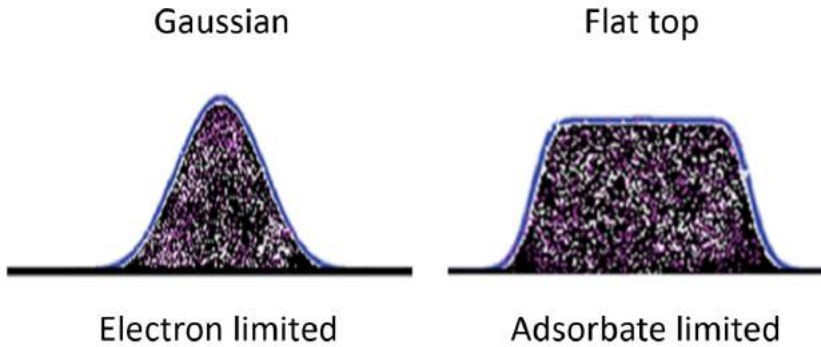


Figure 2.4: Two kinds of deposit profiles obtained during EBID are shown from [22]: Gaussian profile (in the electron current limited regime) and flat top profile (in the gas limited regime).

This can be simplified to yield two growth regimes as: $\frac{gF}{N_0} \gg \sigma f$ and $\frac{gF}{N_0} \ll \sigma f$. If desorption is ignored, τ is infinite and the growth rate in the two cases is given by: $R = V_0 N_0 \sigma f$ and $R = V_0 g F$ respectively. The first case describes a situation where the number of precursor molecules is sufficient and the growth is governed by the electron flux, whereas the second describes the opposite situation - where there are sufficient electrons and the molecular flux determines the growth. This gives us the classification of EBID growth into electron current limited and precursor limited regimes. The precursor limited regime has been studied in a lot of detail by experiments and simulations ([23], [24], [25], [26]), and made use of for the growth of several interesting structures ([27], [28]). Several authors have successfully modelled the growth of pillars in this regime through simulations ([29], [30], [31], [32], [33], [25]) and analytical models ([34]). One of the advantages of working in this regime is the patterning of structures with flat tops ([35], [22]), as opposed to the Gaussian profiles obtained in the current limited regime ([36]). Fig. 2.4 from [22] shows the EBID deposit profiles for the two cases, illustrating this point.

However, the gas limited regime has a disadvantage when it comes to controlled deposition. The first problem is that the local flux at the sample is a quantity that is too difficult to measure experimentally. Instead, an estimate may be obtained by simulations such as in [37] which describes a GIS simulator to calculate the gas flux incident on the sample during EBID given the nozzle orientation and geometry. The results are shown for an SEM chamber similar to the one used in this work (Courtesy J. J. L. Mulders) in Fig. 2.5.

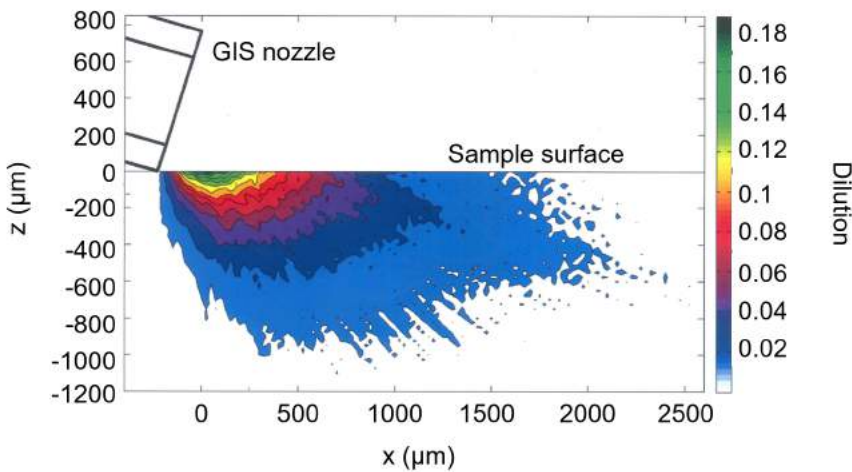


Figure 2.5: Simulation showing the fraction of the molecular flux from the GIS nozzle that is incident on the sample surface as a function of the difference in height between the sample and the nozzle as well as the distance from the centre in x . Courtesy of J.J.L. Mulders and I. Utke

Here, the fraction of the molecular flux from the GIS nozzle that reaches the sample surface, i.e. the dilution factor has been calculated as a function of the height (z -distance between the sample and the nozzle) and x -distance from the nozzle. For a deposition performed at typical distances of $250 \mu\text{m}$ in x and $130 \mu\text{m}$ in z , the dilution factor obtained from Fig. 2.5 is approximately 0.09. For a nozzle having an inner diameter of $500 \mu\text{m}$, effective pumping speed of about 70 L/s and a pressure rise from about 10^{-6} mbar to $3 \times 10^{-5} \text{ mbar}$ upon letting in the gas, the molecular flux leaving the nozzle can be estimated to be $0.3 \text{ moles/m}^2/\text{s}$ or $10^{23} \text{ molecules/m}^2/\text{s}$. Therefore the local gas flux reaching the sample during EBID is about $10^{22} \text{ molecules/m}^2/\text{s}$. Working in the gas limited

regime means that this quantity must be controlled in order to control the deposition, which in turn means that the gas flux leaving the nozzle must be controlled. This must be performed either by manually opening the gas inlet or by changing the temperature of the heater to allow for the desired pressure increase. Both of these methods are inaccurate and unreliable as they do not permit fine tuning of the local pressure.

Moreover, as a consequence of being precursor limited, the growth may differ for different patterning strategies, ie, the same dose delivered using a different combination of parameters would result in different line width as shown in [20]. Therefore, complex writing strategies with waiting times would have to be applied to achieve high resolution, placing EBID at a disadvantage with respect to other techniques like EBL. This regime should therefore be avoided for lithography. On the other hand, the current limited regime offers the highest resolution [34] and appears attractive for lithography. As the electron beam parameters are in general easier to measure, it would also be advantageous to carry out patterning in such a manner that the line dimensions are determined by these alone and not by the gas related parameters which are unknown or hard to measure. Then, by simply varying the electron dose, lines of desired width could be patterned. Therefore the electron current limited regime appears to be an intelligent choice for high resolution lithography.

The next section provides experimental demonstration of this claim. Sub-15 nm half-pitch lines were fabricated to be fairly shallow, with just enough material in them to be visible in the SEM and to determine the dose required to write such small patterns. It is expected that precursor depletion effects would not occur in this regime, and so waiting times between passes can be avoided. The influence of the writing strategy on the line width will be investigated, the contribution of the proximity effects will be discussed, and a typical EBID pattern of dense lines and spaces will be analysed in terms of line width and line width roughness (LWR).

2.3 Experimental details

The deposition experiments were done in an FEI Nova Nano Lab 650 Dual Beam system. The precursor gas MeCpPtMe₃ was introduced from a nozzle that was located 150 μm above the substrate, close to the point

of incidence of the PE beam. The SEM was used in ultrahigh resolution mode with a 20 keV electron beam and a 1.6 nm probe size (spot 2) with a current of 40 pA. The background vacuum of the system was about 2×10^{-6} mbar and rose to about 2×10^{-5} mbar when the precursor gas was introduced. The substrates used are single side polished p-doped (20 to 30 Ω cm) 525 μm thick silicon wafers. Before patterning, the system, including the substrate, was plasma-cleaned overnight for about 12 h to prevent the co-deposition of carbon from contaminants in the microscope. The patterns were defined with FEI patterning software (Nano Builder (Version 2.0.0.897), copyright 2013 FEI Company). The beam step size, i.e., the distance between neighbouring pixels, was 1 nm. With spot size 2, the overlap between pixels is 38.6%. The microscope is equipped with a fast beam blaster to prevent spurious deposition in between patterns. The shortest dwell time per pixel that could be used reliably was 200 ns. After the deposition, the precursor gas was pumped out of the specimen chamber for at least 1.5 h before the deposits were imaged.

2.4 Results and Discussion

When patterning in the current limited regime, the choice of writing strategy is expected to be insignificant. Homogeneous deposition is expected whether the pattern is written in serial or parallel mode, in a single pass or in multiple passes. This is used as a test to determine the regime in which our experiments were performed. A pattern was designed from the outside going inward consisting of five nested L-shaped lines of single-pixel width, seven nested L-shaped lines of 2-pixels wide, and a 10 x 10 array of 2 nm x 2 nm squares. Two of the 2-pixel wide lines are longer than the others to be able to see the difference between isolated lines and dense lines and spaces. In the patterning software used in this work (Nano Builder version 2.0.0.897, copyright 2013 FEI Company.) a single-pixel wide line is defined by setting the line width to a very small value, in this case 100 pm. The spacing between the lines is 25 nm. The pattern was written from the outside inward with 200 passes and a dwell time per pixel $T_{dwell} = 500$ ns. In parallel writing mode, the refresh time, i.e., the time between passes, was 200 ms. The total dose for the lines, defined as the charge delivered in the designed area of 1-pixel (equal to the beam diameter of 1.6 nm) wide, is 2500 C/m², more than 2 orders of magnitude lower than the dose used in Fig. 2.2. An SEM image of the entire pattern is shown in 2.6. Each line

was patterned using a serpentine strategy and the array was written in parallel and serial writing modes as shown schematically in Fig. 2.7.

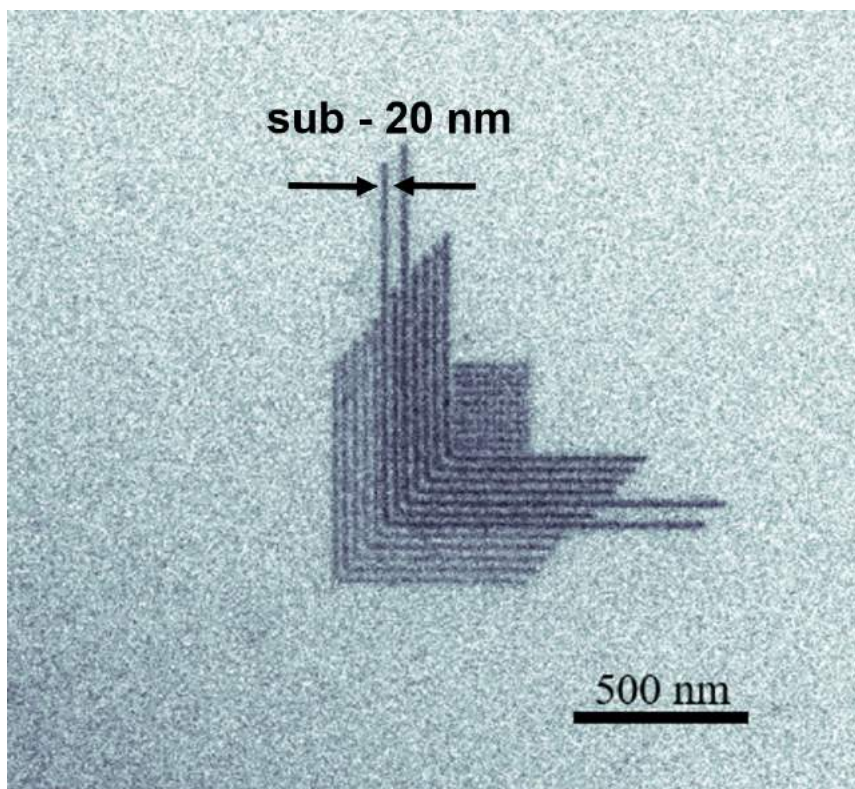


Figure 2.6: SE image of a pattern of five single-pixel wide, 12.5 nm half-pitch, L-shaped lines (outer lines), seven 2-pixel wide L-shaped lines (inner lines) at 12.5 nm half-pitch, and a 10 x 10 array of squares of 2 x 2 pixels.

Higher magnification images of the resulting patterns are shown in Fig. 2.8. The deposition is uniform over the entire pattern in both writing modes, and the isolated lines have the same width as the dense lines, demonstrating that depletion effects are not observed. Therefore, it can be concluded that the growth occurred in the current limited regime. An attempt was also made to verify if the experimental parameters used satisfy the conditions for this regime based on 2.1, ie, to check whether $\frac{qF}{N_0} \gg \sigma f$. A sticking coefficient of 1 was assumed and the estimate of 10^{22} molecules/m²/s was used for the molecular flux F. An approximate value of N_0 equal to 10^{18} molecules/m² and an electron flux f of 10^{25} electrons/m²/s were used, assuming a deposit radius of 1 nm and a current of 50 pA with a spot size of 2 nm. Then $\frac{qF}{N_0} = 10^4$ /s. The values of EBID cross sections were taken

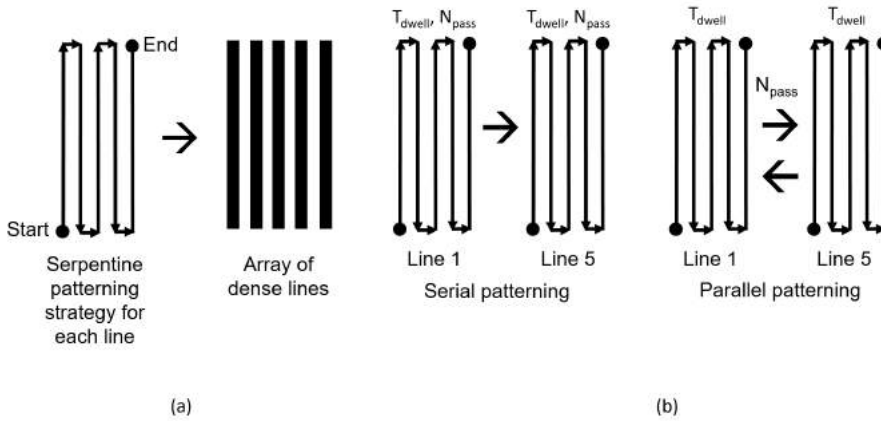


Figure 2.7: Schematic of the patterning showing (a) the serpentine writing strategy used to write every line in the array and (b) serial and parallel modes used to pattern the array

from [38], where an increase was observed, peaking at 150 eV, followed by a decrease at higher energies. For high energy electrons (1 keV), the cross section is of the order of 10^{-21} m^2 , resulting in $\sigma f = 10^4/\text{s}$. For low energy electrons (8 eV), similar values are obtained. For an electron energy of 150 eV, the cross section is an order of magnitude higher (10^{-20} m^2) and $\sigma f = 10^5/\text{s}$. So the two terms may be comparable, and the estimate is sensitive to the value of cross sections used. So this method cannot state conclusively the regime we are in. One of the main reasons is that the energy dependent cross section is not well known in EBID and the numbers used here are integrated values. In addition, the electron flux should in fact be the combined flux of PE's, SE's and BSE's, but only the PE flux is known and therefore used. In order to make use of this relation, the energy distribution of the electrons as well as the energy dependent cross sections should be applied. The conclusion that the growth took place in the electron current regime in this experiment is therefore only based on experimental verification of the absence of proximity effects known to occur when gas limited.

The line width, as measured from the images, is 7 to 8 nm for the thin lines, and 11 to 12 nm for the thick lines. All lines are wider than the designed width, which means that there is considerable line broadening. The origin of this may lie in surface diffusion of dissociated fragments or precursor dissociation by SE's escaping from the sidewalls of the deposits. Monte

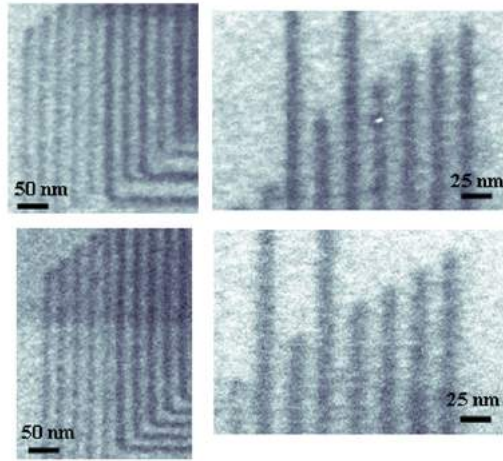


Figure 2.8: Higher magnification SE images of the pattern of Fig. 2.6. Top images: serial writing mode; bottom images: parallel writing mode; left images: 1-pixel lines (left), 2-pixel lines (right); right images: 2-pixel wide lines. The scale of the bottom images is the same as for the corresponding top image. All lines are at 12.5 nm half-pitch. The total dose was 2500 C/m².

Carlo simulations ([39]) seem to suggest that the latter effect may occur even for very shallow deposits. This also explains why the 2-pixel wide lines are not twice as wide as the 1-pixel lines; the width is, in fact, largely determined by the broadening. The conclusion from this experiment is that homogeneous deposition is obtained regardless of the writing strategy, suggesting that the experiments were performed in the current limited regime.

In the current limited growth regime, the exposure dose should be the parameter that determines how much mass is deposited and what the size of the deposited pattern will be, irrespective of how the dose is delivered. That is, the dose can be delivered in a single pass exposure with a dwell time per pixel = T_{dwell} , or in N passes with a dwell time per pixel = $\frac{T_{dwell}}{N}$. This was tested with the following experiment.

A pattern of five horizontal parallel single-pixel wide lines was defined at a mutual distance of 30 nm. The lines were written serially, ie, one after the other from bottom to top. The total dose was 5000 C/m². Six patterns were written with $N = 1, 2, 10, 40, 200,$ and 800 and $T_{dwell} = 200, 100, 20, 5, 1,$ and $0.25 \mu\text{s}$, respectively. The deposited lines were imaged in SE imaging mode, and the results are shown in Fig. 2.9. The image is



Figure 2.9: Six SE images of line patterns stitched together. A pattern was defined of five horizontal parallel single-pixel wide lines at a mutual distance of 30 nm. The patterning strategy is such that the lines were written serially, ie, one after the other, and from bottom to top. The total dose was 5000 C/m^2 . The six patterns, from left to right, were written with 1, 2, 10, 40, 200, and 800 passes, and dwell times of 200, 100, 20, 5, 1, and $0.25 \mu\text{s}$, respectively. The contrast of the images was enhanced for clarity, but was performed identically for all the images to maintain the original intensity differences between them.

a collage of the six images stitched together. The left-most image is the result of single pass patterning and the right-most image is the result of patterning with 800 passes. As expected, there is hardly any difference visible between lines written with the two strategies. The spacing between the lines is seen to be 30 nm, and the line widths are approximately 9 nm. The line width is slightly larger than in the previous experiment. This is probably due to the dose being twice as large, which causes the lines to broaden more.

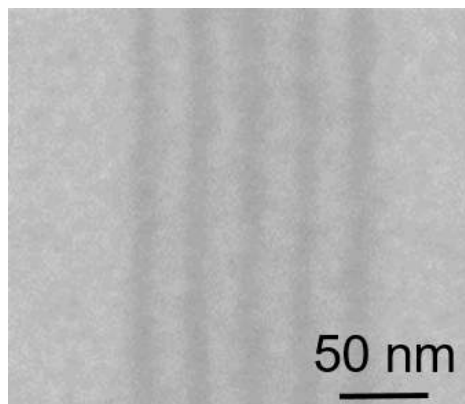


Figure 2.10: SE image of five lines deposited at 15 nm half-pitch in serial patterning mode, from left to right. The total dose was 5000 C/m^2 . The pattern was written with 40 passes and a dwell time of $5 \mu\text{s}$.

The single pass line may have shown the proximity effect due to the angular dependence of the SE yield, but this is not observed. Note that the overlap between neighbouring pixels is much smaller (1 nm beam step size) than in the experiment of Fig. 2.2 (0.12 nm beam step size). The other proximity

effect that enhances the growth of neighbouring lines is not observed for the spacing used in these experiments. This is clearly visible in Fig. 2.8 where the isolated lines have the same width as the dense lines. From these experiments, it can be concluded that in the current limited regime, multiple pass patterning is not required. Homogeneous deposition is obtained even with single pass patterning, which is much more desirable as multiple passes tend to decrease the throughput.

The line widths mentioned above are only approximate widths as measured by eye from the SEM images. To extract a more meaningful measure for the width of the lines and the LWR, one image of a set of deposited lines was analysed in more detail (Fig. 2.10). The writing strategy here was the same as for the fourth image from the left in Fig. 2.9.

To detect the edges of the lines, a recently developed method was used which we describe briefly here. For details the reader is referred to [40]. First, the image is integrated in the direction of the lines to obtain an integrated line profile (see Fig. 2.11). This is only an approximation of the line profile because it contains information of the roughness of the lines. If the roughness increases, the profile widens. However, here, this effect is neglected.

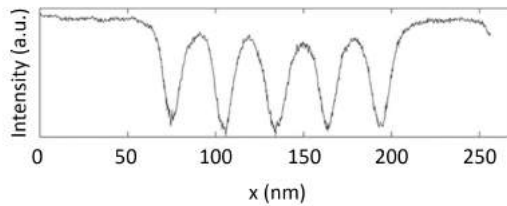


Figure 2.11: Integrated line profile of the five lines shown in Fig. 2.10.

The signal profile is mirrored with respect to the horizontal axis, and then modelled by matching two vertically shifted Gaussian functions, normalized at the centre of the peak. Then the mirrored model function is used to fit each scan line in the image using parameter optimization. The two parameters are the position of the profile and the intensity scaling.

The result is shown in Fig. 2.12(a) where the edges of the lines are plotted, the edge being taken as the position at which the model function is at half-maximum. The centres of the lines are determined as being halfway

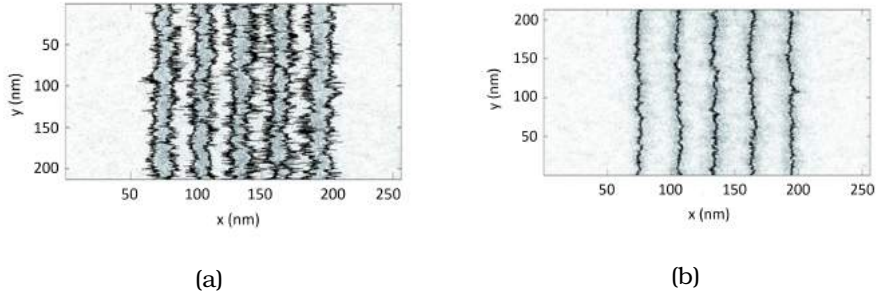


Figure 2.12: (a) Contrast enhanced SE image of Fig.2.10. The black lines indicate the edges of the lines. (b) Contrast enhanced SE image of Fig.2.10. The black lines indicate the centers of the lines (x-coordinate) along the length of the lines (y-coordinate). The average standard deviation in the center position is 1.6 nm.

between the edges and are plotted in Fig. 2.12(b). The mean positions of the lines from left to right are 74.6 nm, 105.7 nm, 134.1 nm, 163.7 nm, and 194.3 nm. The standard deviations are 1.5 nm, 1.6 nm, 1.7 nm, 1.7 nm, and 1.5 nm. The average standard deviation in the centre position is 1.6 nm. From the edge positions, the mean line widths from left to right in Fig. 2.12(a) are calculated as: 13.3, 12.0, 14.5, 12.9, and 15.9 nm. The standard deviations are 4.2 nm, 3.8 nm, 5.2 nm, 4.8 nm, and 4.7 nm. The average linewidth is 13.7 nm with an average LWR of 4.5 nm (1σ value). From this, the average LER of the as deposited lines is estimated as $3.2 \text{ nm} \left(\frac{LWR}{\sqrt{2}} \right)$. It is to be noted that these standard deviation values are determined for each individual line and also include imaging noise. When averaged over a large number of lines and analysing the power spectral density ([40]) the imaging noise can be largely eliminated and the LWR is expected to be considerably smaller. The remaining roughness is not due to shot noise in the exposure as a dose of 5000 C/m^2 corresponds to $31250 \text{ electrons/nm}^2$. It is more likely to be due to the statistical nature of the precursor dissociation process, or surface diffusion of dissociated fragments, or a combination of both.

This can be seen more clearly in high resolution TEM images (Fig. 2.13) of similarly deposited dense platinum EBID lines on a 20 nm silicon nitride membrane coated with 20 nm of sputtered silicon (private communication M. Scotuzzi and D. Ovchinnikov). The statistics of the deposition become more evident from the grains visible all the way to the line edges and beyond, giving rise to diffuse deposit in between the lines.

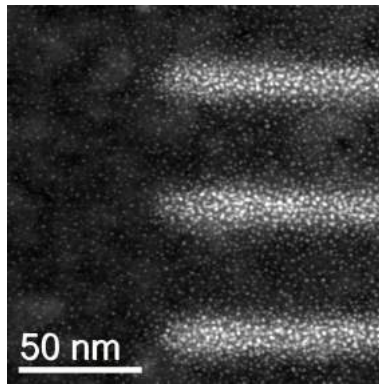


Figure 2.13: HAADF image of dense platinum EBID lines deposited on a 20 nm silicon nitride membrane coated with 20 nm of sputtered silicon and imaged in the TEM. The statistics of the deposition become more evident from the grains visible all the way to the line edges and beyond, giving rise to diffuse deposit in between the lines (private communication M. Scotuzzi and D. Ovchinnikov)

To the best of our knowledge, this is the first time that the LW and LWR have been determined for individual EBID lines. It should be noted here that these values appear to be quite large. In particular, the 3σ values are of the order of the line width. If this is indeed the case, techniques to reduce the LWR must be developed. However, a more sensitive edge detection technique has since been developed, specifically for EBID lines with low SEM contrast and will be described later (chapter 3). This analysis is therefore only performed to provide a consistent measure of line width.

As an example of the capabilities of the EBID technique, a pattern has been fabricated, resembling typical lithography patterns needed to make logic devices (Fig. 2.14). The pattern was written in the same manner as the left-most pattern of Fig. 2.9, i.e., in serial mode, single-pixel wide, single pass, and a dwell time of 200 μs per pixel. The total dose was 5000 C/m^2 . In between writing different lines, the beam was blanked using a fast beam blanker. The linewidths are comparable to the values reported above, i.e., around 10 nm. Homogeneous lines of varying length, both vertical and horizontal, as well as angular patterns and gaps can be fabricated in a controlled manner at desired spacing. This is just a demonstration of some of the capabilities of the technique as practically any shape, such as squares or circles can be fabricated. All it requires is good control over the electron beam positioning.

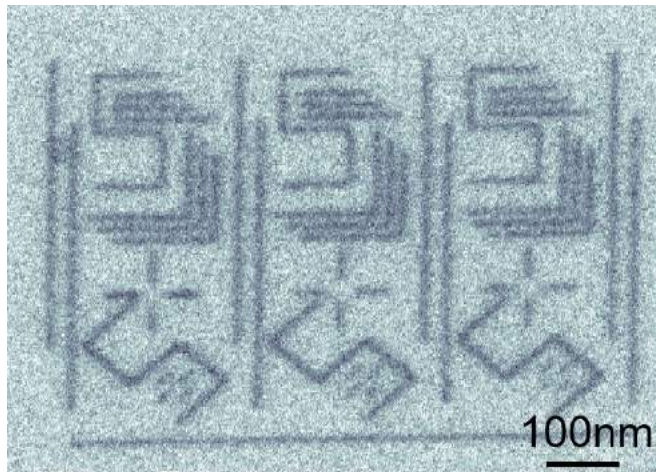


Figure 2.14: An example of an electron beam induced deposition pattern consisting of line shapes resembling lithography pattern designs of logic devices. The pattern was written in serial mode, single-pixel wide, single pass, and a dwell time per pixel of $200 \mu\text{s}$. The total dose was $5000 \text{ C}/\text{m}^2$. In between writing different lines, the beam was blanked using a fast beam blanker. The line widths are comparable to the values reported above, i.e., around 10 nm.

2.4.1 Conclusions

Sub-20 nm EBID lines have been fabricated in the electron current limited regime. Depletion effects that typically occur when working in the precursor limited regime have been demonstrated to be absent. Different patterning strategies were compared: parallel mode, serial mode, single pass and multiple pass. As per our prediction for the current limited growth regime, no difference is observed between lines patterned with different writing strategies. This allows for single pass serial exposure, which is advantageous for lithography for throughput reasons. The proximity effects observed in the previous experiments performed in the precursor limited regime were not observed here. It must be noted that the line patterns presented here were not at such small spacing as the results in [41] and shown in Fig. 2.2. At lower spacing, the proximity effect resulting in increased growth of neighbouring lines may still play a role and needs to be investigated in the current limited growth regime.

A typical set of lines deposited with EBID was analysed to determine the line position, the linewidth, and the edge roughness. Typical values for the EBID lines are an average width of 13.7 nm, an average standard

deviation of 1.6 nm on the centre position of the lines, and an average LWR of 4.5 nm (1 σ value). The edge detection method has since been improved and more reliable measurements of LW and LWR are provided in chapters 3 and 4. As an example of the capabilities of EBID, a logic-resembling lithography pattern was fabricated with a typical dose of 5000 C/m². The challenges that remain are: (1) to reduce the dose needed (2) to devise methods to always be in the current limited regime and (3) to obtain control for patterning at the single nanometre scale.

Chapter 3

Reproducibility of EBID

“ *He tosses gladly on the gale,
For well he knows he can not fail—
Knows if the bough breaks, still his wings
Will bear him upward while he sings!* ”

Edwin Markham,

 he high resolution achievable in EBID has been demonstrated in numerous reports, from sub-5 nm dots [17], [18] to few nanometre wires [42]. Sub-10 nm gaps have been fabricated in devices [15], [43], [44], [45] using EBID directly, as a mask or in combination with a metallic layer to enable specific functionality. To the best of our knowledge, though, there have been no studies on the reproducibility of this technique, nor can this be deduced from a literature survey. This stems mainly from a lack of understanding of the patterning regime in these experiments. The study of reproducibility requires knowledge, or at least maintenance, of patterning conditions and parameters. This is often difficult to achieve due to factors like precursor diffusion and local gas flux, which are hard to control. As described in Chapter 2, this problem can be overcome by patterning in the electron current limited regime where variations in precursor-related parameters are less significant and the reproducibility, by extension, would be expected to be higher. This work demonstrates lithography by EBID in the electron current limited regime. The deposition is controlled by controlling the beam parameters and the sensitivity of deposit dimensions to the remaining parameters is measured. This includes, among others, fluctuations in beam current and temperature, drift, vibrations, varying chamber contamination levels, surface inhomogeneities and accuracy of beam positioning. The next issue in the determination of reproducibility is the metrology of dense EBID lines. Most often in EBID, deposits on bulk substrates are imaged using SE detection and/or AFM, from which the dimensions are determined simply

by inspection. This is obviously not a robust technique and cannot be used for comparing images, especially at the sub-30 nm scale. Moreover, the interpretation of the SE contrast of EBID lines is not straightforward due to effects like enhanced SE emission from a slope ([46], [47]). In conclusion it is safe to say that there is almost no data available on high resolution dense EBID lines, the first report being as recent as 2014 [48]. Here we present a systematic study of the reproducibility of sub-30 nm dense EBID lines. The following section describes the fabrication of the lines, followed by the imaging and characterisation techniques used. We aim to characterise the lines as is commonly carried out in resist-based lithography - by measurement of the line width and line edge roughness using edge detection, as well as line height.

3.1 Metrology of dense EBID lines

The first step in the metrology of EBID lines is imaging, the most commonly used mode being the SE mode, which is also used in the imaging of resist-based lines. The FEI Verios 460 SEM (Fig. 3.1) has two SE detectors - The Everhart Thornley Detector (ETD, not shown) and the Through Lens Detector (TLD) and two BSE detectors - In Column Detector (ICD) and Mirror Detector (MD).

In the ultra high resolution (UHR) mode of the SEM (also used in this work), a magnetic field is applied to achieve a smaller spot size, also immersing the sample. In this mode, the SE's must be collected in the column by the TLD as they no longer reach the ETD located on the side. A typical TLD image of high resolution dense EBID lines is shown in Fig. 3.2 along with the integrated line profile. Clearly, the profile has an asymmetric shape, appearing to dip at the edges, with higher intensity at the centre of the line.

However, contrast in SE images is not purely topographic. It can also contain material contrast as different materials have different yields of SE's, as well as contrast from other sources ([46]). Edge effects coming about due to enhanced SE emission from angular sidewalls of thicker deposits can often lead to misinterpretation of line shapes. Fig. 3.3 (a) shows a cartoon of an EBID deposit whose "real" profile is Gaussian. If this deposit is thick enough, the corresponding SE image would have

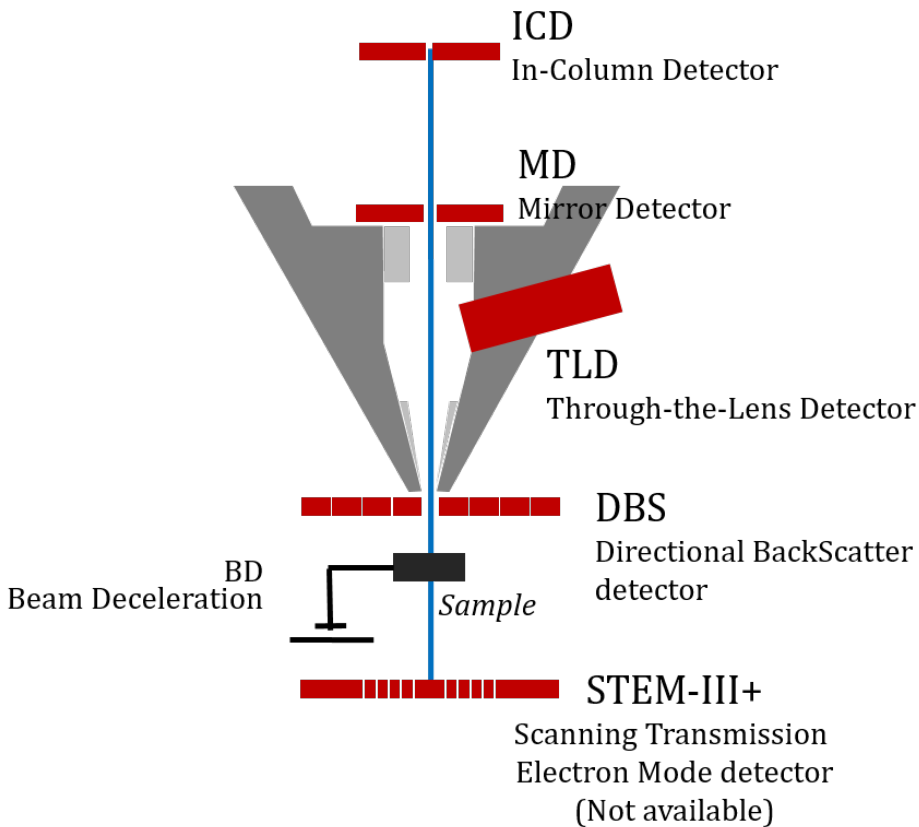


Figure 3.1: Schematic of the FEI Verios 460 SEM illustrating the detection scheme with the Through Lens Detector (TLD) for SE imaging and two BSE detectors - In Column Detector (ICD) and Mirror Detector (MD).

highlighted edges, resulting in a line profile containing peaks at the edges (as shown). On the other hand, if an EBID deposit has a "real" profile which peaks at the edges (b), such as obtained by patterning in diffusion-limited conditions [22], the profile obtained from the SE image could be identical to that in (a).

It is therefore difficult to say anything about the real shape of the EBID lines from the SE image, whereas this is commonly used to image resist-based lines. Since they typically have vertical sidewalls, the highlighted edges are a good indication of the edge position and they can be located quite accurately by fitting a Gaussian function to each edge. And finally,

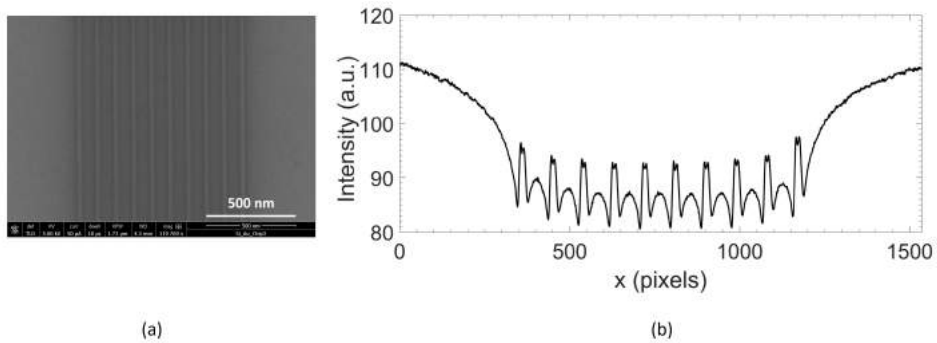


Figure 3.2: (a) Typical TLD image and (b) Integrated intensity profile of a set of dense EBID lines

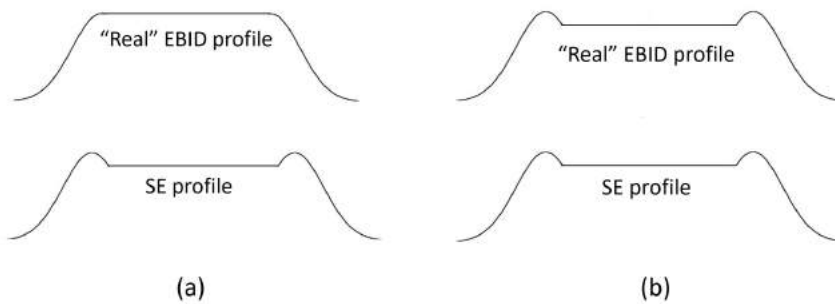


Figure 3.3: Cartoon showing EBID deposits and the corresponding SE images for (a) current limited Gaussian profile and (b) diffusion limited pitted profile. Due to the edge effects resulting from the sensitivity of SE emission to the topography, the actual 3D shape of the deposit cannot always be determined from the SE image.

since the SE's are generated from a depth of a few nanometres in the deposit, the signal is very sensitive to small variations in topology. The fluctuations in the SE profile between identically patterned lines can be quite significant. A zoom in of the profiles of the lines at the left and right extremes of the array in Fig. 3.2 is shown in Fig. 3.4 (a) and (b) respectively. The variation in identically patterned lines is visible, making it difficult to define a function that can be used to carry out a complete fitting of the profile. These differences cannot be due to peculiarities in the detection as the TLD is located on the axis of the microscope column and

the two lines have the same number of neighbours. Moreover, the array is spread over a very small length (the distance between the two lines is 900 nm). They must therefore result from actual topographic variations between the lines that must have come about during patterning. Therefore the interpretation of SE images to conclude the shape and extent of EBID lines is not straightforward. Consequently, the use of BSE imaging was

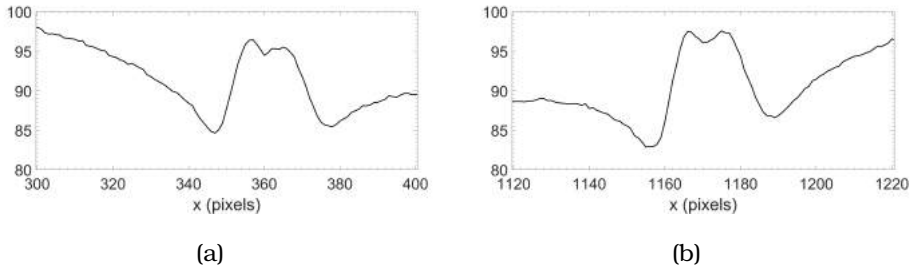


Figure 3.4: Zoom in of the intensity profile of the array in Fig. 3.2 showing the lines at the (a) left and (b) right extremes. The sensitivity of the SE signal to small variations in topology results in differences in the two profiles, making it difficult to define a function that can be used for a complete fitting of all the profiles.

investigated. Images acquired with the ICD detector, simultaneously with the TLD image in Fig. 3.2 are shown in Fig. 3.5. From the line profile

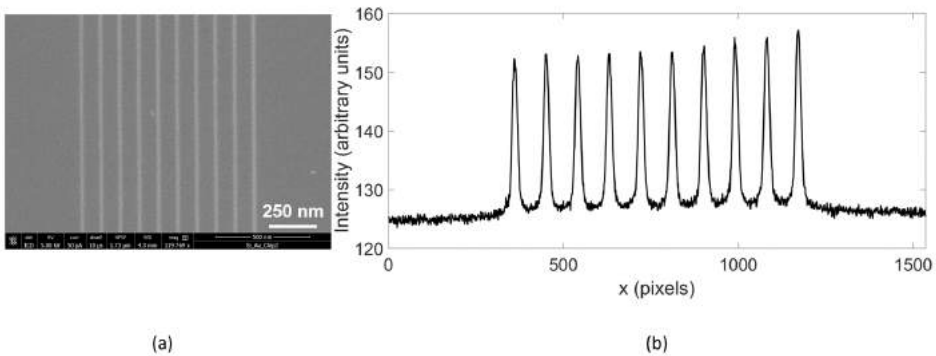


Figure 3.5: BSE image from the (a) ICD acquired simultaneously with the TLD image in Fig. 3.2 and (b) the corresponding integrated intensity profile

shown alongside, a Gaussian shape is evident as a consequence of the fact that BSE contrast in EBID lines arises due to the presence of material of a different atomic number than the substrate. This is promising as the goal of this work is to determine the extent of the material present in the

lines. It must be kept in mind though that this might pose a limitation for very shallow lines where there is hardly any contrast present in the ICD images. Any technique employing BSE imaging would be limited by this fact. It is interesting to note that in this case, the TLD images still show sufficient contrast for analysis and since the lines are so shallow, the SE profile is now Gaussian. This opens up the possibility of using SE imaging in certain cases where BSE imaging may not be useful. In conclusion, BSE imaging seems promising for the determination of line width in EBID. The thickness of the material (or 'halo') that would be sufficient for generating BSE contrast is an important factor, without knowledge of which the extent of the line cannot be concluded in absolute terms. It can however still be used to provide a consistent measure of line width, which is an important step. The ICD image shown in Fig. 3.5 was acquired at high

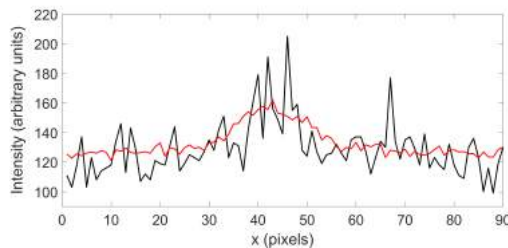


Figure 3.6: A line scan taken over 1 pixel (black) and 32 pixels (red) length of an EBID line showing how noisy such a profile is.

resolution with a horizontal field width of $1.73 \mu\text{m}$ and resolution of 1536×1024 pixels. The pixel size in both x and y is equal to 1.1 nm. For all experimentally acquired images in this thesis, 1 pixel = 1.1 nm unless otherwise mentioned. The direct application of edge detection techniques to such an image presents some challenges. Fig. 3.6 shows a one pixel wide line scan (in blue) taken over one of the EBID lines. The profile is so noisy that there are multiple peaks visible and thresholding, a commonly used technique, cannot be applied as it would lead to loss of information about the line itself. Filtering, another popular technique, may be implemented, for example, by averaging over several pixels along the length of the EBID line. The red plot shows the profile of the same line after averaging over 32 pixels along the length and it may now be possible to detect the edges. However, the effect of filtering on the measurement of line edge roughness has been studied in [40] and the filter strength has explicitly been shown

to alter the measurement. So this is inadvisable. And although commercial edge detection techniques are often used for resist-based lines, EBID line profiles are so different that the method would have to be modified. This is not an easy task as the algorithms are typically not available to the user for editing.

An edge detection technique was developed for sub-30 nm EBID lines, based on a newly developed technique ([40]) with the capacity to detect edges in very noisy images. This is described in detail in the following section.

3.1.1 Edge Detection in dense EBID lines

The ICD image shown in Fig. 3.5 was selected for this analysis.

1. Any slope present in the plot of the integrated intensity (Fig. 3.5(b)) was subtracted, the plot was smoothed and a function was fitted to the profile of each EBID line. Because of the different base levels adjacent to different EBID lines, a combination of a normalised double Gaussian function, vertically shifted and matched at the centre, defined as follows:

$$f(x) = \begin{cases} b_L + (1 - b_L)\exp\left(-\frac{1}{2}\frac{(x-\mu)^2}{\sigma_L^2}\right) & x < \mu \\ b_R + (1 - b_R)\exp\left(-\frac{1}{2}\frac{(x-\mu)^2}{\sigma_R^2}\right) & x \geq \mu \end{cases} \quad (3.1)$$

was fitted, allowing all parameters (μ , σ and left and right base levels - b_L and b_R) to vary. The window used for the fit is the region midway between adjacent EBID lines, to the left and right of the line of interest. The fitting was performed using the matlab function 'lsqnonlin', a least square minimisation algorithm. Fig.3.7 shows the function fitted to one of the EBID lines in the image.

2. Next, this function is fitted to every scan line of that EBID line with μ as the only fitting parameter, thus determining the centre of the EBID line per scan line. A straight line fit through these positions gives us the centre of the EBID line, shown in yellow in Fig. 3.8
3. With the centre positions thus fixed, the function is fitted to every scan line of the EBID line, this time with σ_{left} and σ_{right} as the fitting parameters. The 1σ value (left and right) from the fit are then plotted (Fig. 3.9) showing the position of the edge in every scan line.

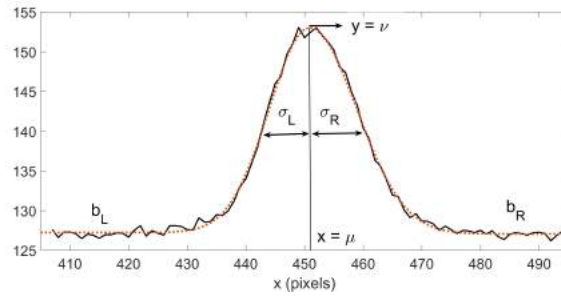


Figure 3.7: Fit of a double Gaussian function (red) to the integrated profile of one of the EBID lines in the image (black).

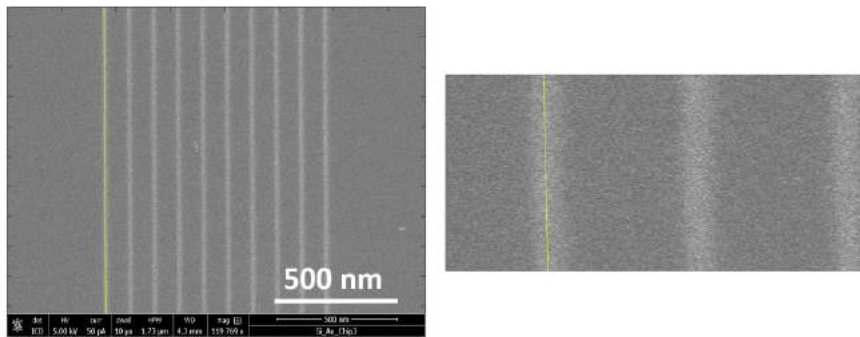


Figure 3.8: Straight line fit (Inset shows a zoom-in) through the set of centre positions determined per scan line from the fluctuations of the double Gaussian function. The yellow line is thus found to be the centre of the EBID line.

4. The 1σ value of line width (LW) determined per scan line per EBID line (as $\sigma_L + \sigma_R$) can be averaged to yield values for each EBID line (LW line), for each image (LW Image) and for a set of identically taken images (LW Set). The line edge roughness (LER) is defined as the standard deviation of the edge position. The LER is calculated for the left and right edges for every EBID line as $\frac{(\sigma_L + \sigma_R)}{2}$. This can be averaged to yield values for LER Line, LER Image and LER Set as before. It is important to note here that the values of LER thus obtained are biased due to noise. The total standard deviation in the

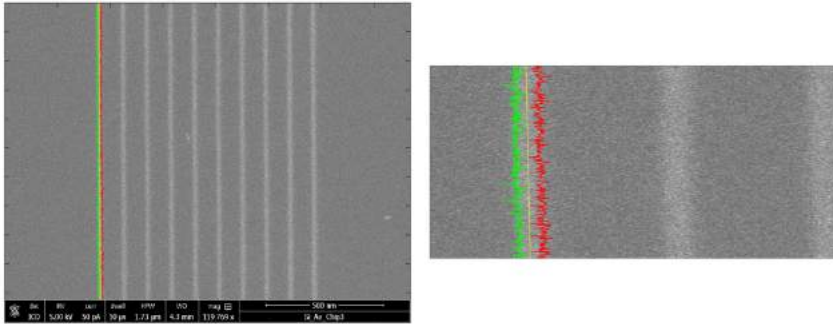


Figure 3.9: The left and right edges (green and red respectively) of an EBID line determined in every scan line of the image. Inset shows a zoom-in of the fit on one of the lines.

edge position is given by:

$$\sigma_{\text{total}}^2 = \sigma_{\text{EBID}}^2 + \sigma_{\text{noise}}^2 \quad (3.2)$$

for the left and right edges separately. The quadratic addition of terms holds under the assumption that the deposition and the noise are independent processes. The noise in turn could contain contributions from various sources like vibrations during patterning, vibrations during imaging and white noise during imaging, each of which contributes a quadratic term. In principle, the noise term can be extracted from the power spectral density (PSD) of a set of identical lines, yielding the unbiased value of LER in the case of Gaussian noise ([40]). This will be discussed in more detail later in the chapter. The method described in the above steps makes it possible to fit the function to every scan line in spite of the noise because several parameters are constrained while σ is used as the fitting parameter. The 1σ value for LW and LER can be determined from this method and although this choice is arbitrary, it provides a consistent measure of width and roughness, sufficient for the study of reproducibility. The calculation of 2σ and 3σ values from this, if needed, is trivial. There is of course also a limit to how noisy an image can be fitted using this

method and this will be dealt with later.

3.1.2 Performance verification of edge detection technique

As in the case of any new technique, its performance needs to be verified before conclusions are drawn from its application to experimental data. The following section provides a direct test of our edge detection method by applying it to lines whose dimensions are known. These lines have been generated by a matlab simulation. A random signal 1024 pixels in length has been generated as described in ([40]) to have a Power Spectral Density (PSD) which is defined by the user by specifying the values of correlation length and roughness exponent (in this case equal to 30 pixels and 0.75 respectively). It comprises the fluctuations of the edge of an EBID line measured from the centre, with the mean value of the displacements equal to the given LER (here 0.5 pixels). The input PSD is shown in Fig. 3.11 and has a noise level of zero as it represents the ideal case. Next, a double

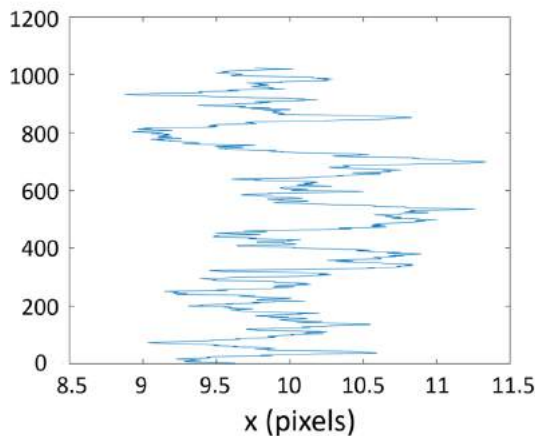


Figure 3.10: A random signal generated having a Power Spectral Density defined by the user.

Gaussian function was generated with the following arbitrarily chosen dimensions: $\sigma_{\text{right}} = 10$, $\sigma_{\text{left}} = 10$, $\nu = 35$ and base level = 20.2. The 1σ point of this function was then stretched to match the extent of the random signal defined above. This was performed for the left and right edges

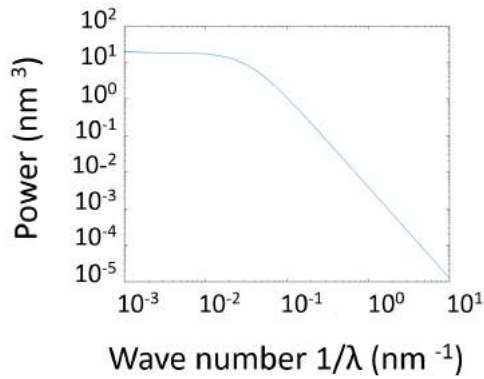


Figure 3.11: Input PSD used to generate the signal in Fig. 3.10. The parameters used were: correlation length = 30 pixels and roughness exponent = 0.75

in each scan line, resulting in a simulated EBID line. The fluctuations described so far are purely due to the deposition process and no noise is included. An SEM image of a set of 9 such EBID lines is shown in Fig. 3.12. The image is 1024 by 1024 pixels in size and the lines are equally spaced with a gap of 70 pixels from the left and right ends of the image. In reality, of course, there is pixel noise present during imaging. This has

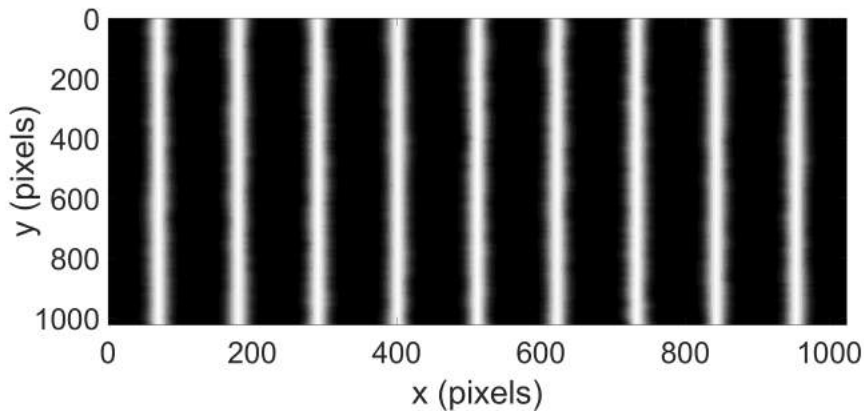


Figure 3.12: A simulated SEM image of a set of 9 dense EBID lines. The fluctuations of the edges shown here come about due to the deposition process alone and no noise is present in the image.

been simulated by adding Poisson noise to the above image and the noise

at any pixel is proportional to $1/\sqrt{n}$ where n is the signal (in number of electrons) from that pixel. Fig. 3.13 shows the simulated noisy SEM image of EBID lines of predefined dimensions. The edges of this image have

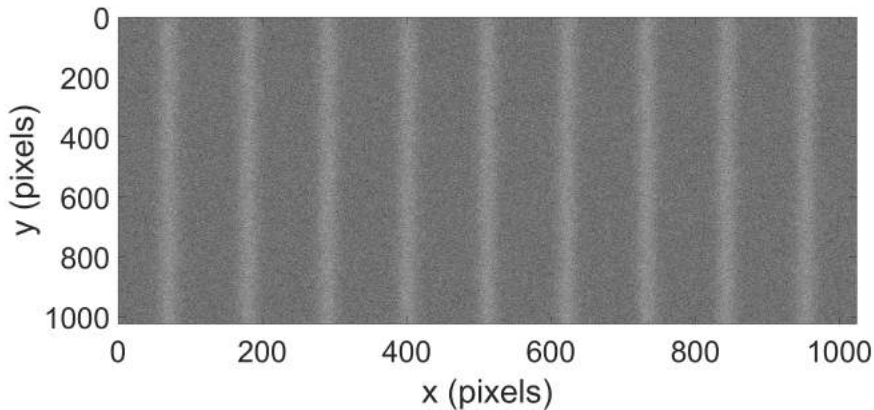


Figure 3.13: A simulated SEM image of the set of 9 dense EBID lines with Poisson noise added to the signal.

been detected using the technique developed here and they are plotted in Fig. 3.14. Detecting the edges from the simulated image (with no noise) should obviously yield the given values of σ , LER, roughness exponent and correlation length. The PSD of the lines might naively also be expected to have a noise level of zero as in the input PSD, but this will not be the case in reality due to the significant bias arising from the fitting in the detection of a mere 20 edges ([40]). So the values determined would be approximate. However, this PSD should overlap very well with the input PSD. Detecting the edges from the simulated image (with noise) should yield biased values of LER and the correct values of σ_{left} and σ_{right} . The unbiased value of LER can be obtained from the PSD by subtraction of the noise level and this should once again be equal to the input value.

From Fig. 3.14 the mean values of σ_{right} and σ_{left} have been determined to be 10.2 and 10.5 pixels which is in excellent agreement with the predefined value of 10 pixels each. This is good evidence that the technique works well for EBID lines and we now proceed to the application of this method to the measurement of reproducibility in EBID.

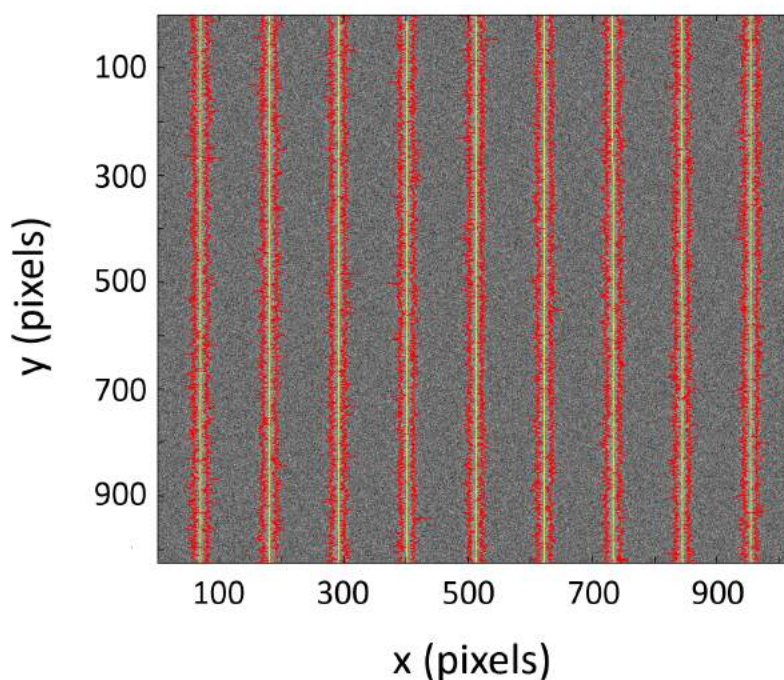


Figure 3.14: Edges of the EBID lines detected in the simulated SEM image using the technique described above.

3.2 Experimental details

This section describes in detail the method of fabrication of dense lines, followed by the imaging and characterisation techniques.

3.2.1 Patterning of dense EBID lines for measurement of reproducibility

Dense EBID lines were patterned on a silicon chip with natural oxide by EBID from the MeCpPtMe_3 precursor. To ensure patterning in the current limited regime, the parameters were chosen based on the results of chapter 2. An FEI Nova Nano 650 Dual Beam system and an FEI Verios 460 SEM were used for EBID and patterning was carried out using an in-house Labview program which positioned the beam as per coordinates defined in

a stream file.

1. Patterning was carried out over approximately 1 mm^2 of the substrate. Multiple data sets were acquired with an interval of about a year. When a stage move of $100 \text{ }\mu\text{m}$ or more was performed, the beam focus was verified before resuming patterning, using grains of gold-palladium on markers adjacent to the patterning field. A part of the layout of a chip is shown in the left image in Fig. 3.15. The circles visible are fields of silicon covered with native oxide, meant for patterning. The labels A2, A3, etc. are also made of silicon. The rest of the chip is covered with a layer of gold-palladium (about 30 nm thick), so that the edges of the fields (indicated by the red square in the left image) as shown in the high magnification image on the right act as markers for focussing the beam. The patterning field itself was not scanned prior to the fabrication of the lines, in order to avoid contamination.

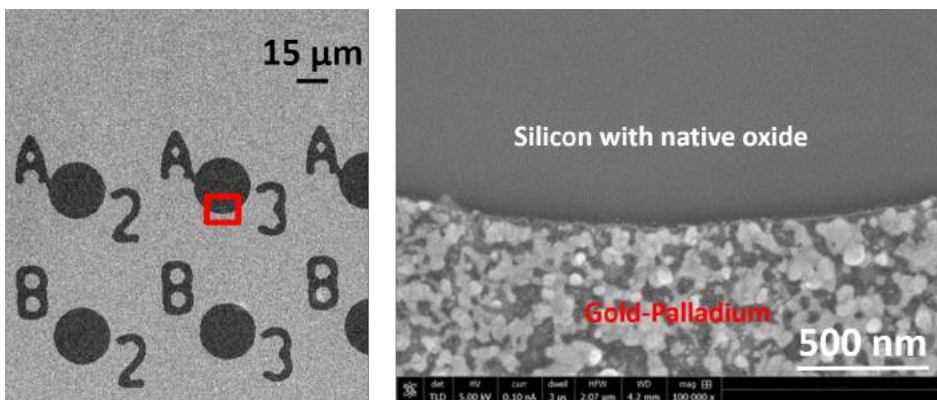


Figure 3.15: Layout of the chip used for patterning. (Left) The circles are fields of silicon covered with native oxide, meant for patterning. The labels A2, A3, etc. are also made of silicon. The rest of the chip is covered with a layer of gold-palladium (about 30 nm thick), so that the edges of the fields (indicated by the red square in the left image) can be used for focussing the beam. (Right) High magnification image of the region indicated by the red square.

2. Lines were patterned in the horizontal as well as vertical direction, mainly to see the effect of possible drift or bias with respect to the nozzle or detectors.
3. Lines were patterned in both serial and parallel mode with serpentine writing strategy.

4. The SEM chamber was vented and pumped down a few times in between, each time to a base pressure in the range 2×10^{-6} mbar to 5×10^{-6} mbar, so the effect of varying contamination levels, if present, could be noted. The sample was always mounted at eucentric height and placed in the same orientation with respect to the door of the SEM.
5. The GIS temperature was maintained at 45°C , and the gas load was 1.2×10^{-5} mbar. The nozzle of the GIS was aligned at the very beginning to be $150 \mu\text{m}$ above the sample at eucentric height and $75 \mu\text{m}$ away from the centre of the field of view, and no special efforts were made to maintain this alignment over time.
6. Patterning was begun 45 minutes after the GIS temperature had reached the set value. After an hour or so of patterning, the GIS valve was closed, the needle retracted and the heater switched off for an hour, before repeating the inlet procedure for the next set of deposits.
7. On one occasion, the chamber was cleaned using an oxygen plasma overnight prior to patterning the next morning. On the others, no special efforts were made to clean the system. It should be noted that during this period, the SEM was also used for other (unrelated) EBID work, involving use of the same precursor and a variety of samples.

The idea of this scheme was to take into account the sensitivity of the process to real-life patterning circumstances where the GIS, for example, is not always realigned prior to patterning, nor is the contamination level of the chamber necessarily the same during all experiments.

Four sets of 10 vertical and 10 horizontal lines each were patterned repeatedly using the following parameters:

1. **Set-1a:** Defined width = 10 nm, spacing = 100 nm, dwell time = $1 \mu\text{s}$, pitch = 1 nm, number of passes = 10, current = 40 pA, Dose = 400 C/m^2 , energy = 20 keV, UHR mode, FEI Nova Nano 650 Dual Beam
2. **Set-1b:** Set-1a repeated after a year
3. **Set-2a:** Defined width = 15 nm, spacing = 100 nm, dwell time = $1 \mu\text{s}$, pitch = 1 nm, number of passes = 10, current = 40 pA, Dose = 400 C/m^2 , energy = 20 keV, UHR mode, FEI Nova Nano 650 Dual Beam
4. **Set-2b:** Set-2a repeated after a year

where the line is patterned by pixel exposure with:

$$\text{Dose}[\text{C}/\text{m}^2] = \frac{\text{current}[\text{A}] \times \text{dwell time}[\text{s}] \times \text{number of passes}}{(\text{pitch})[\text{nm}]^2}$$

Spacing refers to the centre to centre distance between adjacent lines, dwell time refers to the pixel exposure time and pitch is the distance between neighbouring pixels. The estimated spot size at 20 keV and 40 pA is 1.6 nm. Each set was repeated several times (minimum 5, maximum 20) over approximately 1 mm² of the sample. A total of 112 images (1120 EBID lines) were analysed in this experiment.

3.2.2 Imaging of dense EBID lines for measurement of reproducibility

All sets of lines were imaged on the Verios 460 SEM in UHR mode simultaneously with the SE and BSE detectors. The imaging conditions were: working distance of 4 mm, beam energy of 5 keV, beam current of 50 pA and resolution of 1536 by 1024 pixels. The pixel dwell time and the detector settings are parameters that could be quite critical in obtaining a good image. A higher dwell time could improve the image quality by increasing the signal to noise ratio, but it could also lead to increased sample contamination by EBID, thereby worsening it. The detector contrast and brightness determine the greyscale values in the image, and to enable proper information capture and comparison between images, a protocol must be devised to set the right values. The imaging strategy and the influence of these parameters on the measurement of line width have been investigated systematically in separate experiments described below.

Effect of dwell time

The dwell time must be high enough to achieve a good signal to noise ratio, yet low enough that the effect of stage drift and contamination are not significant. A shorter dwell time is also advantageous from the point of view of total imaging time for multiple sets of lines. An array of 10 lines was patterned at 5 keV and 13 pA with a centre to centre spacing of 110 nm as shown in the SE image in Fig. 3.16 (a). The lines were defined to be zero width (single pixel exposure) and the dwell time used per line increased from 420 μs to 600 μs from left to right. The patterning was carried out in 5 passes. Two such arrays were patterned identically - one of them was imaged with a pixel dwell time of 10 μs and the other with 30 μs , at 5 keV

and 13 pA. The line widths were determined for each line using the edge

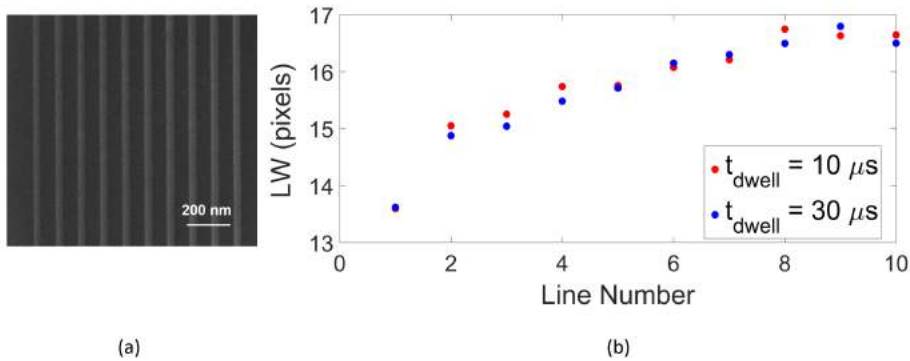
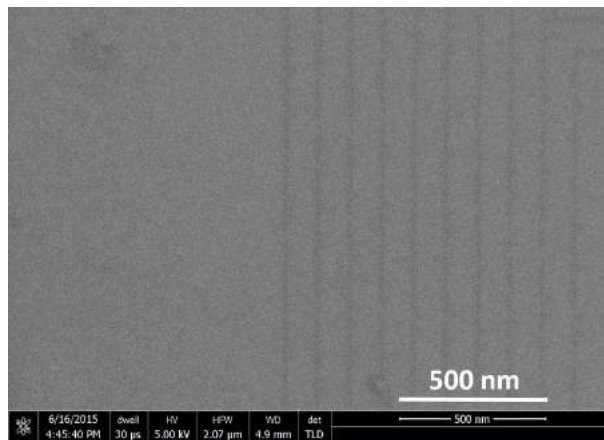


Figure 3.16: (a) SE image of a set of lines having a range of widths patterned by increasing the dwell time ($420 \mu s$ to $600 \mu s$) from left to right. (b) Plot showing a comparison of LW obtained by imaging two identical sets of lines as in (a) with dwell time = $10 \mu s$ (red) and dwell time = $30 \mu s$ (blue). The difference in LW from the two images is less than 0.5 pixels, demonstrating that a dwell time of $10 \mu s$ during scanning would suffice for obtaining good quality images for edge detection.

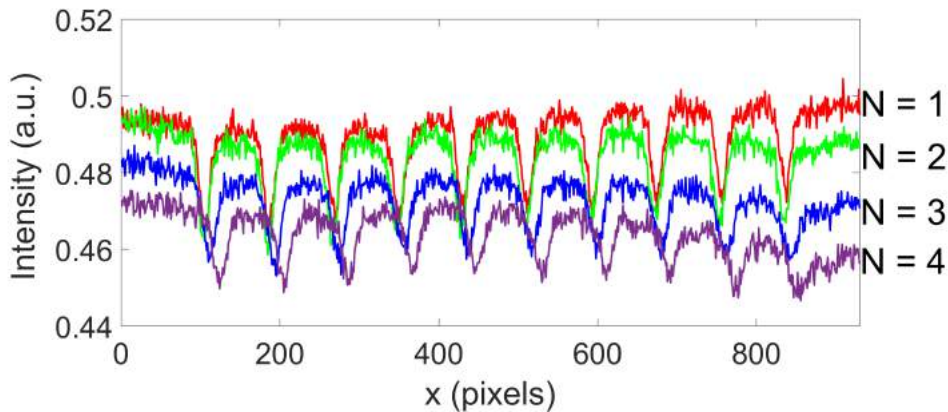
detection technique described above and the 1σ values are plotted in Fig. 3.16 (b) for both images. The red ($t_{dwell} = 10 \mu s$) and the blue ($t_{dwell} = 30 \mu s$) data points are seen to be very close in value. In fact, the difference in LW from the two images is less than 0.5 pixels, meaning that a dwell time of $10 \mu s$ suffices for imaging high resolution lines. Images of an identical set of lines recorded with $t_{dwell} = 100 \mu s$ showed significant stage drift and could not be used for LW measurement. Therefore, a dwell time of $10 \mu s$ has been used for all experiments where quantitative information regarding line dimensions was desired.

Effect of repeated imaging

On a few occasions, while navigating to the region of interest and/or positioning the lines at the centre of the field of view for imaging, multiple scans were performed unintentionally. This was observed to influence the contrast from the region. To quantitatively assess the influence of scanning on the LW, a set of very shallow dense EBID lines was patterned. The lines were defined to be 15 nm wide with a spacing of 110 nm and the SE image is shown in 3.17(a). It was imaged, in total, with four successive scans (corresponding to $N = 1, 2, 3$ and 4) with a dwell time of $10 \mu s$ each



(a)



(b)

Figure 3.17: (a) SE image of a set of very shallow dense EBID lines patterned to assess the effect of multiple scans on imaging and LW measurement. (b) Plot showing a comparison of integrated intensity profiles of images of (a) taken with $N = 1, 2, 3$ and 4 scans. The peak intensity can be seen to decrease and the LW seen to increase with each successive scan.

time. The integrated intensity profiles of the lines from the four images are compared in Fig. 3.17(b). The mean values of FWHM presented in Table 3.1 show a steady increase in LW with number of scans. Additionally, the peak intensity, relative to the substrate signal as well as relative to the original peak intensity can be seen to reduce as a result of repeated scanning. Both these observations could be due to deposition of carbon during scanning, which has a lower SE yield than silicon. Since the lines are lower in intensity than the substrate to begin with, it can be concluded

that they are mostly comprised of carbon (and not platinum). Scanning would initially lead to a reduction in the signal from the substrate due to the addition of a carbon film. The plot in (b) shows that the SE signal from the substrate indeed goes down with scanning. The strength of the SE signal from the lines would also reduce because adding a layer of carbon would suppress the SE's from the underlying silicon that were initially contributing to the signal. Subsequent scans would result in an additional layer of carbon being deposited on the lines and on the substrate. But since the lines are mostly made up of carbon, when the total thickness nears a value equal to the escape depth of SE's (r_{SE}) in carbon, the thickness of the carbon layer on the substrate would still be lower than r_{SE} . Therefore, additional scans would continue to lead to a decrease in the substrate signal intensity, whereas the decrease in the signal from the lines would be less. This would amount to a loss of contrast (peak intensity relative to substrate), as observed in the plots.

Scan number	Mean FWHM (nm)
1	21.8
2	22.6
3	25.4
4	26.8

Table 3.1: Mean values of FWHM of the set of lines shown in Fig. 3.17(a) measured upon repeated imaging (corresponding to scan numbers 1, 2, 3, 4). A broadening of the lines is seen to result from multiple scanning.

It should be noted that this argument is based on the detection of SE1's only. The effect of SE2's is neglected here because the lines are so shallow and thin that the number of BSE's, and therefore SE2's, contributing to the signal would be much lower. Also, for this reasoning to hold, the chamber contamination level must be sufficiently low so as to not have a thick carbon deposit because geometrical effects would then begin to play a role in SE emission. Control experiments show this to be a reasonable assumption for the microscopes used in this study.

Based on this study, it was concluded that multiple scans can significantly influence the LW as a result of contamination and care must therefore be taken to prevent this. Accidentally scanning multiple times during imaging is harmful, as is scanning the area prior to patterning. The exact dose at which this becomes significant, though, would depend on the

contamination level in the system.

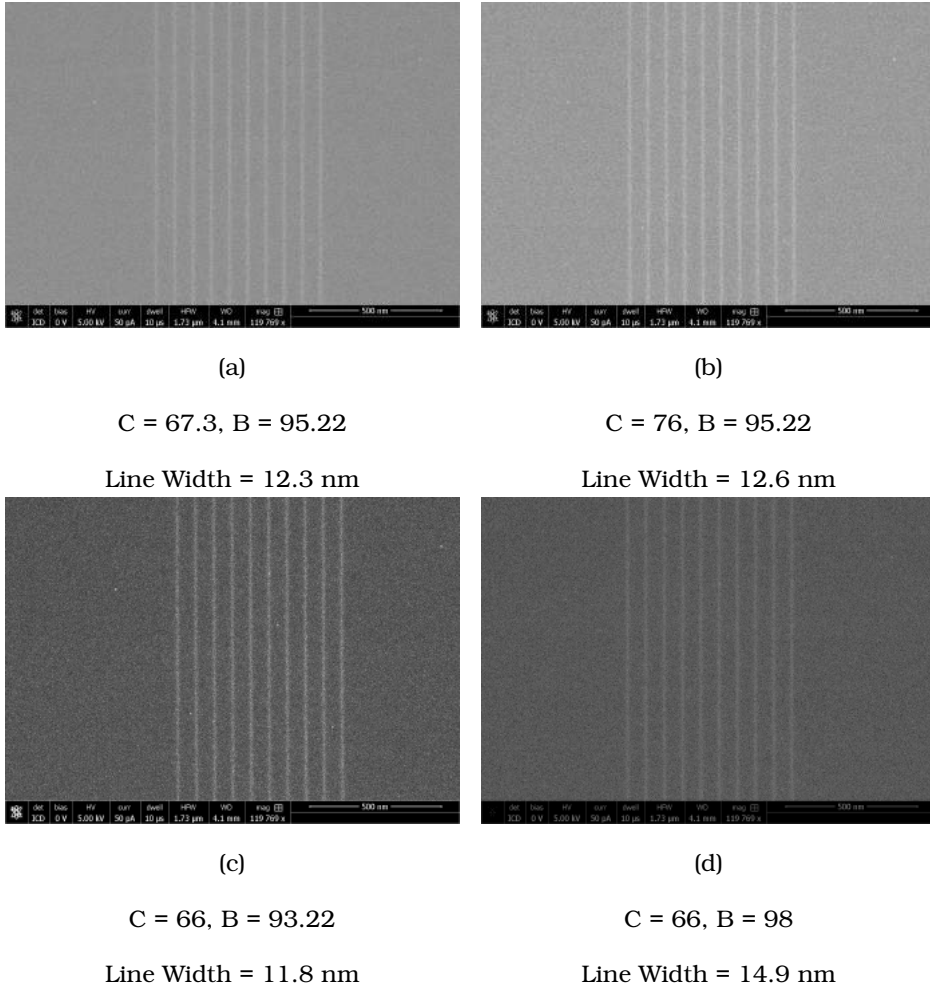


Figure 3.18: 2 pairs of images of EBID lines acquired with the ICD, used to study the influence of detector Contrast and Brightness on line width measurement. (a), (b) The brightness was fixed and the contrast was changed. (c), (d) The contrast was fixed and the brightness was changed. The corresponding values of mean line width per image are shown. Note: The contrast and brightness of the images (c) and (d) have been digitally enhanced. This was performed after the edge detection, purely to enable visualisation in print.

Effect of detector contrast and brightness

Identically patterned sets of EBID lines were imaged simultaneously with the three detectors. The contrast and brightness (C and B) of each detector were optimised independently using the videoscope signal/intensity

histogram once as follows. With the beam off, the values of C and B were set such that the dark noise was barely visible. This would ensure that any signal, when present, is captured. Then with the beam on, a fast scan (dwell time = 50 ns) was made in the region of interest. The contrast was kept low and the brightness was set so the signal on the videoscope was in the middle of the dynamic range. Then the contrast was increased until the signal strength spanned the extent of the dynamic range of the videoscope. As the fast scan displays the 'real' signal without averaging the noise, performing the optimisation under these conditions avoids clipping of the signal, thus obtaining the maximum information. Finally, with these detector settings (C = 67.3, B = 95.22 for the ICD), an image was acquired with a dwell time of 10 μ s. To study the influence of C and B on the measurement of line width, the contrast and brightness were then made sub-optimal by varying them by approximately 15 % and 5% respectively. In this range the signal was still within the limits of the videoscope, but no longer optimally so. The patterns were imaged with all other conditions remaining the same. The ICD images shown in Fig. 3.18 represent the cases of imaging under optimal conditions (in (a)) and sub-optimal conditions (in (b), (c) and (d)).

The integrated line profiles revealed that the peak values were not saturated or clipped in any of the four cases, although it might appear to be so from the images, especially in Fig. 3.18 (d). The edge detection technique was then applied to these images. The measurement of LW was found to be sensitive to the settings used, with a 15 % increase in contrast leading to a 6% increase in LW, and a 5% increase in brightness leading to a 25% increase in LW (as seen from a comparison of Fig. 3.18(a) with (b), (c) and (d)). Based on this study, it was concluded that the detector C and B values influence the measurement of line width significantly. The choice of these settings needs to be made using quantitative information regarding the signal strength and not merely with a view to producing visually pleasing images. An important extension of this result is that images of lines of different thicknesses can be compared most effectively if the settings have been optimised for each image independently, and not, as it might appear naively, by maintaining identical detector settings.

3.2.3 Characterisation of dense EBID lines for measurement of reproducibility

Set-1a

This set contains lines of 10 nm defined width at a spacing of 100 nm. The imaging conditions used were: energy = 5 keV, current = 25 pA, dwell time = 30 μ s. The contrast and brightness of the detectors were maintained at optimal values (within 2% of) ICD contrast = 90, ICD brightness = 99, MD contrast = 91, MD brightness = 90. The ICD and MD images (Fig. 3.19) of horizontal and vertical lines of the set were analysed. The edge positions, defined as the 1σ distance from the centre on either side, were determined from this fit, as well as the line width (LW) defined as the distance between the left and right edge. An example is shown in Fig. 3.20 where the edges are indicated in red and green. The LW was determined per scan line and the mean width of each line in the image is shown in Table 3.2. The results of this analysis performed over all the images is shown in Fig. 3.21 as the scatter in LW over the set.

	Mean Line Width
Line 1	14.2 nm
Line 2	14.3 nm
Line 3	14.5 nm
Line 4	14.2 nm
Line 5	14.3 nm
Line 6	14.0 nm
Line 7	14.2 nm
Line 8	14.0 nm
Line 9	14.2 nm
Line 10	14.1 nm

Table 3.2: Mean line width of each EBID line as determined from Fig. 3.20

The mean line width = mean(LW-Set), defined as the average over 1σ values of line width from the MD and ICD images of the set, is shown in Table 3.3. Since the patterning was carried out blindly, i.e., the field was not inspected by a fast scan prior to patterning, some particulate matter like dirt was occasionally observed in the images. Also, on one occasion, it was discovered that the GIS temperature had accidentally been changed rapidly and frequently in the period prior to the experiment. Likely as

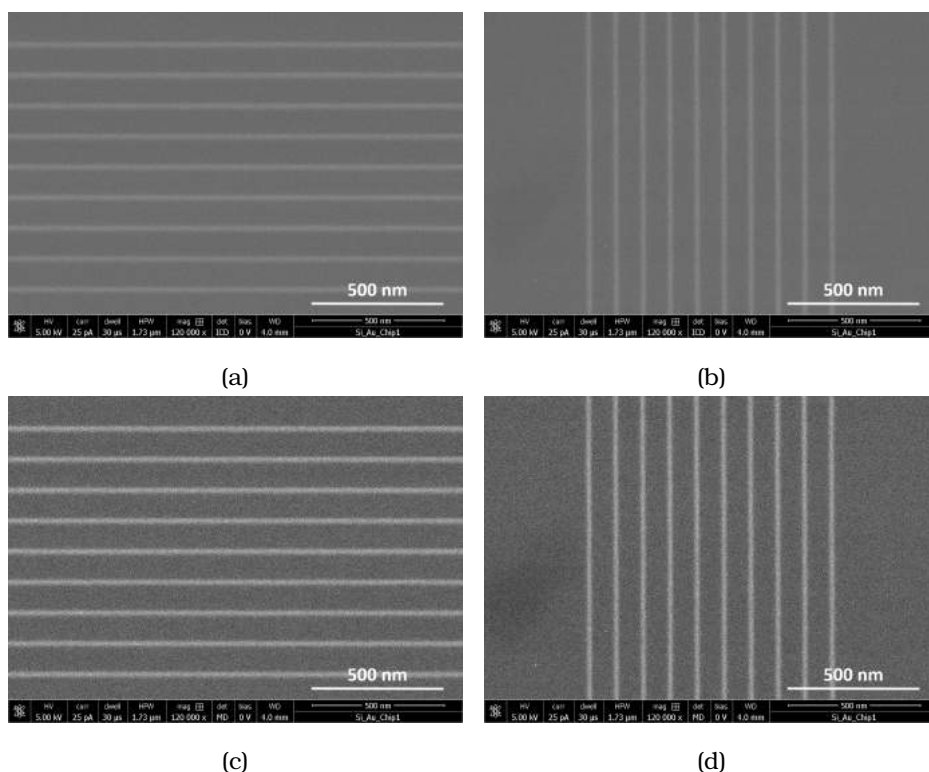


Figure 3.19: Typical images of the dense lines of Set-1a (a) ICD images of 10 nm wide horizontal lines (b) ICD images of 10 nm wide vertical lines (c) MD images of 10 nm wide horizontal lines (d) MD images of 10 nm wide vertical lines.

LW 10 nm horizontal from ICD = 15.7 nm	LW 10 nm vertical from ICD = 14.2 nm
LW 10 nm horizontal from MD = 15.2 nm	LW 10 nm vertical from MD = 13.9 nm

Table 3.3: Mean line widths of the lines of Set-1a imaged using the ICD and MD

a result, droplets of the precursor seemed to land on the sample during patterning, which when imaged, left behind large spots of deposit. The lines themselves also appeared smudged. An example is shown in Fig. 3.22 which corresponds to Image Number 1 in Fig. 3.21 (b) and (d). The edge detection technique is quite sensitive to such pixels of high intensity (such as those indicated by the red circles in Fig. 3.22), leading to a large scatter in the measurement of mean line width in that case. The line width measured from these lines was also significantly larger (> 19 pixels), causing the average line width of Set-1a to increase from 15.1nm to 16.0

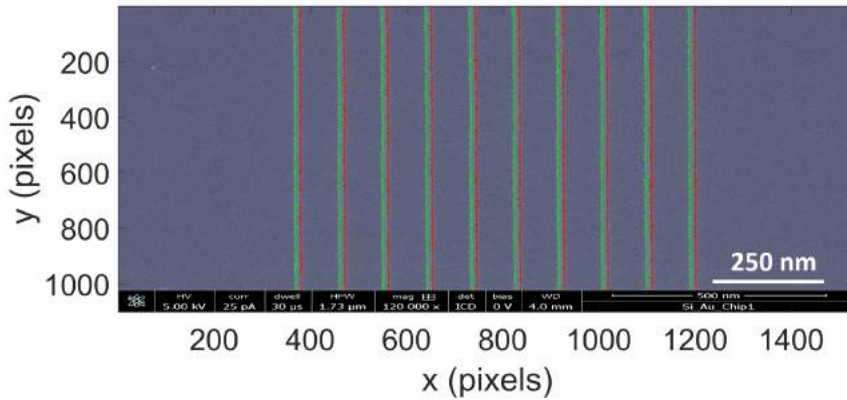


Figure 3.20: An example case, showing the edges of the EBID lines (in red and green) plotted on an ICD image of 10 nm wide dense lines of Set 1a (Conversion: 1 pixel = 1.1 nm)

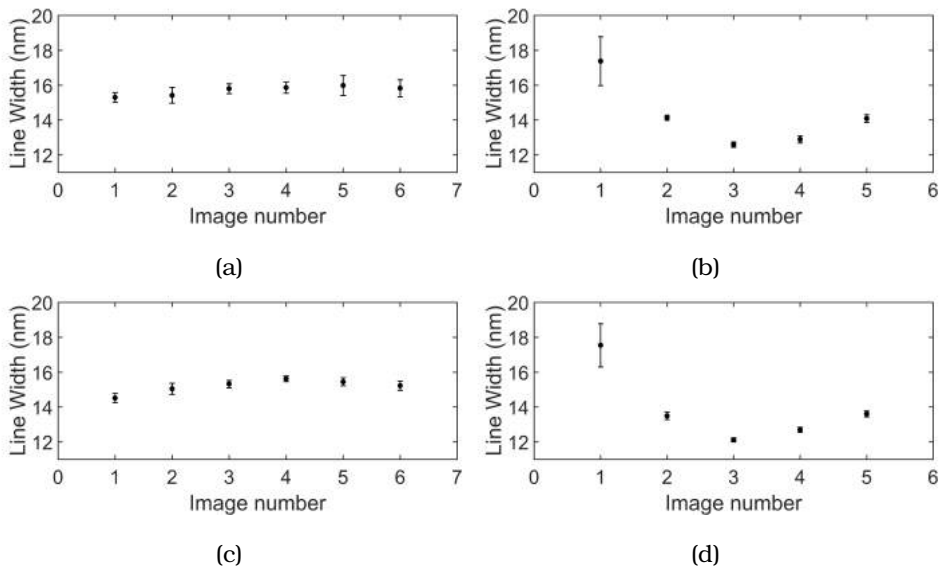


Figure 3.21: Plots showing the reproducibility of LW in Set 1a for (a) ICD images of horizontal lines (b) ICD images of vertical lines (c) MD images of horizontal lines (d) MD images of vertical lines.

nm. Care was therefore taken to exclude such images from the analysis of reproducibility and the numbers reported in Table 3.3. This was deemed honest since the GIS was discovered to not have been operating under standard conditions, a must for lithography.

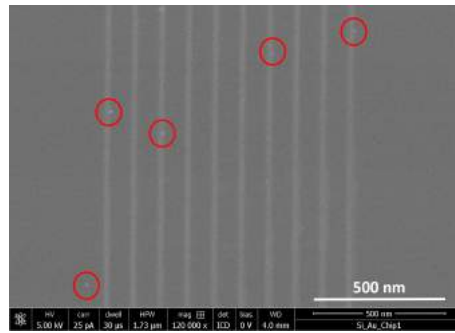


Figure 3.22: Lines of Set-1a patterned under non-uniform GIS conditions. Droplets of the precursor were found to land on the sample from the needle as a result of rapid and frequent changes to the GIS temperature in the period preceding the experiment, resulting in excess deposition at those positions (indicated by the red circles).

Set-1b

This set contains a repetition of the patterns in Set-1a, fabricated after approximately 1 year, to test the reproducibility over time.

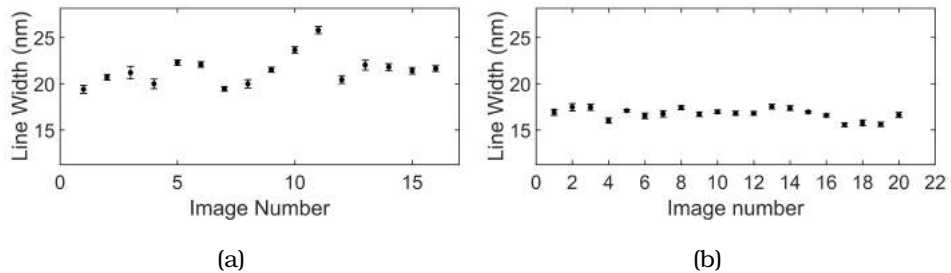


Figure 3.23: Plots showing the reproducibility of line width in Set-1b for (a) horizontal and (b) vertical lines.

The imaging conditions selected were the same as in Set-1a, but due to sustained problems with the Mirror Detector it was not possible to acquire images with it and only ICD images were analysed. The contrast and brightness of the ICD were set at the optimal values of 84.88 and 93.95 respectively and the scatter in LW values over 15 sets of lines is plotted in Fig. 3.23 for horizontal and vertical lines. The mean line widths are shown in Table 3.4.

LW 10 nm horizontal from ICD = 21.5 nm	LW 10 nm vertical from ICD = 16.8 nm
-------------------------------------------	-----------------------------------------

Table 3.4: Mean line widths of the lines of Set-1b imaged using the ICD

Set-2a

This set contains lines of 15 nm defined width at a spacing of 100 nm. The line width was measured as before using MD and ICD images (typical images shown in Fig. 3.24). The scatter in LW over 15 sets of lines is plotted in Fig. 3.25 for horizontal and vertical lines.

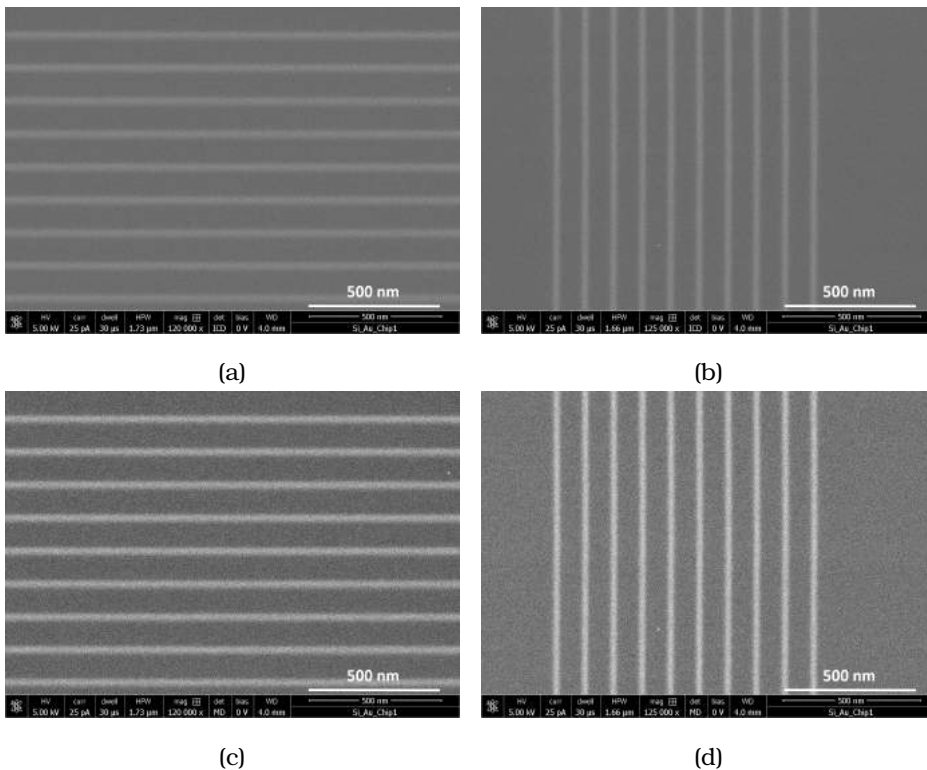


Figure 3.24: Typical images of the dense lines of Set-2a (a) ICD images of 15 nm wide horizontal lines (b) ICD images of 15 nm wide vertical lines (c) MD images of 15 nm wide horizontal lines (d) MD images of 15 nm wide vertical lines.

The mean line widths are shown in Table 3.5.

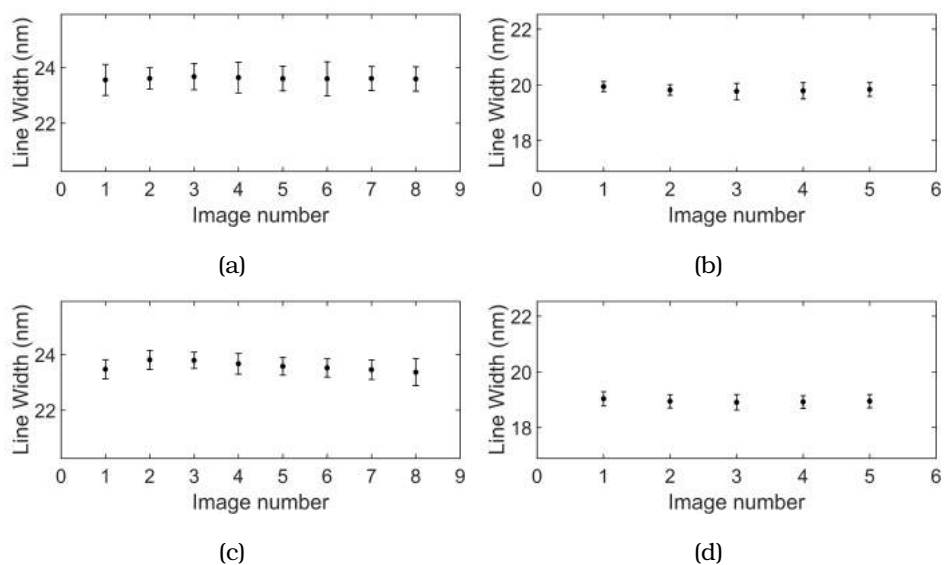


Figure 3.25: Plots showing reproducibility of lines in Set-2a measured from (a) ICD images of 15 nm wide horizontal lines (b) ICD images of 15 nm wide vertical lines (c) MD images of 15 nm wide horizontal lines (d) MD images of 15 nm wide vertical lines.

LW 15 nm horizontal from ICD = 23.5 nm	LW 15 nm vertical from ICD = 19.8 nm
LW 15 nm horizontal from MD = 23.2 nm	LW 15 nm vertical from MD = 18.9 nm

Table 3.5: Mean line widths of the lines of Set-2a imaged using the ICD and MD

Set-2b

This set contains a repetition of the patterns in Set-2a, fabricated after approximately 1 year, to test the reproducibility over time. As in the case

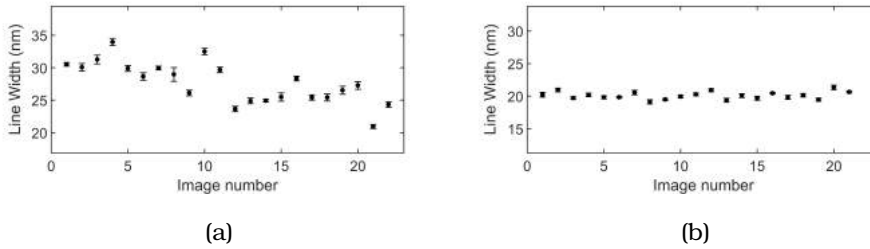


Figure 3.26: Plots showing the reproducibility of line width in Set-2b for (a) horizontal and (b) vertical lines

of Set-1b, it was only possible to acquire ICD images. The scatter in LW over 15 sets of lines is plotted in Fig. 3.26(a) and (b) for horizontal and vertical lines. The mean line widths are shown in Table 3.6.

LW 15 nm horizontal from ICD = 27.6 nm	LW 15 nm vertical from ICD = 20.0 nm
-------------------------------------------	-----------------------------------------

Table 3.6: Mean line widths of the lines of Set-2b imaged using the ICD

3.3 Results - Reproducibility of EBID lines

The scatter in line width observed in the above plots gives a measure of the reproducibility of high resolution patterning by EBID. The error bars in the reproducibility plots of the different sets are the variation in LW within an image, ie, over 10 lines. Since the patterning and imaging conditions for lines within an image and within a set were the same, the variation in LW across the set is an indication of the sensitivity of EBID to ambient conditions and the statistics of the process. There is also a scatter in LW over a single line. This is evident from the SEM images where it can be seen that the deposited lines are not perfectly smooth but have rough edges. This is referred to as the Line Edge Roughness (LER) and is equal to the standard deviation in the edge position per EBID line. It is an important quantity to specify together with LW. A high LER attests to large variations in the deposition process during the patterning of a line and would make

the technique unattractive. Very rough lines also restrict the proximity at which the next line can be patterned by creating interconnects.

The LER can easily be calculated from the edge positions, but this value is biased due to noise. In the case of resist based lines, a Power Spectral Density (PSD) analysis is often performed to extract the value of LER inherent to the process (unbiased LER). It yields the power of each frequency component present in the line. From this plot, the noise level in the set of images can be determined and the unbiased LER can be calculated from equation 3.2. A typical PSD of lines fabricated by resist-based lithography [40] is shown in Fig. 3.27. The profile can be seen to flatten out towards lower wave numbers, whereas at high wave numbers the PSD would fall to zero in the ideal case (Fig. 3.11). However, in reality, due to the presence of noise the profile is clipped and the noise level can be extracted by fitting the data as in [40].

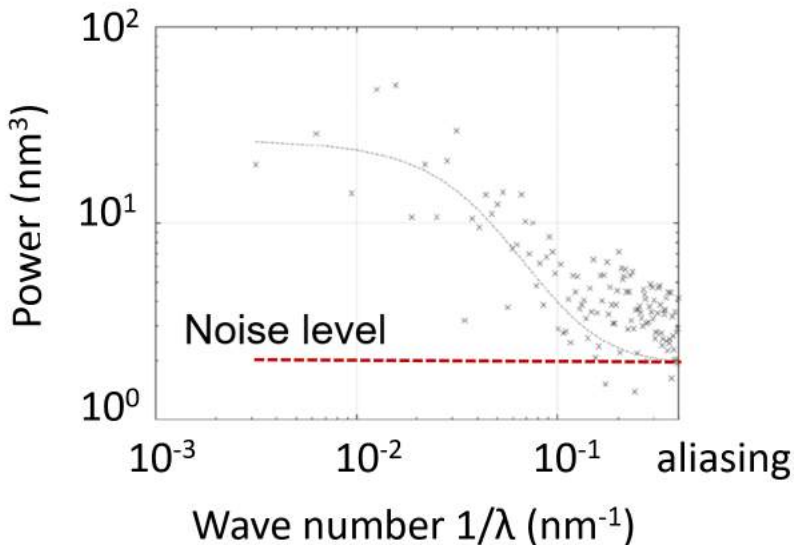


Figure 3.27: Typical PSD of resist-based lines [40]. The profile flattens out towards lower wave numbers, whereas at high wave numbers the PSD would fall to zero in the ideal case. However, due to noise, the profile is clipped and the noise level (shown in red) can be determined from the plot.

3.3.1 Power Spectral Density of EBID lines

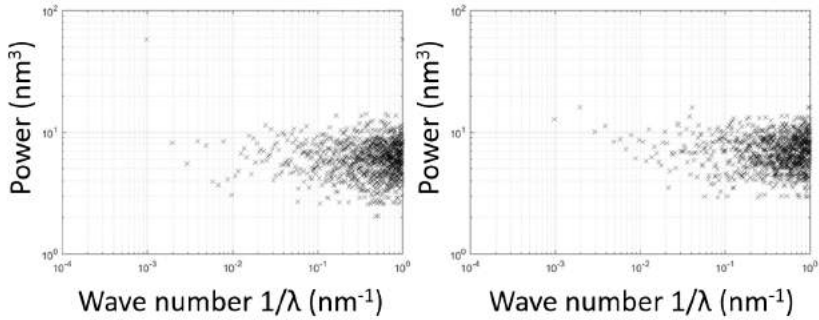
The analysis of the EBID lines resulted in a very different PSD from the one shown above. The differences can be seen in Fig. 3.28 where selected plots from the analysis of Set-1b (ICD images) are shown. Firstly, the PSD of vertical lines is not consistent within the set. Fig. 3.28 (a) shows two different kinds of PSD profiles obtained from the images within Set-1b. This was somewhat unexpected as no remarkable differences could be observed in the images themselves and the lines were patterned and imaged under identical conditions (as far as known). Secondly, while the same is true of horizontal lines as well, the profile is markedly different from that of vertical lines, as shown in Fig. 3.28 (b).

In Fig. 3.28 (a), the contributions to the PSD from the EBID line and that from the imaging noise seem impossible to distinguish. As there is no clear clipping of the curve at high wave numbers as in Fig. 3.27, the noise level cannot be captured. The profile in Fig. 3.28 (b) shows a dip at high wave numbers but once again, no distinct noise level is discernible. Based on these observations, we conclude that although the lines are homogeneous and reproducible, the unbiased LER cannot be determined from such a PSD. A more detailed analysis would first need to be performed to explain the frequency components observed. LER values are therefore not provided here, but will be discussed in Chapter 4.

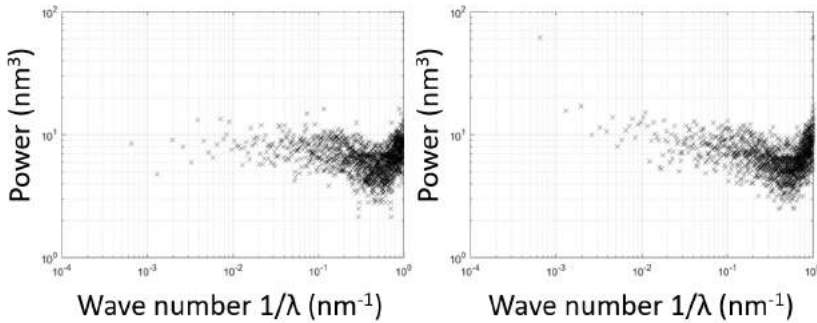
The observation of different PSD profiles in the horizontal (x) and in the vertical (y) directions could be a result of vibrations having different amplitudes in the two directions. During patterning, the vibrations in the x-direction were observed to be less than 5 nm, but were not measured in the y-direction. In the following section, an EBID simulator has been set up in which vibrations can be incorporated to assess their effect on the PSD.

3.3.2 EBID simulator including the effect of vibrations

An EBID simulator was developed in Section 3.1.2 to generate dense lines with a given width and PSD. To incorporate the effect of vibrations during patterning, however, a different model has been developed (Appendix B). An (ideal) EBID line 1024 pixels in length is generated in multiple passes



(a)



(b)

Figure 3.28: Two kinds of PSD profiles obtained by analysing individual ICD images of (a) vertical and (b) horizontal lines in Set-1b. The profile of the horizontal lines shows a dip at high wave numbers which is not the case for vertical lines, and in both cases a strong contribution is sometimes present at low wave numbers.

as in the experiment. Every pixel exposed to the electron beam is modelled as having a 2D Gaussian deposit patterned in each pass. The 1σ value of this deposit is a parameter in the model ('spot size') and corresponds roughly to the SE escape radius. The patterning pitch which was 1 nm in the experiment is also a user defined input parameter. The beam velocity is defined as the stepping velocity of the beam, which can be calculated from the dwell time and pitch. As the most likely source of vibrations in the setup is the electrical pickup from 50 Hz power sources, this was modelled as a sinusoidal wave of fixed amplitude and frequency independently in x

and y . The fluctuations in the two directions were defined as:

$$dX = A_x \times \sin\left(\frac{2\pi y}{\text{beam velocity}/F_x} + \phi_x\right)$$

$$dY = A_y \times \sin\left(\frac{2\pi y}{\text{beam velocity}/F_y} + \phi_y\right)$$

where $[dX, dY]$, $[F_x, F_y]$, $[A_x, A_y]$ and $[\phi_x, \phi_y]$ are the displacement, frequency, amplitude and phase of vibration in the x and y directions.

The EBID line was built in every pass by adding the displacements so generated in each direction to the existing Gaussian deposit at that pixel. It should be emphasised that the phase of the vibrations added to the line in each pass was random in order to mimic the experimental scenario. After the line has been built, random fluctuations are added to the line in the form of Poisson noise as in Section 3.1.2 to incorporate the effect of noise that may result from patterning and/or imaging.

An EBID line was generated in 4 passes with spot size = 5 nm, pitch = 1 nm, $F_x = 50$ Hz, $F_y = 50$ Hz. The resolution of the image is 1024×1024 pixels. Consider the ideal case where no vibrations are present ($A_x = 0$, $A_y = 0$). An EBID line (with no edge roughness) was generated as shown in Fig. 3.29(a). By adding Poisson noise = $\sqrt{200 \times P}$ where P is the signal from every pixel in the image, a new line was created as shown in (b), which is now rough. Both lines were analysed using the edge detection technique and the PSD's determined from the left and right edge combined are plotted in (c) and (d).

The addition of Poisson noise to the image alters the PSD of the EBID line considerably. Not only is the base level shifted towards higher power, the profile is flat as compared to that of the no-noise line (c). The consequences of adding vibrations to the no-noise EBID line has been investigated and Fig. 3.30 shows the resultant EBID line for three separate cases of 50 Hz vibrations in x (a), in y (b) and in both (c). All patterning parameters were the same as in Fig. 3.29. It is at once evident that a vibration amplitude as low as 3 nm is sufficient to introduce unwanted effects such as curvature

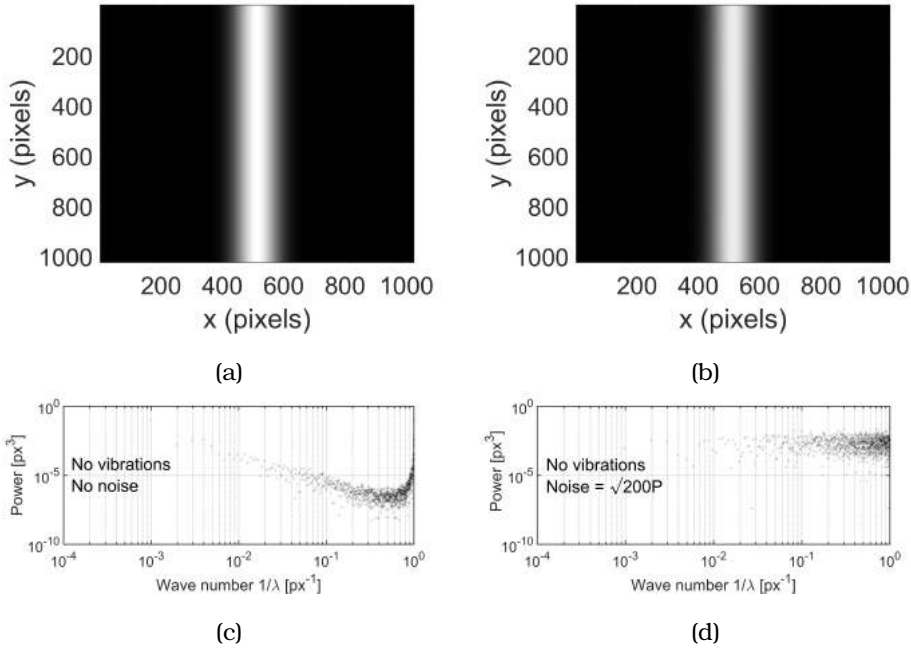


Figure 3.29: (a) Simulated EBID line modelled as overlapping pixels composed of 2D Gaussians patterned in 4 passes with spot size = 5 nm and pitch = 1 nm in the ideal case of no vibrations ($A_x = 0$, $A_y = 0$) and no noise. (b) Simulated EBID line generated with the same parameters with added roughness due to Poisson noise = $\sqrt{200 \times P}$ where P is the signal from every pixel in the image. (c) PSD of the ideal EBID line in (a) with no vibrations and no noise. (d) PSD of the EBID line in (b) with no vibrations but added roughness.

in the patterned line (a,c). However, the shape of the PSD is quite similar in all three cases and remains similar to the situation where there were no vibrations such as in Fig. 3.29(c). A typical profile is shown in Fig. 3.30(d). Since the phase is generated in a random fashion, repeating the simulation results in somewhat different results each time. Qualitatively, though, the same conclusions can be drawn regarding the shape and PSD of the line. It is also worthwhile to note that these unwanted effects were also observed when patterning was carried out in a single pass. While this simulation clearly demonstrates the effect of vibrations on a Gaussian EBID line, the experimentally observed PSD's therefore cannot be explained simply by vibrations added to a no-noise line.

Next, we consider the case of a rough EBID line simulated as before with Poisson noise = $\sqrt{200 \times P}$. The presence of 3 nm vibrations in the two

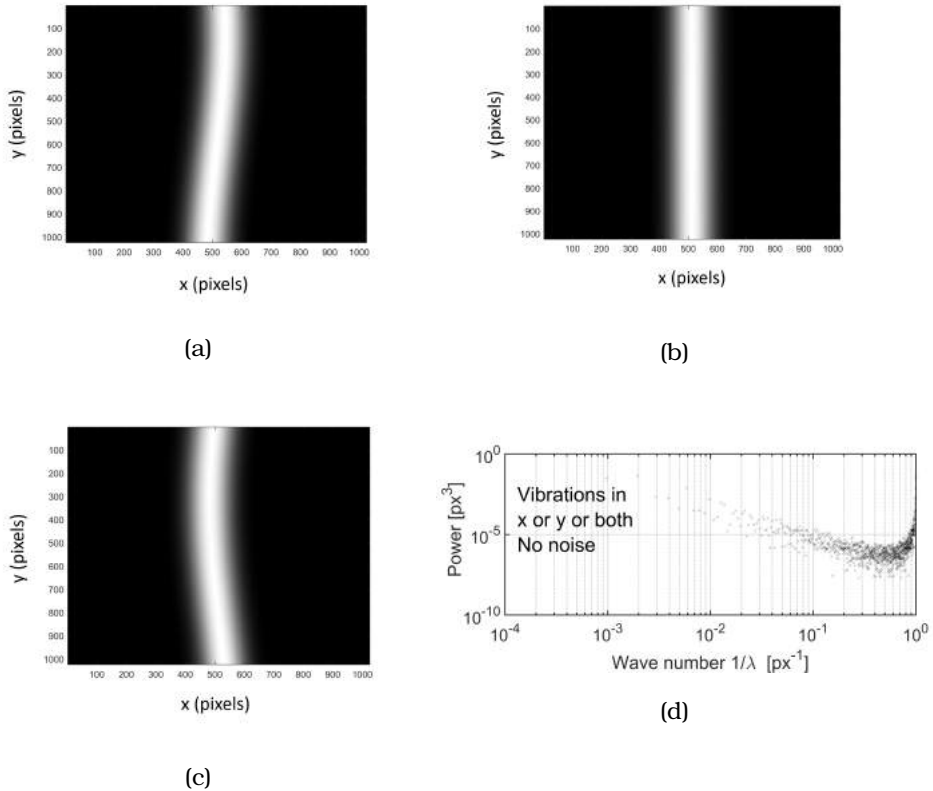


Figure 3.30: Simulation of a no-noise EBID line with 3 nm vibrations (50 Hz) in (a) x-direction (b) y-direction and (c) both x- and y-directions. The detected edges are shown here to bring out the shape of the line and it is evident that unwanted effects such as bending and curvature can be seen even at such low amplitudes of vibration. (d) A typical PSD of a no-noise EBID line obtained for the case of vibrations in either x or y or both.

directions resulted in bending and tilting of the deposited line as before, but in addition, significantly different PSD's were observed as shown in Fig. 3.31. This result shows that the presence of vibrations can lead to PSD profiles that are different from that in Fig. 3.27 and similar to the experimentally observed PSD's in this work. It is therefore critical to address the issue of vibrations for the metrology of EBID lines. Several sets of lines were selected from the experiments and the plot of the standard deviation of the left and right edges shown in Fig. 3.35 shows that the edges are correlated. This is true in the case of both horizontal and vertical lines and suggests the presence of vibrations in both directions, which

could have been present during patterning or imaging or both.

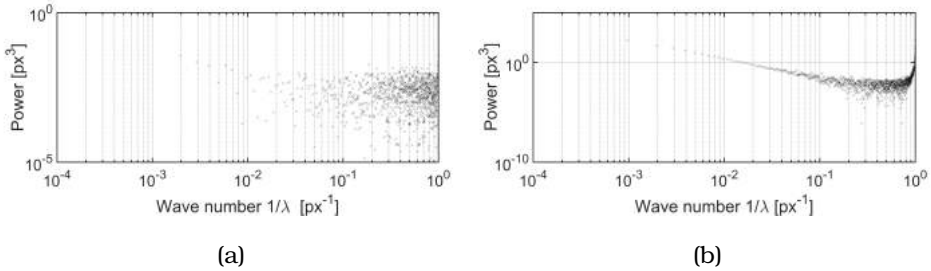


Figure 3.31: PSD of a rough EBID line generated with Poisson noise = $\sqrt{200 \times P}$. Vibrations of 50 Hz with an amplitude of 3 nm have been added in (a) y-direction and (b) both x- and y-directions.

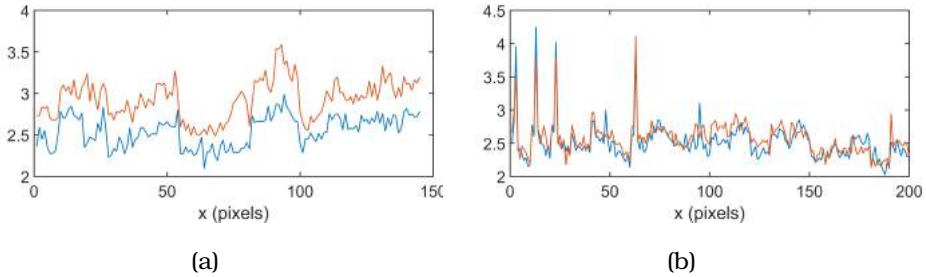


Figure 3.32: Plot of the standard deviation of the left and right edges for the horizontal and vertical lines of Set-1b, averaged per line, clearly showing that the edges are correlated, likely as a result of the presence of vibrations in both directions.

3.3.3 Reproducibility

We define reproducibility as the standard deviation of line width over the set.

$$\text{Reproducibility} = \text{std}(\text{LW-Set}) \quad (3.3)$$

The width of a new line patterned under identical conditions can therefore be predicted to be:

$$\text{LW-New} = \text{mean}(\text{LW-Set}) \pm \text{std}(\text{LW-Set}) \quad (3.4)$$

The data above show a spread in LW for 10 nm and the 15 nm lines over time and there appears to be a significant difference between horizontal

and vertical lines in some cases. Some interesting observations regarding SE and BSE imaging also bear reflection. A comparison of LW from MD and ICD images, for example, would reveal whether the choice of BSE detector is significant. This is important because their positions ensure the collection of BSE's of different angular range and consequently carrying different information which seems at first glance to be an important factor. Similarly, due to the disadvantages of SE imaging discussed previously, it is interesting to know whether it can be used as a measure of reproducibility. In the following section, an analysis of the scatter in LW is presented in terms of these observations, followed by results on the reproducibility of EBID.

3.3.4 Comparison of LW of horizontal and vertical lines

Set-1a, 1b, 2a and 2b clearly show that the width of vertical lines is on average lower than that of identically defined horizontal lines. Since the order of patterning within a field was: 10 nm horizontal lines, 10 nm vertical lines, 15 nm horizontal lines, and finally 15 nm vertical lines, this could not be attributed to loss of beam focus. But it could possibly be explained by drift or vibrations. To verify this, an Atomic Force Microscope (AFM) was used to measure the line heights. The AFM image of the lines of Set 2b (Fig. 3.33), acquired using a Bruker Fast Scan AFM, shows that the horizontal lines are in fact also less in height than the vertical lines, suggesting that this effect occurred during patterning. A comparison of the total deposited volume of the horizontal and vertical lines, however, is inconclusive. While the two volumes are not equal, they are within 20% of each other, as determined by gaussian fits to the AFM line scans (Fig. 3.33(c),(f)). The patterning time per line was in the range of 10 ms, from which we can deduce that if the broadening came about due to drift, it must be about 1 nm/ms, which is unrealistically high (a typical value for the system is 10 nm/s). It might be due to vibrations that have a larger amplitude in one direction. It must be noted that the same observation holds for lines patterned a year later on this microscope (FEI Nova NanoLab 600). Also, no significant difference in LW of horizontal and vertical lines was observed while patterning on the Verios 460 SEM. So it is most likely due to stage vibrations in the system. If that is the case, the vibrations must have occurred during patterning because the Verios 460 SEM was

used for imaging of all the sets. The horizontal lines are also seen to have a highly asymmetric profile compared to the vertical lines of the same set from inspection of the integrated SEM profiles. For the example case from Set-1b presented in Fig. 3.34, the mean position of the left edge is 9.1 nm from the centre and that of the right edge is 13.0 nm, for the horizontal lines. For the vertical lines, the numbers are 9.2 nm and 9.9 nm respectively, much lower in comparison. This also supports the idea that there were effects interfering with the patterning.

In another test, several sets of lines were selected from the experiments and the plot of the standard deviation of the left and right edges shown in Fig. 3.35 shows that the edges are correlated. This is true in the case of both horizontal and vertical lines and suggests the presence of vibrations in both directions, which could have been present during patterning or imaging or both.

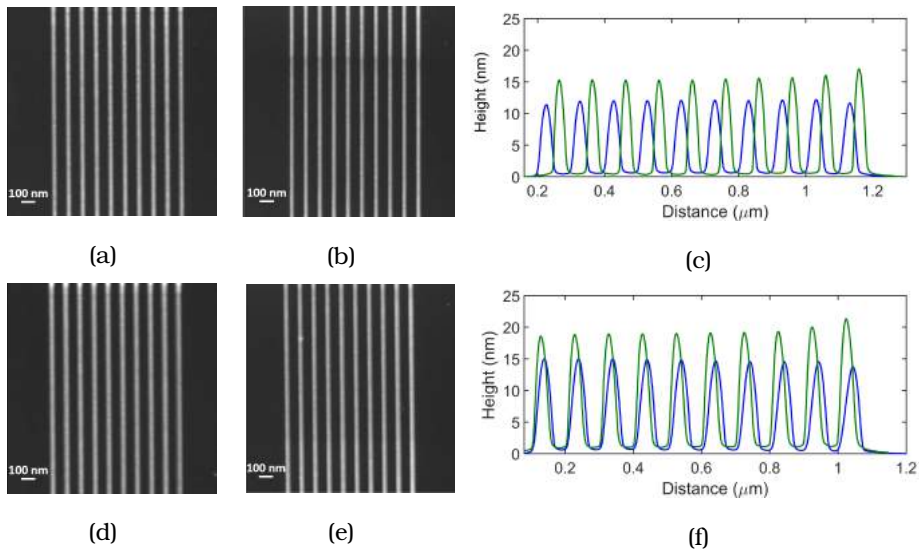


Figure 3.33: (a) AFM image of 10 nm horizontal lines and (b) 10 nm vertical lines. (c) Comparative integrated intensity plot of (a) and (b). The profiles of the horizontal and vertical lines are shown in blue and green respectively (d) AFM image of 15 nm horizontal lines and (e) 15 nm vertical lines. (f) Comparative integrated intensity plot of (d) and (e).

3.3.5 Reproducibility over space and time

The reproducibility of the EBID lines of each set is shown in Table 3.7

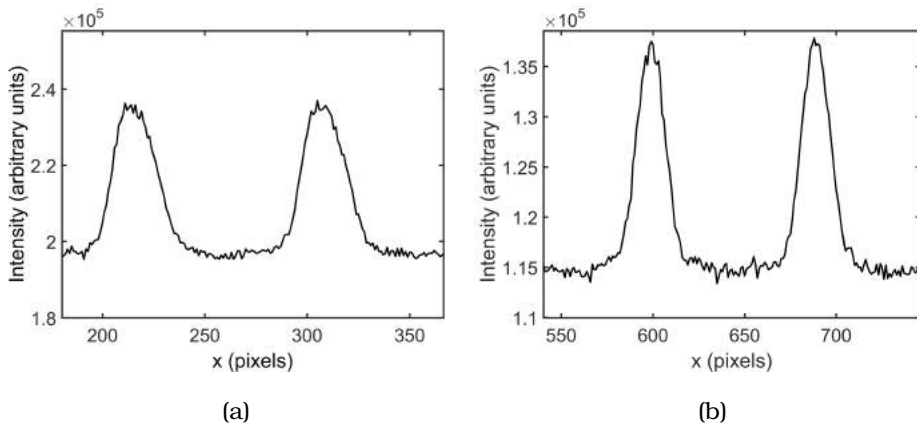


Figure 3.34: Plot comparing the line profiles of horizontal and vertical lines, showing the asymmetry in the case of the former.

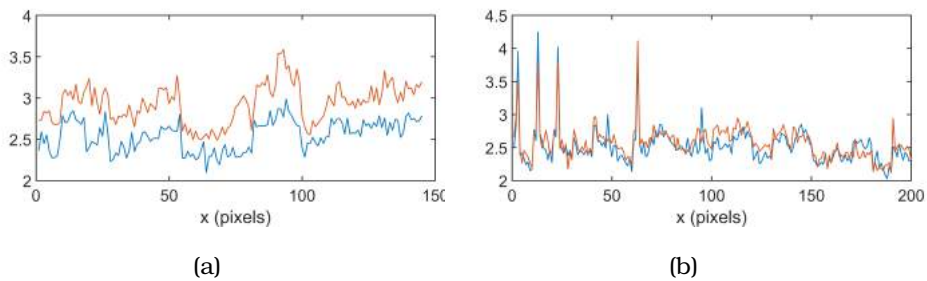


Figure 3.35: Plot of the standard deviation of the left and right edges for the horizontal and vertical lines of Set-1b, averaged per line, clearly showing that the edges are correlated, likely as a result of the presence of vibrations in both directions.

Set	Type	Reproducibility
1a	vertical	0.9 nm
1b	vertical	0.6 nm
2a	vertical	0.1 nm
2b	vertical	0.6 nm
1a	horizontal	0.3 nm
1b	horizontal	1.6 nm
2a	horizontal	0.03 nm
2b	horizontal	3.1 nm

Table 3.7: Reproducibility of EBID lines of each set

The reproducibility of vertical lines is within 1 nm and that of horizontal lines is within 3 nm. These values are very low, which is promising for high resolution patterning. It should be kept in mind, however, that

reproducibility of a set has been defined as the scatter in LW within the set of lines patterned, and it is not, for example, a physical quantity like the line edge roughness. The inherent reproducibility of high resolution EBID patterning can therefore be as good as 1 nm. The lower reproducibility observed in the patterning of horizontal lines may be due to the stage vibrations that also led to the asymmetric line profiles observed.

The reliability of patterning over time emerges from a comparison of Set 1 (1a and 1b) and Set 2 (2a and 2b) which were patterned with a gap of approximately one year. In this time, although changes such as refilling and realigning the GIS and major repair work including replacement of the pole piece and remounting of the stage had taken place, it is reassuring to see that the maintenance of identical beam parameters during patterning is sufficient to ensure reproducibility in the process. A comparison of the mean LW of vertical lines of Set-1a and Set-1b as well as Set-2a and-2b shows differences of less than 1 nm.

3.3.6 Comparison of line width measurement from ICD and MD images

The LW determined from simultaneously acquired ICD and MD images is the same to within 1 pixel. Although the LW from the MD images is consistently lower, this difference falls within the error of the measurement and is not significant. For the study of reproducibility, either detector can be used to image the lines.

3.4 Discussion

In order to detect the edges in every scan line of the image, as is performed by the edge detection technique, a certain amount of contrast between the EBID line and the background is needed. As the lines become shallower, it becomes increasingly difficult to detect the edges. A set of EBID lines has been patterned using a very low dose, serving to demonstrate this challenge:

Defined width = 9 nm, spacing = 110 nm, pitch = 1 nm, dwell time = 20 μ s, number of passes = 1, current = 6.3 pA, Dose = 126 C/m², energy = 5 keV,

UHR mode, FEI Verios 460 SEM

This set contains lines patterned with a much lower dose than that used in the previous sets. The first challenge in the metrology of such lines was that the amount of material present was too low to obtain BSE contrast and it could not be imaged using the ICD. Therefore the lines were imaged using SE detection with the TLD instead, and a typical image is shown in Fig. 3.36(a). The lines appear to have a Gaussian profile, albeit with a very low contrast, and edge detection was attempted.

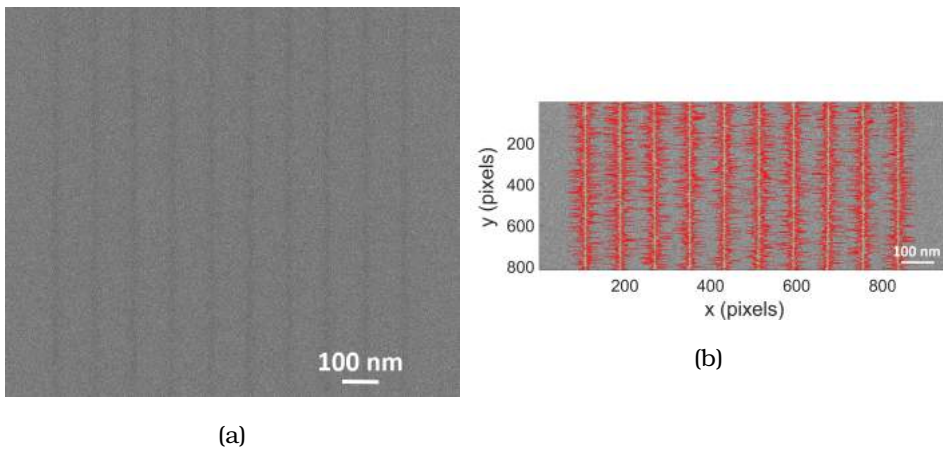


Figure 3.36: (a) Typical TLD image of dense EBID lines patterned with a very low dose (126 C/m^2) (b) Plot of the left and right edges detected in (a). Clipping can be seen to occur as the very low signal from the EBID lines makes the detection of edges difficult.

The LW characterisation was carried out as before, on the TLD images, only modifying the code to take into account the reversed contrast in the image. In Fig. 3.36(b) the edges plotted on the TLD image of the lines appear to be clipped at several locations. The low signal to noise ratio in these images is responsible for the failure of the fitting function to find an edge within the specified interval. This leads to the edge being determined as being at the boundary of the interval for that scan line. Such an image thus serves to demonstrate the limit of the fitting technique. For such lines, a simple analysis could still be performed with the TLD images by fitting the double Gaussian function to the integrated profile and determining its 1σ value from that fit. This would give a number for the LW for each EBID line, but without proper edge detection the variation in LW over the EBID line

cannot be estimated. It should also be pointed out that this set represents an extreme case, where the lines are so shallow that edge detection fails. Lines patterned with a somewhat higher dose, intermediate to the doses of Set-1 or Set-2 and the dose used here, for example, may still result in lines where the BSE contrast is insufficient for edge detection, but where the SE contrast is enough to enable the application of the technique. SE imaging could then be used for metrology.

3.4.1 Line Edge Roughness of EBID lines

The Line Edge Roughness of EBID lines has been measured from the edge fluctuations using the edge detection software. However, as it was not possible to extract the imaging noise from the PSD analysis, only biased values could be determined. These do not attest to the real roughness of EBID and so LER values are not reported here. This is addressed in the next chapter.

3.5 Conclusions and recommendations

Sub-20 nm dense EBID lines have been fabricated in the SEM using the standard platinum precursor MeCpPtMe_3 . The line width has been measured for several sets of lines of different defined widths, using a newly developed edge detection technique, providing quantitative 2D characterisation of dense EBID lines.

Most often in literature, the dimensions of EBID deposits are measured merely by eye. This is entirely insufficient for high resolution patterns. The lines shown below (Fig. 3.37), for example, appear to be about 12 nm wide when measured by eye. But an accurate measurement performed by edge fitting reveals the 1σ value of LW to be 16.4 nm. The error in the measurement by eye is about 4 nm; in other words, the measured value is about 37 % higher than it appears to be by visual inspection, which is quite significant. The 3σ value, therefore, containing almost the entire extent of the line, is 49.2 nm. Moreover, for electrical measurements where it is important to know the extent of the deposited material that is conducting, the 3σ value is perhaps more relevant, in which case the error is huge. Metrology of EBID lines is therefore crucial at high resolution. In fact, even

for large deposits, depending on the application, it may be unwise to report numbers by eye as that amounts to ignoring the shallow deposit present in the tails of the pattern.

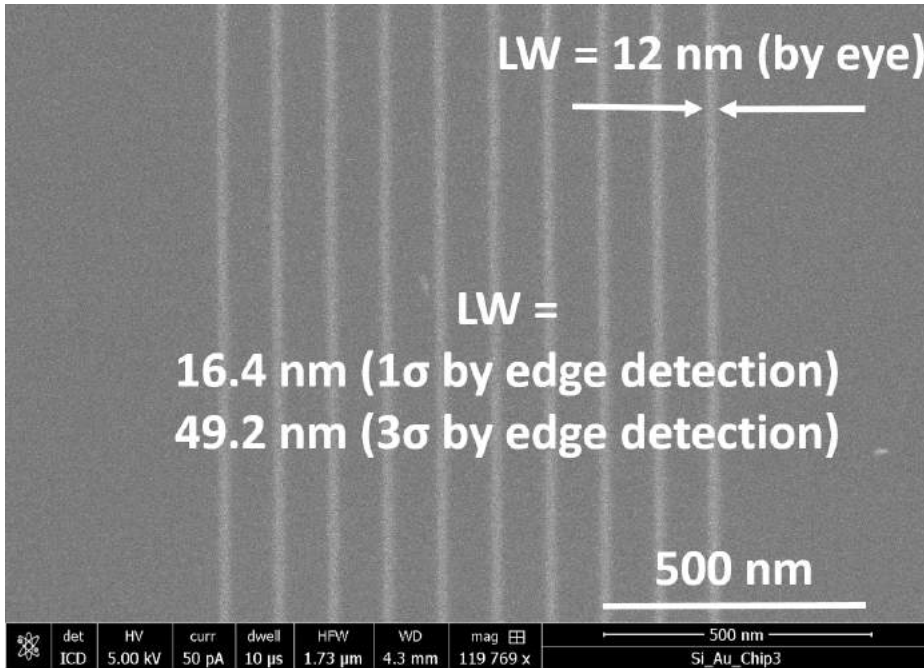


Figure 3.37: An SE image of dense EBID lines that appear 12 nm wide upon measurement by eye. Edge detection reveals the 1σ value of LW to be 16.4 nm and the 3σ value to be 49.2 nm, attesting to the necessity of accurate metrology in high resolution EBID.

The reproducibility of sub-20 nm dense EBID lines patterned in the electron current limited regime has been measured and found to be very high. The line width is reproducible to within 1 nm. Varying contamination levels, gradual GIS misalignment (over a year), small variations in gas load, fluctuations in temperature, variations in diffusion rates and surface roughness of the silicon sample have been found to not affect the deposited line width by more than 1 nm. This is reassuring because it means that these parameters, which are difficult to measure, do not in fact need to be monitored if standard working conditions are maintained.

Some sample orientations with respect to the stage seem to result in broader and more diffuse deposits, possibly due to vibrations. It has been

Parameter	Criterion
Patterning regime	Current limited
Beam focus	confirm after movement > a few μm
GIS temperature	stable (wait at least 45 minutes)
Sample position	fixed distance in z from GIS nozzle
Drift	monitor amount and direction
Vibrations	measure in x and y

Table 3.8: Checklist to ensure reproducibility in patterning

shown that a vibration amplitude of a few nanometres is sufficient to cause unwanted effects in patterning. If it is not possible to take steps to reduce the vibrations in the system, it is important to take this directional dependence into account prior to patterning. Failure to do so would lead to loss of resolution and reproducibility. Since the source of this problem is not entirely evident, this test needs to be performed prior to patterning and the images analysed. This could be overcome by the installation of a high stability stage as used in standard lithography. Not only would it solve this problem, it would also provide the opportunity to perform large area patterning, stitching of lines by stage movement and perhaps also permit the use of higher dwell times while imaging, as a result of not being limited by stage drift. All of this would help take another step forward in the application of EBID as a lithography technique and go a long way towards improving process control.

For shallow lines, where the BSE contrast is insufficient for edge detection, SE contrast can be used for metrology. If, however, the lines are so shallow that the SE signal from the lines is also very low, the limit of the edge detection technique is reached. An estimate of the LW can still be provided by fitting the double Gaussian function to the integrated intensity profile of the lines, but the variation of LW over the line cannot be measured. A comparison of LW from SE and BSE images would seem like the next step to attempt to learn the true width, but this is quite complex and will be addressed in the next chapter.

The LW is much more than the electron beam spot size. So the resolution is currently limited by other parameters than the probe size. In all cases, the lines themselves are also much broader than defined. From the results of [48], it is clear that this is not induced by proximity effects. This

prompts the question as to the mechanism behind the growth and must be examined in detail.

To ensure reproducibility in patterning over time and over a large area, it is recommended to consult the checklist shown in Table 3.8.

Chapter 4

Patterning of dense lines - EBID profile evolution and characterisation

“ *Some say the world will end in fire,
Some say in ice.
From what I've tasted of desire
I hold with those who favor fire.*

”
Robert Frost,

 In lithography, control refers to the ability to pattern dense lines of desired width and spacing. In EBID, the line width must be controlled via the patterning parameters, which in the current limited regime translates into the electron dose. In the patterning of dense lines, this is complicated by the fact that although the dose of PE's is known, the effect of SE's and BSE's depends additionally on the position of the neighbouring lines. So the first step is to understand how much a line broadens (with respect to the defined width) as a function of dose and line spacing. There have been several studies ([17], [29], [49], [50], [51], [39], [52]) on the growth of EBID structures and some relevant work is discussed in the following section to see if it could guide the patterning in this study. Existing EBID models were also reviewed to see if it was possible to make predictions regarding the resultant widths of dense lines. As a very rough approximation, we attempted to model the growth of a line similarly to that of a pillar because a good model simulating point exposure was available ([34], [22], [37]). The results of this study as well as conclusions from some other relevant models are presented, paving the way for this work. Finally, experiments were performed to study line widths in dense arrays, towards developing a recipe for high resolution patterning via dose control. The

challenges of imaging and the interpretation of SEM images are discussed, together with new techniques to measure EBID profiles.

4.1 Deposit growth in EBID

The lateral resolution and growth rate are two of the most important aspects of EBID. In literature, several experiments have been performed to study the growth in EBID rate by depositing pillars ([53], [54]). A continuum growth model first developed by Christy [13] has been applied and improved in several works over the following decades. Scaling laws have been developed by Utke et al. [34] that allow the estimation of growth rates for the different patterning regimes, i.e., determined by the balance between the electron beam flux, gas flux and diffusion. In this model, as in Chapter 2, for a primary electron beam of energy E_{PE} the growth rate $R(r)$ at a distance r from the position of the beam is given by:

$$R(r) \approx Vn(r)\sigma f(r) \quad (4.1)$$

where R is in units of nm/s

V [nm^3] = volume of a deposited molecule

$n(r)$ = number of adsorbed molecules/ nm^2

σ [nm^2] = dissociation cross section, which is energy dependent in reality, but is approximated by the integrated cross section over the range 0 to E_{PE}

$f(r)$ [electrons/ nm^2/s] = electron flux, integrated over the same energy range

The density of adsorbed molecules $n(r)$ is estimated from the differential equation for the net adsorption rate arising from the balance between the various processes involved:

$$\frac{\partial n}{\partial t} = sJ\left(1 - \frac{n}{n_0}\right) + D\left(\frac{\partial^2 n}{\partial r^2} + \frac{1}{r}\frac{\partial n}{\partial r}\right) - \frac{n}{\tau} - \sigma f n \quad (4.2)$$

where s = sticking coefficient

J [molecules/nm²/s] = precursor flux

D [nm²/s] = diffusion coefficient

τ [s] = residence time of the molecules on the surface

The first term in this equation represents adsorption, the second represents diffusion, the third represents desorption and the last represents EBID. In steady state,

$$\frac{\partial n}{\partial t} = 0$$

Next, they define a term $\tau_{\text{effective}} = [sJ/N_0 + 1/\tau + \sigma f(r)]^{-1}$, called the effective residence time of the molecules. This accounts for the residence time against the following processes: thermal desorption after a time τ , instant desorption if the adsorption site is occupied as well as EBID. This results in the following expression for $n(r)$ in the absence of diffusion:

$$n(r) = sJ(r)\tau_{\text{effective}} \quad (4.3)$$

Two dimensionless parameters have been defined that are relevant for the description of the patterning regime and resolution in EBID. The distinction between the current limited and gas limited regimes is made essentially on the basis of the extent of depletion of gas molecules due to dissociation by the electrons. In the first case, the monolayer coverage is complete throughout the time of exposure to the electron beam, whereas in the second, the adsorbed monolayer is depleted by the electrons, creating a concentration gradient and allowing molecules outside the region of e-beam exposure to diffuse towards it. In the model, depletion has been quantified by defining $\tilde{\tau} = \frac{\tau_{\text{out}}}{\tau_{\text{in}}}$ which is the ratio of the effective residence time of the molecules far away from the position of irradiation ($r = \infty$) to the effective residence time at the beam position ($r = 0$). In the current limited regime, $\tilde{\tau} = 1$ and in the gas limited regime it is greater than 1, with a value dependent on σ and f .

$$\tilde{\tau} = 1 + \frac{\sigma f_0}{\left(\frac{1}{\tau} + \frac{sJ}{n_0}\right)} \quad (4.4)$$

The resolution of EBID has been defined by a dimensionless parameter $\tilde{\psi} = \frac{\text{FWHM}_D}{\text{FWHM}_B}$ where the numerator is the FWHM of the EBID deposit and the denominator is the FWHM of the beam profile $f(r)$. This proves that the highest resolution is achieved in the electron current limited regime where depletion = 0. The FWHM of the deposit is then equal to that of the beam $f(r)$. While simple and easy to use, the limitation here is that the beam profile is not known in experiments. The spot size mentioned in specification sheets usually refers to the FWHM of the primary electron beam only. The distribution of the SE's (SE1's and SE2's) and BSE's is difficult to measure and their contribution to the deposition cannot be accurately estimated. Utke et al. approximated the beam profile as that of the PE's and were able to successfully model their experimental results using deposits whose dimensions were a few hundred nanometres. Since the model is in terms of dimensionless parameters, however, an attempt was made to use it to describe the growth of sub-30 nm lines. As this has been carried out in the electron current limited regime, many of the parameters used in the model describing depletion and replenishment of precursor molecules are not relevant and this simplified case was simulated using the codes made available online ([55]). Typical experimental parameters from the work described in previous chapters were used: electron flux at the centre of the beam = 10^8 / electrons/nm²/s, total exposure time in the range 10^{-6} s to 10^{-4} s ($t_{\text{dwell}} \times N_{\text{pass}}$), $\text{FWHM}_{\text{beam}} = 2$ nm and molecular flux = 10^4 molecules/nm²s (estimated in Chapter 2). Typical values of other parameters were taken from literature ([25]): sticking coefficient = 0.01 and residence time = 1 ms. The diffusion coefficient was turned off (= 10^{-70} nm²/s). The deposit profiles generated from this model for the relevant range of exposure times using a dissociation cross section $\sigma = 10^{-3}$ nm² are shown in Fig. 4.1.

For short exposure times, Gaussian deposit profiles are observed. An increase in exposure time from 1 μs to 10 μs results in an increase in the peak height, from approximately 9 nm to 60 nm. Higher dwell times (50 μs to 500 μs) result in deposits with flat tops. The transition between the two profiles has been discussed in [22] where they show that in the absence of diffusion, large dwell times result in a shift to the precursor limited regime as there is no longer complete monolayer coverage. Indeed, for the parameters used in this simulation, the value of $\tilde{\tau}$ calculated from 4.4

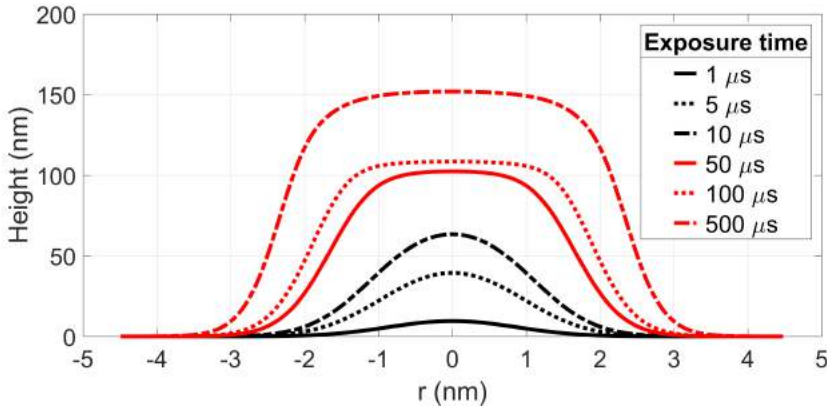


Figure 4.1: EBID deposit profile predicted by the continuum model-based simulation in [37], [34] for typical experimental parameters used in patterning high resolution lines. As the simulation models an isolated deposit, the total exposure time used as input was that of a single pixel of the line, ie, $(t_{dwell} \times N_{pass})$ in the range 10^{-6} s to 10^{-4} s.

turns out to be 90 which is much greater than 1. As $\tilde{\tau}$ is a function of σ and an accurate value for this is not available, the sensitivity of this simulation to σ was tested using three different values. The deposit profiles for $\sigma = 10^{-3} \text{ nm}^2$, 10^{-2} nm^2 and 10^{-1} nm^2 are plotted in Fig. 4.2 for exposure times of $1 \mu\text{s}$ and $100 \mu\text{s}$.

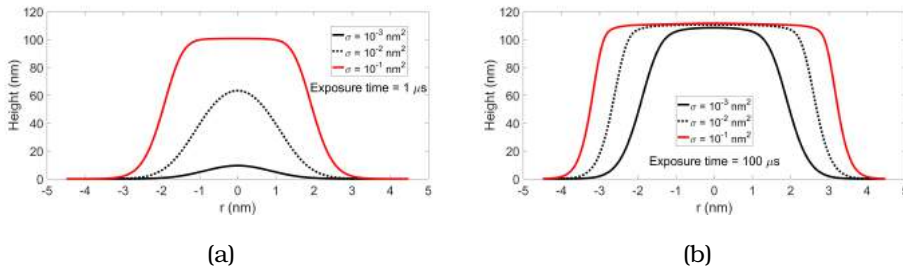


Figure 4.2: Measurement of the sensitivity of the deposit profile to the value of EBID cross section ($\sigma = 10^{-3} \text{ nm}^2$, 10^{-2} nm^2 and 10^{-1} nm^2) for an exposure time of (a) $1 \mu\text{s}$ and (b) $100 \mu\text{s}$

For the case of exposure time = $1 \mu\text{s}$, the deposit profile remains Gaussian for $\sigma = 10^{-3} \text{ nm}^2$, 10^{-2} nm^2 , flattening out at $\sigma = 10^{-1} \text{ nm}^2$. A high cross section would mean more dissociation events, leading to a thicker deposit. As σ increases, a depletion of molecules due to EBID would result and the accompanying regime change would lead to a flat top profile as observed

in Fig. 4.2(a) for $\sigma = 10^{-1} \text{ nm}^2$. At a higher exposure time as in Fig. 4.2(b), the same reasoning holds with lower values of σ sufficient to cause the switch to the gas limited regime. The increase in vertical growth rate is known to be maximum in the current limited regime [37], appearing to flatten out as the gas limited situation is reached. This is in accordance with Fig. 4.2(b) where no significant increase in deposit thickness is seen with increase in σ , presumably due to the decreased monolayer coverage at the point of electron exposure.

This simulation provides a qualitative explanation of the experimentally observed growth in EBID lines. While the model has been used to fit experimentally obtained AFM profiles [34] resulting in the estimation of some parameters such as the diffusion coefficient, the reverse case: a successful prediction of the deposit profile using experimental parameters as input, in terms of height and FWHM, for example, could not be found. Further, the experimental parameters in [34] were quite different from those used here - the most important differences being the electron flux and FWHM of the beam, which were of the order of $10^4 \text{ electrons/nm}^2/\text{s}$ and 100 nm respectively. Upon attempting to make a quantitative prediction based on the parameters used in this work, it is immediately evident that the results are not a good match. The height of sub-30 nm EBID lines patterned in the previous chapters using a total pixel exposure time of $10 \mu\text{s}$, for instance, is always less than 20 nm. The model, however, predicts a height of more than 60 nm. The FWHM of the simulated deposits (Fig. 4.1) is less than 4 nm, whereas the experimentally observed LW are much larger. There could be several reasons for these discrepancies. The model describes the growth of an isolated deposit. So it is not obvious that the same model would explain the case of high resolution lines patterned by exposure of overlapping pixels. Another important factor is the electron beam profile used in the model which has been assumed to be a Gaussian function representative of the PE distribution. While this may be sufficient for making predictions regarding growth at large scales, the SE profile would be critical at sub-30 nm resolution and would need to be incorporated in order to explain the results of high resolution patterning.

For example, the BSE's and forward scattered electrons have been shown to play an important role in the deposition of large structures [56]. Deposits of different thicknesses were fabricated using a range of primary electron

energies and the composition and extent of the halo were studied. A qualitative description of broadening due to electrons escaping from the deposit and from the substrate was provided to explain the deposit profile and the shape of the halo at different primary energies. Based on their observations, patterning using a high energy beam was recommended in order to achieve structures with sharp edges. For sub-30 nm structures, though, the picture is quite different. Due to the low dose used in the deposition, the contribution of BSE's is expected to be much less significant. If the deposition is governed by low energy SE's, the effect of the substrate would become insignificant as even a very shallow deposit of, say, 1 nm^3 is known to result in increased SE emission ([39]). Continued growth would then largely be governed by SE emission from the deposit itself, resulting in a different deposit profile. Silvis-Cividjian et al. ([16]) explained the role of SE's in EBID by refining the model in 4.1 and 4.2 to deposit dots or pillars, taking into account the evolving surface of the deposit using a Cellular Automata technique. Beginning with the initial stage where the SE's emerged from the substrate to the later stages where they were emitted from the deposit, their Monte Carlo-based fast secondary electron simulation showed that while the SE emission peaked at the beam position, the profile itself was not identical to that of the deposit and was therefore not responsible for the broadening in a simple manner. It was necessary to take the combination of the SE profile and the energy dependent dissociation cross section to obtain a realistic estimate and they concluded that the effect of SE's become increasingly important as the spot size of the beam reduces. The theoretical estimate of the ultimate resolution achievable in EBID was found to be 0.23 nm (FWHM) in the very early stages of EBID and a more realistic number of 2 nm was determined for deposits a few nanometres thick. This was supported by experiments where 1 nm dots were fabricated by EBID. While providing some of the highest resolution results in the field, these results were obtained using a zero diameter beam and a thin film substrate and are only directly applicable to the deposition of isolated dots. Much work is needed before this model could be used to make predictions of line width, where the patterning has been carried out by exposure of overlapping pixels. The added complication of dense lines would require a deeper analysis of the various kinds of proximity effects and a better model for the generation and tracking of SE's. And an experiment is still more complicated because of the difficulty in interpreting 2D images to gain an understanding of 3D

phenomena responsible for growth in EBID.

Monte Carlo simulations have been developed by [29] and [33] that model the spatial distribution of electrons of different energy.

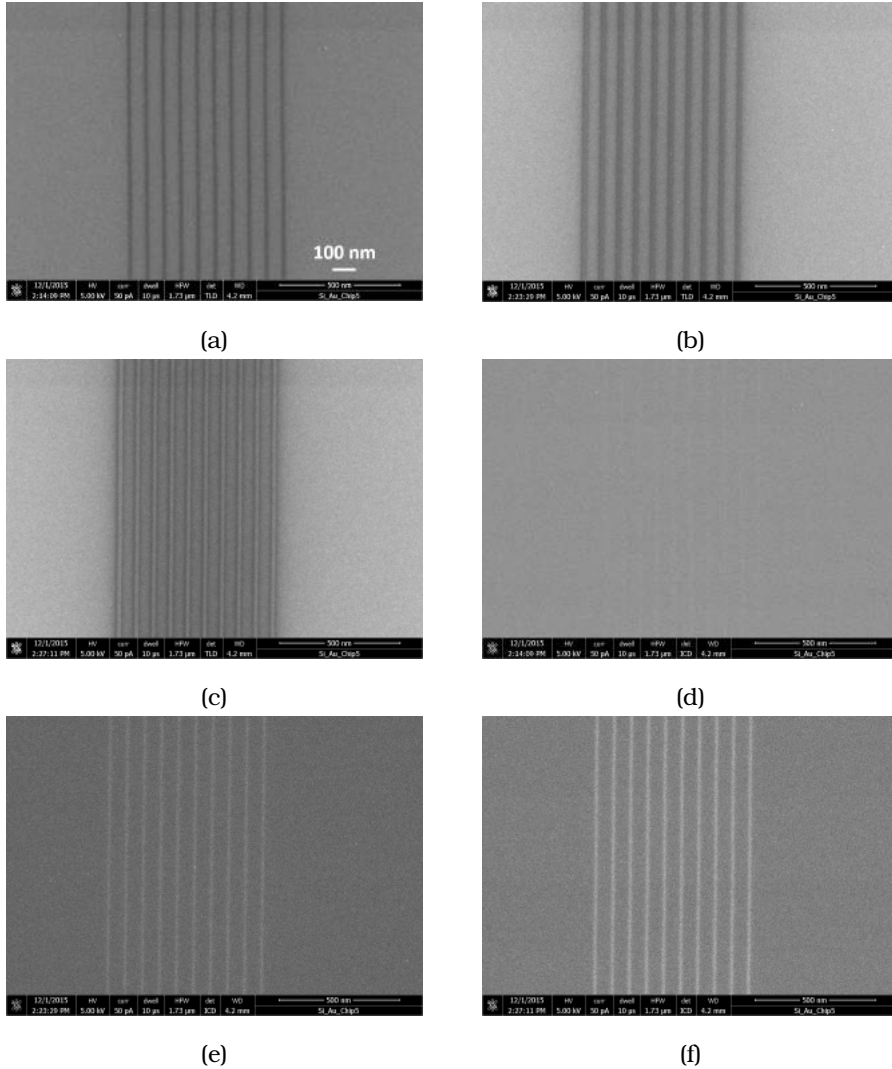


Figure 4.3: (a)-(c) TLD image of EBID lines patterned with increasing dose. The lines were defined as 4 nm wide with a centre to centre spacing of 70 nm and patterned in serial mode with: 20 keV, 40 pA, $t_{dwell} = 20 \mu\text{s}$, pitch = 1 nm, $N_{pass} = 1, 5, 10$. (d)-(f) Corresponding ICD images of the dense lines acquired simultaneously with the TLD images.

The form of the surface is continuously updated during exposure and thus

simulates 3D growth. The deposition of pillars of about 60 nm height has been simulated using two precursors: WF_6 and TEOS using substrate and precursor input parameters relevant for deposition like energy, current, beam profile, deposit work function, energy-dependent dissociation cross sections, etc. The composition of the pillar could be determined in terms of contributions of electrons of different energy to different regions of the pillar. Incorporating PE, SE, BSE and FSE-induced growth as well as gas dynamics, the vertical and lateral growth rates could be studied as a function of electron energy. The effect of PE's and SE1's was found to be dominant in inducing vertical growth of the pillars. They concluded that the growth was governed by the interaction volume of the electron beam in the pillar. For high resolution structures, on the other hand, simulations performed by [39] showed the growth to be dominated by SE's in the deposit even in the very early stages of EBID, which is not in agreement with this result. So although the model in [33] successfully explains experimentally observed growth in tall pillars which are considered essentially 1 dimensional structures, it may not be realistic to apply it directly to simulate low aspect ratio lines at the sub-30 nm scale.

4.2 Imaging and characterisation of dense lines

In Chapter 3, a line width measurement technique has been presented that is especially tailored for the characterisation of EBID lines. The line profiles obtained from BSE images were found to be Gaussian, but those obtained from the corresponding SE images were not always Gaussian. Thick lines can appear to have a very different profile due to edge effects in SE imaging. So, unlike in the case of resist-based lines, the edge detection technique developed for EBID cannot directly be applied to lines of all thicknesses. As the EBID lines in Fig. 4.3 and the corresponding integrated profiles in Fig. 4.4 show, the SE profile can change quite drastically with dose and the fitting technique does not survive the line profile evolution. The BSE profile does not show such a pronounced change but the lines may be too noisy to permit edge detection (Fig. 4.3(d)). Most of the lines patterned for the measurement of reproducibility had sufficient thickness to give rise to contrast in BSE imaging. But it was also observed that upon approaching higher resolution, BSE imaging could no longer be used and SE imaging was the only option. In lines of still higher resolution, even the SE signal has a lower signal to background ratio and the edges could no longer be

detected as accurately by this technique. This presents the first challenge in the development of a recipe for lithography using EBID: how to provide a consistent measure of LW for EBID lines of varying width and thickness that is applicable even at single nanometre resolution?

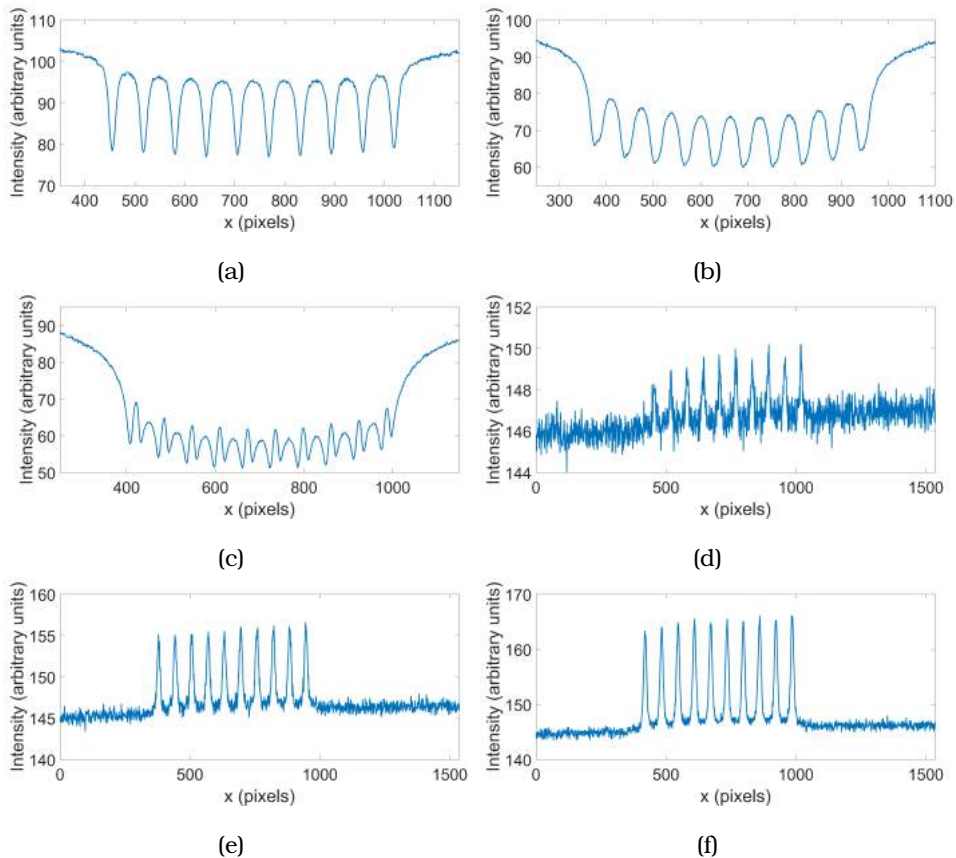


Figure 4.4: (a)-(c) Integrated TLD profiles of the dense EBID lines in Fig. 4.3 showing the evolution of the SE profile with increase in dose. (d)-(f) Corresponding integrated profiles of the ICD images. It is evident that while some measure of LW may be determined from the ICD images in (e) and (f), the signal to noise ratio in the shallow lines in (d) is too low to permit this. Analysis of the TLD images, on the other hand, is hindered by the continuously changing SE profile.

To address this, we begin with a detailed study of the line profile, which is a combination of the actual 3D profile and the imaging technique. As the patterning was carried out in the current limited regime, it is expected that the "real" EBID line profile is in fact Gaussian. The problem in characterising them comes about because the LW is determined from an image that is a 2D projection of this profile onto the detector. A more

reliable measurement of the real profile might be possible using AFM as it is a pseudo-3D technique involving direct measurement of height. But this technique is limited in the lateral resolution achievable due to the convolution with the tip shape. We first perform a theoretical investigation of the extent to which AFM measurements can be used to accurately determine line width in EBID.

4.2.1 Line Width determination by AFM

A rough model was devised based on the convolution between the AFM tip and the shape of the deposit. The tip was approximated as a circle with a radius of 7 nm and the deposit was modelled as having a Gaussian profile. The schematic of the arrangement is shown in Fig. 4.5.

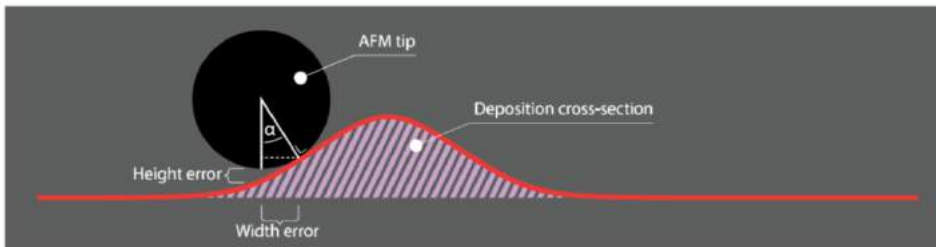


Figure 4.5: Schematic of model to estimate the error in LW from AFM measurement. The AFM tip is modelled as a circle of 7 nm radius and the EBID deposit is modelled as having a Gaussian profile.

Based on this model, the AFM image is formed by the set of points where the tip actually touches the surface of the deposit. The actual position of the tip (detected) is some distance away from this point laterally as well as in height, inducing an error in the measurement. The error is $-R\sin(\alpha(x))$ in the lateral direction where $\alpha(x)$ is the angle at the point of contact as shown in Fig. 4.5 and the error in height is $R(1 - \cos(\alpha(x)))$. In fact, the error in height measurement is the distance between the lowest point of the tip and the height of the deposit at that point, but what we refer to here is the error between the convolved profile and the position of the tip. In this manner, the path of the AFM tip can be described and the line width can be estimated from this measurement. Fig. 4.6 shows the theoretical error in line width measurement obtained from an AFM image. The left plot shows three Gaussian deposits (solid curve) with increasing height, in the range of some typical values encountered in this work. The

width of the deposits is taken to be the same in all cases ($\sigma = 7$ nm). The corresponding convolved AFM profile obtained from the model is shown for each deposit (dotted curve) as well. The plot on the right shows the relative error in LW measurement, ie, between the defined value of $\sigma = 7$ nm and the value measured from the resultant (convolved) AFM profile. The error in LW measurement increases with line thickness. Since the dimensions of the deposits were chosen arbitrarily, it is worthwhile to mention here that narrower lines would have a greater measurement error. This has to do with the size of the tip and could be lowered by using a smaller tip.

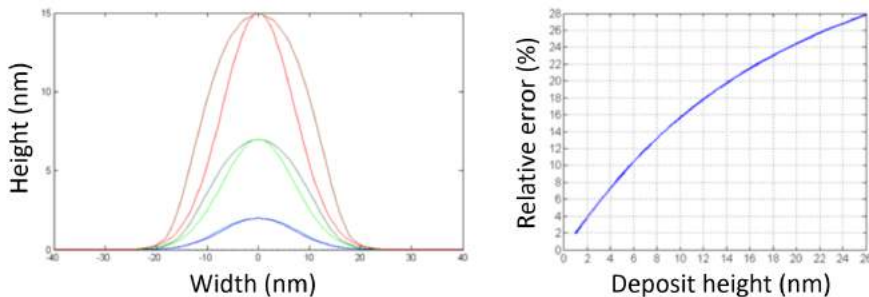


Figure 4.6: Left: Three Gaussian deposits and their convolved AFM profiles determined from the model. Right: Plot showing the error in LW measurement obtained by fitting a Gaussian function to the convolved profile as a function of deposit height.

This study shows that for very shallow lines, the line width can be determined from AFM measurements with high accuracy. Based on Fig. 4.6, the LW of 2 nm thick lines can be measured with a relative error of approximately 4 % and that of 10 nm thick lines with approximately 15 % error. This is assuming certain values for the size of the AFM tip and the EBID line profile. For dense lines, the line spacing is another parameter to take into account as the aspect ratio of the tip, and not just the radius, comes into play. For the general purpose of LW measurement in EBID, we can conclude that AFM imaging is useful because it is a reflection of the true line profile and can therefore be used to provide a complete 3D characterisation of EBID lines. This is demonstrated in the following section.

4.2.2 3D characterisation of dense EBID lines using AFM

A set of 10 EBID lines were patterned on a silicon substrate having a natural oxide layer, using the platinum precursor MeCpPtMe_3 and imaged using a Bruker Fast Scan AFM. The image is shown in Fig. 4.7 and the mean height of the lines was measured to be 10.1 nm with a standard deviation of 0.7 nm.

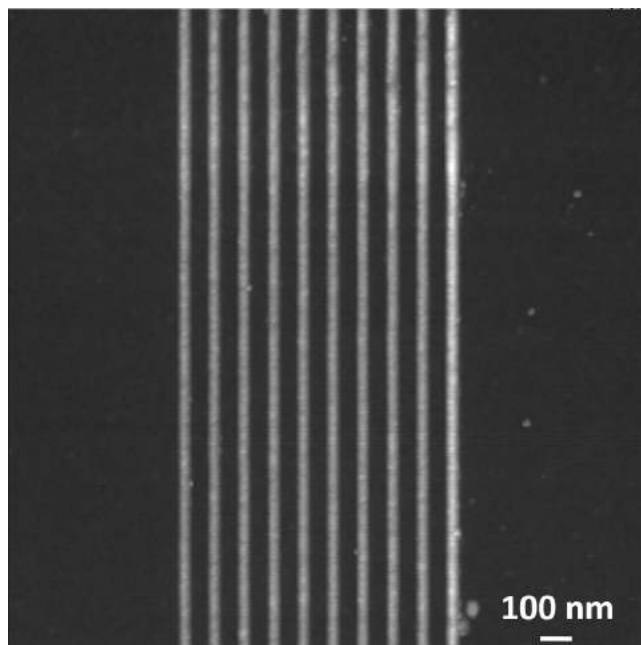


Figure 4.7: AFM image of a set of 10 shallow Pt/C EBID lines patterned on a silicon substrate having a natural oxide layer, acquired using a Bruker Fast Scan AFM. The mean height has been measured to be 10.1 nm.

The edge detection technique described in Chapter 3 was used to determine the LW from the AFM image and was found to yield a mean value of 32.3 nm with a standard deviation of 1.0 nm. Next, the 3D profile of the lines has been analysed in terms of the distribution of material contained. The area in each peak in the AFM profile was calculated using a Gaussian fit, by integrating the profile in a window selected to be approximately halfway between two adjacent peaks. Since the lines were patterned at identical spacing, the same window was used over the entire plot. The area under the curve (which is proportional to the volume in the line) was calculated after performing a baseline correction. In order to understand

the distribution of material in the lines, the total area under each peak (within the bounds of the window) was compared with the area in the bounds of the 1σ , 2σ and FWHM values and the results are shown in Fig. 4.8(b) for each EBID line. The integrated height profile of the lines is shown in (a) for reference.

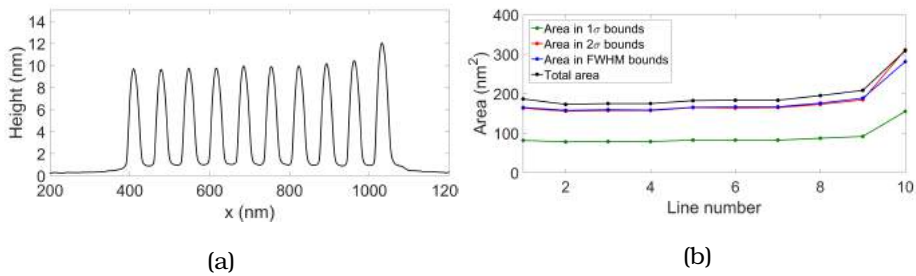


Figure 4.8: (a) Integrated height profile of the dense lines shown in the AFM image in Fig. 4.7 (b) Plot showing a comparison of the total volume contained in an EBID line with the volume contained between the 1σ , 2σ and FWHM points, as determined from the AFM image.

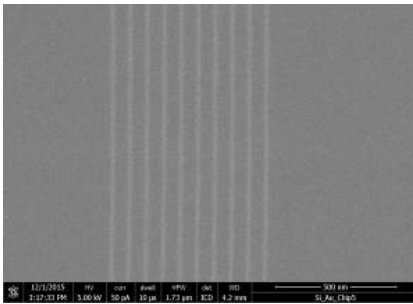
The mean values for the area under the curve in the four bounds are shown in Table 4.3. We observe the following: The total area is clearly somewhat greater than that in the 2σ bounds. And the area in the 2σ bounds is approximately the same as that in the FWHM bounds. This is on account of the fact that for a Gaussian function, $\text{FWHM} = 2.35 \times \sigma$. It would be interesting to make a similar comparison of the total area with the area in the 3σ bounds, but this could not be performed here as this region extended into that of the neighbouring peaks. There are often concerns regarding the "halo" of EBID lines and the resulting consequences for the device or pattern. This is especially relevant at high resolutions for making electrical measurements, for example. So it would be useful to make a rough estimate of the amount of material present in the halo. This can be obtained by calculating the area of the line that is present outside the 2σ bounds, which, for the EBID lines in Fig. 4.7, constitutes 1.8 nm^2 or 9% of the total area. This is then the percentage of the total deposited volume that is present in the halo.

As SEM imaging is much faster than AFM, it is more commonly used for measurement of deposit dimensions in EBID. The same analysis was therefore performed with SEM images to see if the volume of the halo so

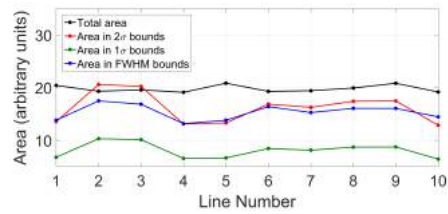
Bounds	Mean Area (nm ²)	std
Total	19.4	3.3
Between 2σ points	17.6	3.0
Between FWHM points	17.5	2.1
Between 1σ points	8.8	1.5

Table 4.1: Mean values and standard deviation of the area under the curve for the EBID lines, determined from the AFM image shown in Fig. 4.7

estimated corresponds to that from the AFM measurement. As described in Chapter 3, BSE imaging is usually preferable to SE imaging for interpreting line shapes, particularly when fitting of lines profiles is involved. So an image of the same set of lines was acquired on the FEI Verios 460 SEM using the ICD backscattered electron detector and the areas were calculated from the integrated intensity plot as before.



(a)



(b)

Figure 4.9: (a) ICD image of the dense lines shown in Fig. 4.7 (b) Plot showing a comparison of the total volume contained in an EBID line with the volume contained between the 1σ , 2σ and FWHM points, as determined from the ICD image.

It should be noted here that the intensity in the ICD image is not equal to the height in the AFM image. This is merely an attempt to see if any scaling exists which may make it possible to compare integrated plots in the two cases. This is not trivial to conclude as the contrast in the image is the combined result of BSE emission from the sample, travel through the fields in the electron column and collection by the ICD. Fig. 4.9 shows the comparative plot of the areas within the four different bounds, from which the mean values were calculated. The percentage of the total integrated intensity contained in the halo turns out to be 17% - very different from that measured by AFM. The comparison with AFM serves as a simple

demonstration of the fact that the interpretation of contrast in SEM images is not straightforward as far as determining "real" physical dimensions is concerned. This issue will be addressed in detail in the rest of this chapter.

4.3 Interpretation of contrast in SEM imaging

Next, the two kinds of SEM imaging techniques: SE and BSE imaging are studied to see how the contrast correlates with the deposit shape. The deposit material and topography are the two factors responsible for contrast. In theory, a perfectly flat deposit of uniform composition would give rise to one grayscale value in the image. The shape of the deposit affects the SE and BSE signal differently. The presence of a slope, for example, results in increased SE signal but could lead to a decrease in the BSE signal due to some BSE's now being scattered away from the detector, i.e., downward, such that they are not detected efficiently. In the UHR mode, the electrons leaving the sample experience a magnetic field and are sucked out more efficiently, followed by being focussed onto the different detectors. The FEI Verios 460 SEM was used for imaging and a schematic of the detection scheme is shown in Chapter 3. The DBS (Directional Backscattered detector) is made up of annular rings, one or more of which can be selected such that an image can be acquired consisting only of BSE's emitted in a certain angular range. As there are no fields present on the annular rings, the signal from the DBS detector in field-free mode might be relatively easy to interpret. However, the UHR mode is necessary for imaging sub-30 nm lines and so the DBS detector was not used in this work. The TLD is the detector that is located lowest in the column and can be used to detect SE's or BSE's depending on whether a positive or negative voltage is applied to the suction tube located just inside the pole piece. In the latter case, the detected BSE's are converted to SE's and the signal so generated is used to form an image. The MD located higher up in the column is efficient for the detection of BSE's with energy $> 1\text{keV}$. It has an aperture in the centre through which the low loss BSE's are focussed onto the ICD located still higher up. Therefore, the MD and ICD collect BSE's of a different range of energy and emission angle. When a beam deceleration is used, the SE's are also accelerated to high energies and can no longer be differentiated from the BSE's. They can both be detected by the ICD and MD.

The interpretation of contrast from the ICD and MD is in general quite complicated as detailed information regarding the fields in the column is needed to know with accuracy the energy and emission angle of the emitted BSE's, from which information regarding the material and topography are to be determined. Instead, we attempted to study the EBID line profile by combining information from simultaneously acquired SE and BSE images with AFM images as described in the next section.

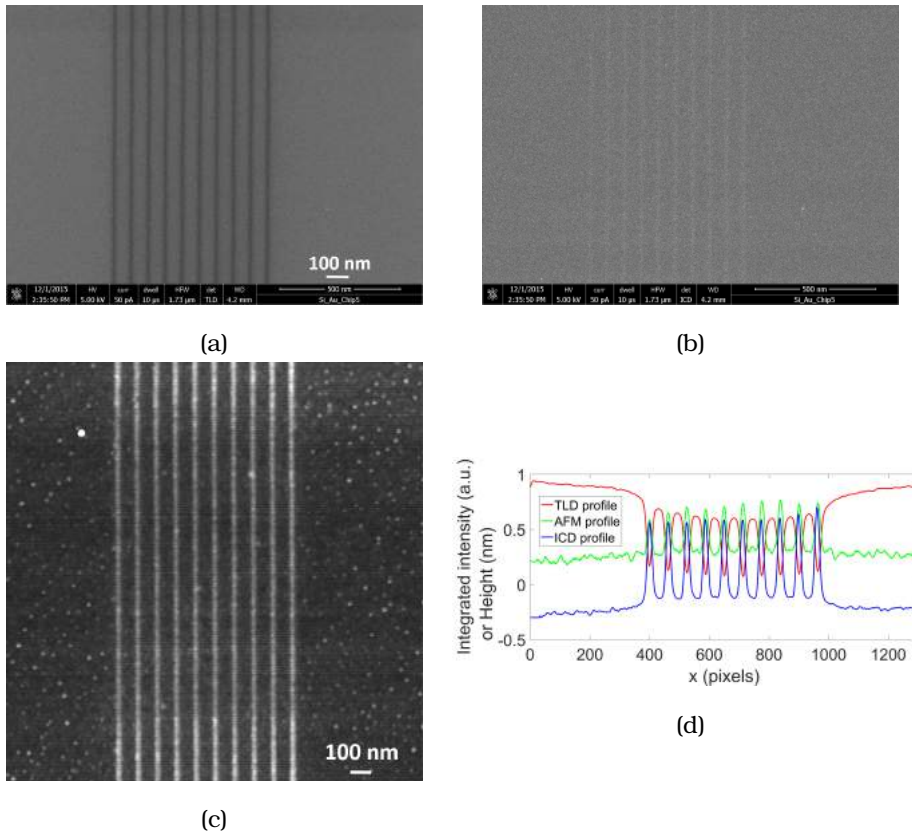


Figure 4.10: Simultaneously acquired (a) TLD and (b) ICD images, together with (c) an AFM image of a set of dense EBID lines. (d) Integrated profile of the array from TLD, ICD and AFM imaging shown in red, blue and green respectively. The AFM profile was scaled to the SEM images based on the known centre to centre separation of the lines, and then shifted in x to match the peak positions.

4.3.1 Combining SE, BSE and AFM imaging

Simultaneously acquired TLD and ICD images of a set of dense EBID lines are shown in Fig. 4.10. The lines were defined as 5 nm wide with a centre

to centre spacing of 70 nm and patterned in serial mode with: 20 keV, 40 pA, $t_{dwell} = 20 \mu\text{s}$, pitch = 1 nm, $N_{pass} = 1$. The integrated line profiles from the two images are plotted (ICD in blue, TLD in red) after normalising and smoothing in Fig. 4.10 (d). The AFM profile is plotted alongside in green, after normalising and smoothing of the image shown in (c). The known centre to centre distance (70 nm) was used to scale the AFM plot to the SEM plots and then shifted in x to match the peak positions. A surprising observation was then made regarding the shape of the lines. Fig. 4.11 shows the plot of the first derivative of each of the profiles. The points where this function is maximum or minimum are called the points of inflection. These are the positions at which the slope of the profile is maximum or minimum and the second derivative is zero there. Zooming in on the first (leftmost) EBID line (Fig. 4.12), surprisingly, all three profiles appear to have the same points of inflection. The maxima in the derivative of the TLD profile occur at the same position as the minima in the derivative of the ICD and AFM profiles, and vice versa (Note: In the TLD image, the EBID lines have a lower signal than the substrate, which is the opposite of the case in the ICD image. So the first point of inflection in the TLD profile corresponds to a minimum in the derivative, whereas the reverse holds for the ICD and AFM images.)

If we now define the width W to be the distance between the points of inflection, it can be estimated from any one of the three profiles. This was performed systematically using a matlab code. A polynomial was fitted to the integrated profile in each case and the points of inflection were determined by detecting the positive and negative peaks in the first derivative of the profile using the "peak detect" function. For the array shown in Fig. 4.10, the values of W are shown in Table 4.2 for every EBID line from each of the three profiles.

Image	L1	L2	L3	L4	L5	L6	L7	L8	L9	L10	std
TLD	18.7	18.9	18.8	18.8	18.9	19.0	18.9	19.0	19.3	19.1	0.2
ICD	17.2	17.3	17.7	18.1	18.1	17.9	17.6	17.4	17.4	18.0	0.3
AFM	19.3	18.9	18.7	18.8	18.9	18.9	18.8	18.8	18.7	19.0	0.2

Table 4.2: Measured values of W (in pixels) for each EBID line (L1 - L10) in the array, measured using the points of inflection of the TLD, ICD and AFM profiles

The values of mean width are: $W_{TLD} = 18.9$ pixels, $W_{ICD} = 17.7$ pixels and $W_{AFM} = 18.9$ pixels. The values of W measured from the three images are very close, although W_{ICD} is always lower than W_{TLD} and W_{AFM} .

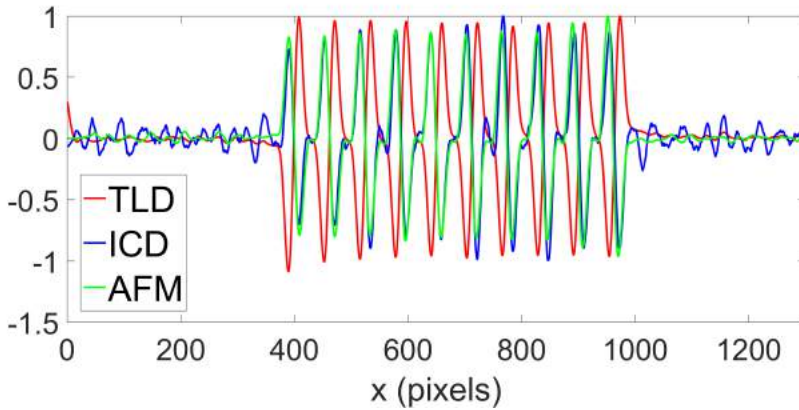


Figure 4.11: Plot of the first derivative of the TLD, ICD and AFM profiles

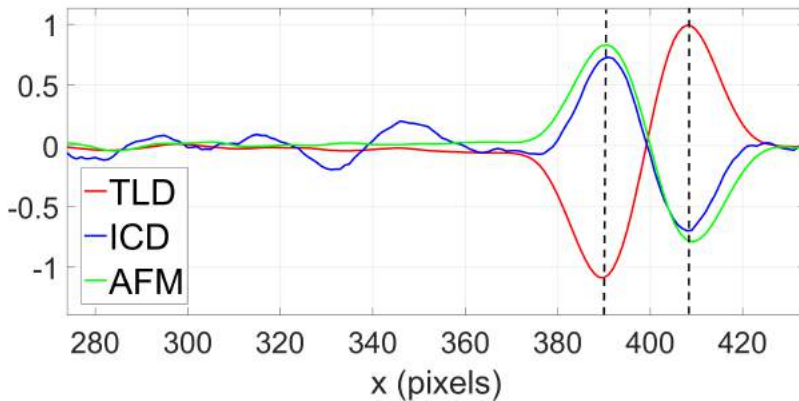
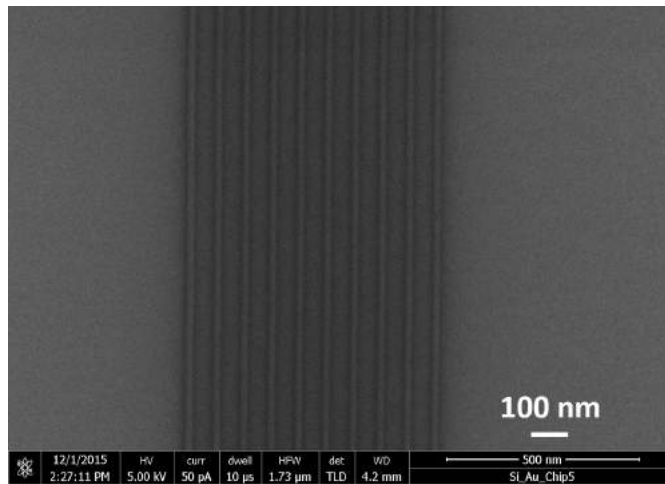


Figure 4.12: Zooming in on the first (leftmost) EBID line, it can be seen that all three profiles have the same points of inflection. These positions are indicated by the two vertical dashed black lines in the plot. The maxima in the red plot occur at the same position as the minima in the blue and green plots, and vice versa. This corresponds to the points of inflection in the TLD, ICD and AFM images respectively.

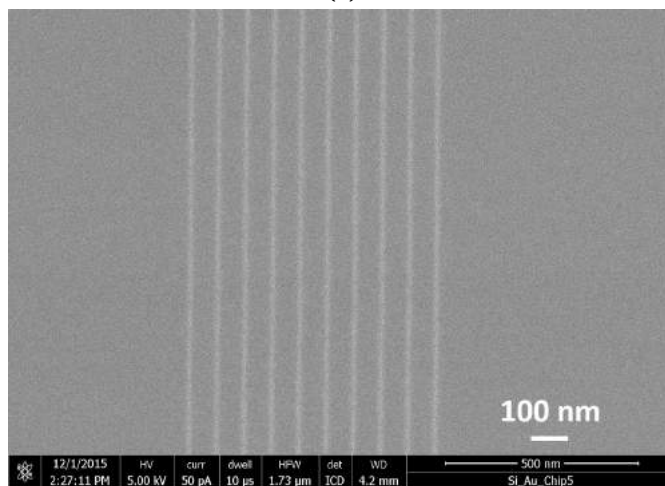
The difference between the mean values of W is at most 1.2 pixels. For individual lines, the difference between the values of W as measured from the three images is at most 2.1 pixels. The std in the mean W is 0.2 pixels for the TLD, 0.3 pixels for the ICD and 0.2 pixels for the AFM. This demonstrates that any one of SE, BSE and AFM imaging techniques can be used to determine W with reasonable accuracy. Note: The values of W are mentioned in pixels here because that is what results from the direct

measurement. However, after scaling of the AFM to the SEM plot, the conversion to nanometres is straightforward and the same for all of them (1 pixel = 1.1 nm).

Next, consider EBID lines having a different TLD profile as shown in Fig. 4.13 (a) with the corresponding ICD image in (b). The lines were defined as 4 nm wide with a centre to centre spacing of 70 nm and patterned in serial mode with: 20 keV, 40 pA, $t_{dwell} = 20 \mu\text{s}$, pitch = 1 nm, $N_{pass} = 10$. These



(a)



(b)

Figure 4.13: Simultaneously acquired images: (a) from the TLD and (b) from the ICD, of a set of dense EBID lines with a different profile than in Fig. 4.10.

lines were not imaged by AFM due to time constraints, but from images of lines patterned under similar conditions, it is known that the AFM profile of these lines is Gaussian. It is evident from the integrated profiles shown in Fig. 4.14 (a) that the extent of the deposit as measured by the TLD is greater than that by the ICD. A possible explanation of the shape seen in the TLD image is as follows: the signal from the central part of the line is stronger than that from the substrate because the line is sufficiently thick in that region to cause a higher SE emission. In addition, the platinum content of the thick region of the deposit could contribute to the increased signal. Moving to the edges of the line on either side, dips are seen in the integrated profile. This could be due to the fact that the composition of the shallow part of the deposit is carbon whose SE yield is lower than that of silicon, or due to the shadowing of the SE's emitted from the part of the substrate adjacent to the line. This would prevent some of the SE's from reaching the detector as they might go into the line and be lost there. On closer inspection, the extent of the ICD profile seems to overlap fairly well with that of the central part of the TLD profile. The first derivative of the two are plotted in Fig. 4.14 (b) and a zoom-in of the region of one of the lines (the left-most was selected as an example) is shown in (c). The four points of inflection coming about as a result of the peak in between the two dips in the TLD profile are marked.

The measurement technique described above was applied to these lines. The distance between the points of inflection 2 and 3 was recorded for each EBID line in the TLD image and compared with the distance between the points of inflection of the ICD profile. The values of mean line width obtained were: $W_{\text{TLD}} = 14.8$ pixels and $W_{\text{ICD}} = 17.6$ pixels. For these lines, the width W as measured by the ICD and the TLD differs by about 3 pixels.

There are some questions arising from this analysis. One: What is the physical significance of the point of inflection and why do the values of W determined by this method from the TLD and ICD profiles match? Two: Is the distance W between the points of inflection a sensible measure of line width? In the following section, an SEM simulator has been used to image Gaussian lines in an effort to find an explanation for the profiles obtained from SE and BSE imaging.

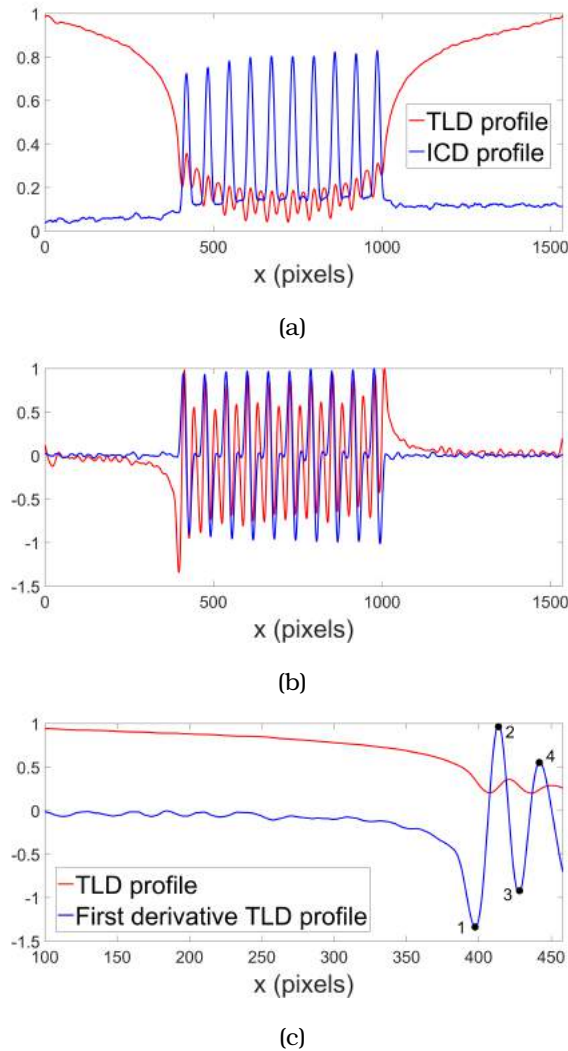


Figure 4.14: (a) Integrated profiles of the images shown in Fig. 4.13. The red plot corresponds to the TLD image and the blue plot to the ICD image. (b) Plot of the first derivative of the integrated profiles shown in (a). (c) Plot showing a zoom-in of the first derivative profile of the left most EBID line from the TLD image (in blue). The same extent of the integrated profile of the TLD image is plotted alongside for reference. The points of inflection are marked 1 to 4.

4.4 Simulated EBID line profiles

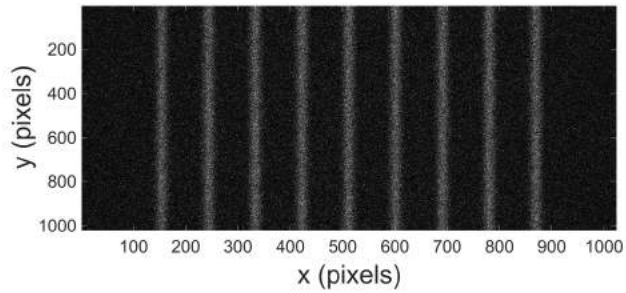
An SEM simulator developed by Verduin et al. [57] has been used to generate SE and BSE images of dense EBID lines of known geometry. In the simulator, the lines have a Gaussian profile and are generated using

a 3D triangular mesh by specifying the parameters: width (1σ), height and centre to centre spacing for the input Gaussian function. The desired energy, dwell time and electron dose for imaging can be put in and the electron trajectories in the material are calculated. The composition of the deposit and substrate material can be selected as well, provided data on the scattering cross section is available.

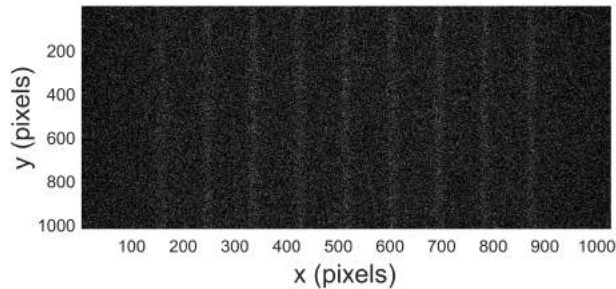
The simulation was run using typical parameters from the experiments described above. The input function height = 10 nm, width = 10 nm and spacing = 70 nm, selected to resemble experimental line profiles obtained in this work. A primary electron imaging dose of $100 \mu\text{C}/\text{cm}^2$ was used and the detector plane was positioned immediately above the sample such that all the electrons leaving the sample surface were detected as soon as they entered vacuum. This means that even high energy electrons leaving the sample are not allowed to be scattered into a neighbouring deposit. This may seem unrealistic but the tracking of the actual electron trajectories until they reach the detector is too difficult as the fields present in the microscope are not known. As no realistic criteria can be imposed, the detection was performed under this condition.

The SE image was formed by the detection of electrons $< 50 \text{ eV}$ as per the conventional definition of SE's and the BSE image was formed by the detection of electrons $> 1 \text{ keV}$ as this is the energy above which the MD and ICD have been found to be efficient at collecting BSE's based on GEANT4 simulations performed at FEI (private communication S. Hari and S. Sluyterman). In reality the EBID deposit is essentially carbon, with platinum grains. As this cannot be simulated, the lines were defined as silicon on a PMMA substrate. Two materials were selected that have been used extensively in scattering models. Between the two, PMMA was chosen as the substrate as it has a higher SE yield than silicon, therefore resembling the situation in the experiment where the substrate (silicon) has a higher SE yield than the lines (carbon).

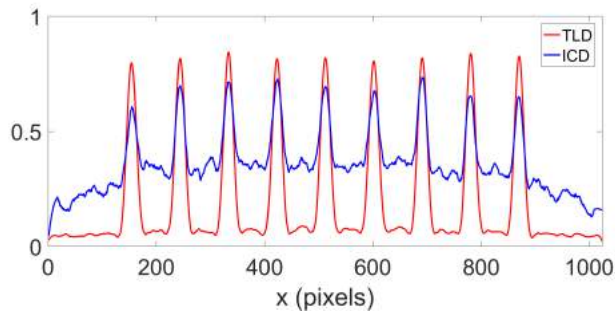
The simulated SE and BSE images are shown in Fig. 4.15 along with their integrated profiles. Both profiles appear Gaussian, like in Fig. 4.10 with the difference that the lines in this case have a higher SE intensity than the substrate. The background in the BSE image is also of a distinctly different shape than that observed in the experiment, but the signal is



(a)



(b)



(c)

Figure 4.15: (a) Simulated SE and BSE images of dense EBID lines of height = 10 nm, width = 10 nm, line spacing = 70 nm imaged with a 5 keV beam using a dose of $100 \mu\text{C}/\text{cm}^2$. (b) Plot of the SE (red) and BSE (blue) integrated profiles. Note: The contrast and brightness of these images have been digitally enhanced, purely to enable visualisation in print.

strong enough for this to not pose a problem in this analysis. The peak positions as well as the width at the base are about the same and a plot of

the first derivative in Fig. 4.16 confirms the match between the points of inflection in the two profiles. The explanation for this comes from the form of the Gaussian function:

$$y = ae^{-\frac{(x-\mu)^2}{\sigma^2}}$$

The points of inflection corresponding to $\frac{d^2y}{dx^2} = 0$ are $(\mu - \sigma)$ and $(\mu + \sigma)$. Therefore, Gaussian profiles having the same peak position and FWHM have the same points of inflection. What is not obvious, however, is the observation that the line profiles obtained from TLD and ICD images would have the same FWHM. However, this does appear to be the case in both the experimental (Fig. 4.10) as well as the simulated images (Fig. 4.15). The match in the points of inflection is particularly surprising in the case of Fig. 4.13 as the SE line profile (Fig. 4.14) is not even a Gaussian and the match in the value of W is between the central part of the SE profile and the BSE profile. In order to understand the physical significance of the points of inflection in the line profile, we define a quantity R :

$$R = \frac{A_W}{A_{\text{total}}} \times 100 \quad (4.5)$$

where A_W is the area under the Gaussian curve between the points of inflection and A_{total} is the total area under the curve. The values of R calculated from the simulated images are shown in Table 4.3 for the input Gaussian function (height = 10 nm, $\sigma = 10$ nm) and the SE image.

Image	R
Input Gaussian function	$\approx 85\%$
SE image	$\approx 60\%$

Table 4.3: Value of R calculated from the input Gaussian function and the simulated SE image)

The $W_{\text{TLD}} = 19.0$ pixels and $W_{\text{ICD}} = 17.9$ pixels, confirming the match between the points of inflection. This can now be compared with:

$$W_{\text{input Gaussian function}} = 10.0 \text{ pixels.}$$

The width W is a very interesting quantity because its value as measured from the TLD and ICD images is equal. This is an important result because

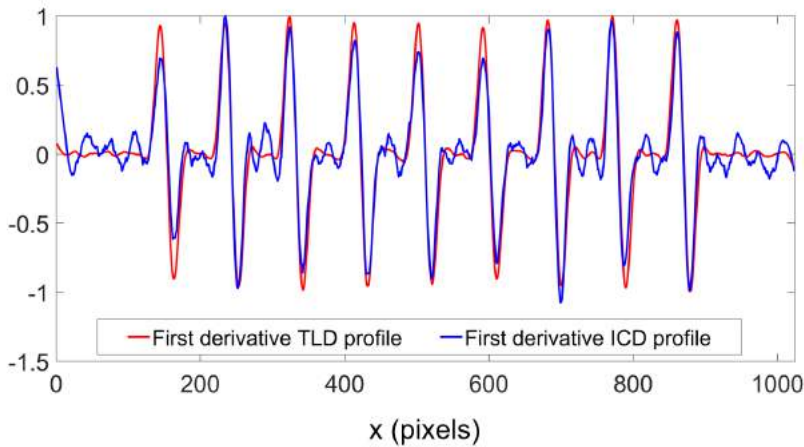


Figure 4.16: Plot of first derivative of the SE and BSE integrated profiles, confirming the match between the points of inflection in the two.

it is then a quantity that survives the evolution of the profile and can therefore be used as a measure of line width for EBID lines of different profiles. In the next section, this measure of width will be used to analyse a series of lines with different widths and a comparison with the LW measured by edge detection is discussed. It should be noted that the area under the curve in the width W could not be determined as easily from the lines in the simulated BSE image due to the rising background level in between the lines which leads to an erroneous estimation. For the same reason, it was difficult to compare the values of R obtained from the simulation with those from the TLD or ICD in the experiments. It is an intriguing observation for which a physical explanation is not apparent. In order to provide one, lines having TLD profiles as in Fig. 4.13 should be simulated for comparison with the experimentally obtained shapes. However, this profile could not be obtained from the simulation for input Gaussian shapes with any reasonable parameters. The issue is twofold - firstly, the experimentally obtained TLD contrast depends on the composition of the substrate and deposit material, neither of which could be selected in the simulation to resemble the experimental case. The contrast also depends on the detection scheme in the microscope. The fields present in the column determine the electron trajectories to the detector and need to be taken into account for an accurate simulation

of the image. The assumption that the signal is comprised equally of all electrons emitted from the material, regardless of their energy, is not realistic. Knowledge of these fields would be very beneficial in improving the simulation.

Then, by patterning lines at a large separation so that less material is deposited in between them, with sufficient dose to enable good contrast in both SE and BSE imaging, the value of W from experiments and from the simulation could be compared for both SE and BSE images, and its significance determined. By patterning lines with the two kinds of profiles described previously and comparing them to the SEM simulation, it may be possible to determine the physical significance of the parameter W .

4.5 Recipe development for the patterning of dense lines

An experiment was designed to study the growth of dense EBID lines as a function of the defined LW . Unlike the patterning of isolated structures, it is to be expected that the issues of proximity effects at low separation, among others will play a role as in resist-based lithography. We have seen that existing models in EBID are not sufficiently advanced to make accurate predictions of the resultant LW given certain patterning parameters. In order to develop a recipe for patterning lines of desired width at desired spacing, it is essential to study the growth by carefully designed experiments taking into account all the important parameters and apply reliable measurement techniques. Arrays of Pt/C EBID lines were patterned on a silicon substrate with a native oxide layer at 20 keV, 50 pA, $t_{dwell} = 20 \mu s$, pitch = 1 nm, $N_{pass} = 10$ (dose = 10000 C/m²). A range of parameters was used: defined $LW = 1$ nm, 2 nm, 5 nm, 10 nm, 15 nm, 20 nm, 25 nm and 30 nm; centre to centre spacing = 100 nm and 700 nm. The patterning was carried out in serial mode in the FEI Nova NanoLab 600 Dual Beam system using a home built Labview program for beam positioning and blanking. A total of approximately 200 lines were patterned and analysed for the experiments described in this section.

The lines were imaged with the TLD, ICD and MD in the FEI Verios 460

SEM and Fig. 4.17 shows the SE images of the arrays patterned at 100 nm line spacing. The wider lines appear darker, suggesting that they are thicker. From the integrated line profiles (Fig. 4.18), they also appear broader than defined. This has been quantified in the following section.

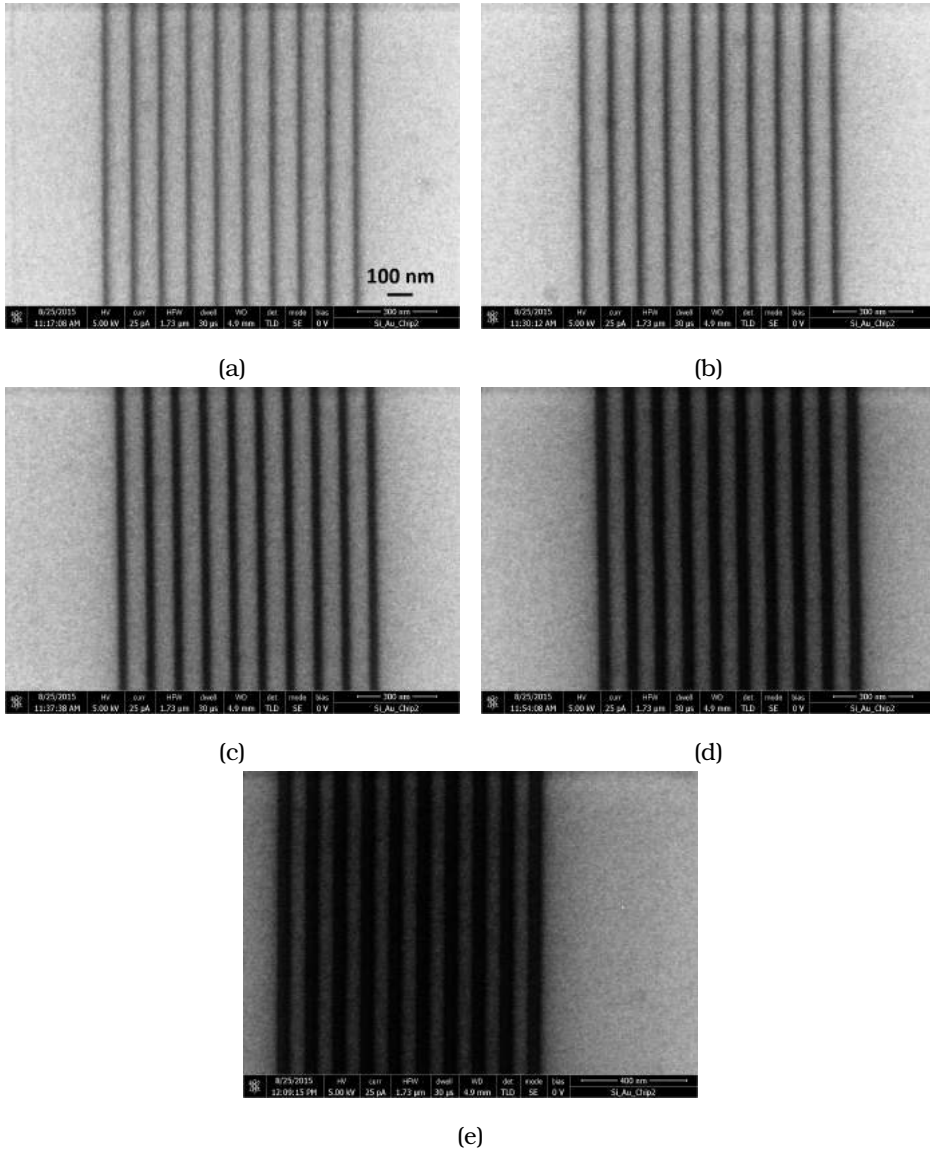


Figure 4.17: TLD images of lines of defined width (a) 1 nm (b) 2 nm (c) 5 nm (d) 10 nm (e) 15 nm patterned at line spacing = 100 nm.

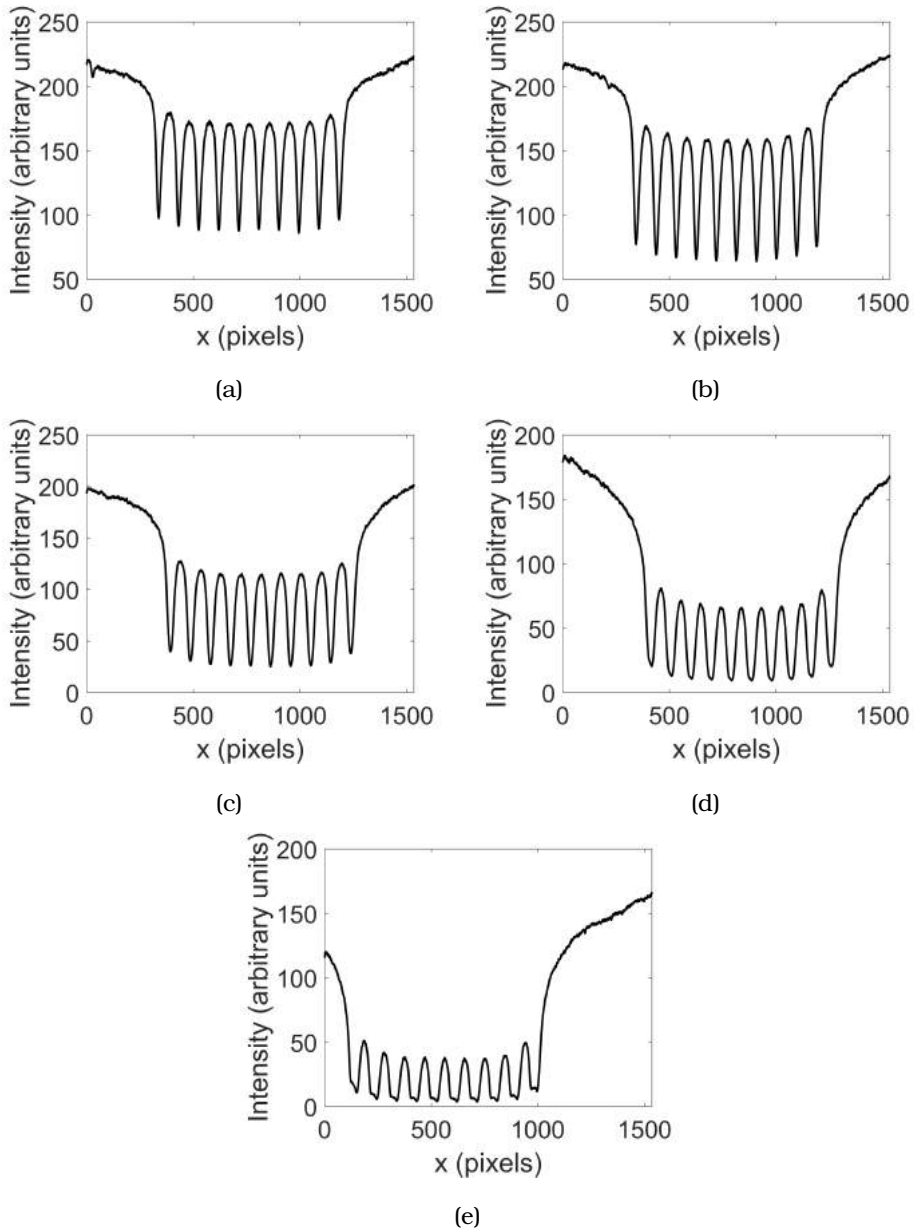


Figure 4.18: (a)-(e) Integrated intensity plots of the lines shown in Fig. 4.17.

4.5.1 Evolution of line width

As the line profiles are Gaussian, the LW was measured by edge detection and Fig. 4.19 shows the plot of the measured LW (1σ) versus the defined

LW. The width appears to increase linearly and a straight line fit can be made having a slope of 2. This fit can be used to predict the LW of lines patterned with any width between 0 and 15 nm, for the parameters used here. Alternatively, this provides a recipe for patterning lines of any desired width in this range by using the parameters described. An important observation that must be made here is that the fit does not pass through the origin. This may seem surprising at first because for a defined LW = 0, the resultant LW is expected to be zero as well. However, in the terminology used here, 'defined LW' refers to the distance between the edges of the defined line. So defined LW = 0 actually refers to a single pixel wide line. For the dose and parameters used in this experiment, a width of 23 nm is achieved for such a line.

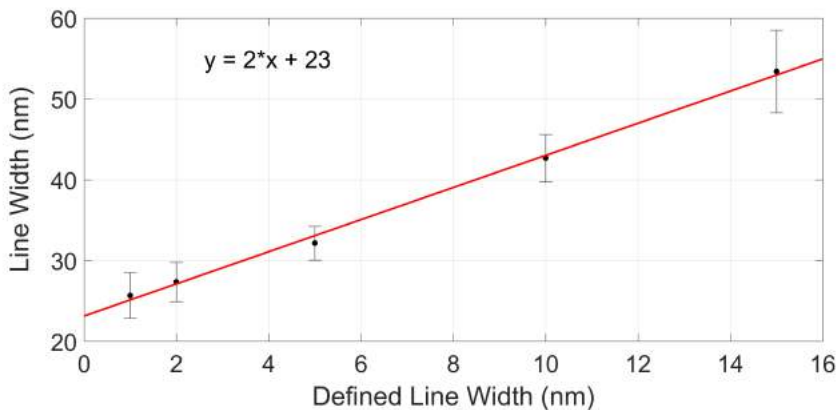


Figure 4.19: Plot of measured 1σ Line Width (by edge detection) as a function of defined Line Width for spacing = 100 nm. A straight line fit through the data results in a slope of 2 and the width of a single pixel wide line (defined line width = 0) can be seen to be 23 nm.

A 1 nm wide line becomes 25.7 nm wide, a 2 nm wide line becomes 27.3 nm wide, a 5 nm wide line becomes 32.1 nm wide, a 10 nm wide line becomes 42.7 nm wide and a 15 nm wide line becomes 53.4 nm wide. The lines of defined width = 20 nm, 25 nm and 30 nm were not analysed as their resultant width turned out to be so large that the lines were no longer separated. It is immediately evident that the resultant width of the lines in all cases is much more than defined, with a single pixel wide line (defined width = 0) itself becoming 23 nm wide, as seen from the fit. The first question that arises is of course: why are the lines so broad? It

has been discussed in Section 4.1 that existing models cannot correctly predict the deposit dimensions at this scale. So a thorough analysis of the physical processes cannot be performed here. Instead, a simple model has been used to try and address the more practical question: can we predict the resultant line width? We begin by accepting that for the dose used in this experiment, a line of defined width = 0 becomes 23 nm wide. We assume that the patterning of each pixel takes place on a flat surface. This means that the evolving surface and the accompanying enhancement in SE's are ignored. Each patterned pixel along the width of the line is then expected to become 23 nm wide, i.e., a broadening of 11.5 nm on either side is predicted. Then, as the patterning pitch = 1 nm, a line of defined width = 1 nm would result in a width of 11.5 nm + 11.5 nm + 1 nm = 24 nm (Shown in Fig. 4.20). Similarly, defined widths of 2 nm, 5 nm, 10 nm and 15 nm would result in lines of 25 nm, 28 nm, 33 nm and 38 nm width respectively. This is clearly not the case and the predicted slope of 1 (from this model) is not in agreement with the observed slope. This simple analysis makes it clear that the phenomenon of broadening is more complex.

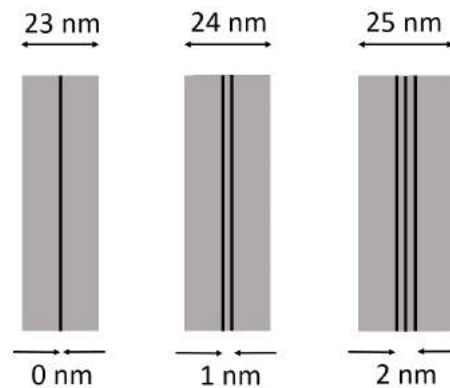


Figure 4.20: Cartoon explaining the broadening expected based on the simple model which assumes that the patterning of every pixel takes place on the flat substrate. The predicted width of a line of defined width = 0 (from the fit) is 23 nm, and this is taken to be the broadening for every patterned pixel along the width of the line. Then, for the patterning pitch of 1 nm used here, the resultant widths of lines of defined width = 1 nm and 2 nm are calculated to be 24 nm and 25 nm respectively. The resultant widths of lines defined as 5 nm, 10 nm and 15 nm wide are calculated similarly (not shown) to be 28 nm, 33 nm and 38 nm respectively.

By means of this experiment and the subsequent characterisation of the dense lines, we have demonstrated that it is possible to control and/or predict the width of EBID lines in a dense array. It is vital to point out that the numbers for LW obtained here are a result of the patterning parameters used and do not represent the resolution limit of EBID patterning. Much smaller lines can and have been patterned by EBID in the current limited regime as in [48] using a lower dose (2500 C/m^2). However, no attempt was made to achieve smaller lines in this experiment. Instead, the aim was to pattern lines with sufficient contrast such that the trend in growth could be studied by performing edge detection and better control over EBID can be achieved for the purpose of lithography. This was achieved by careful selection of patterning parameters, ensuring that the dose was appropriate for the deposition of sufficient material while at the same time achieving lines with a Gaussian profile. Interestingly, the PSD of these lines had a profile that matches well with lines patterned in lithography. A typical profile is shown in Fig. 4.21(a) which could be fitted as in [40] to yield the noise level. This was subtracted from the biased LER as described in Chapter 3 and the unbiased values of LER could be obtained (Fig. 4.21(b)). Based on the discussion in Chapter 3, it can be concluded that the vibrations were either much lower in this experiment or due to a combination of various other factors did not influence the PSD significantly. LER values lower than 1.5 nm (1σ) were obtained and since no special patterning strategy was employed here (merely pixel exposure in a serpentine strategy), these values can be said to be inherent to the EBID process and the error bars on the LW data are the corresponding values of LWR (Line Width Roughness). An increase in LER can be observed for higher LW as the data in Fig. 4.21(b) indicates. This may be because the patterning time is more for wider lines, making the deposition more sensitive to fluctuations in the process. The noise in the image is 1.4 nm , which gives an estimate of the error in the measurement.

One of the key considerations in any lithography technique is the variation in LW along the line and over a set of lines which amounts to roughness in the pattern. A low LER is therefore a strong selling point of this technology and the values seen here are very satisfactory. The lines were also analysed using the point of inflection technique described above and the values of W are plotted in Fig. 4.22. Once again, a linear increase in width is observed. For defined $\text{LW} = 1 \text{ nm}$, 2 nm and 5 nm the values of W are within a few

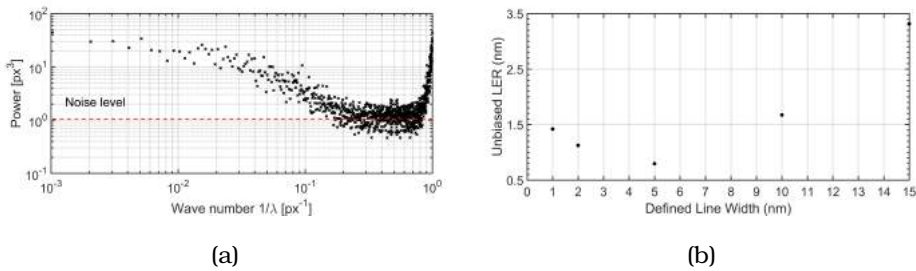


Figure 4.21: (a) Typical PSD of the lines shown in Fig. 4.17. The noise level has been determined as described in [40] and the unbiased value of LER has been determined for one of the images as described in Chapter 3 (b) Plot of LER (unbiased) for each of the images in the set, showing typical 1σ values lower than 1.5 nm

pixels of the LW values measured by edge detection. However, for the lines with a larger defined width, the values of W and LW differ by as much as 6 nm. This is possibly because of the increase in patterning time for wider lines, which could in turn lead to an increase in dose fluctuations. Due to the sensitivity of the SE signal to fluctuations in surface topography, this would result in fluctuations in the width of the patterned lines within an image. This is supported by the observed increase in the LER in Fig. 4.21 (b). In addition, the scatter in values of LW and W within the image are reflected in the error bars on the corresponding plot in Fig. 4.22, from which it seems possible that the difference in the sensitivity of the two measurement techniques to fluctuations in SE topography could be responsible for the difference in measured line width. Efforts could be made to overcome this problem if it is of interest to pattern such wide lines (> 40 nm), but it is important to note that the values of W and LW are in fact a good match for the high resolution lines (< 40 nm), which is the focus in lithography.

Next, several sets of lines were patterned with the same dose and parameters at 700 nm line spacing. At this separation it was possible to analyse lines in the entire range of defined width (1 nm to 30 nm). The values of LW measured by edge detection (black dots) and W measured by the point of inflection method (blue squares) are shown in Fig. 4.23. Once again, a straight line fit is possible through the data points in both cases (solid and dashed red plots). The line width that should be exposed to the electron beam in order to obtain a desired LW can be determined from

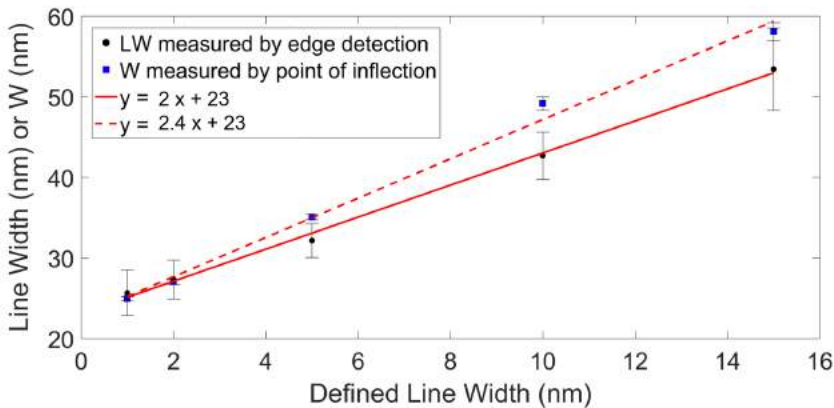


Figure 4.22: Plot of measured W by point of inflection (blue squares) as a function of defined LW for spacing = 100 nm. The straight line fit (dashed red plot) shows a slope of 2.4 and the width of a single pixel line is found to be 23 nm. The line widths measured by edge detection (black dots) and the corresponding straight line fit (solid red plot) are shown for reference.

this plot by reading off the appropriate values. The values of W and LW are seen to differ by a few nanometres for defined $LW = 1$ nm, 2 nm, and 5 nm, and the difference increases as the defined LW increases. But the error in the measurement of LW also increases (as seen from the error bars in the plot). For a single pixel line, $W = 19.2$ nm and $LW = 18.0$ nm, significantly lower than for 100 nm spacing and the slopes of the plots corresponding to 100 nm spacing (Fig. 4.19 and 4.22) are greater than that for 700 nm spacing (Fig. 4.23). More densely spaced lines therefore result in more broadening, which may be explained by proximity effects during patterning ([17], [58]). Two kinds of proximity effects are known to be relevant in patterning dense structures. The first is the broadening of a line due to the patterning of another line in its vicinity. When the second line is being exposed, the SE's generated in the substrate can cause deposition on the existing line itself, causing it to broaden. The second kind refers to the broadening of the line that is being patterned causing it to be broader than the one deposited previously in its proximity. This comes about due to the fact that the second line is being grown not on the substrate but actually on the tails of the previously patterned line. Due to the angular dependence of the SE yield, more deposition is observed in the case of this line. This must be taken into account when discussing control over EBID patterning as both LW and spacing must be considered

for recipe development. In [58], a solution to the second kind of proximity effect has been proposed and shown through experiments to be successful in reducing it. It essentially involves correcting the dose applied to the pixels of the second line so as to compensate for the extra growth. However, this requires an accurate estimate of the proximity effect to begin with, or more experiments to investigate this as a function of dose and line spacing. Secondly, they observed that a change in patterning strategy (random patterning and patterning in multiple passes) reduced this effect significantly. From the results in Chapter 2, we know that this is not the case for the lines patterned in the current limited regime. This difference makes sense in light of the much higher pixel dwell times used in their experiment: 4 ms as opposed to the 20 μ s used here, suggesting that the patterning regimes are not the same. Also, while there is a scatter in LW within an array (indicated by the error bars in the plots of LW), it does not follow a trend such as an increase along the patterning direction (L-R). So the broadening observed here cannot be explained in terms of this effect alone and it is perhaps a combination of the two kinds of proximity effects.

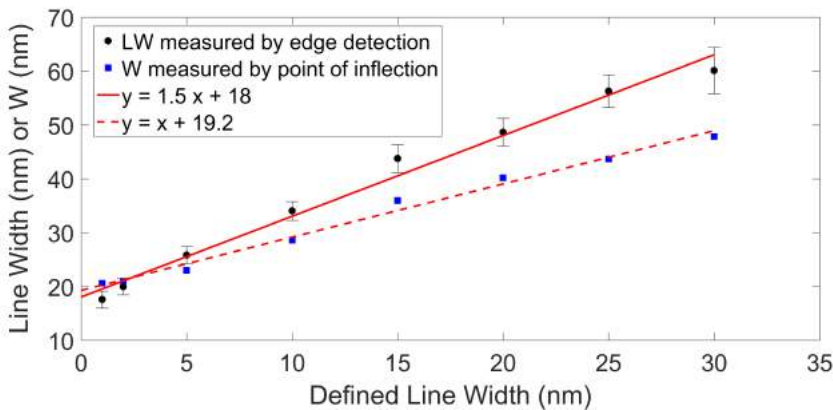


Figure 4.23: Plot of resultant LW measured by edge detection (black dots) and W measured by point of inflection analysis (blue squares) versus defined LW for lines patterned at 700 nm spacing with the same parameters as in Fig. 4.17. Straight line fits through both data sets are shown by the dashed (inflection method) and solid (edge detection method) red plot. At this spacing, lines with Defined LW = 20 nm, 25 nm and 30 nm are also seen to be well separated.

The LER measurement for these lines also results in low values of unbiased line edge roughness with a similar increase in LER with defined LW as shown in Fig. 4.24. A similarity between the 1σ LW and W is promising as

the latter can be measured from different kinds of SE profiles and is not limited to Gaussian profiles. Moreover, it does not require edge detection, using instead the integrated intensity profile. It therefore has the potential to be used for very high resolution lines which do not have sufficient material in them to provide the high contrast SEM images necessary for edge detection. If a concrete physical relation can be established between the W and LW, the point of inflection analysis would be a good method to measure the width of dense EBID lines.

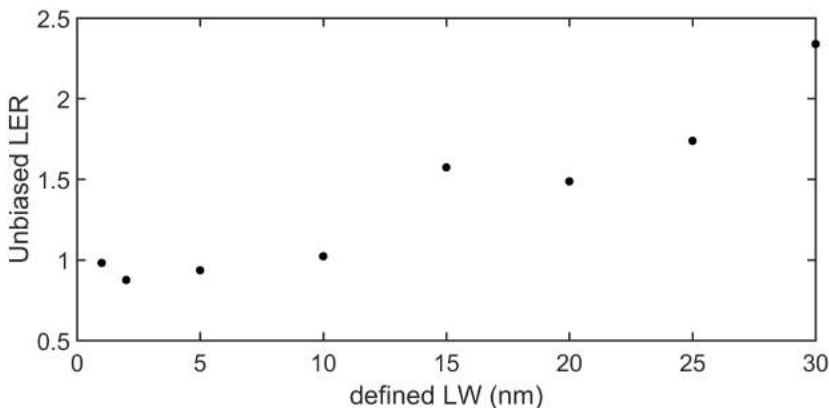


Figure 4.24: Unbiased LER values for the lines analysed in Fig. 4.23 at 700 nm spacing.

4.6 Discussion

The interpretation of contrast in SEM images is vital for metrology. From this follows the need to understand the different detection techniques used. As discussed in Chapter 3, simply measuring the apparent width by eye from an image is often misleading. Here we see that simply measuring the FWHM from images can be problematic as well. For the lines in Fig. 4.13, for example, the LW measured from the SE image would be larger than that from the BSE image, resulting in two different values of LW. This issue has been encountered in imaging resist-based lines and analysed by Postek et al. [59]. They found that for lines with vertical sidewalls, the widths measured from SE images and simultaneously acquired low-loss BSE images were systematically different, with the former always being larger than the other. This was supported by JMONSEL simulations of lines with input line shape similar to the experimental case of vertical

sidewalls, i.e., lines whose real profile was modelled as a step function. It should be mentioned here that the system was somewhat simpler than ours in that material contrast was avoided by simulating lines of the same material as the substrate (silicon on silicon). Nevertheless, their results and analysis provide an analogy to the problem encountered in the metrology of EBID lines. An important result from their simulation was the finding that imaging a structure with vertical sidewalls using an infinitely small electron spot resulted in almost identical LW measured from SE and BSE images. On the other hand, the combination of vertical sidewalls and a 5 nm electron spot saw a significant increase in the difference in LW from the two. Additionally, they note that the combination of sloping sidewalls (slope = 14°) also resulted in the LW from SE images being larger than that from BSE images. The reasons for the broadening were discovered to be (1) the convolution of the structure with a gaussian electron profile having a finite size (2) the spread of the beam in the structure (3) drift. By modelling the SE and BSE profiles at the deposit edges, they were able to show that the two signals are affected differently by these effects, resulting in the observed difference in LW. So it is necessary to understand and interpret SEM images in order to report LW measurements. Another valuable observation has been made regarding the role of the line profile itself in the measurement of LW. The claim that the LW measured from two kinds of images is different is itself entirely contingent upon the definition of LW. As there is no physical reason to measure LW from SE and BSE images in the same way, i.e., by measuring FWHM, for instance, doing so only results in arbitrary numbers for either case. So the fact that the two measurements are different is not in itself physically significant. In Fig. 4.25, taken from [59], the simulated input line shape (red curve), SE profile (blue curve) and BSE profile (green curve) are shown and it can be seen that while the SE profile may appear broader, if the LW is measured at approximately 90% of the maximum in the SE profile and at approximately 50% of the maximum in the BSE profile, the numbers would be in good agreement with each other as well as with the actual LW. This would then be a better criteria for LW measurement.

Such simulations would greatly help interpret the parameter "W" and understand the EBID line profiles. They would perhaps also help in finding out the actual line profiles. In order to do this, exact knowledge of the detection scheme and the fields present in the microscope column is

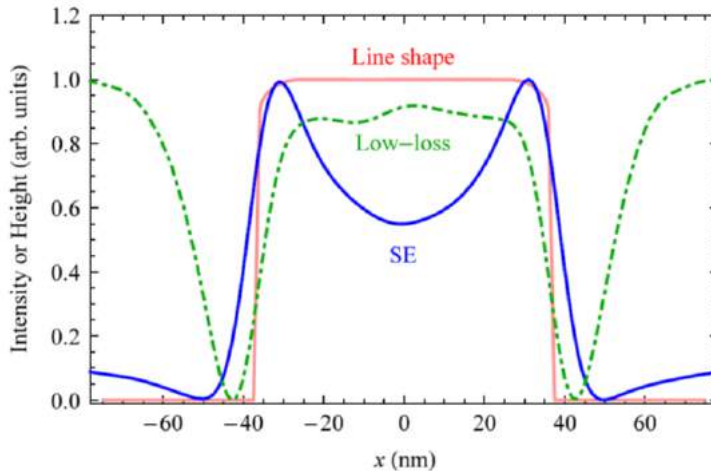


Figure 4.25: Simulation results from [59] illustrating the problem in measuring LW from SEM images. The input line profile with vertical sidewalls (red curve), SE profile (blue curve) and BSE profile (green curve) are shown. While the SE profile is clearly broader than the BSE profile, measurement of LW at 90% of the maximum in the SE profile would result in approximately the same value as the measurement at 50% of the maximum in the BSE profile.

needed as they determine the electron trajectories and collection efficiency.

4.7 Conclusions and recommendations

This chapter addresses the controlled patterning of dense EBID lines. The work consists primarily of two parts - patterning and imaging. High resolution dense lines of a range of widths have been patterned and a recipe has been suggested for the fabrication of lines of desired width and spacing, based on the experimentally observed trends. The lines were found to always be broader than the defined width, with a single pixel line becoming more than 20 nm wide at the dose used. However, this observation does not in any way indicate the limits of the resolution achievable in EBID. Much smaller lines have been demonstrated to be possible by simply using a lower dose. A higher dose was used in this study in order to obtain lines with sufficient material content to provide relatively low noise images. By this we mean that the SEM images of the lines were required to have enough signal for edge detection and other analyses to be performed. This leads to the second part of the study: imaging and

dimensional characterisation of EBID lines.

The profiles of EBID lines patterned with different parameters have been discussed and a qualitative analysis of the evolution of line profiles has been given. The line profiles have been discussed in detail in terms of the imaging techniques. It has been shown through a simple analysis that AFM can be used to measure LW of shallow lines and the error in this method has been theoretically estimated. A quantitative comparison of LW from AFM and SEM images has been provided to demonstrate this. This is an interesting result as it makes it possible to estimate the volume of a line, by measurement of height and width, using a single technique. Complete 3D information about a set of dense Pt/C lines has been obtained by AFM. A comparison of SE, BSE and AFM images has been provided from which a new technique to measure line width based on the detection of the point of inflection of the Gaussian shapes has been realised.

The study of EBID line profiles undertaken here has raised several important issues in the imaging and metrology of sub-30 nm lines having a Gaussian profile. The choice of LW as the 1σ value from the gaussian fit to the line profile is completely arbitrary. The numbers obtained from the analysis of SE and BSE images are therefore different as expected. An alternative definition of line width as the distance between the points of inflection in the profile has been provided and arguments provided for its use. A big advantage of this technique is that it is based on the integrated intensity profile and not on edge detection. So it can be used for very small lines which do not contain enough material to provide the high contrast SEM images needed for edge detection. It also provides a measure of width that is not limited to the analysis of Gaussian profiles but can be used for a variety of profiles. An attempt has been made to provide a physical explanation for the agreement between the numbers obtained from SE and BSE images from this technique. From this work, it becomes clear that the exact detection scheme and knowledge of the fields present in the microscope is essential for accurately simulating the line profile.

The EBID line profiles measured using AFM have been interpreted to provide information on the distribution of the material contained. The total volume present in a 10 nm thick EBID line in a dense array of spacing = 100 nm has been estimated. The fractions of the total volume contained

in the 1σ and FWHM range have been measured to be about 45% and 91%. The amount of material present in the halo has been estimated to be approximately 9% of the total volume. This together with the accurate measurement of line width presented here provides important information on the size and shape of the deposit that would be useful for a variety of EBID applications. This adds to the observation of the broadening of a single pixel wide line and indicates that the material contained in the tails or halo of the deposit is significant and could contribute to the LW being much greater than the spot size specified. Although this halo appears shallow, the material contained in it seems sufficient to generate contrast in SEM images. Edge detection is therefore sensitive to the extent of this material, resulting in the observed values of LW. For applications involving the fabrication of conducting deposits, this information is crucial and could aid the design of devices.

A full 3D simulation of growth in the very early stages of EBID, incorporating, in particular, SE emission from a continuously evolving surface would be immensely helpful in explaining the observed broadening of dense lines. Together with more experiments patterning lines at reduced spacing and lower dose, this could pave the way for controlled patterning for lithography using EBID.

The high resolution EBID lines patterned in this work have a low aspect ratio (close to 1). Lines of 25.7 nm, 27.3 nm, 32.1 nm, 42.7 nm and 53.4 nm were fabricated using an electron dose of 10000 C/m^2 to pattern dense lines with defined widths of 1 nm, 2 nm, 5 nm, 10 nm, 15 nm, 20 nm and 25 nm, at a spacing of 100 nm. The plot of resultant line width versus defined line width yielded a straight line fit, from which a recipe for patterning lines of desired width can be obtained by reading off the corresponding value of defined width. By performing similar experiments at different line spacing and electron dose, greater control over the fabrication can be obtained, allowing fine tuning of the resultant line width. This work presents the first attempt at recipe development for the controlled fabrication of dense lines in EBID.

The LER of high resolution EBID lines patterned in the current limited regime is quite low. Typical values of unbiased LER < 1.5 nm were obtained. This is promising for the use of EBID for lithography, as a progressive

reduction in LW and spacing makes the fabrication of well separated lines increasingly challenging. A low LER is therefore critical for high resolution patterning.

Chapter 5

Removal of interconnects in dense EBID lines

“ *We must away, ere break of day
To seek the pale enchanted gold.* ”

J. R. R. Tolkien,

he characterisation of the width of dense EBID lines in the previous chapters revealed that the width of a line depends on its proximity to neighbouring lines. As the spacing between the lines is reduced, the lines begin to broaden, leading to the question of how well separated they are. This chapter addresses the issue of interconnecting material in dense lines. As the scattering of the high energy electron beam in the substrate during EBID results in the generation of BSE's and SE2's over a radius of several hundreds of nanometres, all of which have some probability of dissociating the adsorbed precursor molecules, a thin film of (often) carbonaceous material is deposited over this range. So it is to be expected that in the patterning of dense EBID lines, this would contribute to the deposition of material in between the patterned areas. As the thickness of this film falls off very gradually, it adds to the challenge of characterisation of EBID line profiles and any measure of line width must somehow take this interconnecting material into account. EBID patterns have also found several applications in electrical measurements, especially since the development of techniques to improve their conductivity ([60], [61], [62], [63], [64], [65]). There remains, however, the problem of crosstalk due to the halo deposited alongside. This has been demonstrated by Gopal et al. [66] who patterned Pt/C EBID lines on a Si/SiO₂ substrate using a range of primary beam energies. They measured a leakage current between them that increased exponentially with increasing beam energy and decreased with line spacing. This observation of the connecting material

being conducting is an important result, based on which patterning at lower beam energies appears attractive. However, this is only a solution for lines separated by several microns. As the semiconductor industry approaches the single nanometre regime, the material deposited in between the lines becomes increasingly significant. The TEM image of Pt/C EBID lines deposited on a thin membrane (shown in Fig. 2.13) clearly reveals the presence of interconnecting granular deposits between lines spaced approximately 50 nm apart. Such deposits are a problem not only for electrical measurements but also for shape control. Here we explain how this comes about as a result of EBID: Fig. 5.1(a) and (b) show simulated

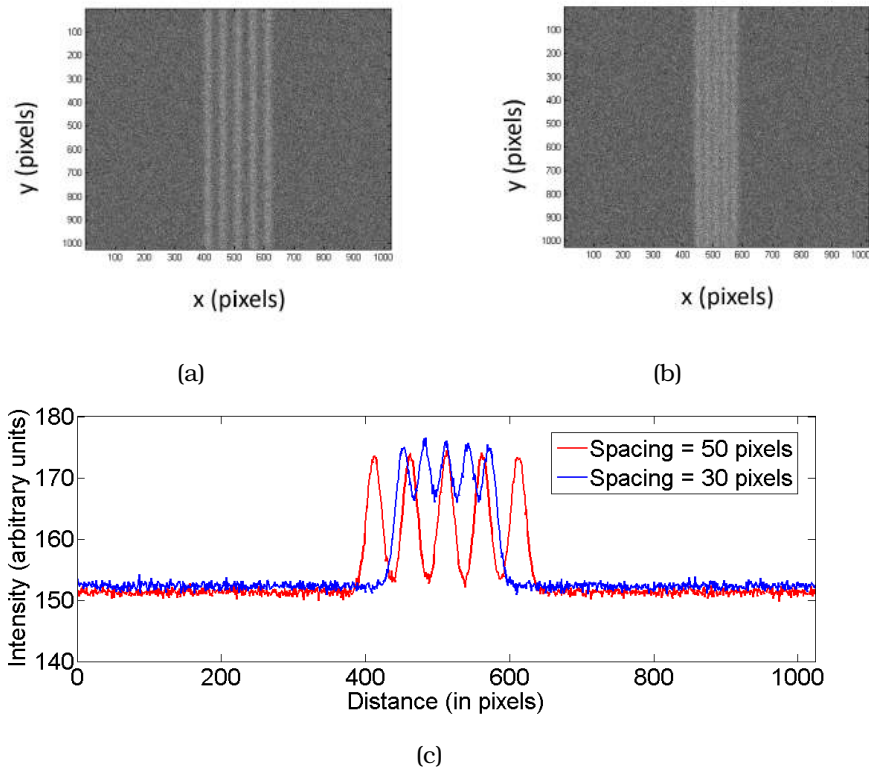


Figure 5.1: Simulated SE images of dense EBID lines with Gaussian profiles, generated as described in Chapter 3, subsection 1. The centre to centre spacing between the lines is (a) 50 pixels and (b) 30 pixels. (c) Comparison of the integrated intensity profile of the two images, clearly demonstrating the increase in amount of material deposited in between the lines as the spacing decreases.

SE images of two sets of dense EBID lines at centre to centre separation

= 50 pixels and 30 pixels. The lines have been generated as described in Chapter 3. Each image consists of 5 EBID lines having Gaussian profiles. The parameters used to define the Gaussian function, chosen arbitrarily, are: $\sigma_L = \sigma_R = 10$ pixels, $LER = 0.5$ pixels, $Base\ level_L = Base\ level_R = 20.2$ pixels, $\nu = 35$ pixels, correlation length = 30 pixels, roughness exponent = 0.75. As a result of the linear addition of the Gaussian profiles at the specified separation, the material deposited in between the lines increases with decrease in spacing as is clearly visible from the integrated intensity plot of the two images shown in Fig. 5.1(c)). This is therefore an unavoidable consequence of patterning lines that have Gaussian profiles.

At the values of line separation of interest to us, the cause of this interconnecting deposit (here onwards referred to as interconnects) is expected to be primarily SE1's, in contrast to the mechanism suggested in Gopal et al. This is because their spatial density is much more than that of BSE's or SE2's (as estimated in Section 2.1). Proximity effects could add to the deposition, causing a line to grow due to electron beam exposure of nearby pixels, resulting in a different integrated profile than the one shown here. However, the composition of the interconnects would be similar to that in Gopal et al., resulting in a conduction path, and therefore needs to be addressed. One solution would be to pattern lines with vertical sidewalls and no interconnecting tails. However, to do this using EBID would require complex patterning strategies, not desirable for commercial lithography. Moreover, it is yet to be proven experimentally to be possible at all. We choose instead to remove this connecting material using a one-step technique that can be implemented in the SEM post-EBID. The following section describes experiments to implement this at high resolution with minimum damage to the bulk of the line itself. We describe the principle, choice of materials, issues involved and verify the removal of interconnects using SEM and AFM measurements.

The removal of interconnecting material in dense EBID lines essentially requires a technique that:

1. is high resolution
2. can be implemented inside the SEM and
3. involves the minimum number of additional steps

so that all the advantages of focused electron beam induced process-

ing are retained. Electron Beam Induced Etching, reported for the first time in 1979 ([67]) is a chemically selective nanofabrication technique that is complementary to EBID in that it is top down, with a significant advantage over ion milling due to the absence of sputtering. Adsorbed precursor molecules are dissociated by the electron beam, leading to the formation of reactive fragments which in turn react with the substrate to locally volatilize it. Considering EBIE in light of the requirements mentioned above, the high resolution of the technique has been demonstrated by ([68], [69], [70]). While the inherent high resolution of the process is apparent as a result of being electron beam induced, it is to be noted that EBIE is in some ways more complex than EBID as a result of surface site activation and secondary reactions involving etch by-products which could govern the process and limit the resolution ([71], [72], [73], [74]). Gas-assisted etching has been demonstrated inside a high vacuum SEM with precursor injection through a nozzle ([75]), as well as in the ESEM ([76], [77]) where the SEM chamber is flooded with the precursor gas upto pressures of 1-2 mbar while maintaining differential vacuum. While the difference in gas flux in the two cases would alter the surface chemistry somewhat, the processes governing the etching remain the same. Further, as EBIE involves electron beam exposure in the presence of a suitable precursor, just like EBID, it involves no post processing, adding only one step to the process. This motivates the choice of EBIE to effect cleaning in dense EBID lines, referring to the removal of carbon deposit around and in between EBID structures coming about as a result of the patterning itself.

5.1 Experimental methods

5.1.1 Choice of precursor

A large number of EBID precursors contain carbon, which then often remains in the deposit. A few popular precursors for the deposition of metals are MeCpPtMe_3 , Co_2CO_8 and $\text{W}(\text{CO})_6$, all of which result in deposits containing metal nanocrystallites in a carbonaceous matrix ([62], [78], [79]). The tails of the deposit, being shallow, are often carbonaceous but contain metal grains (Chapter 2 Fig. 2.13), providing a conduction path between neighbouring structures. Therefore, the development of a technique that enables the removal of carbonaceous interconnects would be widely applicable and relevant in EBID. Based on this, carbon was

selected as the material to be deposited. Two commonly used precursors for carbon deposition are naphthalene and phenanthrene, the first composed of two benzene rings bonded to each other and the second composed of three. Both precursors have been labelled as carcinogenic and so a better alternative was sought. R. P. G. Siebers and J. J. Mulders (unpublished) studied several linear chain alkanes as potential carbon precursors as they also contain only carbon and hydrogen, with the advantage that they are not hazardous to health. Alkanes having 8 to 14 carbon atoms: octane, nonane, decane, undecane, dodecane, tridecane and tetradecane were investigated as they had favourable values of melting point, boiling point and vapour pressure (high enough to carry out deposition in a reasonable time, yet low enough to maintain the chamber pressure below 10^{-4} mbar to allow proper functioning of the turbo pump). Larger alkanes were deemed unsuitable as a result of being waxy and therefore very sticky, leading to contamination of the chamber. Systematic measurements of deposition yield were made with these alkanes at 5 keV and GIS temperature of 28 °C, yielding the highest values for dodecane and tridecane of approximately $1.7 \times 10^{-3} \mu\text{m}^3/\text{nC}$. The choice between these two precursors was made based on another important criterion: the pumping out time. Upon closing the GIS valve after the use of dodecane, the chamber pressure was restored to 1×10^{-6} mbar within a few minutes, whereas this time was longer in the case of tridecane. A series of depositions made after the GIS valve was closed confirmed that dodecane was pumped out faster. And finally, dodecane also compared favourably with naphthalene when the yields were compared at 28 Celcius. Based on this analysis, dodecane ($\text{C}_{12}\text{H}_{26}$), a liquid at room temperature, was selected as the precursor for carbon deposition by EBID. It was loaded into the crucible of a standard FEI gas injection system and let in through a nozzle at room temperature.

Next, a choice had to be made for the etching of carbon. There are several reports in literature on the removal of carbon by EBIE, such as the fabrication of holes in thin carbon membranes ([68]) and the slimming of carbonaceous nanowires ([76]). H_2O , XeF_2 ([69]), NH_3 ([77]) and O_2 ([80]) have been used as etch precursors. As the use of a corrosive gas such as NH_3 is undesirable and very high pressures of O_2 are known to be needed ([81]) for EBIE, H_2O was selected as the etching precursor for this work. Crystals of $\text{MgSO}_4 \cdot 7\text{H}_2\text{O}$, a hygroscopic material, were loaded into a crucible mounted on another GIS. The absorbed water molecules were let

in through the nozzle at room temperature.

Both EBID and EBIE were carried out inside a high vacuum SEM. An FEI Helios 650 Dual Beam system fitted with two separate gas injection systems for precursor delivery was used. The needles were each aligned to be 150 microns above the sample and 100 microns away from the centre of the field of view. The base pressure in the experiments was in the range of 2×10^{-6} mbar to 4×10^{-6} mbar. The chamber pressure during patterning (in the case of both precursors) was in the range 2.5×10^{-6} mbar to 4.5×10^{-6} mbar. Following a few hours of deposition, the chamber would take increasingly longer to pump down and electron beam induced sample contamination was observed to increase. This was likely due to dodecane sticking to the walls of the chamber and other open surfaces. Additionally, on letting in water after deposition, the contamination level was found to be higher. This is consistent with reports of increased diffusion of hydrocarbons in the presence of adsorbed water layers. To work in clean conditions therefore, all carbon depositions were performed in succession, after which the chamber was allowed to pump down for at least two hours, and overnight when possible. The etching experiments were then performed in succession.

5.1.2 Choice of substrate

The choice of substrate is significant in experiments involving deposition and etching as it determines the interaction volume, adsorption and diffusion rates, and eventually the deposition/etching rate. For electrical measurements, it is obviously necessary to have an insulating substrate. An important effect to take into account then is charging. Since the focus of this study is to control the shape of the deposits, though, this is not necessary and easily available silicon substrates with a native oxide layer should suffice. But the presence of SiO_2 presents an issue as it is known to be decomposed under electron beam exposure ([82]). This could lead to effects that might interfere with the interpretation of results in this work as we aim to remove deposited carbon alone and not affect the substrate in any way. To prevent this, silicon substrates with a native oxide layer were coated with 20 nm of gold-palladium with a 5 nm titanium adhesion layer. This has the additional advantage of ensuring a strong SE contrast with the carbon deposit due to its significantly higher SE yield.

5.1.3 Imaging

The patterns were imaged in an FEI Helios 650 Dual Beam system fitted with an in-column Through-Lens SE detector (TLD) and two BSE detectors located higher up in the column (ICD and MD). Images can be acquired simultaneously with the three detectors and the imaging conditions were optimised as described in chapter 3, Section 3.2.2. A Bruker Fast Scan Dimension AFM was used to characterise the height of the patterns before and after etching.

5.2 Removal of carbon halo

An experiment was performed to test the etching of EBID carbon material using water. An array of four identical squares 500 nm x 500 nm in size was patterned on the substrate at 5 keV, 400 pA, dwell time = 100 μ s, number of passes = 200, patterning pitch = 5 nm (Fig. 5.3 (a)) using the carbon precursor. The parameters were selected to result in a deposit height of approximately 200 nm, based on preliminary experiments to characterise the deposition from dodecane. Such a tall structure would give rise to forward scattering in addition to backscattering and secondary electron generation, which would together give rise to a thick halo around the deposit that could be imaged with the SE detector. Indeed, CASINO simulations show that the BSE range in the substrate is approximately 60 nm at 5 keV, but the extent of the halo can be seen from (a) to be at least 200 nm which is no doubt a consequence of deposition from forward scattered electrons (FSE's). An integrated intensity profile (b) was taken across one of the squares (marked by the blue rectangle in (a)) for reference. The two peaks in the centre of the plot (b) correspond to the positions of the left and right edges of the square which have a high SE signal due to their slope. During the deposition of the array, which took approximately 3 minutes per square, some drift was observed, resulting in structures that are not perfectly square as defined but appear to have some asymmetry and rounded edges. As a consequence of this drift, the left and right sidewalls of the square may not be identical and this is reflected in the difference in the SE intensities of the two peaks. Moving outwards from the peaks on both sides, the intensity can be seen to drop due to the presence of the halo made up of carbon. As the number of BSE's and FSE's decreases with the distance from the pattern, so does the thickness of this

film and the SE signal is seen to go up again, flattening off as we approach the unexposed part of the substrate.

The goal of this experiment was to remove the carbon film surrounding the deposits. It was decided to clean approximately $1.5 \mu\text{m}$ around the deposits to ensure the removal of the entire extent of the halo. After allowing the dodecane to be pumped out over several hours, water was let into the SEM chamber through the GIS nozzle. When a stable pressure of 4.4×10^{-5} mbar was reached, the etching was begun. A high current was used in order to etch faster, keeping in mind the large area that needed to be cleaned. In comparison to EBID, EBIE is complicated by the fact that it is in fact a two precursor system, with hydrocarbons being present in the chamber in addition to the water that has been let in. The partial pressure of these is of course lower than that of water, but the EBID cross section resulting in the deposition of contamination is higher. So a careful choice of parameters is needed to ensure that etching dominates over the competing EBID. It seems advantageous to use a high current, increasing the number

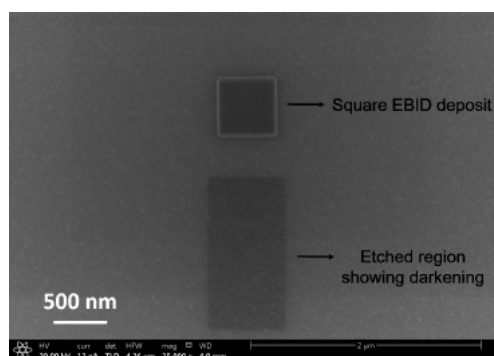


Figure 5.2: Darkening observed in place of etching when a large area of the halo (about $1.5 \mu\text{m} \times 500 \text{ nm}$) near the lower side of a square EBID deposit was exposed to EBIE using 3.2 nA with a pixel dwell time of $1 \mu\text{s}$.

of SE's generated. This would increase the number of etching events, while not necessarily increasing the deposition because of the low partial pressure of hydrocarbons. In other words, EBID of contamination would become precursor limited at a lower current than the etching of carbon, shifting the balance in favour of the latter if the current is increased further. In the interest of extending the results to high resolution experiments, a beam energy of 20 keV was selected as a small spot size can be achieved.

The choice of dwell time was made following an interesting observation.

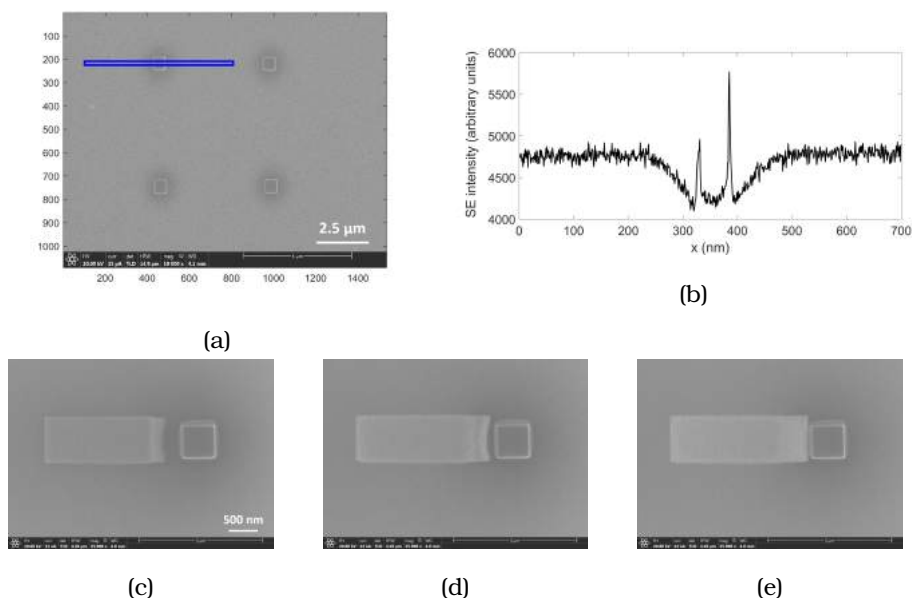


Figure 5.3: (a) SE image of four identical carbon squares on a silicon substrate covered with 20 nm of gold-palladium patterned by EBID from dodecane. The blue rectangle indicates the area of one of the squares over which the SE intensity is integrated and plotted in (b). The two peaks in the centre indicate the positions of the edges of the square and moving outwards from the centre, it can be seen that the signal flattens off to the left and right of the deposit on approaching the unexposed part of the substrate. (c) Cleaning of halo beginning from the left end of the image. An area of about 700 nm length and 100 nm width was exposed until brightening was seen in the SE image. It was then moved rightwards all the way to the edge of the square (d,e). The total time taken to etch the area in (e) was about 90 s.

Since the substrate has a higher SE yield than carbon, the SE signal is expected to go up upon removal of the carbon film. A square EBID deposit 500 nm in size was patterned (Fig. 5.2) and an area of about 1.5 μm length and 750 nm width was selected at a distance of about 300 nm from one of the edges, to include the halo. It was exposed to a 3.2 nA, 20 keV electron beam in the presence of water. A pixel dwell time of 1 μs was used and the SE signal was continuously monitored as this area was scanned for several minutes. The exposed region was observed to darken (Fig. 5.2), suggesting that it was being contaminated. A range of dwell times from 300 ns to 30 μs was tried, with the same result. However, when the same area was divided into smaller "strips" roughly 100 nm in length and scanned one

after the other, brightening was observed for dwell times in the range 1 μs to 30 μs . Moreover, the dose needed depended on the area of the strip, with a smaller area showing an increase in SE intensity sooner (at a lower dose). In general, the dependence of the etching not only on dose but on the manner in which the dose is delivered suggests that in the conditions existing in the system, EBIE is taking place in the precursor limited regime. This is perhaps unsurprising given the high current being used. This particular dependence further indicates that precursor diffusion has a significant role to play here. A possible mechanism is as follows: When a large area is being scanned, the time taken before a given pixel is revisited by the electron beam is also large. In this time, contaminants could diffuse into the region being scanned, increasing their local density, because the hydrocarbon molecules initially present there would have been dissociated. As mentioned earlier, the presence of water would enhance this process. In contrast, when a smaller area is scanned, the etching overcomes the deposition which is no longer enhanced by diffusion because a given pixel is rapidly revisited with a high current. The mechanism proposed here is based purely on these observations and a model incorporating surface chemistry or well-designed experiments would be needed to confirm what is really taking place.

For the purpose of this work it was decided to perform etching in the manner just described: by dividing the area of interest into regions of about 100 nm length and exposing it to electrons until the SE image was observed to brighten. Fig. 5.3(c)-(e) show this sequence, beginning with the left end of the image. An area of approximately 700 nm length and 100 nm width was scanned at 20 keV, 3.2 nA, dwell time = 1 μs in the presence of water until the SE image was seen to brighten. It was then shifted to the right and the exposure was repeated all the way to the edge of the deposit as shown in (e). The total exposure time was about 90 s. A high magnification image of the etched region next to the square is shown in Fig. 5.4 (a), where close inspection reveals the grains of the underlying gold-palladium confirming the removal of the carbon film. A similar etch sequence was performed on the remaining three sides of the square (Fig. 5.4 (b)), in each case approaching the deposit from the outside in. The etched area is marked in blue in (c) and an integrated intensity profile (d) was taken across the image over the region marked in yellow. With Fig. 5.3 (b) as reference, we can see from the bright regions that carbon has

been effectively etched by EBIE using water. However, since the etching

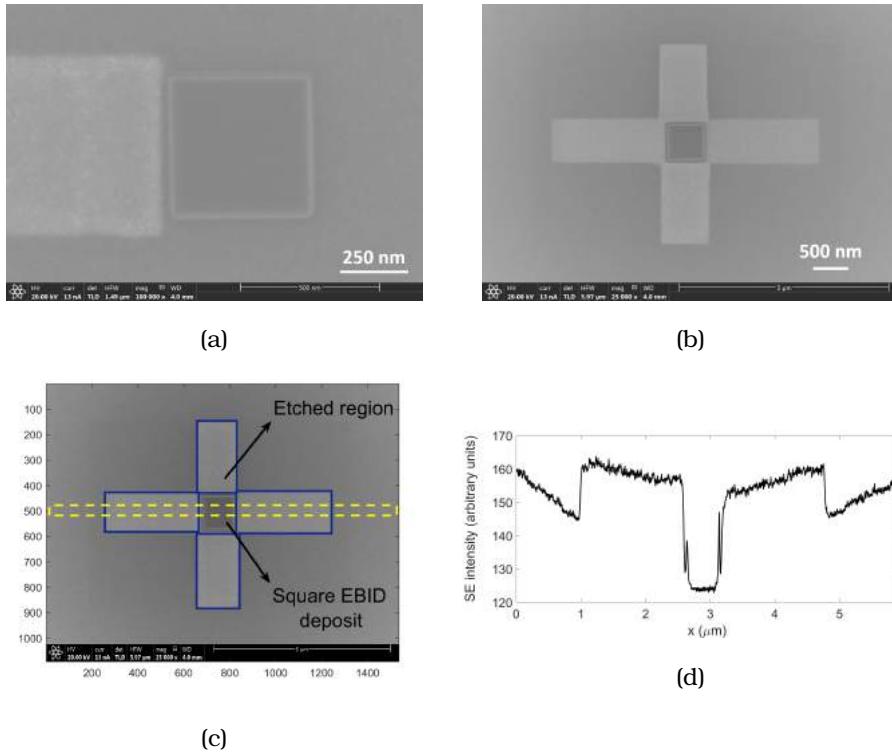


Figure 5.4: (a) High magnification image of the square after the rectangular area to the left of the deposit has been etched by EBIE with water. The brightening of the etched region indicates the removal of carbon resulting in the substrate, which has a higher SE yield, being exposed. Closer inspection reveals the grains of the gold-palladium layer, confirming the process. (b) SE image of the square after etching identically on all four sides. The etched regions are outlined in blue in (c) and the integrated intensity profile (d) of the area shown in yellow confirms the removal of carbon.

was carried out over a total length of about $1.5 \mu\text{m}$, the halo ought to have been completely removed. From Fig. 5.4(b) it is evident that there remains carbon deposit beyond this extent as the SE intensity farther away does not become as high as that of the cleaned area. The only explanation for this is that there is contamination present everywhere on the sample as a result of the manufacturing process. This includes applying a resist on the sample for the patterning of markers by optical lithography. This was performed in the cleanroom prior to use in the SEM in order to be able to easily locate the patterns for imaging on a later date. Sample contamination due to incomplete washing off of resist is known to occur and this contamination

was also verified as being present on other samples not exposed to EBID or EBIE at all.

5.3 Removal of interconnects

Dense lines of carbon were patterned by EBID at 20 keV, 3.2 nA, dwell time = 1 μ s, patterning pitch = 1 nm, number of passes = 1000. Two recipes are described to remove interconnects by EBIE:

Recipe 1: Large area EBIE

Cleaning was carried out by exposing a large area containing an array of EBID lines to EBIE at 20 keV, 3.2 nA and 10 μ s dwell time as shown in the schematic in (Fig. 5.5). The dose was determined by observing the SE signal from the etched region and the exposure was stopped when the region in between the lines appeared uniformly bright. The dose needed was found to be in the range mC/m^2 . Due to the higher SE yield from a

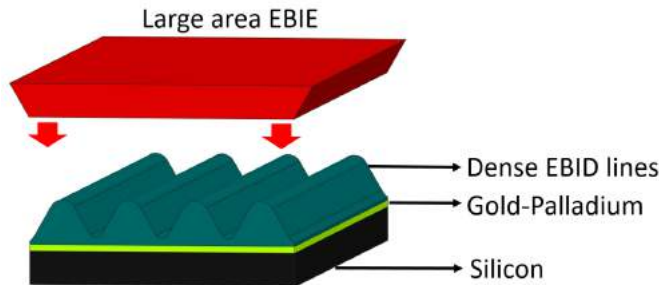


Figure 5.5: Schematic for large area EBIE exposure of dense EBID lines for the removal of interconnects

slope, there is a risk that exposing the line itself to EBIE would result in it being eaten in from both sides. Such an effect was in fact exploited in [76] to slim carbon-containing nanowires. We investigated this by performing large area EBIE for a series of doses. The black dashed rectangle in Fig. 5.6 indicates a typical etched region (approximately 500 nm x 250 nm) containing two EBID lines. The total etching time used was in the range 2 s to 120 s, corresponding to electron doses of 50 $\mu\text{C}/\text{m}^2$ to 3 mC/m^2 . The parameters were the same as in the previous experiment. Cleaning around the lines is observed in all cases, but with increase in dose, the

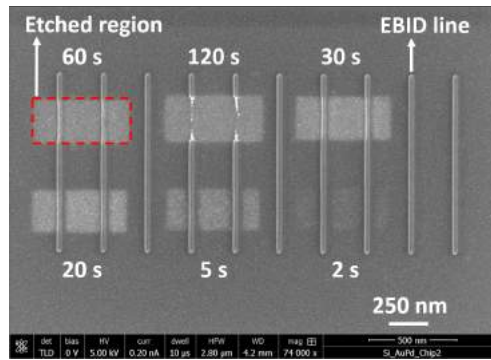


Figure 5.6: SE image of an array of carbon EBID lines after large area EBIE. The red dashed rectangle indicates a typical etched region containing two EBID lines. A range of doses of $50 \mu\text{C}/\text{m}^2$ to $3 \text{ mC}/\text{m}^2$ was used, corresponding to etching times of 2 s to 120 s. Cleaning around the lines takes place in all cases, but damage to the line is observed at the higher doses, eventually causing it to become discontinuous (etching time = 120 s). This effect is known to take place due to an increase in the number of SE's escaping from a sloping sidewall, resulting in etching of the bulk of the line itself from both sides [76].

damage to the line can be seen to increase, finally causing it to become discontinuous at exposure time = 120 s. A pattern comprising three arrays of lines spaced 150 nm, 300 nm and 450 nm apart is shown in Fig. 5.7 (a). It was designed so that lines with 3 different values of spacing could be

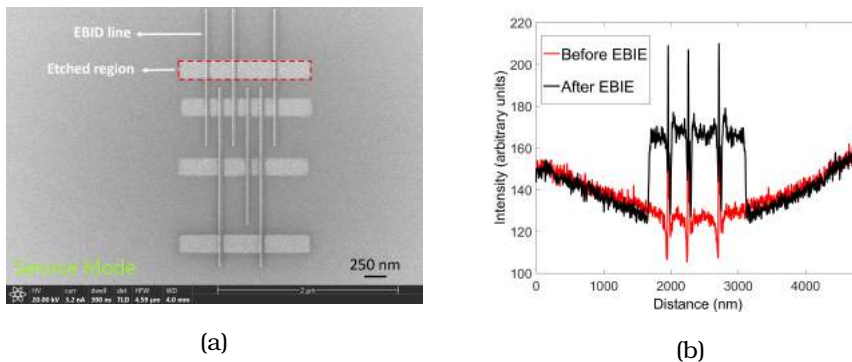


Figure 5.7: (a) SE image of array of carbon EBID lines after large area cleaning. The red dashed rectangle indicates a typical etched region. Four regions containing lines of spacing 150 nm, 300 nm and 450 nm were etched for a time of 7 s each. (b) Integrated intensity plot of topmost region before EBIE (red) and after EBIE (black). The increase in SE signal observed in between the lines demonstrates the removal of carbon and the extent of this region corresponds with the exposed area.

cleaned in one experiment. Also, AFM measurements can be carried out on the lines that are sufficiently far apart, which may not be possible in the denser arrays. The black dashed rectangle in Fig. 5.7 (a) indicates a typical etched region containing the EBID lines. The total exposure time was 7 s. This was determined, as in the previous experiment, from the change in SE signal of the exposed region. Etching was performed in four different regions of the EBID pattern (seen as bright regions in (a)) in serial mode from bottom to top, with one area being cleaned completely before moving on to the next. The removal of interconnecting material is evident from the brightening and the integrated intensity plot in (b) allows a clear comparison of the array before and after EBIE. The final confirmation must however come from AFM measurements (Fig. 5.8). The AFM scan area was

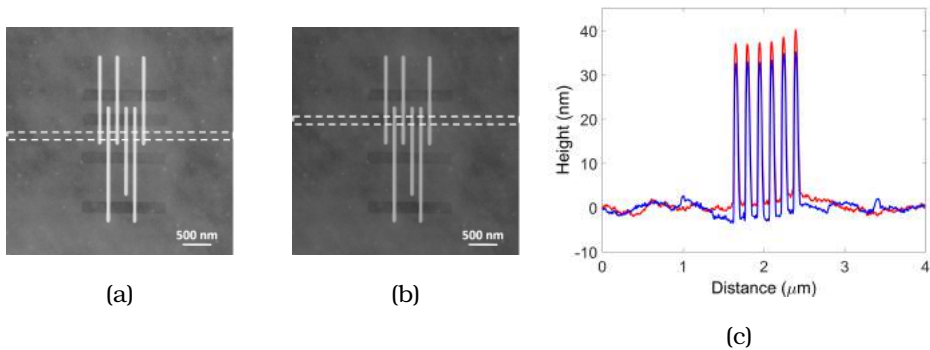


Figure 5.8: AFM image of array after etching. The dotted lines indicate the region containing dense lines spaced 150 nm apart that were (a) not etched and (b) etched. (c) Integrated height profile of regions marked in (a) and (b), which on comparison confirm the presence of well separated lines with little or no interconnecting material. The removal of the surrounding halo can also be seen as a result of EBIE.

chosen such that the signal from the substrate sufficiently far away from the pattern, before and after cleaning, could be verified as being the same. This ensures that a valid comparison between the two can be made. The integrated line scan of the most dense array (containing lines spaced 150 nm apart) is shown in Fig. 5.8 (c), taken over the area marked in (b) with dotted lines. Fig. 5.8 (c) shows the area used as reference (not etched). The red and blue plots represent the profile of the as-deposited array and the array post-cleaning, from which it is evident that the carbon has been successfully removed from the exposed areas. In one step, therefore, the lines have been separated and the halo around the deposit has been

removed. An AFM scan at the outer edge of the cleaned region (dotted lines in Fig. 5.9) shows the thickness of the carbon film removed there to be as little as 1 nm. So it is interesting to note that the BSE image of the array (Fig. 5.10) also shows a change in contrast. Since no change in the crystal structure of the substrate is expected to occur here and other changes such as chemical modification of the surface would not affect the BSE contrast anyway, we conclude that BSE imaging using the ICD is highly sensitive to changes in height. This is useful when cleaning dense arrays where the spacing between lines is too small to allow reliable AFM measurements. The increase in BSE signal can be used as confirmation of successful carbon removal.

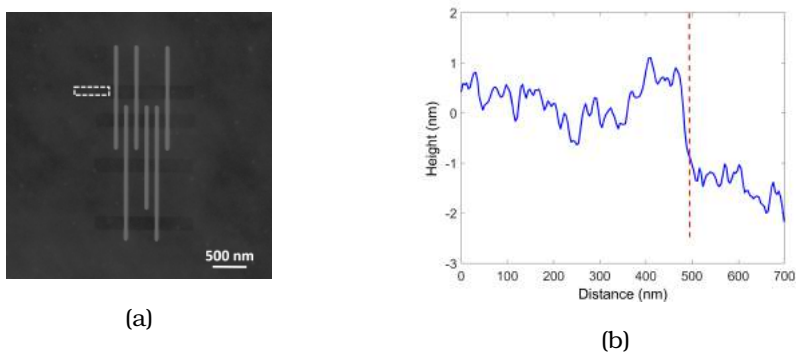


Figure 5.9: (a) AFM image with the dotted lines indicating an area at the edge of the etched region, where the thickness of the carbon film removed is measured from (b) to be about 1 nm

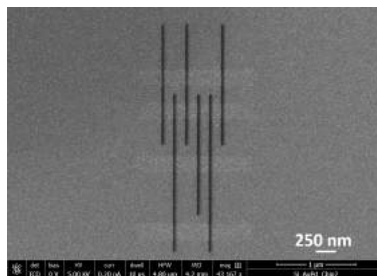


Figure 5.10: BSE image of array, also displaying a change in signal from the etched region. The thickness of the carbon film removed is reflected in the BSE contrast even for as little as 1 nm, meaning that BSE imaging would be a good method to monitor height changes. This is especially useful for lines at smaller spacing where AFM would not be an accurate measure of material removed in between the lines.

Recipe 2: High resolution etching in between EBID lines

In an array of thicker EBID lines, the connecting material might be thicker as well. Even for shallow lines, as the separation between the lines is reduced, the connecting material becomes relatively more significant. If such a high dose is required to clean the interconnects that the lines themselves would be damaged in the process, a large area etch is no longer an attractive technique. We describe an experiment to remove material from the interconnects by positioning the patterns in between the lines as shown schematically in Fig. 5.11. The dimensions of the etch pattern

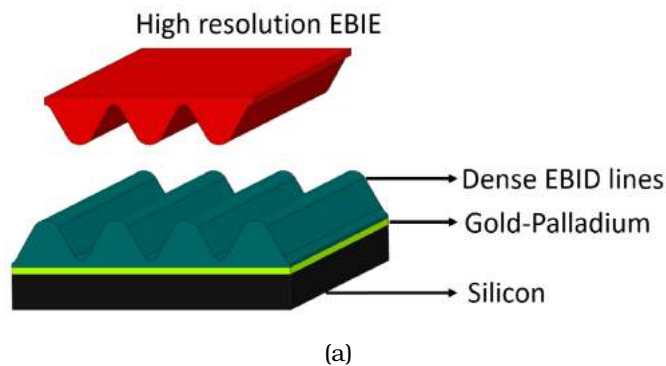


Figure 5.11: Schematic for high resolution EBIE in between dense EBID lines for the removal of interconnects

were determined by eye based on the TLD image, exposing the entire gap between the lines (as indicated by the dashed red rectangles in Fig. 5.12(a)). The EBIE parameters were the same as in the previous experiment and the dose was determined in the same manner. It was typically in the range of a few mC/m^2 . Fig. 5.12 shows the pattern that was cleaned, consisting of three sets of arrays with line spacing of 150 nm, 300 nm and 600 nm. EBIE was carried out in serial mode from left to right. The array with the largest spacing (lowest region in the image) was etched first and that with the lowest spacing (middle region in the image) was etched last. The SE (a) and BSE (b) images show brightening in the exposed regions and the integrated AFM line scan of one of the arrays in the pattern (spacing = 300 nm) shown in (c) provides a comparison of the line profile in the etched region with the as-deposited profile taken on the same array. The red and blue plots represent the as-deposited array and the array post-cleaning, as before, with a clear reduction in background deposit visible between the lines.

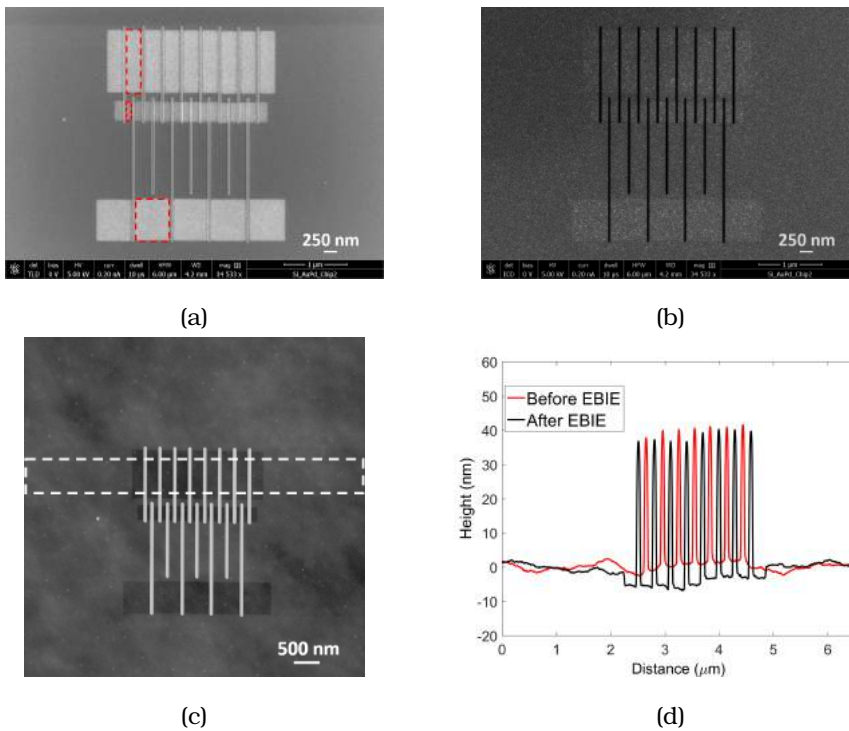


Figure 5.12: (a) SE (b) BSE and (c) AFM images of an array of carbon EBID lines containing line spacings of 150 nm, 300 nm and 600 nm after high resolution EBIE in between the lines. The dimensions of the area to be etched were determined by inspection of the TLD image and selected to just fill the gap between the lines as shown by the dashed black rectangles. (d) Integrated height plot of array of lines spaced 300 nm apart before and after cleaning, demonstrating successful removal of interconnects.

5.4 Discussion

An interesting observation was made during the etching of the EBID halo regarding the increase in SE signal from the clean region. It was initially expected that since etching away the halo would result in exposing the substrate, the SE signal of the "clean" region would be the same as that of the substrate far away from the deposition. This was found to not be the case. Exposing pristine samples (no deposition performed) directly to EBIE with water resulted in similar brightening. Further, this was observed on two different substrates - silicon with a native oxide layer and silicon covered with a layer of gold-palladium. This comes about most likely due to the removal of adsorbed hydrocarbons or contamination

from the wafer manufacturing process, which would be carbonaceous and present everywhere on the sample. This is supported by the observation that even when no water is let in through the GIS, merely scanning the sample in poor vacuum ($\approx 10^{-5}$ mbar) which has a high partial pressure of water, leads to brightening. Surprisingly, though, this effect remains for a long period. Samples inspected after hours and even days were found to retain the bright regions intact. An understanding of the mechanism of the cleaning would be beneficial in its application as a sample cleaning technique for SEM use, and help in improving process control.

5.5 Conclusions

Electron Beam Induced Etching in a high vacuum SEM using water as a precursor has been applied to successfully remove interconnects in dense EBID lines of carbon. The influence of etching dose and strategy have been analysed to enable selection of the most suitable method. The effect of this exposure on the shape of dense EBID lines has been studied using SE, BSE and AFM measurements and this can be used to tailor the cleaning technique. This result has broad applications in EBID as several commonly used precursors contain carbon which remains in the deposit, giving rise to unwanted conducting channels between deposits. For lithography, it is of utmost importance to have well separated lines and this has been shown to be possible using two recipes. Large area EBIE of an entire field of view containing the lines is a fast and easy process that results in the successful removal of the interconnecting carbon film. The increase in SE signal upon removal of carbon, exposing the underlying gold-palladium substrate has been used to determine the electron dose needed for EBIE. The height of the lines is somewhat affected by the exposure and for applications where this is undesirable, another technique has been proposed. By carefully positioning an etch pattern in between the lines using the SE image, it is possible to effect the same process, this time with no change to the height of the line. By further reducing the width of the etched area, it is possible to perform the same without affecting the bulk of the line. This allows the line width to remain intact - another advantage of this method. An identical pattern to the one described in Fig. 5.12 was etched in this manner and Fig. 5.13 shows that the technique is sufficiently well controlled to tune the extent of the etching. This would of course become increasingly difficult to perform at higher and higher resolution. This can

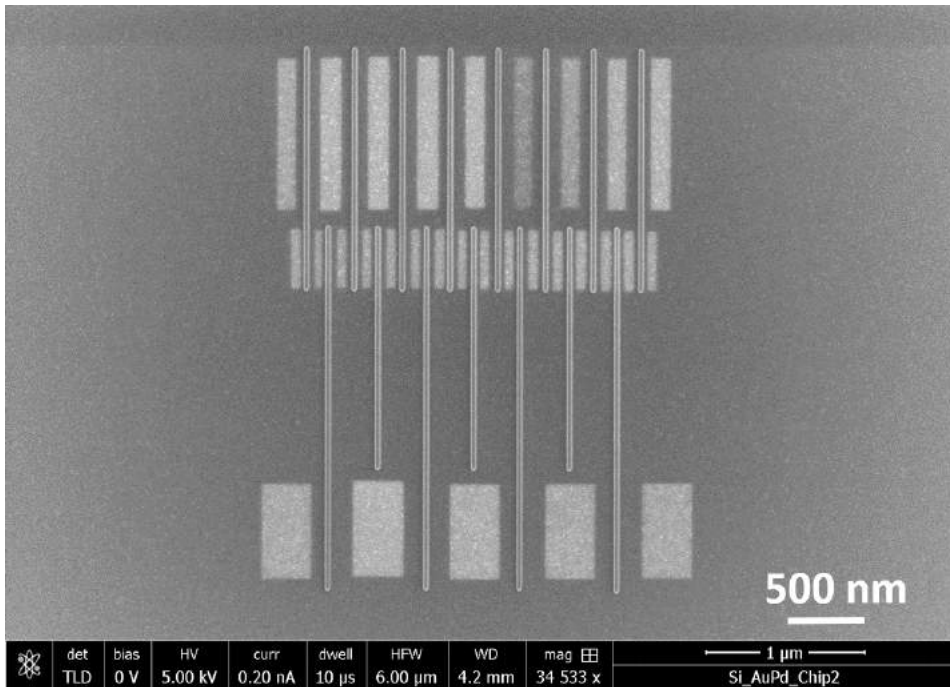


Figure 5.13: SE image of array identical to that in Fig. 5.12 after etching in between the lines with higher resolution, making sure to leave the bulk of the EBID line unaffected.

be addressed by improving the resolution of the EBIE process. As it is an electron beam induced process, it has in principle similar resolution as EBID. The problem arises because of the use of high current, which as discussed before is necessary to suppress co-deposition of contamination. By working in a very clean system, ideally one where no precursor other than water is let in, and by following strict guidelines for samples that are allowed to be mounted in the SEM, it would be possible to perform EBIE with a low current. A high resolution beam could then be used to perform the etching in a very local manner with even more control. The time taken for the process would increase if the current were lowered, but since the doses used are quite low to begin with, this would remain an attractive cleaning technique. The use of the carbon precursor dodecane also presents some challenges since it appears to remain in the chamber for quite some time after the GIS valve has been closed. Although the pressure in the chamber was found in initial experiments by Siebers to drop to the base value (1×10^{-6} mbar) within minutes, this was found to

not be the case after continuous use over some hours. While the sticking capability of dodecane is responsible for its high EBID yield, this is not the limiting factor in high resolution experiments. Since the lines patterned are narrow and shallow, it would be beneficial to use a precursor that pumps out quicker instead. The introduction of water in the chamber was found to worsen the situation and the sequence of experiments was modified to prevent this situation. Alternatively, another precursor such as oxygen could be used for EBIE, avoiding this problem. Some modifications to the GIS would have to be implemented to ensure sufficient local flux of oxygen while maintaining high vacuum in the SEM chamber. Regular cleaning of the SEM using an oxygen plasma would also help in the maintenance of a clean environment for both EBID and EBIE. It should be pointed out here that the etching of other materials than carbon would require a precursor that volatilizes that particular deposit material. This work demonstrating the etching of carbon not only provides proof of concept of the technique, but it is also directly applicable to the removal of the carbonaceous halo surrounding EBID deposits made with a variety of precursors. Although the metal particles in the halo would remain (see Fig. 2.13), etching of the carbon would ensure the removal of conducting paths between them.

Chapter 6

3D shape control - sidewall angle tuning in FEBIP

“ *I come from haunts of coot and hern,
I make a sudden sally
And sparkle out among the fern,
To bicker down a valley*

”

Tennyson,

 BID lines typically have a Gaussian profile when seen in cross section, as a result of patterning in the electron current regime. Fig. 6.1 shows the SE image of an EBID line patterned using a 5 keV beam and 100 pA current, along with the FIB cross section of the line profile. The patterning parameters were: defocus = 100 nm, dwell time = 500 μ s, pixel overlap = 90 %, number of passes = 500. The resultant line in (a), however, appears much wider with long tails extending up to more than 200 nm from the centre on either side. The FIB cross section was made by first covering the deposit with a thick layer of Pt/C by EBID from the standard platinum precursor, followed by milling along the cross sectional profile. The image in (b) was acquired with a stage tilt of 52 degrees and shows a Gaussian cross sectional profile that is typical of EBID structures patterned in the electron current limited regime. EBID literature contains several reports ([56], [83], [30]) of the effect of long range BSE's on the broadening of lines as seen here. This effect is inherent to the dissociation processes involved in EBID. A high energy electron beam interacting with a substrate necessarily gives rise to a host of scattering events, resulting in electrons with a range of energies and corresponding cross sections. So while the broadening due to deposition by SE's and BSE's can be minimised by varying the process parameters such as beam energy and dose ([56]), it cannot be done away with.

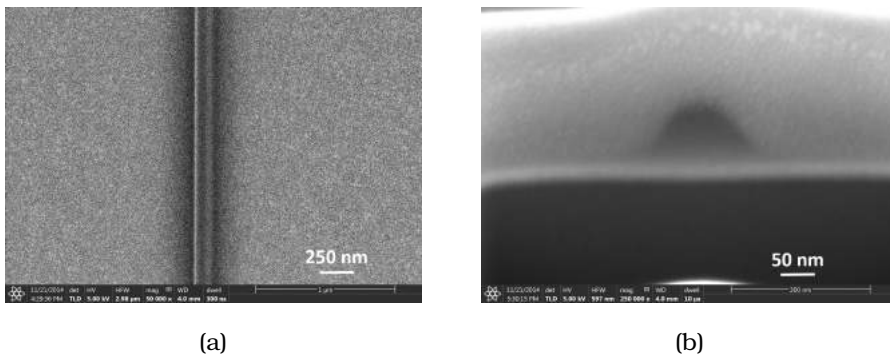


Figure 6.1: Typical profile of an as-deposited EBID line seen in top view SE image and FIB cross section. The line was deposited by EBID from a carbon precursor (dodecane) on a silicon substrate coated with a 20 nm gold-palladium layer. The patterning was carried out in 500 passes with a dwell time of 500 μs using a 5 keV beam and 100 pA current with a defocus of 100 nm.

Unlike resist-based lines which have vertical sidewalls (Fig. 6.2), making the definition of line width quite straightforward, the width of EBID lines is defined differently by different users (Fig. 6.2). Although it is possible to have a consistent measure of line width (Chapter 3 and 4), an absolute measure is still elusive due to this characteristic profile.

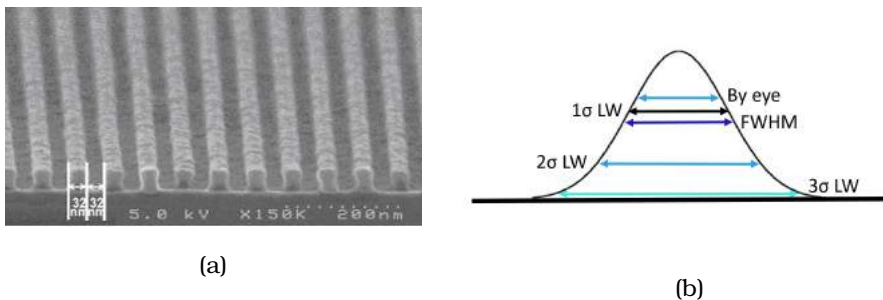


Figure 6.2: (a) Typical profile of resist-based lines (b) Cartoon demonstrating the ambiguity in the definition of line width in EBID

Further, sloping sidewalls together with long tails pose a problem in the use of EBID for lithography, limiting how closely lines can be spaced. The goal of this work is therefore to fabricate EBID lines with vertical sidewalls, and consequently, well-defined width, followed by the demonstration of their application in high resolution lithography by the patterning of dense lines.

Directly patterning lines having the desired profile by EBID would require complex patterning strategies. So we chose instead to modify the profile of as-deposited EBID lines using a suitable technique. Based on the considerations mentioned in 5.3, EBIE appears attractive for use in combination with EBID to achieve high resolution patterns with well controlled 3D shape.

6.1 Sidewall slope modification by EBIE - proof of principle simulation

This section describes a simple analytical model to conceptually demonstrate modification of the slope of EBID sidewalls using EBIE. The electron induced processes involved in FEBIP are summarised well in Fig. 6.3 taken from [29]. The interaction of a high energy primary beam with the EBID nanodeposit results in a host of scattering events. Backscattered

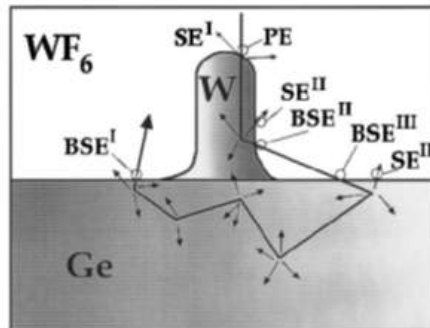


Figure 6.3: Possible electron scattering events resulting from the interaction of a high energy primary electron beam with an EBID nanodeposit [29]. Backscattered electrons can emerge from the substrate (BSE1's) and from the deposit (BSE2's). Backscattered electrons generated in the deposit may also enter the substrate, causing another backscattering event, leading to the creation of BSE3's. SE's are generated from a depth of a few nanometres, emerging from the deposit and from the substrate (SE1's) or from the interaction of a backscattered electron with either of the two (SE2's).

electrons can emerge from the substrate (BSE1's) and from the deposit (BSE2's). Backscattered electrons generated in the deposit may also enter the substrate, causing another scattering event, leading to the creation of BSE3's. Low energy SE's are generated from a depth of a few nanometres, emerging from the deposit and from the substrate (SE1's) or from the

interaction of a backscattered electron with either of the two (SE2's). In the presence of an adsorbed film of water molecules, all of these electrons could contribute to the dissociation process, resulting in the deposit being etched at that location. Since molecular bond energies are typically a few eV, low energy SE's are expected to play a major role in the dissociation. Experimental studies and simulations have also illustrated the importance of SE's in FEBIP ([84], [47]). Therefore, this proof-of-concept simulation is based on the simple scenario of EBIE induced by SE's. Since BSE's are generated over a large radius, their density and consequently the density of SE2's is much lower than that of SE1's. In this model, only SE1's are assumed to be responsible for EBIE.

A large EBID deposit was simulated on a substrate to have a flat top and symmetric sidewalls defined by half-Gaussian functions as shown in Fig. 6.4. The etch profile was defined similarly by a Gaussian function:

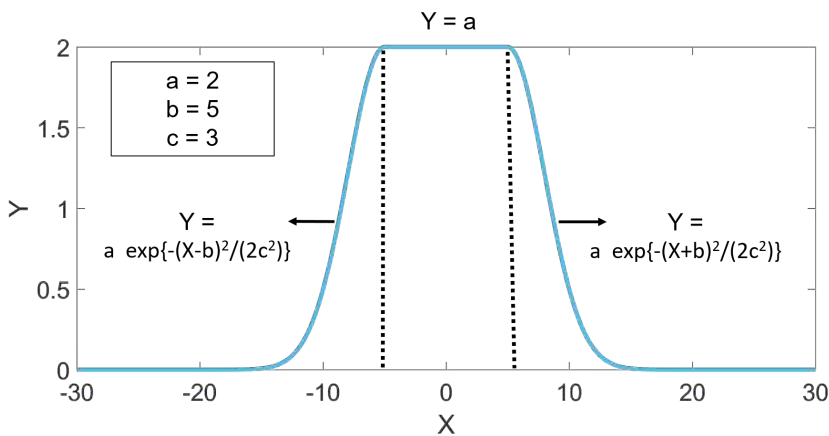


Figure 6.4: Simulated EBID deposit with a flat top ($Y = a$). The sidewalls are defined by half-Gaussian functions: $Y = a e^{-\frac{(X+b)^2}{2c^2}}$ for the left sidewall and $Y = a e^{-\frac{(X-b)^2}{2c^2}}$ for the right sidewall. The values used here are $a = 2$, $b = 5$, $c = 3$.

$$Y_2 = a_2 e^{-\frac{(X-b_2)^2}{2c_2^2}} \quad (6.1)$$

The results of etching the deposit are shown in Fig. 6.5 where the red curve in (a) and (b) represents the etch profile on a plane surface. When the beam is positioned on the flat top of the deposit for etching (a), the

material removed results in a Gaussian profile as shown by the green curve. The situation is different when etching takes place on a sloping surface. The SE yield from the slope is enhanced by a factor proportional to $1/\cos\alpha$ where α is the angle between the beam and the normal to the surface at the point of incidence ([46]). The proportionality constant "k" now determines the strength of etching. The dimensions of the deposit and the strength of etching are variables in the model and for the purpose of this simulation, all parameters are in arbitrary units.

Upon positioning the beam symmetrically, but at an arbitrary distance from the centre, on each of the sloping sidewalls, the deposit is etched by SE's. The etching was performed in 7 steps with a fixed beam position and etching strength and the resultant profile (Y_3) of the EBID deposit evolves as:

$$Y_3(i) = Y_3(i-1) - k Y_2 \frac{1}{[\cos \alpha]_{at Y_3(i-1)}} \quad (6.2)$$

where "i" represents the etching step. The slope of the sidewall (Y_3) evaluated for the step "(i-1)" is used to determine the enhancement in SE yield as shown by the second term in equation 6.2. Convolved with the etch profile Y_2 together with the proportionality constant "k", this represents the material removed from the current profile Y_3 (i-1) to give the resultant deposit profile (Y_3 (i)). The sidewall slope is negative (ie, sloping outwards) at the beginning as shown by Fig. 6.4. After the first etching step, this slope becomes less negative indicated by the profile marked "Step 1" in Fig. 6.5(b). The process continues with the slope becoming increasingly less negative with every etching step until a well defined deposit with nearly vertical sidewalls is achieved in "Step 7".

It should be pointed out here that the etching strength in (a) was chosen to be low to give an indication of the initial stages of etching. For a higher value such as that in (b), the etching would result in removal of material all the way to the substrate. This would be unrealistic because after the initial stages of etching, the deposit surface is no longer plane and the enhanced SE emission from a sloping surface must be taken into account similarly to what was described in (b). This simple model shows that EBIE can be

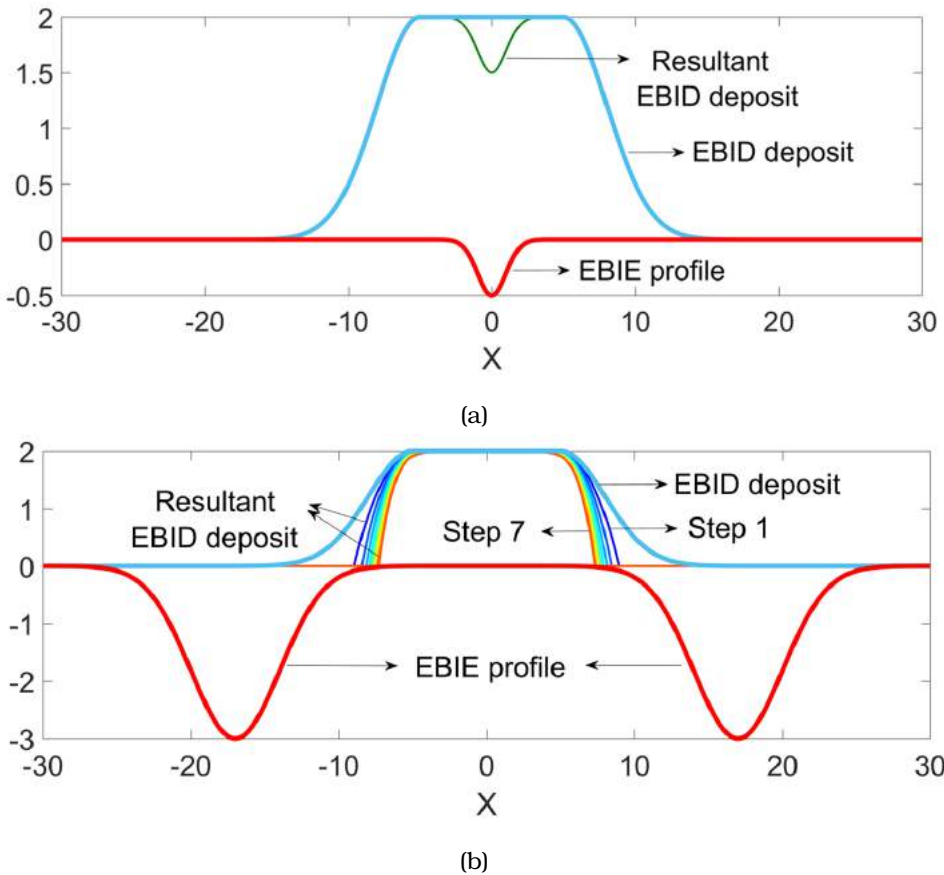


Figure 6.5: (a) Simulation demonstrating etching of a plane EBID surface by EBIE using a stationary beam (b) Modification of an EBID structure by EBIE, resulting in well-defined vertical sidewalls. The beam was positioned at an arbitrary point on the slope and 7 etching steps were performed at the same location with a fixed strength. The sidewall slope is negative (ie, sloping outwards) at the beginning as shown by the outermost plot, and becomes less so with every etching step (from blue to orange). The resultant profiles following the first and last etching steps are indicated as "Step 1" and "Step 7". In the final step, a well defined deposit with nearly vertical sidewalls can be seen.

applied to as-deposited EBID structures to achieve vertical sidewalls.

6.2 Electron beam induced etching of carbon with water

Experimentally, EBIE has been performed by several groups and the relation between the etch profile and etching parameters has been studied using continuum models ([37], [50]) based on the EBID model first proposed by [13]. As more experimental results have emerged, the model has been improved. As in EBID, the most straightforward scenario in EBIE is the electron current limited regime. Assuming constant precursor pressure, the etch depth is expected to increase with exposure time for a fixed energy and current. But in [74] Toth et al. observed a decrease in etch rate of SiO_2 by XeF_2 with exposure time. A transition from the electron current limited regime to the precursor limited regime is described as taking place after a time of the order of milliseconds, following which the etch rate is limited by diffusion of the precursor into the pit, leading to the observed slowing down of etching. Lassiter [85] studied EBIE using the same precursor and studied the etch pit profile as a function of exposure time and beam current under spot exposure. For high beam currents they observed almost no etching at the centre and a maximum at a specific radius, and as the current decreased the maximum was found to shift towards the centre. They explained this by incorporating diffusion, residence time and subsequent redissociation of etch products into the continuum model. Therefore the exact mechanism of etching can be crucial in determining the rate and resultant profile. This is observed in [72] where electron beam induced desorption of oxygen from SiO_2 is proposed as the first step in EBIE, followed by the fluorination of silicon which in turn is the rate limiting step. Even as this work demonstrates the potential of EBIE for nanofabrication, it stresses the need for an understanding of the fundamentals of the process. EBIE of carbon using H_2O has been carried out by [86] and claims that the most likely mechanism involves the ionisation of water molecules by the electron beam and subsequent volatilisation of carbon. Based on energy considerations, they rule out the direct activation of the carbon surface which could then react with water to produce volatile oxides. Studies of water on carbon ([87], [88], [89], [90]) show that the residence time, rate of diffusion, rate of monolayer formation and spontaneous dissociation, of water on carbon surfaces are significant parameters in EBIE, which in turn depend strongly on the chemical and

structural properties of the type of carbon present. For example, the nature of the deposit determines the relative strength of water-water interactions with respect to water-surface interactions. If the former are stronger, clusters are formed, whereas if the latter are stronger, water molecules can be dissociated on the surface ([87]), leading to fragments like OH, H and O which have very different reactivity to the electron beam than H₂O. Another example is provided by Toth et al. in [71] where the density of active sites was shown to limit the etch rate and determine the profiles achieved in EBIE. In experiments, many of these parameters are often unknown, making it difficult to formulate an exact model.

With respect to the shape of the etch profile, most studies have been limited to etching of plane surfaces. Although etching on a slope has been experimentally demonstrated in [76] with the slimming of nanowires, we could not find any models in literature describing the shape evolution. The situation is complicated by enhanced SE emission from the sidewalls, influencing the etch rate, resulting in a different profile than on a plane surface. In the case of etching the sidewalls of an EBID deposit, we also need to take into account the tails extending to hundreds of nanometres that may be only a few nanometres thick. This material can be removed, exposing the substrate having a different SE yield from the deposit, changing the etch rate.

6.3 Experimental details

This section describes an experiment to etch the sidewalls of an as-deposited EBID structure to obtain vertical sidewalls. The first step was to understand the process by studying experimentally the evolution of the 3D profile and comparing it to the model described in 6.1. Details of the precursor as well as the substrate are given in Chapter 5.

First, the process of electron beam induced etching of the carbon EBID deposits using water vapour was studied to determine the suitable parameters for the experiment. Since the EBIE experiments performed by Toth et al. ([76]) were in an ESEM, the flux of gas molecules is expected to be different from that in a high vacuum SEM with directed gas flow, from which it follows that the rates of various processes would be different as well. An EBID deposit 1 μm wide and 4 μm long was patterned as shown

schematically in Fig. 6.6(a) and the thickness was measured by making a FIB cross section. In order to do this, it was coated with a protective layer of Pt/C (by EBID from the commonly used platinum precursor MeCpPtMe₃) as shown schematically in Fig. 6.6(b) and the cross sectional profile is shown in Fig. 6.6(c). A series of squares 50 nm x 50 nm in size was etched

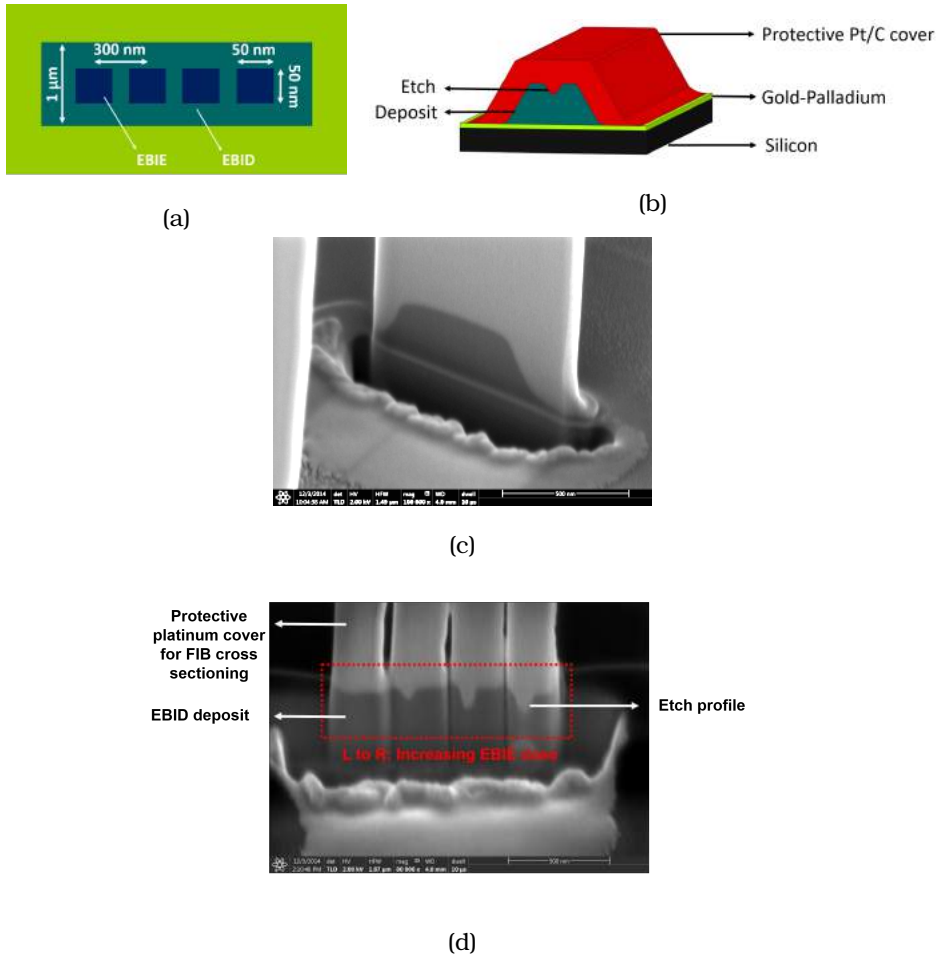


Figure 6.6: (a) Schematic of experiment to test EBIE of carbon in the high vacuum SEM with precursor injection (b) Schematic showing an as-deposited EBID structure covered with a protective Pt/C deposit in order to make a FIB cross section. (c) FIB cross section of as-deposited EBID structure with a plane top etched with a range of doses. (d) FIB cross sections of the deposit after etching with 5 keV, 400 pA, dwell time = 10 μ s, pitch = 5 nm, number of passes = 20000, 50000, 100000, 300000. The red dashed rectangle indicates the region of interest where an increase in etch depth can be seen with increase in EBIE dose (L to R).

in the centre of the deposit with increasing electron dose (from left to right).

The parameters used for EBIE were: 5 keV, 400 pA, dwell time = 10 μ s, pitch = 5 nm and number of passes = 20000, 50000, 100000, 300000. The etched depth was measured from the cross sectional profile made using an FIB (as shown in Fig. 6.6(d)). The deposits were covered with a protective Pt/C cover at least 1.5 μ m thick by EBID from MeCpPtMe₃. It should be noted that as this step was performed after the etching, it caused the etched holes to be filled with the deposit material. The sample was tilted by 52°, milled with a gallium FIB and the cross sectional profile imaged at low energy (2 keV) with the SE detector. For the etching, the electron beam and gas flux parameters were selected from a range of values as they were found to influence the process significantly.

6.3.1 Influence of electron current

During EBIE, simultaneous deposition of carbon can take place by EBID from contamination present in the chamber (Chapter 5). By altering the electron flux, switching between the two processes has been demonstrated ([91]). Exposing a shallow carbon deposit such as a contaminated gold-

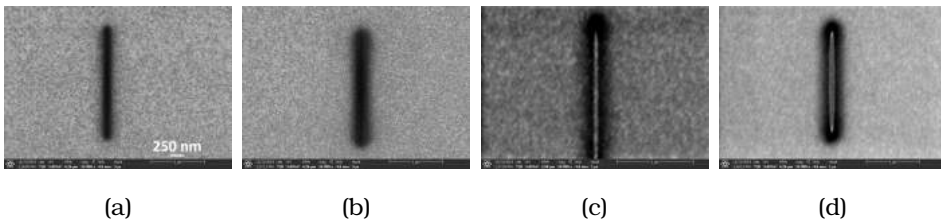


Figure 6.7: The influence of electron current on the etching of a contaminated gold-palladium surface. (a),(b) EBIE of a line pattern at low current (5 keV, 100 pA, Npass = 300, 1000, dwell time = 500 μ s) can be seen to be unsuccessful in cleaning/ etching the surface contamination. Instead, darkening of the exposed line is observed which broadens on increasing the dose in (b). (c),(d) EBIE at high current (5 keV, 1.6 nA, Npass = 1000, 5000) can be seen to cause brightening of the exposed line, indicating etching. The darkening on the outside of the line can be understood in terms of deposition from chamber hydrocarbons caused by the tails of the electron beam.

palladium surface to a line scan with low current (100 pA) in the presence of water vapour resulted in no etching (cleaning) over the dose range (N pass = 300 to 1000). Instead, a deposit was observed in the SE image (Fig. 6.7(a)). This is due to insufficient electron-water collisions for etching. The electron dose was however enough to deposit carbon from the chamber contamination which led to the darkening seen. Continued electron expo-

sure would then result in more carbon deposition, leading to a broadening of the line as in Fig. 6.7(b) but no etching. Exposing such a deposit to high current (1.6 nA) and $N_{\text{pass}} = 1000$, while all other parameters were kept unchanged resulted in a brightening of the scanned line (Fig. 6.7(c)) as expected from this reasoning. Additionally, some carbon deposition is observed on the rim of the etched line, which can also be explained as coming about due to the tails of the electron beam profile. A higher dose ($N_{\text{pass}} = 5000$) at the same current resulted in a broadening of the etched/cleaned line (Fig. 6.7(d)) along with the deposition of carbon on the outside as before, lending experimental support to this explanation.

6.3.2 Influence of gas flux

The use of a high current (a few nA) for etching suggests that the process is not current limited. The gas flux is therefore expected to be a critical parameter. This was verified using the same current to expose lines on two identical carbon deposits when a chamber pressure of 0.9×10^{-5} mbar of water vapour resulted in unsuccessful etching (Fig. 6.8(a)) whereas at a pressure of 2.5×10^{-5} mbar the advent of etching was visible (Fig. 6.8(b)). The local gas flux incident on the sample (estimated in Chapter 2) in the two cases is 4×10^{17} molecules/cm²/s and 1.6×10^{18} molecules/cm²/s respectively. This difference was therefore sufficient to bring about a change in the balance between EBID and EBIE and gives an idea of the sensitivity of the process to the gas flux.

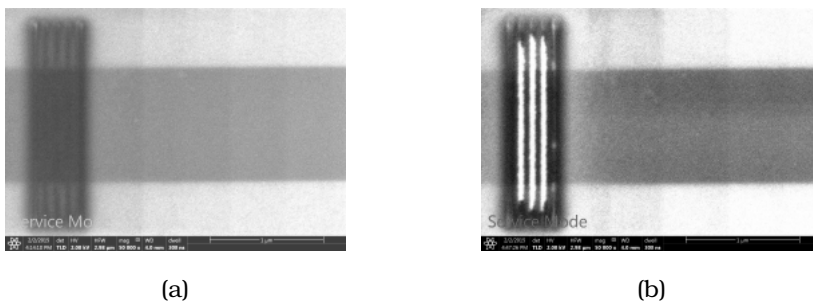


Figure 6.8: EBIE at gas pressures of 0.9×10^{-5} mbar and 2.5×10^{-5} mbar. The local gas flux incident on the sample (Chapter 2) in the two cases is 4×10^{17} molecules/cm²/s and 1.6×10^{18} molecules/cm²/s respectively.

The choice of current and gas pressure, while clearly significant, are not independent of each other and together govern the balance between etching and the deposition of contamination.

6.4 Sidewall slope evolution under EBIE

A large ($2.5\ \mu\text{m}$ by $500\ \text{nm}$) EBID structure thick enough to be imaged using FIB cross sectioning was deposited on the substrate described above. Based on the tests, the patterning parameters selected were: Beam energy = $20\ \text{keV}$, Beam current = $3.2\ \text{nA}$, Dwell time = $1\ \mu\text{s}$, Pitch = $5\ \text{nm}$, Number of passes = 3000 , to result in a deposit approximately $70\ \text{nm}$ thick. The top view SE image of this reference deposit is shown in Fig. 6.9. The

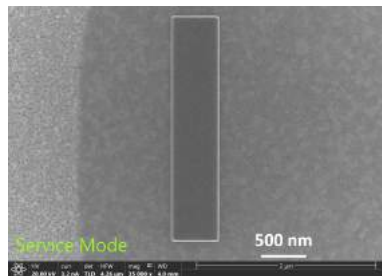


Figure 6.9: Top view SE image of deposit as reference

chamber was pumped for several hours (often overnight) to remove the carbon precursor and subsequently water was let in from the reservoir at room temperature. EBIE was carried out on one of the sidewalls of the deposit at a series of locations at increasing distances from the centre. Fig. 6.10 shows the top view and cross sectional view of the etching scheme comprising 7 etch lines of $150\ \text{nm}$ length each, with a horizontal separation of $10\ \text{nm}$ between successive lines. Such an etch series was carried out on identical deposits for a range of etching doses. The etching parameters used were: Beam energy = $20\ \text{keV}$, Beam current = $3.2\ \text{nA}$, Dwell time = $10\ \mu\text{s}$, Pitch = $5\ \text{nm}$, Number of passes = 25000 . A quick scan was taken after etching and the SE image is shown in Fig. 6.10(c).

To study the evolution of the sidewall profile with the position of the etch, a protective Pt/C EBID cover was first deposited on each etched structure as shown in Fig. 6.10(d), before making FIB cross sections at each etch location. The evolution of the 3D profile of the sidewall can be seen in Fig. 6.11. There is a clear indentation visible in Fig 6.11 (a) and (b) as predicted by the simulation for etching a plane EBID surface (Fig. 6.5). Subsequent etch locations where the beam is positioned farther away from the centre of the deposit reveal a change of the sidewall angle, but the nature of

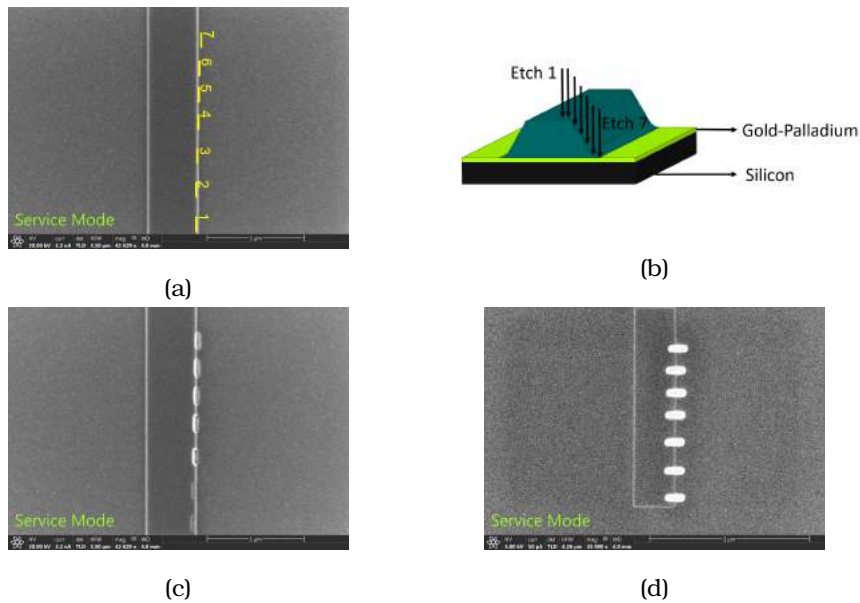


Figure 6.10: (a) Etch locations indicated by the numbers 1 to 7 on deposit sidewall for the series of etches described (b) Schematic showing cross sectional view of the same etch series (c) Top view SE image of deposit after etching (d) Etch locations covered with protective platinum cover.

the evolution cannot be precisely determined from these images due to the noise. The images were therefore processed by applying a threshold, followed by a Gaussian low pass filter to remove the noise. A contour plot was made of each image, using the absolute values of intensity to enable comparison between them. Fig. 6.12 shows the processed images corresponding to those in Fig. 6.11 and will be used for a first analysis of the experimental results.

From Fig. 6.11(c) to (f), there is a surprising trend visible in the sidewall angle. There seems to be an underetch taking place, the strength of which changes with etch position. The lower half of the sidewall in (c) appears to have a positive slope, ie, underetching, and the top half appears to either be unchanged or still have a negative slope. This is followed by a straightening of the sidewall in (d) and (e), albeit to different extents. When the position of the beam is sufficiently far away from the centre, the effect of etching on the slope decreases steadily, and finally, in (g) the sidewall angle seems to be the same as that of the as-deposited structure. Due to the original images being noisy, strong filtering was required to

generate these plots. This resulted in a change in the parameters of the filter leading to a significant change in the deposit profile in the contour plots. The edges of the deposit, for example, appear rounded to different extents, making the determination of the slope of the sidewall unreliable.

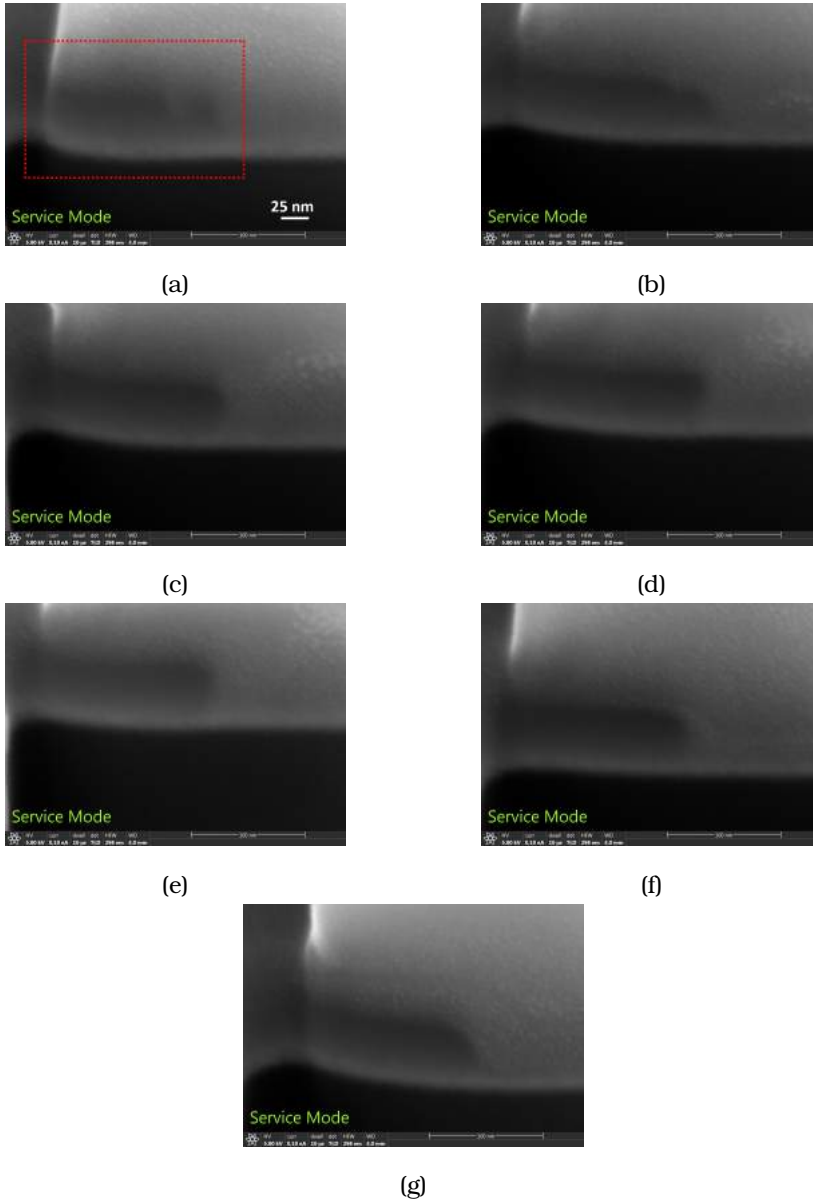


Figure 6.11: Evolution of sidewall profile as seen in FIB cross sections of the etch series. (a)-(g) Resultant EBID profiles after etch series: Etch 1 to Etch 7. The red dashed rectangle in (a) indicates the region of interest containing the deposit.

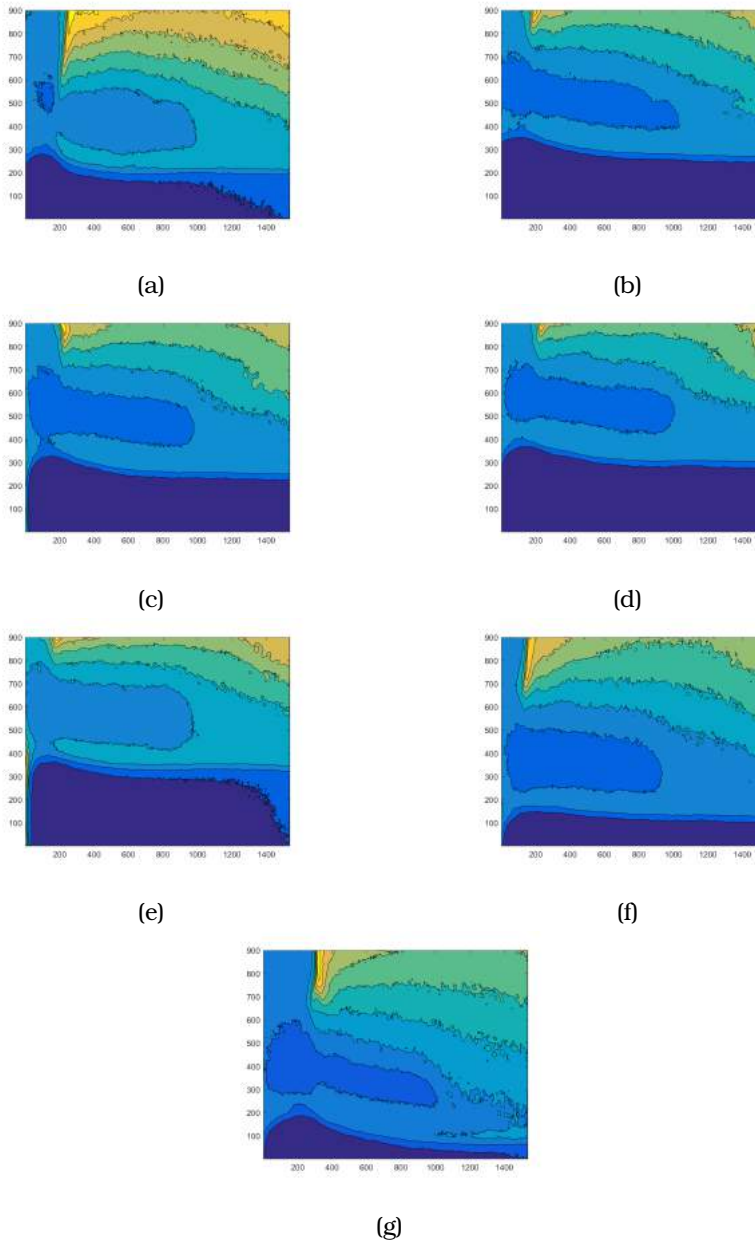
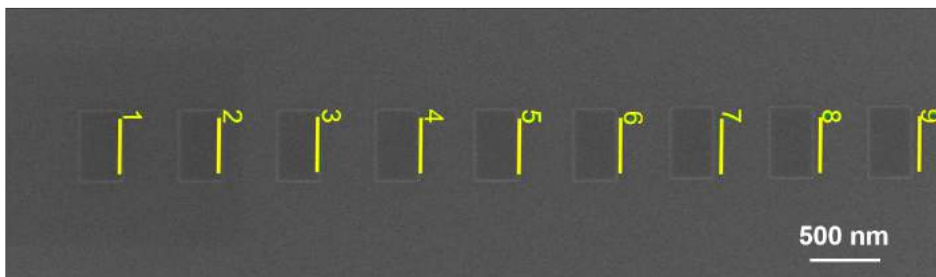


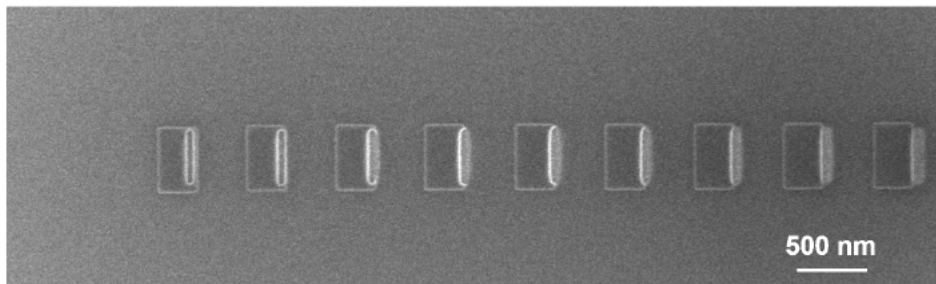
Figure 6.12: Contour plots of the images in Fig.6.11 made in an attempt to see the sidewall evolution more clearly. The colours indicate intensity levels in the corresponding images of the original image. (a)-(g) Resultant EBID profiles after etch series: Etch 1 to Etch 7. Some changes in sidewall slope can be seen, but the images are still not good enough to allow a reliable study of the trend.

These images are therefore not good enough to study the process in detail,

nor is it sufficiently clear that vertical sidewalls have been created. TEM imaging, the most popular technique for obtaining high resolution images, would provide much more information. A similar etching experiment was performed, now with 10 etch patterns instead of 7, separated by 20 nm, beginning with a position on the plane top of the deposit and moving outwards as before. But while the FIB slices of the etch patterns were made sequentially and each profile was imaged before the next was sliced, this scheme would be too laborious for imaging the entire experiment in the TEM. In order to minimise the time needed for the preparation of the



(a)



(b)

Figure 6.13: (a) Top view SE image of the array of EBID deposits along with the etching scheme: The array of etch patterns was aligned with the deposit array at increasing distance from the deposit centre from left to right. The 9 deposits shown are to be etched and their profile compared with that of the last deposit (not shown) on the far right. (b) Top view SE image of the deposit array after etching.

TEM sample, while at the same time capturing the profile of every etch pattern, the experiment was redesigned. It consists of 10 deposits (called Deposit 1 to Deposit 10), 300nm in width and 500 nm in length, identically patterned at a centre to centre separation of 700 nm. The deposition parameters were: 20 keV, 3.2 nA, pitch = 5 nm, dwell time = 1 μ s and N_p = 3000, chosen so as to yield a deposit of approximately 40 nm height which

could then be easily imaged. An etch pattern comprising 9 lines (L-R: Etch 1 to Etch 9) of 400 nm length was defined to etch the right sidewall of each deposit. This array was aligned such that each Etch was positioned 20 nm farther away from the centre of the corresponding deposit than the previous Etch was. Fig. 6.13(a) shows the scheme that was used, beginning with Etch 1 that was placed (by inspection) somewhere on the plane top of Deposit 1, to Etch 9 located farthest from the centre. Deposit 10, not shown in the figure, was not etched and functioned as the reference. The etch parameters were: 20 keV, 3.2 nA, pitch = 1 nm, dwell time = 10 μ s and $N_P = 35000$ and the lines were etched serially from left to right. The distance between the deposits was chosen to be larger than the BSE range of the electrons so that each deposit could be etched independently. Fig. 6.13(b) shows a quick scan top view SE image of the array after etching, revealing, as before, brightening indicating successful removal of material.

A lamella was made of this experiment as a whole, spanning the region from the left of Deposit 1 to the right of Deposit 10, and imaged in the bright field mode in an FEG Tecnai 20 D239 S-Twin TEM using an acceleration voltage of 200 keV and spot 3. The evolution of the right sidewall is shown in Fig. 6.14 where a clear, albeit still surprising, trend is visible which appears to be in agreement with the preliminary results shown in Fig. 6.11. The profile of the as-deposited structure (Deposit 10) is shown in Fig. 6.14(j) for reference. Clearly, etching with the same PE dose at different positions on the slope, separated by as little as 20 nm, results in very different profiles. Although the profiles of Etch 1 and Etch 2 appear Gaussian as expected from the etching of a plane surface, proceeding outwards brings about the abrupt onset of underetching. Deposit 3 shows a modified sidewall with the lower half sloping inward, forming a sideways cap, and some material protrudes from the right of the deposit indicating an incomplete etch. Moving further right, and therefore etching thinner material, Etch 4 results in a smoother profile, still capped. Here, the dose was sufficient to perform a complete etch and the connecting material previously seen adjacent to the deposit is gone. The profile becomes still smoother after Etch 5, showing a sidewall that slopes inward completely. 20 nm further to the right, however, the trend seems to reverse and Etch 6 results in the much desired vertical sidewall. This is therefore the position where the etching dose used is optimal, and upon moving further outward, the sloping sidewall is visible once again with some clipping of the long tail.

And finally, on etching sufficiently far away from the centre, the profile

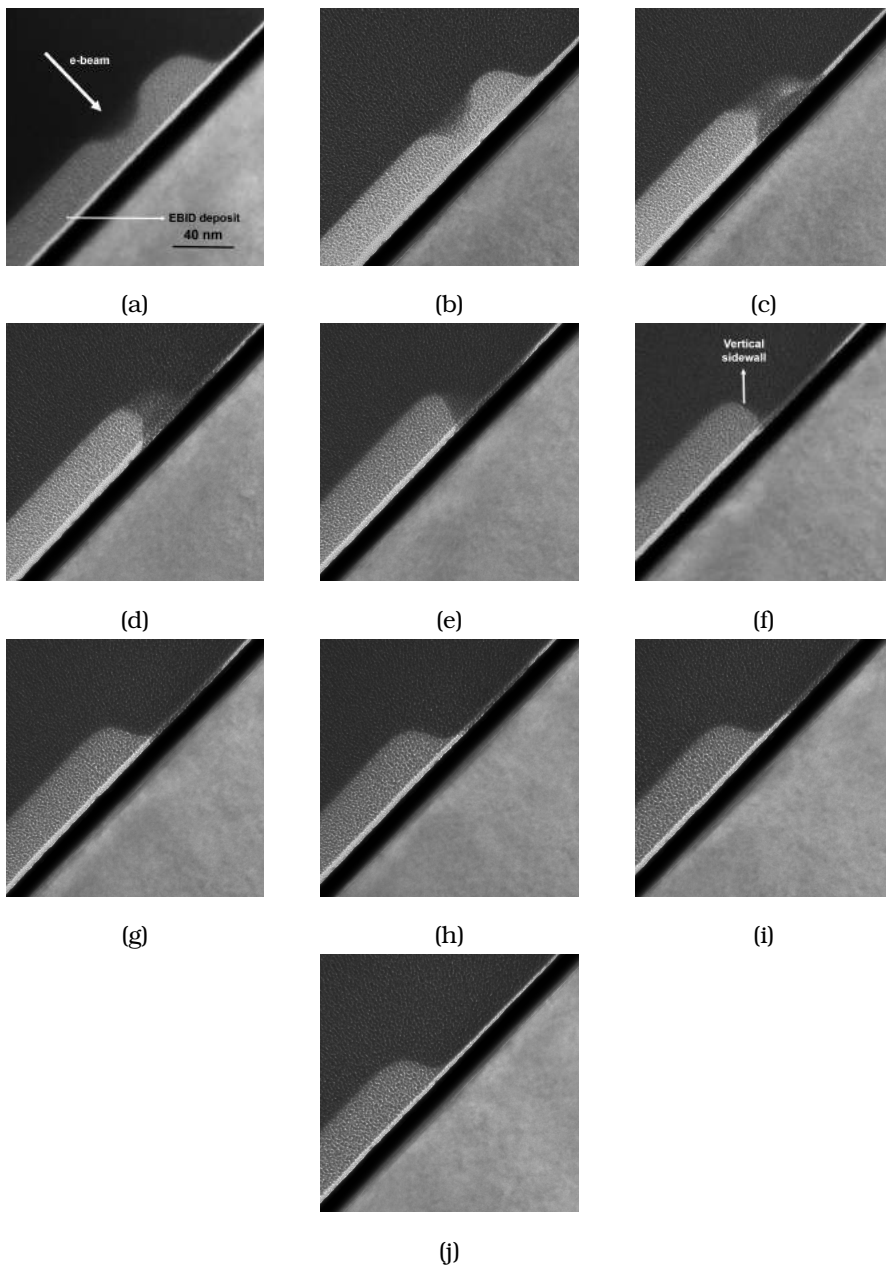


Figure 6.14: (a)-(j) Sidewall evolution as a result of the etching series. The images were acquired in bright field mode in an FEG Tecnai 20 D239 S-Twin TEM using an acceleration voltage of 200 keV and spot 3. The EBID deposit is indicated in (a) and the white arrow shows the approximate position of the electron beam for EBIE. The successful creation of a vertical sidewall is visible in (f).

remains as deposited. The angular dependence of the SE yield alone cannot be responsible for this evolution because, as seen in Deposit 10, this would not change dramatically across the slope. Moreover, according to the simulation, an underetch or even a perfectly vertical sidewall is impossible to achieve, the best case being a nearly vertical, but still outward-sloping profile. The experimental results therefore demonstrate the need for a new model. We begin by taking into account all the relevant physics based on our understanding of the process, while still performing an analytical calculation.

6.5 Modelling of sidewall modification by EBIE

In reality, EBIE is governed by the host of electrons generated by the interaction of the primary beam with the deposit, as described in Fig. 6.3. In addition, the secondary reactions of the etch products, residence time of the fragments on the deposit, sticking and diffusion of the water molecules also play a role in the manner and rate of etching. The obvious complexity of the process makes modelling this system a huge challenge. Models developed by [91] and [85] take off from the continuum model for EBID described in previous chapters. However, while in EBID, the deposition is governed by the dissociation of precursor molecules, EBIE is not quite as straightforward. The considerations for current limited or precursor limited regimes were found to be insufficient in determining the experimentally observed etch rates [85]. It was found that the formation of the volatile etch product was what determined the etch rate, which is not necessarily the same as the rate of precursor dissociation. It was also found by [85] that the etch product remaining on the surface for a finite time could be the rate limiting factor. Etching of a tantalum-based thin film was used to validate the results of the model. Since the goal of this work was to explain etching rates, the substrates used were plane and while it provides insight into the etching process and illustrates the complexity of the process, it does not address slope effects such as etching of a sidewall. The continuum models described in [37] are also successful in simulating, for example, etching of holes by spot exposure with the electron beam, but do not address the evolution of the deposit shape under etching. Monte Carlo simulations taking into account the sloping sidewall and a continuously evolving surface are needed to address this in a thorough fashion. We start by developing a simple analytical simulation with the goal of modelling the

shape evolution alone.

A two-dimensional analytical model has been developed to simulate the etching of a Gaussian deposit by EBIE. The evolution of the deposit geometry has been studied as a function of etching location as well as exposure dose. Etching of the sloping sidewall has been addressed in detail as it is critical for tuning the 3D shape of EBID structures. The units in this model are arbitrary.

The cross section of an EBID deposit having a flat top and Gaussian sidewalls has been defined as in Fig. 6.4. This is henceforth referred to as the deposit and consists of points on a fine grid whose values are stored in a matrix "Deposit_Profile". Water molecules adsorb onto the surface and, for simplicity, are assumed to form a complete monolayer. This deposit is exposed to the primary beam in spot mode, which has a Gaussian profile. We begin with the simplest scenario: where EBIE is governed purely by SE1's generated in the deposit, whose profile is also assumed to be Gaussian. The adsorbed water molecules can be dissociated by SE's emitted from that location, causing material to be etched. The SE profile from a flat deposit surface is defined as:

$$\text{SE_Profile} = \text{ProfileHeight} \times \exp\left(-0.5\left(\frac{\text{x-CntrBeam}}{\text{Sx_PE_Profile}}\right)^2\right) \quad (6.3)$$

where ProfileHeight is a constant that represents the strength of the etching, Sx_PE_profile is the FWHM of the SE emission and CntrBeam = the beam position. The etching dose is delivered by repeated exposures. Therefore, a parameter called "Exposure" is defined to represent the total electron dose, whose value is user defined. The principle of the model is as follows. The deposit profile, beam position and beam parameters are defined by the user. A counter "j" is defined that is incremented from 1 to "Exposure". Over this loop:

1. The slope of the deposit surface is calculated at all x positions of the SE profile that overlap with the deposit, as shown in the schematic in Fig. 6.15. At every x ($x_0, x_1, -x_1, \dots$), a step of $\Delta x = \pm 1$ is made and the corresponding y-values of the deposit are recorded. The slope = $\tan \alpha$ is calculated as $\frac{\Delta y}{\Delta x}$, where α is the angle between the beam and the normal

to the surface at the point of incidence. The slope is calculated for every x position of the SE profile that overlaps with the deposit, as shown in Fig. 6.15. 2. The enhanced SE emission profile due to the presence of

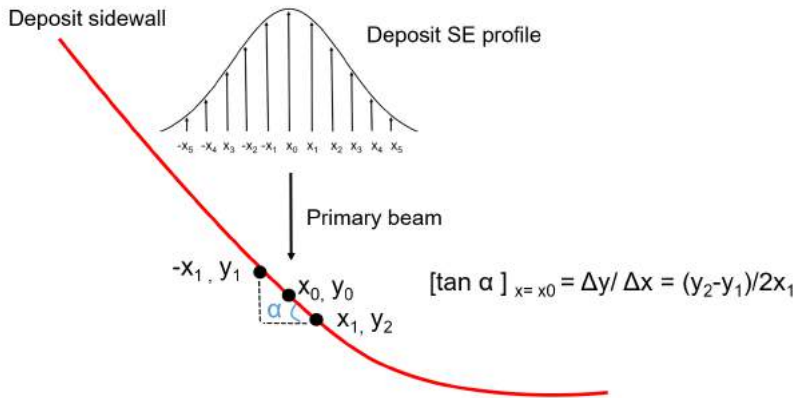


Figure 6.15: A schematic showing the calculation of the slope, performed for every x position of the SE profile that overlaps with the deposit. A step of $\Delta x = \pm 1$ is made and the corresponding y-values of the deposit are recorded. The slope = $\tan \alpha$ is calculated as $\frac{\Delta y}{\Delta x}$.

the slope called "SE_ProfileCorrected" is determined by the convolution of the original Gaussian profile (SE_Profile) with the function $\frac{1}{\cos \alpha}$ for every x position, determined in the first step.

$$\text{SE_ProfileCorrected} = \text{SE_Profile} \times \frac{1}{\cos \alpha} \quad (6.4)$$

3. The deposit is etched from the top by the SE's and the x and y values of the new profile are stored in a matrix "Deposit_Top".

$$\text{Deposit_Top} = \text{Deposit_Profile} - \text{SE_ProfileCorrected} \quad (6.5)$$

The condition that the substrate cannot be etched is imposed by setting all negative values of Deposit_Top equal to zero instead.

4. When the deposit material at any location has been removed and the substrate there is exposed directly to the electron beam, SE's generated in the substrate (SE_s) cause further etching to take place from below. So if Deposit_Profile (at x = beam position) = 0, another loop is implemented over a counter "k":

(a) Stepping left from the beam position by decrementing k , as long as $\text{Deposit_Profile} = 0$ (upto $x = A_1$ in Fig. 6.16), the values of k are written into the matrix "Deposit_Top". This is performed until the left edge of the deposit is detected and Deposit_Profile is no longer $= 0$.

(b) Then the left edge of the deposit is detected in the bottom profile, so called as it results from etching of the deposit from below. Beginning from $x = A_1$ (corresponding to the last recorded value of k), the program keeps stepping left by decrementing k for as long as the bottom profile > 0 , i.e., upto $x = A_2$ in Fig. 6.16. The values of k are written into a matrix "Deposit_Bottom" representing the bottom profile.

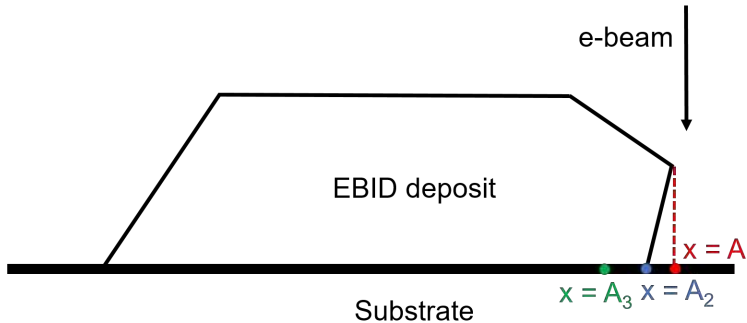


Figure 6.16: Cartoon showing the determination of the range of x values over which etching from below can take place due to SE's from the substrate.

(c) A parameter "w" is defined which determines the width of the band that over which the etching can take place in one step. This is a user defined quantity.

(d) Etching now takes place over this band along two directions: left of A_2 (etching further into the deposit) and right (etching from A_2 to Cntr-Beam). The program steps left from $x = A_2$ (Fig. 6.16) by the amount "w", defining the point $x = A_3$. Finally, material is removed from the bottom profile over the range $x = A_3$ to $x = \text{CntrBeam}$ as:

$$\text{Deposit_Bottom} = \text{Deposit_Profile} - \text{SE_s_Profile} \quad (6.6)$$

where SE_s_Profile refers to the profile of the SE emission from the substrate.

5. Steps 4 (a)-(d) are followed for etching to the right of CntrBeam
6. The plot of Deposit.Top and Deposit.Bottom for etching on the left and right of CntrBeam together makes up the resultant deposit profile.

This section provides a detailed description of the simulation and explains the choices made in the model. The evolution of the deposit profile is studied with specific examples. An EBID deposit with Gaussian sidewalls is simulated on a substrate to have a height = 400 and width = 1600 between the positions of the left and right sidewalls. The cross section of this deposit is shown in Fig. 6.17. The sloping sidewalls are defined by identical Gaussian functions with HWHM = 200. For CntrBeam = 2500

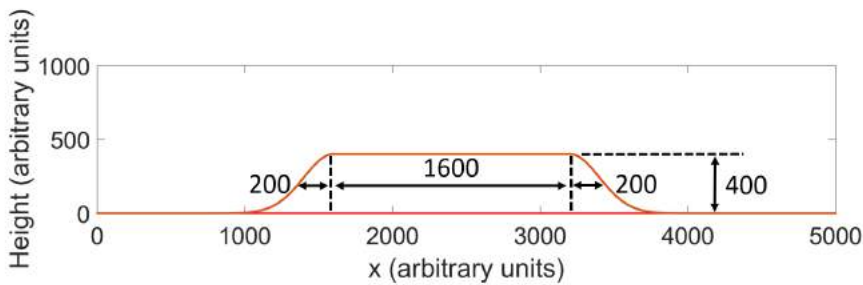
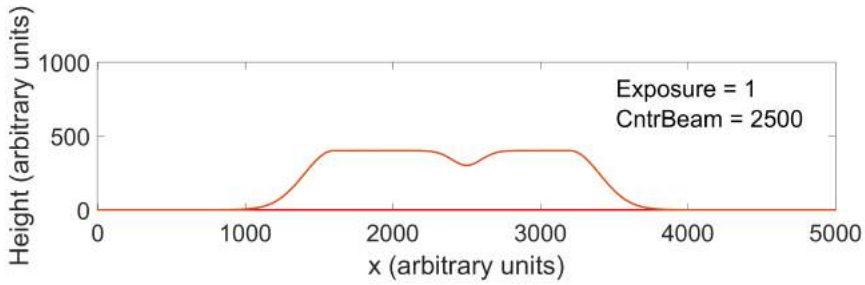


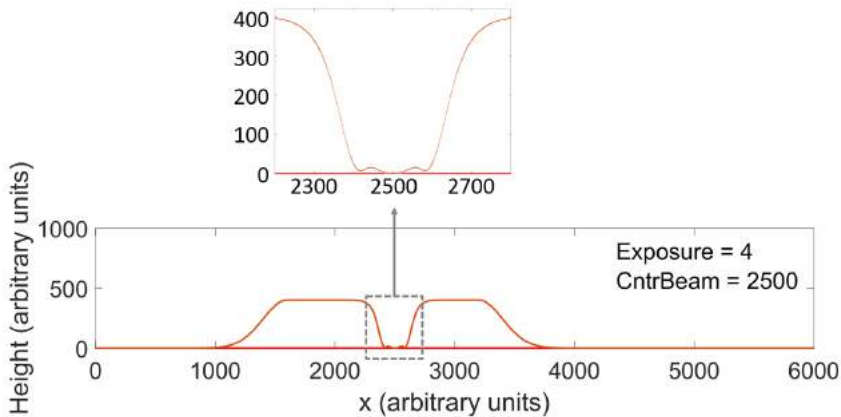
Figure 6.17: An EBID deposit of height = 400, width (between edge positions) = 1600, HWHM of slope = 200 simulated on a substrate. The cross section shown is defined by a fine grid. All dimensions are in arbitrary units.

and Exposure = 1, if the ProfileHeight = 100 and Sx_PE_profile = 100, etching takes place on the plane top of the deposit resulting in a hole with a Gaussian profile shown in Fig. 6.18(a). Continued exposure results in etching of the new surface, which is no longer plane. The SE emission at every point on the deposit is now enhanced by a factor of $1/\cos\alpha$ as in Section 6.1 and the corrected SE profile is calculated as in Equation 6.4. For Exposure = 4, for example, the resultant profile is shown in Fig. 6.18(b). The corresponding SE profiles for the two cases of 6.18(a) and (b) are shown in Fig. 6.19(c) and (d), together with the plot of the correction factor $1/\cos\alpha$ in Fig. 6.19(a) and (b). The inset in Fig. 6.18(b) shows a zoom-in of the deposit in the region of etching and it can be seen that for the dose used,

etching has taken place all the way to the substrate. Continued exposure in this manner would not result in any more etching at that point, but only remove material where the tails of the SE distribution are present. It



(a)



(b)

Figure 6.18: Deposit profile after etching with SEI's by spot exposure with the primary beam on the plane top for (a) Exposure = 1 and (b) Exposure = 4. Inset in (b) shows a zoom-in of the deposit profile in the region of exposure where it can be seen that the deposit has been etched all the way to the substrate.

is evident that this model would never result in an underetch. As in Fig. 6.5, the sidewalls can be made steeper but a sidewall angle of 90 degrees

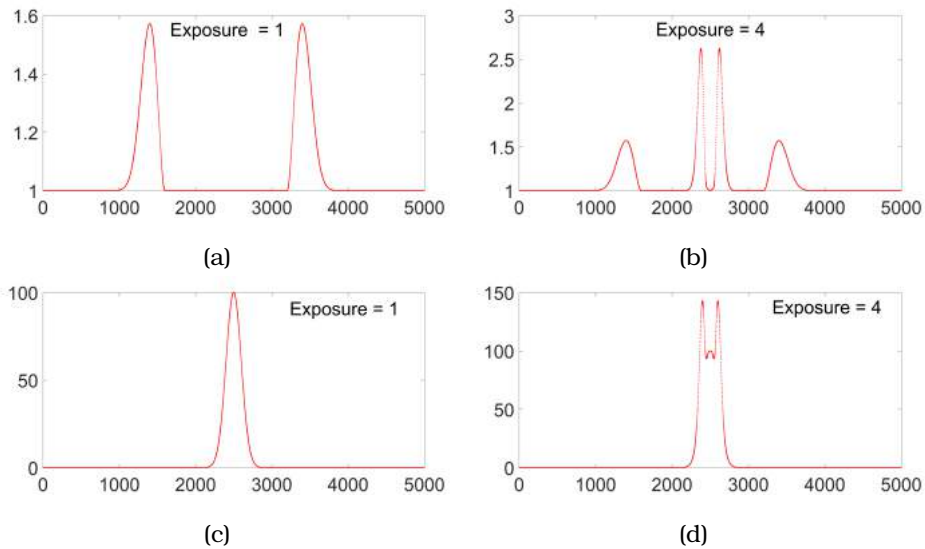


Figure 6.19: (a),(b) Corresponding values of the correction factor $1/\cos \alpha$ for Fig. 6.18. (c),(d) Corrected SE profiles for Exposure = 1 and 4. Exposure = 1 results in the creation of a hole with a Gaussian profile as a result of the SE profile. Continued exposure results in etching of a surface which is no longer plane. The etching is now governed by the corrected SE profile (SE_ProfileCorrected) due to enhanced SE emission from every point on the sloping surface, resulting in the profile in (b).

cannot be achieved. Other effects must therefore be responsible and they must be taken into account in order to formulate a realistic model. Upon considering Fig. 6.18 (b), an important stage in the etching process can be seen to occur. The question arises as to what happens once the deposit has been etched all the way to the substrate as in this case (at $x = 2500$ and a few pixels on either side of it). Once the bare substrate is exposed, the SE1's from the substrate there (SE_s) can cause etching to take place from below. These SE's also have a Gaussian profile but since the substrate (gold-palladium) has a higher SE yield than the deposit (carbon), the SE_s profile is broader. The parameters for etching from below are therefore $SE_ProfileHeight =$ etching strength and $Sx_SE_Profile =$ FWHM of the SE profile. Since the presence of adsorbed water molecules is an essential condition for etching, the SE's from the substrate are not effective unless the deposit there has first been removed and the substrate is exposed to the precursor. The substrate itself is assumed to not be etched or affected by the process in any way. Proceeding from Exposure = 4, the next etching step is plotted in Fig. 6.20 (a) for Exposure = 5. Etching by the SE's

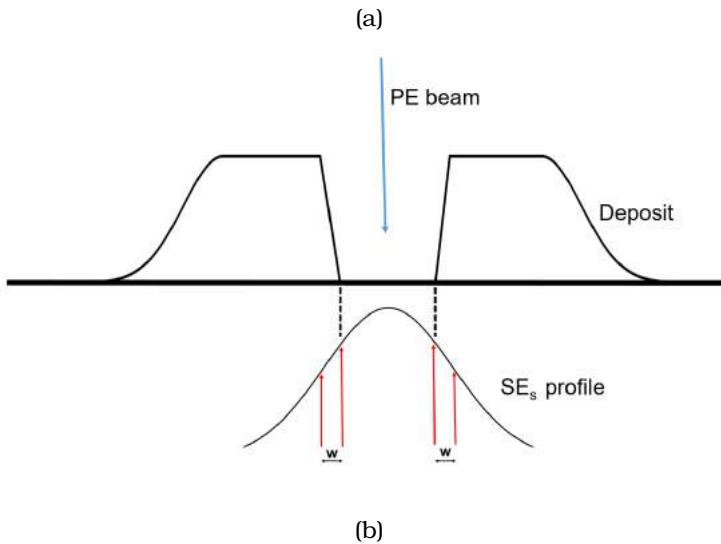
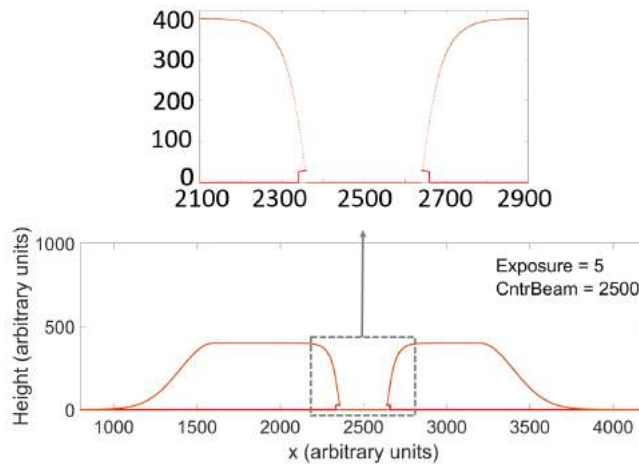


Figure 6.20: (a) Deposit profile for etching at CntrBeam = 2500 with Exposure = 5. The inset shows a zoom-in where the beginnings of underetching can be seen due to EBIE from below by SE's emitted from the substrate. (b) A schematic showing how etching from below takes place. The parameter "w" defines the length in x over which material can be removed in one etching step.

from the deposit continues, and is accompanied by etching from below by SE_s at those locations where the bare substrate is exposed. A schematic of etching from below is shown in Fig. 6.20 (b). Although exposure to

the SE's generated in the deposit continues throughout, this ceases to be significant when material has been etched away completely (as in the central region of (b)). The same holds for the SE_s, which cannot effect any more etching in that region, but as their profile is broader, they can effect etching farther away from the centre. An important parameter in this process is the amount of material removed in one step. Since the water molecules must have sufficient time to form a monolayer on the newly exposed region, it is unrealistic to assume that the entire extent of the SE_s profile is removed in one step. This is therefore controlled by a parameter "w" which determines the width of the band that can be etched in one step as shown in (b). Setting SE_ProfileHeight = 40, Sx_SE_Profile = 180 and w = 20, for the first time, the beginning of an underetch can be seen in (a). The result of etching from the top is shown in orange and that of etching from below in red (Fig. 6.20). This colour scheme is maintained throughout this chapter. The step in the underetch is a consequence of the profiles being described by a discrete grid and would in practice be a more gradual slope. Continuing to etch at the same position with the same parameters, the cases of Exposure = 10, 20 and 45 are shown Fig. 6.21 (a), (b), (c) respectively and the underetch can be seen to become more and more pronounced with dose. Although the SE_s profile is in theory infinite in extent, the profile evolution comes to an end when the band "w" is so far away from the centre of the beam that the strength of the SE profile there is negligible.

From this model, it emerges that the crucial condition in achieving under-etching is:

$$\text{FWHM}(\text{SE}_s) \text{ is significantly } > \text{FWHM}(\text{SE}_d)$$

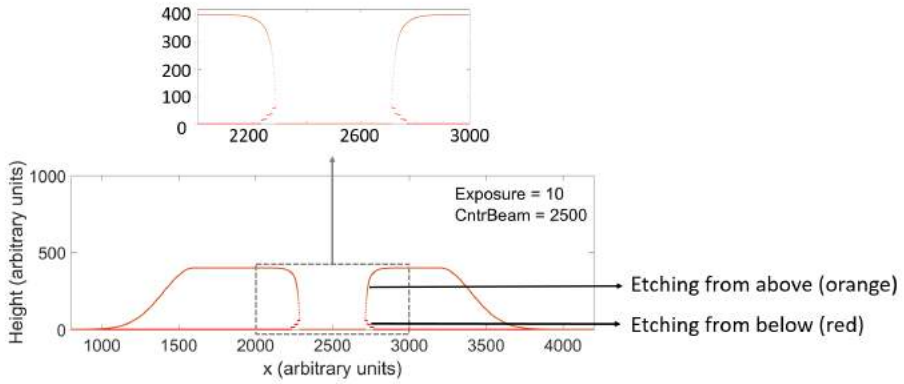
where SE_d is the profile of SE's generated in the deposit. The relative strength of etching is less important.

Three cases are considered here and the corresponding beam profiles shown in Fig. 6.22:

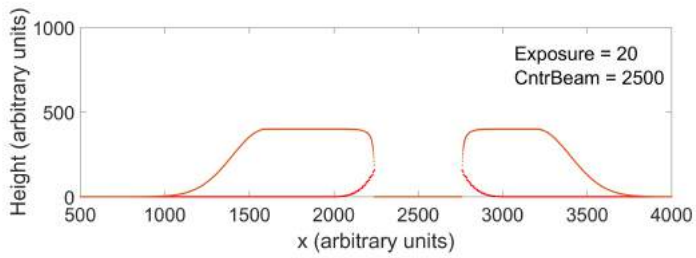
(a) FWHM (SE_s) = 180, FWHM(SE_d) = 100, ProfileHeight = 100,
SE_ProfileHeight = 40

(b) FWHM (SE_s) = 180, FWHM(SE_d) = 100, ProfileHeight = 100,
SE_ProfileHeight = 140

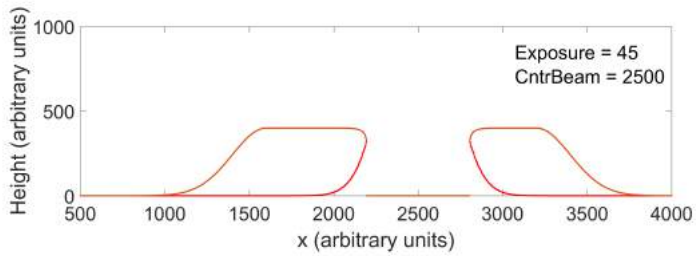
(c) FWHM (SE_s) = 70, FWHM(SE_d) = 100, ProfileHeight = 100,
SE_ProfileHeight = 140



(a)



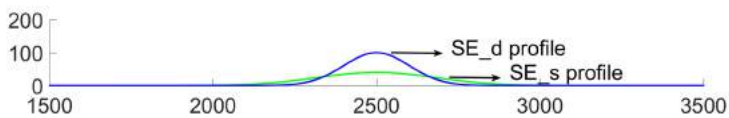
(b)



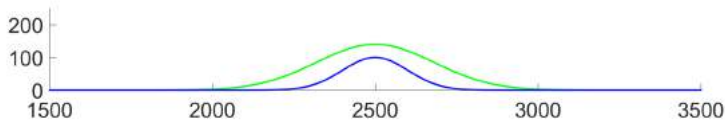
(c)

Figure 6.21: Resultant profiles for continued etching at CntrBeam = 2500 for (a) Exposure = 10 (b) Exposure = 20 (c) Exposure = 45, demonstrating the increase in underetching with dose.

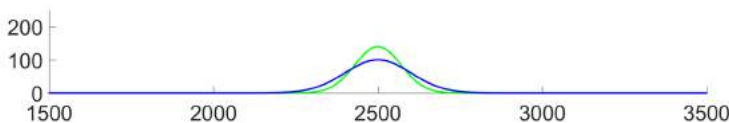
While (a) represents the case where the SE_ProfileHeight is much less than the PE_ProfileHeight, an underetch is observed in this situation due to the fact that the SE_s profile is significantly broader than the SE_d profile. An underetch is also observed in case (b) where the SE_s profile is both broader and stronger than the SE_d profile. However, in case (c), no underetch is observed even with Exposure = 40 because although the SE_s profile is stronger than that of the SE_d, it is much narrower. Such conditions can be argued to exist in the experiment as the SE yield of the gold-palladium substrate is known to be higher than that of carbon. This is further corroborated by the fact that a shallow carbon EBID deposit appears darker than the substrate. So an underetch is expected to occur in the experiment.



(a)



(b)



(c)

Figure 6.22: (a)-(c) Input SE profiles from the deposit (blue) and from the substrate (green) for three cases: (a) FWHM (SE_s) = 180, FWHM(SE_d) = 100, PE_ProfileHeight = 100, SE_ProfileHeight = 40, (b) FWHM (SE_s) = 180, FWHM(SE_d) = 100, PE_ProfileHeight = 100, SE_ProfileHeight = 140, (c) FWHM (SE_s) = 70, FWHM(SE_d) = 100, PE_ProfileHeight = 100, SE_ProfileHeight = 140

6.5.1 Sidewall evolution with electron dose

Based on this model, the effect of etching dose on the sidewall geometry was studied. EBIE was performed in spot mode, as described above, at the edge of an EBID deposit and the evolution of the profile has been plotted in Fig. 6.23. The right sidewall of a deposit of height = 400, width between

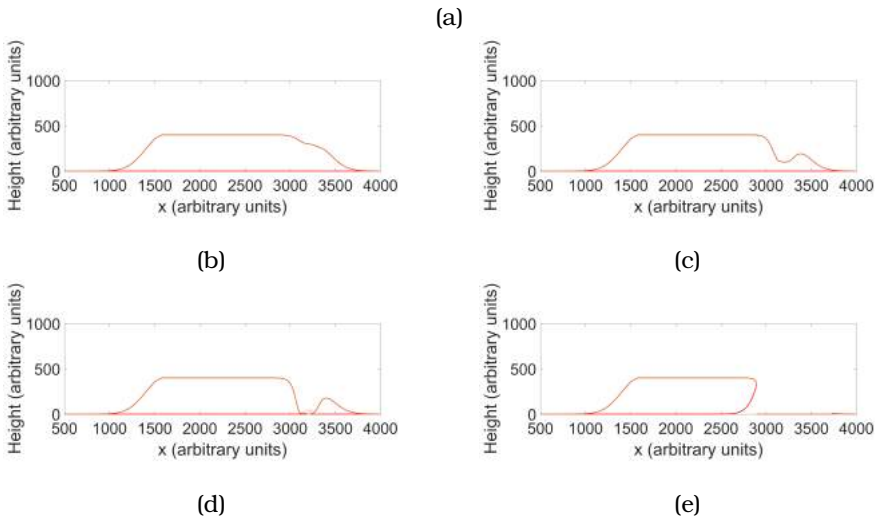
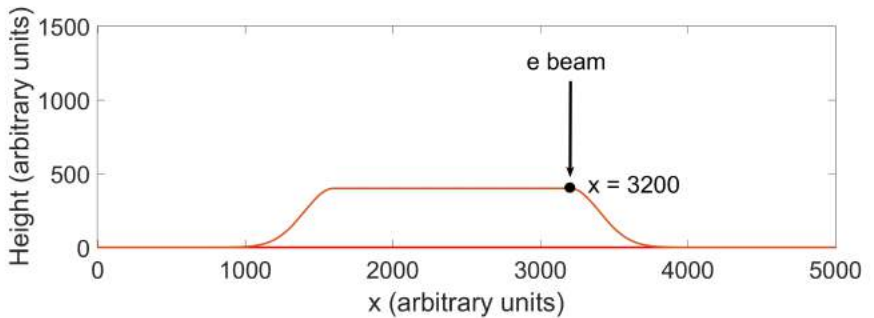


Figure 6.23: (a) Simulated deposit with the position of etching ($x = 3200$) indicated. (b)-(e) Simulation results showing the evolution of the Gaussian sidewall with Exposure = 1, 3, 4 and 45 for CntrBeam = 3200. In the initial stage, a dent is created in the sidewall which deepens until Exposure = 4 where etching has taken place all the way to the substrate. This is followed by etching from below, resulting in the steep underetch in (d) for Exposure = 45.

edge positions = 1600 and HWHM of sidewalls = 200, was etched with CntrBeam fixed at 3200 as shown in (a) for Exposure = 1, 3, 4 and 45. All

other parameters (SE_s and SE_d profiles) were kept the same as before. The etch position and the number of exposures were chosen somewhat arbitrarily to provide the best visual demonstration of the sidewall angle evolution. The progression from (b) to (e) shows etching as described above, beginning with an indentation (for Exposure = 1), followed by complete removal of deposit material and subsequent underetching. Etching at a position on the sidewall is, as expected, similar to etching on the plane surface for the case of Exposure > 1 as they are both governed by the principle of etching of a sloping surface.

6.5.2 Sidewall evolution with etch position

The experiment described in Fig. 6.13 has been simulated by etching a series of positions on the sidewall. The dose of PE's was the same at all locations and the evolution of the profile is shown in Fig 6.24(a)-(f). From (b) to (e), the distance between the etch locations is equal. It is at once evident that the trend of the experiment is reproduced quite accurately. On moving outwards from the centre, a steep underetch is visible in (b) from the black curve. When sufficient material has been removed for the substrate to be exposed to the beam, additional etching by SE's from the substrate takes place giving rise to the underetch seen in the images. It is important to note that this effect is essential in producing an underetch, and etching from the top alone would always result in an outward slope. Further, the extent of underetch depends on the ratio between the SE yields of the deposit and the substrate, which has been chosen arbitrarily here to simply demonstrate the phenomenon. As in Fig. 6.14(c), there is a small amount of material remaining to the right of the deposit in (b). In (c), the etching still results in an inward slope but this protrusion is not present. Further out, the underetch remains until (d) where the sidewall appears vertical. On moving sufficiently far away (e) the slope is unaffected with the long tail alone etched away and finally, in (f), the profile is unchanged with respect to the as-deposited structure.

6.5.3 Discussion

Although the trends in Fig. 6.14 and Fig. 6.24 are qualitatively similar, there are several differences visible too. The underetch is much more evident in the experimental results than in the simulation. This could be due to the fact that a simple analytical model is not sufficient to

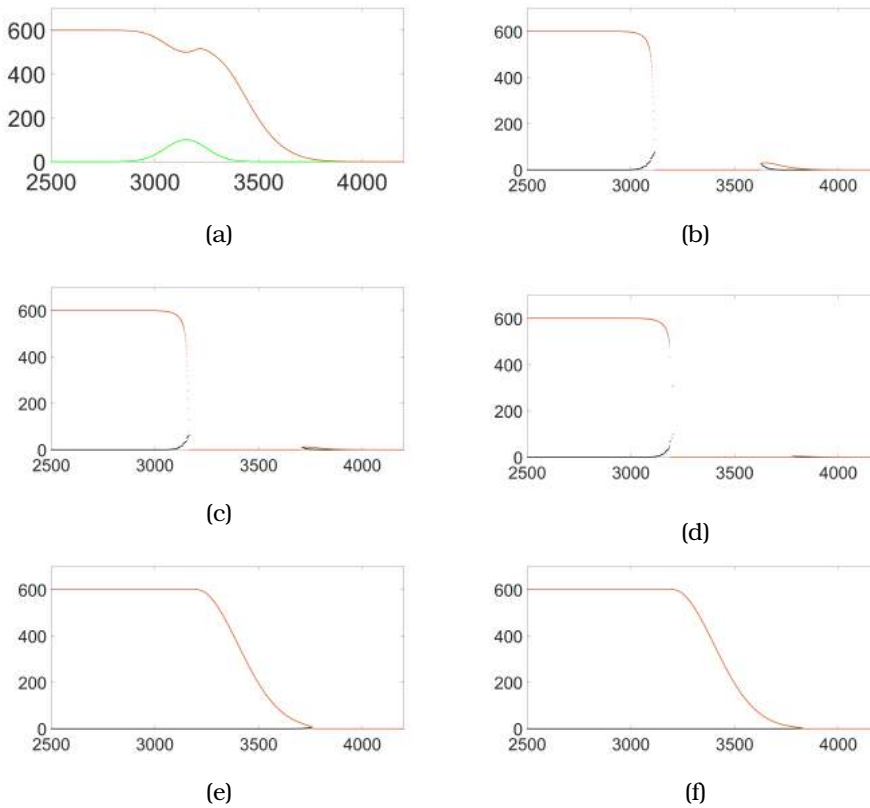


Figure 6.24: (a)-(f) Simulation results showing the evolution of the sidewall as a function of etch position. The red and black plots are the profiles of "Deposit_Top" and "Deposit_Bottom" respectively. The green plot in (a) represents the SE profile on the plane, whose peak indicates the position of the beam for reference. The creation of a vertical sidewall is clearly visible in (d).

fully simulate the experimental conditions. Further, the parameters used in the model are in arbitrary units. They were chosen such that the experimentally observed trend could be replicated, and not from physical considerations. The etching related parameters, in particular, and their values relative to the deposit geometry might therefore be unrealistic. This is supported by the fact that attempts to scale the parameters against the experimentally observed values were unsuccessful.

One of the main issues comes about due to the fact that the regime in which the etching takes place is unknown. As shown in 6.3.2 a small change in the pressure of water vapour leads to a significant change in the etching rate, suggesting that the process is gas limited. The role of

diffusion could therefore be significant. The diffusion rate of adsorbed contamination is known to be enhanced by the presence of water layers [91]. But since the relevant quantities are hard to measure, it has not been included in the model, nor have some other factors such as scattering, porosity and secondary etch product reactions.

Another major difference is that in the experiment, a line is being etched with a PE beam having a finite spot size. The effect of pixel dwell time, pixel overlap and multiple passes has not been taken into account, all of which could play an important role in circumstances involving surface diffusion. The goal of this model is only to provide a qualitative explanation of sidewall evolution under etching, which is not addressed by existing models and which is necessary for carrying out a well controlled experiment.

In the experiment, the positioning of the etch series with respect to the deposit array was performed by eye using the same field of view ($8\ \mu\text{m}$) each time. As this is rather large, it is reasonable to assume that when the experiment was repeated for confirmation, even assuming that the deposits were identical, etching might have taken place at a somewhat different location in each instance. The images showed that the trend in the profile is reproduced, although a certain profile may occur at a different location each time the series is repeated. This means that, at least within a range of 100 nm on the sidewall, given a position, a suitable electron dose would result in a vertical sidewall.

This suggests that etching can be carried out at any position on the sidewall if the right dose can be applied to make it vertical. From a practical point of view, it would be advantageous if this entire process, etching as well as imaging, could be implemented in situ in the SEM. The above result is encouraging because it suggests that if the sidewall evolution could somehow be monitored, we could begin etching at an arbitrary position (within a certain range, still determined by eye) and stop when the desired profile is attained. The following section presents experimental proof of this concept.

up to a few hundred nanometers. The SE image of the resultant structure is shown in Fig. 6.26(b). The deposit was then covered with a protective layer of Pt/C as before and a cross section made using a FIB (Fig. 6.26(c)), clearly demonstrating the creation of vertical sidewalls.

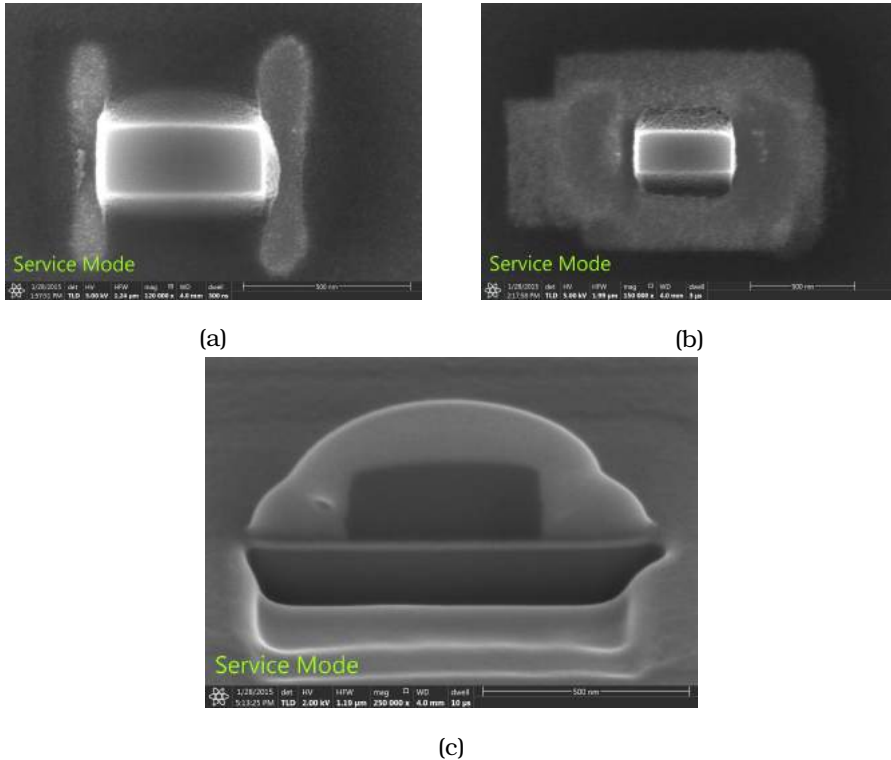


Figure 6.26: Top view SE image (a) after etching of the sidewall and (b) after the cleaning step. (c) FIB cross section of deposit after sidewall etching clearly demonstrating the creation of vertical sidewalls.

6.7 Repeatability

The ability to obtain these results reproducibly is contingent upon the accurate monitoring of the etching. To test how well SE imaging serves to monitor the profile change, which in turn determines the etching dose, the process was repeated for several similar deposits and the outcomes of a few are shown in Fig. 6.27.

It is evident from Fig. 6.27(a) and (b) where the left sidewall was etched that it is in fact possible to reproducibly modify the deposit to sharpen the

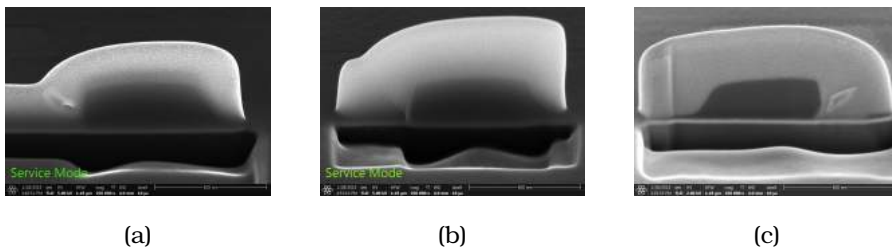


Figure 6.27: Images showing repeatability of sidewall modification by monitoring of the SE signal.

sidewall angle, using an electron dose that is determined by monitoring the relative change in SE emission from the sidewalls. However, the resultant profiles are not identical, with the sidewall in (b) being somewhat sloped or rounded. There are several possible reasons for this: SE monitoring may not be sufficiently sensitive. An extreme case is shown in Fig. 6.27(c) where the experiment to etch the right sidewall was performed in the same manner as in (a) and (b), but created an undercut that could not be deduced by monitoring the SE image. Another possibility is that the deposits may not have been identical to begin with or the etching may not have been carried out at the same location relative to the edge, in which case the dose needed would be different. It is also possible that the surface roughness of the substrate is responsible for these differences. This is also suggested by the area exposed in Fig.6.28 where the pattern that was etched was rectangular in shape whereas the resultant pattern is far from symmetric. In fact, we investigated EBIE of a thin layer of carbon on the substrate and found that in spite of uniform electron beam exposure, the etching begins at a few seemingly random points, perhaps determined by the local surface irregularities, and expands to cover a larger area. Any irregularities on the substrate could act as a nucleating centre for water molecules to be dissociated due to the increased SE yield.

So while this work demonstrates proof of concept, more studies are needed to achieve complete control over the process, most importantly the development of a sensitive in-situ technique to monitor the 3D profile. As a next step, this process was carried out on structures in proximity to each other with the goal of applying it to modify dense EBID lines. Fig. 6.29 shows a linear array of three connected carbon EBID deposits which have been etched successfully to result in separate structures with vertical sidewalls.

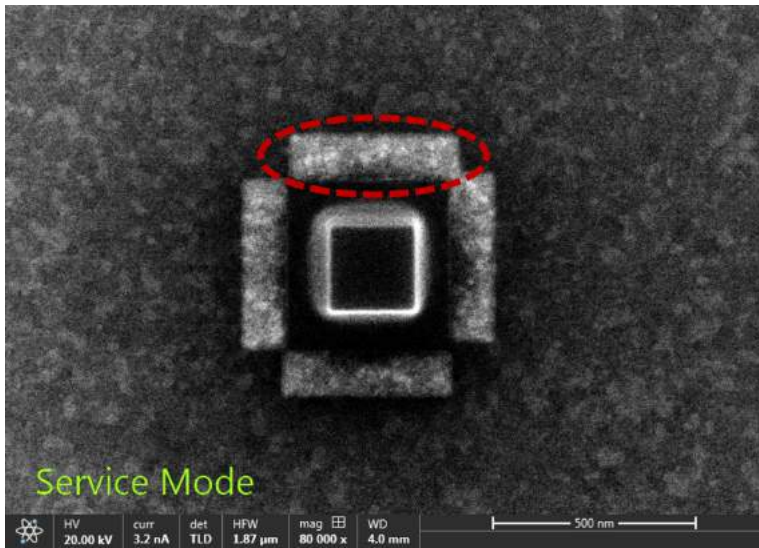
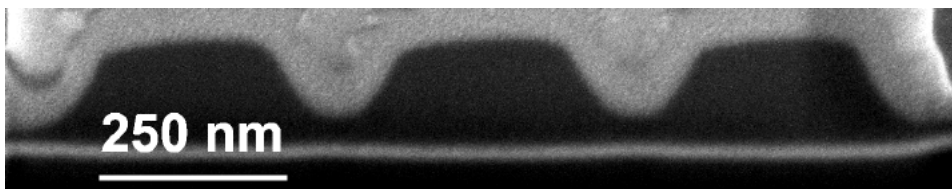
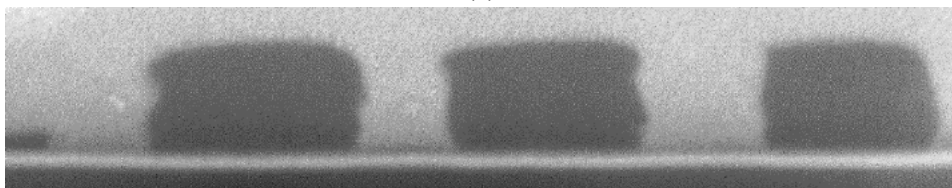


Figure 6.28: A square EBID deposit (centre) after cleaning has been performed on four sides. The region encircled in red shows the irregularities in a seemingly uniform etch exposure.



(a)



(b)

Figure 6.29: FIB cross section of an array of EBID structures (a) as-deposited and (b) after etching of the sidewalls.

6.8 Sidewall modification in high resolution dense lines

The ultimate goal in combined EBID-EBIE is the patterning of high resolution dense EBID lines with vertical sidewalls. Very simply: to go from the as-deposited case (a) in Fig. 6.30 to (b) post-etching.

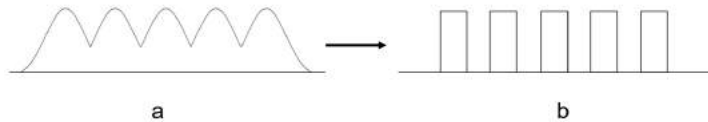


Figure 6.30: Cartoon showing combined EBID-EBIE in high resolution dense lines to go from the as-deposited case of lines with Gaussian sidewalls and inter-connecting material in (a) to well-defined, well-separated lines with vertical sidewalls in (b).

This requires the etching of very accurately positioned high resolution lines, which first requires the demonstration of etching of high resolution dense lines. Towards this goal, a large shallow carbon EBID deposit was patterned (thickness estimated by inspection of SE image) and several arrays of dense lines were patterned by EBIE. It should be noted that while the term 'patterning' is used for EBIE here, it actually refers to the fabrication of spaces and the lines are comprised of carbon from the EBID deposit. A shallow deposit is desirable both because it is faster and easier to etch and because underetching can be avoided. Moreover, since EBID lines usually have a low aspect ratio, the same was attempted here. Fig. 6.31 shows the SE image of a carbon EBID deposit (dark) in which 6 arrays of dense lines (A1 to A6) have been etched. From A1 to A6, the lines in the arrays were defined to have a width of 1 nm, 2 nm, 3 nm, 5 nm, 10 nm and 20 nm. The centre to centre spacing was 100 nm and the EBIE parameters used were: 20 keV, 13 nA, dwell time = 1 μ s, pitch = 1 nm, number of passes = 500. For the dose and spacing used, defined line widths in the range 1 nm to 5 nm result in well separated lines. Ignoring the regions near the edges of the deposit, the etched lines appear to be very uniform. A high magnification image of a large array of dense lines etched in a shallow carbon deposit with similar parameters (Fig. 6.32) shows them to be quite reproducible and homogeneous with a resultant EBID line width of approximately 30 nm. This array was patterned with a defined etch width of

2 nm (resulting in approximately 50 nm etched lines). Approximate values of etch widths and the corresponding (deposit) line widths obtained for the case of dense lines are shown in Fig. 6.31, which give an indication of the resolution in this work. The smallest lines etched in this experiment were about 30 nm wide (array A1), but this in no way represents the resolution limit of EBIE. This must be determined by performing a dose series and by varying the etching parameters. This experiment is therefore a successful demonstration of high resolution etching in a high vacuum SEM and is the first step towards using combined EBID-EBIE for lithography.

The next step would be etching in between dense EBID lines as in Chapter 5. As observed there, the contamination deposited on the edges of the etched area is currently the limiting factor in achieving control over the process at high resolution. Exposing a line to a sufficiently high electron dose in the presence of water resulted not only in etching of the material there, but in the deposition of hydrocarbon contamination on the edges of this area. At high resolution, this would result in the modification of neighbouring lines, which is obviously undesirable. Taking special steps to ensure very low contamination levels in the SEM is necessary and would go a long way towards enabling the application of this technique at sub-20 nm resolution. Imaging of the line profiles is a big challenge as SE contrast would not be sufficient to monitor changes in sidewall angle for such shallow lines. The preparation and imaging of TEM slices is labour intensive and therefore inconvenient but in the absence of an in-situ imaging technique, might be the only option. In that case, a better understanding of the process is needed to predict the right combination of dose and etch position that would result in the desired line profile.

6.9 Interesting observations during EBIE of EBID patterns

An interesting effect was observed while attempting to etch through a thick carbon EBID deposit. In order to understand what parameters are effective in etching thick deposits, one of the systematic experiments performed is shown in Fig. 6.33. A large carbon structure (length = 5 μm , width = 50 nm) was patterned by EBID with: 5 keV, 100 pA, defocus = 100 nm, pixel

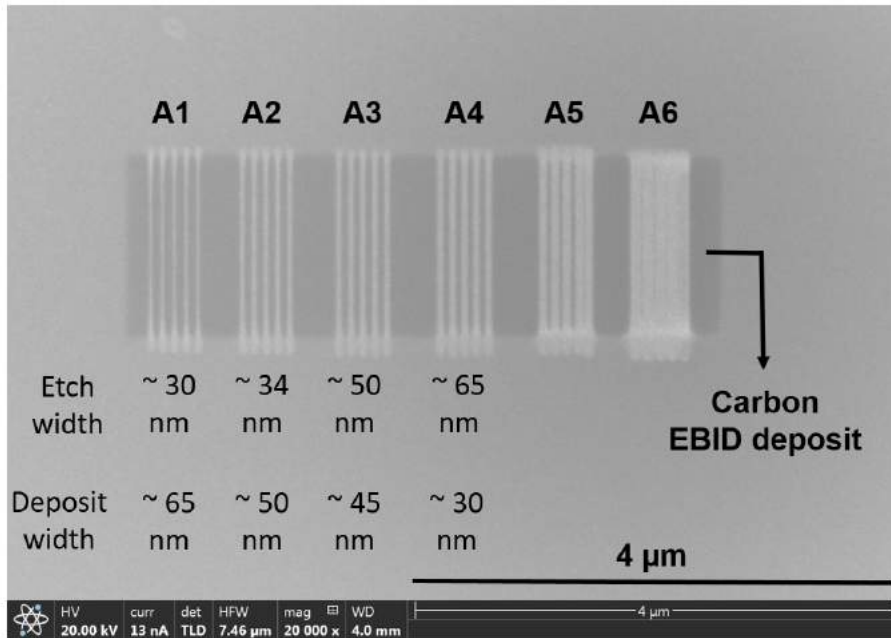


Figure 6.31: Arrays of dense lines and spaces patterned by etching lines in a shallow carbon EBID deposit by EBIE. The etching was carried out at 20 keV and 13 nA. The centre to centre spacing was 100 nm in all the arrays and the defined etch widths (A1 to A6) were 1 nm, 2 nm, 3 nm, 5 nm, 10 nm and 20 nm. Approximate values of the resultant etch widths and (deposit) line widths obtained in arrays A1 to A4 are shown. The highest resolution etched line obtained in this experiment was 30 nm (A1), but this is by no means is it the resolution limit in EBIE.

overlap = 90 %, dwell time = 500 μ s, number of passes = 300. A series of lines of increasing etching dose were then patterned to etch through the deposit as shown by the yellow lines in the figure. The etching parameters were: 5 keV, 1.6 nA, pitch = 5 nm, dwell time = 10 μ s. The number of passes was in the range 500 to 50000 and the results of the experiment imaged with the TLD are shown in Fig. 6.34.

From the lowest dose ($N_{pass} = 500$) to the highest ($N_{pass} = 50000$), removal of carbon is observed far away from the EBID deposit as brightening in the SE image. At and next to the deposit, where the carbon thickness is greater, the etching is clearly dose dependent. Lower doses ($N_{pass} = 500$, 1000) are unsuccessful in removing material and it is at $N_{pass} = 2000$ that

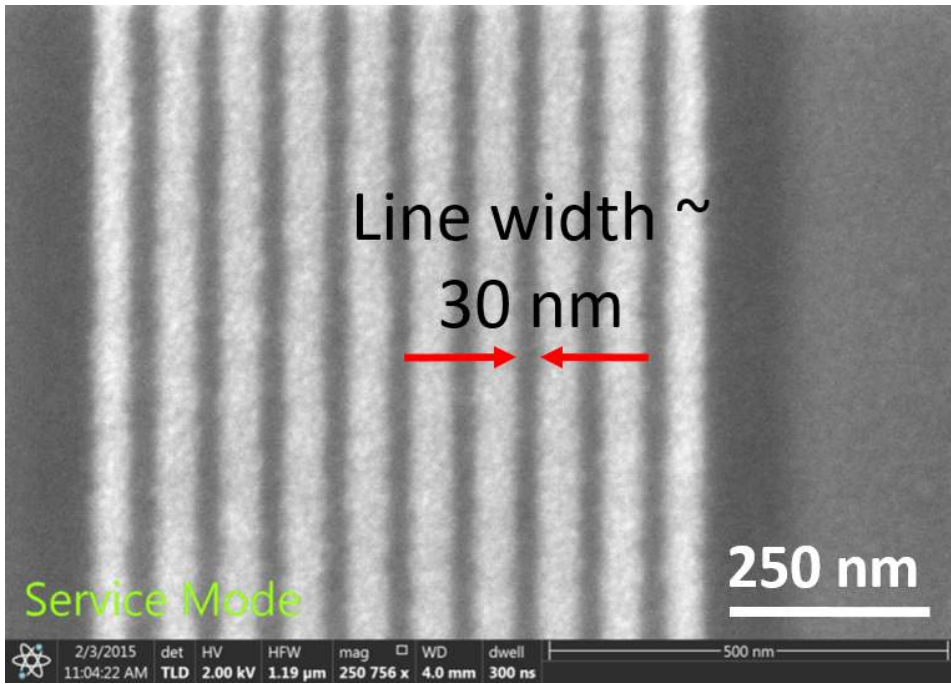


Figure 6.32: A large array of high resolution lines and spaces illustrating the fabrication of uniform, homogeneous and reproducible dense lines of approximately 30 nm width by EBIE into a large uniform EBID deposit.

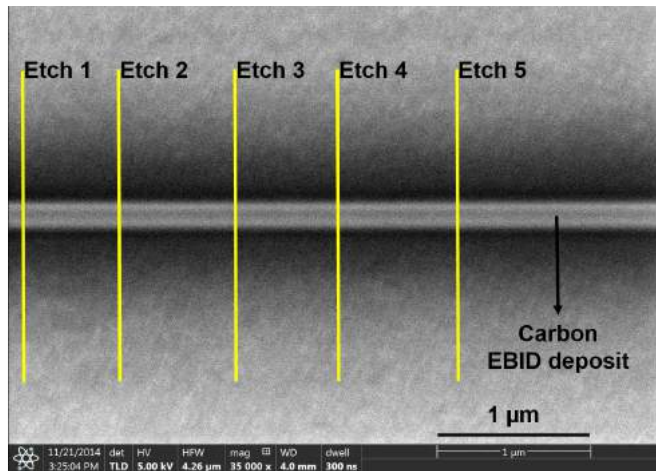


Figure 6.33: Schematic of an experiment to etch through a large carbon EBID structure. The five yellow lines indicate etch positions 1 to 5, to be exposed to EBIE with increasing number of passes.

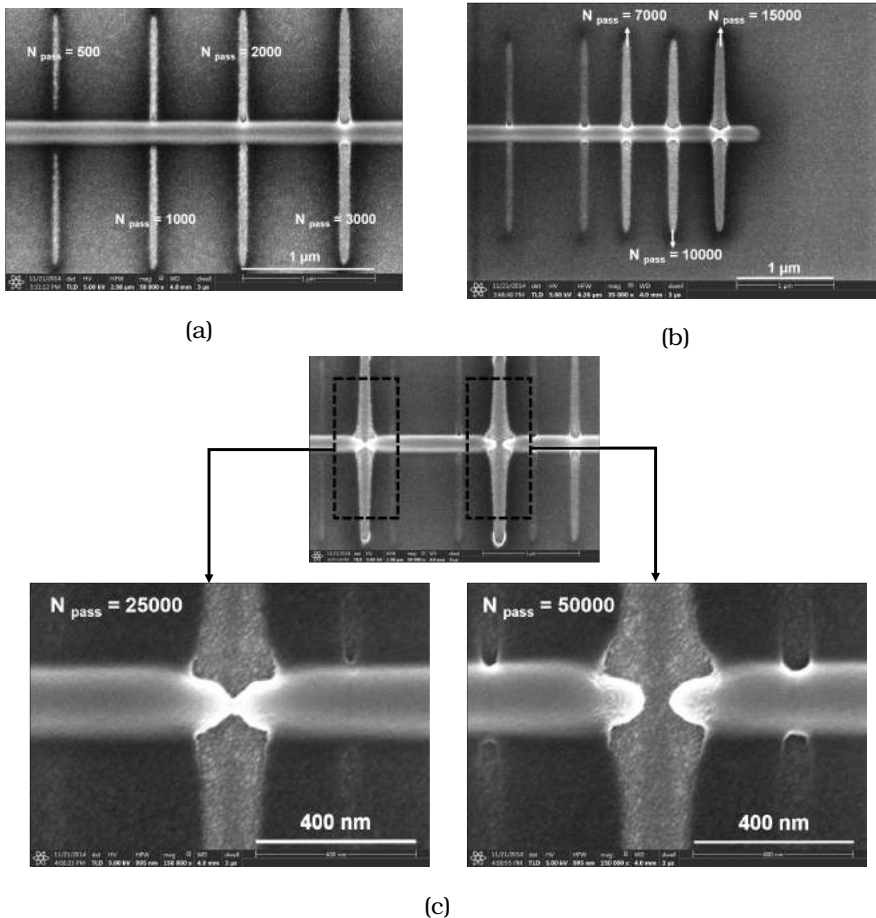


Figure 6.34: (a)-(c) SE images showing the result of etching through a carbon EBID deposit. EBIE was performed at 5 keV, 1.6 nA, pitch = 5 nm, dwell time = 10 μ s and the number of passes was in the range 500 to 50000 as shown in each image. The inset in (c) shows a zoom-in of the two lines etched with the highest dose ($N_{pass} = 25000$ and 50000)

the deposit begins to be etched at what appears to be the sidewall position. At $N_{pass} = 3000$ and higher, the deposit appears to be underetched in what can be assumed as the same mechanism as described in Section 6.5. At a sufficiently high dose ($N_{pass} = 25000$), the underetching resulting from EBIE of the top and bottom halves of the deposit causes the deposit itself to become narrow in the region around the etch position. Simultaneously, a channel seems to be created underneath as the central part of the deposit has not been etched yet. This is an interesting effect and although it was not investigated in any more detail in this thesis, there might be potential

applications in other fields. At a still higher dose ($N_{pass} = 50000$) the deposit is etched through, including in the centre, as indicated by the exposed grains of the underlying gold-palladium substrate. This method could be used to cut a deposit and create a tapered channel between the halves, whose shape could possibly be tuned by controlling the EBIE dose.

6.10 Conclusions

A new technique combining EBID and EBIE has been developed to fabricate structures with vertical sidewalls. The Gaussian profile of as-deposited carbon EBID structures has been modified by etching with water, and controlled tuning of the sidewall angle has been demonstrated, including the creation of vertical sidewalls. By simply varying the etch position on the sidewall using the top view SE image for reference, the slope of the deposit can be tuned from negative (outward) to positive (inward). The evolution has been studied in detail by high resolution imaging in a TEM. A surprising trend was observed which was not indicated by the simple model based on etching due to SE's from the deposit, that was the starting point of the study. While etching proceeds as expected for very low doses, underetching was observed at higher doses. An analytical model was developed that nevertheless incorporates the effect of water adsorption in a simple manner. In this model too, the etching is governed by SE's but once the deposit material at a location has been removed, exposing the bare substrate, water molecules are adsorbed there. The SE's generated from the substrate by continued exposure to the beam are now effective in removing the deposit material from below, resulting in underetching. The role of the substrate is crucial, without which etching would always result in an outward sloping sidewall whose angle varies with position and dose.

This experiment has also been carried out in situ in the SEM. Making use of the phenomenon of enhanced SE emission from an edge, the evolution of the sidewall angle during etching was continuously monitored using the SE signal. It has been demonstrated that this technique is sufficiently sensitive to determine the dose at which the sidewall angle becomes 90 degrees, but not sufficiently so to achieve other profiles as desired. The repeatability of the technique has been investigated and the limitations detailed.

High resolution carbon lines and spaces have been fabricated by a complementary patterning method to that described in Chapters 1,2 and 3. EBIE was used to etch spaces in a shallow carbon EBID deposit, resulting in lines with a width of about 30 nm spaced approximately 60 nm apart. The lines were found to be uniform, homogeneous and reproducible. By optimising the etching parameters, it would be possible to pattern still higher resolution lines although no attempts were made to do so in this work. Finally, by controlled modification of the sidewall angle by EBIE, high resolution EBID dense lines with vertical sidewalls should be possible. Such a demonstration would make FEBIP a more competitive technology for lithography applications.

6.11 Recommendations

One of the main challenges in modifying the sidewall slope in high resolution lines is the alignment of the etch pattern with the deposit. Positioning the etch pattern on the sidewall by eye introduces significant error in the process. This may be acceptable for large structures where continuous monitoring of the SE signal may be used to gauge the total exposure time while performing an etch. As the etch location itself is not unique and it is only the right combination of etch location and dose that is required, this method provides a technique to tune the sidewall angle to the vertical if the SE intensity is strong enough to monitor accurately, i.e., for thick deposits. For high resolution patterns, the height of the deposit is not sufficient to be able to measure changes in the SE signal during sidewall evolution. The use of an improved sample stage, free of drift over the time taken for EBID and EBIE combined, would help the process immensely. Even in doing so, another challenge arises. The carbon precursor used here was found to take a long time to be pumped out and this problem was made worse by the inclusion of water in the chamber. As a result, several hours of waiting time were introduced between deposition and etching. The requirement for the stage to be drift-free becomes unrealistic in the face of such a large patterning time. This may be overcome by the use of different precursors. Although a high sticking coefficient is needed for FEBIP itself, the problem of increased hydrocarbon diffusion due to the use of water may be circumvented by using oxygen instead of water, and perhaps a different carbon precursor as well.

Chapter 7

Conclusions

“ *There is a place to which I often go,
Not by planning to, but by a flow* ”

Nissim Ezekiel,

his thesis is a developmental effort in performing sub-20 nm lithography in the Scanning Electron Microscope using Focussed Electron Beam Induced Processing. The following conclusions can be drawn from this work:

1. Electron Beam Induced Deposition can be used for the controlled fabrication of dense lines at the sub-20 nm scale.
2. A patterning regime has been identified where the growth is governed by the electron current and is independent of the gas flux. Dense lines have been fabricated in this regime and different writing strategies such as serial and parallel patterning have been investigated. Lines were also patterned by a fixed dose delivered using different combinations of dwell time and number of passes. Identical homogeneous lines were obtained regardless of the writing strategy used, and diffusion-induced proximity effects were not observed. Single pass patterning of high resolution dense lines, which is desirable for large scale commercial applications of this technology, has been shown to be possible in this regime. At still higher resolutions, though, proximity effects could be significant and this needs to be experimentally investigated.
3. The necessity of metrology in high resolution EBID and the challenges in the development of techniques to measure line width and line edge roughness have been discussed. As a consequence of EBID line profiles being Gaussian with a low signal to noise ratio, the techniques commonly used in the characterisation of resist-based lines cannot

be applied directly. An edge detection technique has been developed especially for these profiles and the first measurement of LW and LER of dense lines in the field of EBID has been presented for sub-20 nm lines patterned with doses in the range of a few 1000 C/m². For high resolution patterning in general, and for applications in lithography in particular, estimating the line width by eye is unacceptable. The error in such a measurement with respect to the 1σ value of LW measured by edge detection has been shown to be about 37%.

4. EBID lines are always broader than defined. A single pixel line patterned with a dose of 1000 C/m², for example, was found to be 23 nm wide (1σ value). A complete simulation taking into account electron scattering events as well as an evolving deposit shape would be needed to explain the extent of this broadening as a function of patterning parameters. It must be noted that these numbers do not represent the resolution limit in EBID patterning as using a lower patterning dose would result in higher resolution lines. This was not attempted here solely due to the images being noisy and impossible to characterise using the existing techniques.
5. The reproducibility of EBID in this regime has been studied by the patterning of arrays of sub-20 nm dense lines over several millimetres of a bulk silicon sample over a period of one year, and found to be very high. The maintenance of standard working conditions is sufficient to achieve reproducible patterning in the electron current limited regime: the line width is reproducible to within 1.2 nm. This is in spite of possible variations in the contamination level, gas load, temperature, diffusion rates, surface roughness and gradual GIS misalignment taking place over this range of time and space. These parameters, which are hard to measure, are in fact not a matter of concern if operating in standard working conditions. A checklist has been provided for verifying this and it is recommended to consult it before every patterning session.
6. The line edge roughness has been measured from the edge positions determined using the new edge detection technique. As the values are biased due to imaging noise, the power spectral density was measured from the set of edge positions for all lines in an image, and the noise level in that image determined. After subtracting this, unbiased values of LER as low as 1.4 nm were measured.

7. The effect of vibrations on LW and LER has been studied. A simulation was set up to pattern lines in multiple passes by pixel exposure, and it was shown that vibrations having an amplitude of a few nanometres are sufficient to cause distortions in the patterned line as well as in the power spectral density. It is suspected that this caused, at least in part, the experimentally observed differences in the width of lines patterned along x and y directions. If restricted to using such a (standard) SEM stage, it is recommended to measure the vibrations prior to the experiment to determine if there is a preferred orientation for patterning. The feasibility of the installation of a high stability stage should be studied as this could increase the potential of EBID for high resolution patterning by avoiding this directional dependence. In addition, it would make large area patterning and stitching of patterns possible.
8. An imaging technique has been developed that enables the metrology of high resolution EBID from SEM images, based on a systematic study of the influence of the choice of detector and the imaging parameters on the line width measured. SE and BSE imaging have been compared and the limitations of each detailed with regard to the extraction of quantitative information on edge position and line width.
9. In EBID, an increase in height or width can result in a change in the line profile as well. This has been demonstrated using SE images and is thought to result from the sensitivity of SE emission to deposit topography. For thick lines having a Gaussian profile, the line shape from BSE images was Gaussian, whereas that from SE images was peaked at the edges. This is very different from the case of lines patterned in resist and presents a challenge in the use of SE imaging for EBID lines.
10. The values of line width measured from edge detection used in this work, while providing a method for comparison of lines, are not an absolute measure. For this reason, the 1σ values of LW determined by SE and BSE detection are found to be different. They are the result of different electron-matter interactions and in the absence of a knowledge of the relation between the measured LW (from the 2D image) and the physical shape of the (3D) deposit, there is no reason

to expect different detection techniques to yield the same value. The choice of the 1σ value, or for that matter, any value, is arbitrary.

11. A relation between experimentally measured line widths from SE and BSE images has been established and found to hold for EBID lines having different profiles, i.e. a range of width and thickness. The distance between the points of inflection in the integrated intensity profiles from simultaneously acquired SE and BSE images were found to be equal, providing a new measure of line width that can be even used to compare lines that do not have the same intensity profile. Gaussian lines patterned using an SEM simulator provide partial confirmation of this result, the limitation being a lack of knowledge of the fields present in the SEM due to which the imaging conditions used in the experiment could not be accurately simulated. A complete model taking into account electron scattering in materials, the fields and the detection scheme in the SEM, as well as the material properties of the deposit would facilitate an understanding of the physical basis for the relation between line width measured from SE and BSE images.
12. A technique has been developed for the fabrication of lines of desired width using EBID. The broadening of a pattern due to the interaction of the primary beam with the deposit and the substrate has been studied by the patterning of lines of a series of defined widths. A linear fit to this plot can be used to determine how wide a line must be patterned in order to obtain the desired width. This has been experimentally demonstrated for dense lines (spacing = 100 nm) and lines at a large separation (700 nm), using an electron dose of 1000 C/m². Lines of 25.7 nm, 27.3 nm, 32.1 nm, 42.7 nm and 53.4 nm width were patterned at 100 nm separation using defined line widths of 1 nm, 2 nm, 5 nm, 10 nm and 15 nm respectively. The next step, in order to achieve greater control as well as to fabricate smaller lines, would be the fabrication of lines at different electron doses. Lines of widths intermediate to the ones listed above should be patterned by using different combinations of electron dose, defined width and spacing. These plots could be used to determine the best patterning parameters needed for the fabrication of dense lines of desired dimensions.
13. Atomic Force Microscopy, a reliable measure of height, has also been

demonstrated to be a good measure of line width for the case of shallow EBID lines (with an estimated error of 4% for 2 nm thick lines and 15% for 10 nm thick lines), with the error in the measurement increasing with line height. It can therefore be used to measure the complete 3D profile of high resolution lines. The volume contained in an EBID line and the amount of material present in the "halo" have been estimated using AFM.

14. The presence of interconnects in dense EBID patterns has been verified using cross sectional profiles made using FIB. A technique to modify the line profile has been developed that can be implemented in the SEM, adding only one step to the fabrication process and not requiring any sample preparation. Electron Beam Induced Etching of the tails of carbon EBID lines patterned with a hydrocarbon precursor ($C_{12}H_{26}$), performed using water ($MgSO_4 \cdot 7H_2O$), was shown by both SEM imaging and AFM to be successful in removing the interconnecting material at high resolution, with the possibility of minimising the damage to the lines by the use of an appropriate exposure strategy. Lines with a width of about 40 nm and centre to centre spacing of 150 nm were successfully separated using an EBIE electron dose of a few mC/m^2 . As the use of water was found to require long pumping times in between etching and subsequent patterning sessions, it is recommended to investigate other etch precursors, such as O_2 .
15. An analytical model has been developed to study the possibility of achieving the desired vertical sidewalls for lithography, using EBIE. It is based on etching initiated by the combined presence of SE1's, which have a Gaussian profile similar to that of the primary beam, and water molecules. A typical EBID deposit with outward sloping (negative) Gaussian sidewalls was simulated on a substrate which was not etch-sensitive. It was shown that "etching from the top", i.e., due to SE's generated in the deposit alone, while successful in making the slope less negative, could never result in vertical sidewalls. Taking into account "etching from below" due to SE1's generated in the substrate, however, makes it possible to achieve several profiles including a positive slope and vertical sidewalls.
16. Sidewall angle tuning in FEBIP has been demonstrated by the combination of EBID and EBIE. Positive and negative slopes have been

obtained by varying the dose and position of etching. Vertical sidewalls, much desired for lithography, have been fabricated using this technique for isolated structures and structures in proximity. The high resolution of EBID and EBIE have been demonstrated independently by the fabrication of sub-20 nm dense lines using each of the two techniques. The next step would be the combination of the two, i.e., the fabrication of dense EBID lines with vertical sidewalls by controlled high resolution EBIE on the sidewalls. This experiment is quite challenging as the right combination of etch position and dose is needed to create the desired sidewall angle, which must somehow be determined in situ. While monitoring the SE signal has been shown to be effective in tuning the sidewall angle for larger structures, this is not sufficiently sensitive at the sub-20 nm scale, and another method needs to be devised.

Summary

Focused Electron Beam Induced Processing is a high resolution direct-write nanopatterning technique. Its ability to fabricate sub-10 nm structures together with its versatility and ease of use, in that it is resist-free and implementable inside a Scanning Electron Microscope, make it attractive for a variety of applications in nanofabrication. FEBIP comprises two complementary techniques: Electron Beam Induced Deposition and Electron Beam Induced Etching. In EBID (EBIE), the electron beam is scanned in the presence of a precursor gas that has been let into the chamber of the SEM. The precursor molecules adsorbed onto the sample surface are dissociated by the electron beam, as well as by secondary and backscattered electrons that are generated at the surface by the interaction of the electron beam with the sample. The non-volatile dissociation product forms a deposit (etch) on the surface, while the volatile products are pumped out. A pattern can thus be deposited (etched) by merely scanning the beam in the presence of the precursor. As the secondary electrons are lower in energy (< 50 eV), they contribute more significantly to the dissociation than the higher energy backscattered or primary electrons. At the outset therefore, the resolution in EBID is limited by the emission radius of the secondary electrons, which can be as low as a few nanometres. The fabrication of lines as little as 3 nm wide on bulk silicon attests to the high resolution patterning capability of EBID, which in turn makes it potentially attractive for lithography. The development of a laboratory nanofabrication technique into a viable alternative for lithography, however, requires several criteria to be met.

In this thesis, we investigate the possibility of using EBID to perform high resolution (sub-20 nm) lithography. State-of-the-art lithography techniques like EUV and EBL have come a long way in terms of control and reliability. So we began by studying the aspects of EBID that appear necessary for reliable and controlled patterning. In EBID literature, with the exception of the patterning energy and current used, there is usually little mention of the parameter space involved in an experiment. This comprises current, gas flux, chamber pressure, contamination level, surface diffusion, etc. and can broadly be divided into beam-related and gas-related

parameters. As a standard EBID system consists simply of an SEM fitted with a gas injection nozzle, gas-related parameters such as local gas flux and precursor diffusion are hard to measure. Patterning was therefore carried out in the electron current limited regime, using a low current (100 pA or lower). As the growth in this regime is known to be independent of the local gas flux and governed by the electron current alone, a higher degree of control as well as reproducibility could be expected. Indeed, broadening due to diffusion-induced proximity effects was shown to be absent, resulting in uniform dense lines of sub-20 nm width.

A large part of this thesis is devoted to the development of methods for the metrology of EBID lines, which is challenging for a few reasons. Unlike resist-based lines which have vertical sidewalls, EBID lines typically have a Gaussian profile with sloping sidewalls and long tails. This introduces uncertainty in determining the extent of the lines by SEM imaging and in the measurement of line width. Moreover, the profile of EBID lines, as measured by the commonly used SE imaging, is not fixed but evolves with dose. This makes it hard to develop a consistent characterisation technique and unsurprisingly, there exist no such methods in literature. An edge detection technique has been developed for the measurement of the width of EBID lines. SE and BSE imaging, as well as the choice of imaging parameters have been investigated in detail. The edge detection technique has been implemented on both types of images, on lines having a range of widths and subsequently, different profiles. BSE imaging has been determined to be better suited for quantitative characterisation as it is less susceptible to imaging artefacts such as enhanced SE emission from a slope. For very shallow lines giving rise to a BSE image that is so noisy that edge detection cannot be implemented, SE imaging must be used. While this result provides a quantitative measure of line width, the issue of evolving line profiles still needed to be addressed. Upon comparison of simultaneously acquired SE and BSE images, the points of inflection in the integrated line profiles from the two were found to be the same. This formed the basis of another technique that could provide a link between the line widths measured from SE and BSE images, enabling its use over a range of widths and profiles. An important measure of the quality of high resolution dense lines is the line edge roughness (LER). This has been determined for EBID lines using the edge detection technique and the values for roughness found were as low as 1.4 nm.

Subsequently, the reproducibility of high resolution EBID was measured at an interval of 1 year, by patterning several series of dense lines over an area 1 mm^2 each time. The variations in line width over lines patterned with identical parameters were found to be less than 1.2 nm. The technique is therefore highly reproducible, which is a very promising result because it means that the maintenance of standard working conditions is sufficient to ensure reproducibility. This avoids the extra effort and cost that would be incurred if the monitoring or control of additional parameters was needed. Further, it is only due to the reproducibility being high that "typical" measurements reported from any given experiment conducted in this regime are in fact reliable.

With this result, we proceeded to the controlled fabrication of lines where the broadening due to generation of SE's and BSE's plays a significant role. This was quantified by studying the resultant line width as a function of defined width for lines patterned at a fixed dose. For an EBID dose of 10000 C/m^2 , a single pixel wide line was found to become 23 nm wide. From this experiment, a recipe has been determined for patterning lines of a desired width and spacing. The study can be extended by using different patterning doses to make a more precise selection of width possible.

The issue of carbonaceous interconnecting material present in between dense EBID lines has been addressed by developing two recipes for cleaning using Electron Beam Induced Etching with water. The removal of material has been demonstrated using AFM measurements and in-situ monitoring of the process using SE imaging has been shown to be successful in determining the electron dose required for cleaning.

Finally, tuning of the 3D shape of EBID patterns has been demonstrated by the application of EBIE on the sloping sidewalls of an as-deposited structure. TEM images of an experiment to follow the sidewall evolution as a function of etch position clearly demonstrate the successful creation of vertical sidewalls. An analytical model based on physical principles has been developed and the results match well with the experimental observations. An important conclusion that arises from the simulations is that underetching due to electrons emitted from the substrate is critical in achieving vertical sidewalls.

Samenvatting

efocusseerde elektronenbundel geïnduceerde processing is een hoge resolutie en directe nano patroonvormings techniek. De mogelijkheid om sub 10 nm structuren te fabriceren in combinatie met haar veelzijdigheid en gebruikersgemak, er zijn namelijk geen resistlagen vereist en het kan geïmplementeerd worden in een raster scannende elektronmicroscop (SEM), wat het aantrekkelijk maakt voor een variëteit aan toepassingen in nanofabricage. FEBIP bestaat uit twee complementaire technieken: Elektronenbundel-geïnduceerde depositie en elektronenbundel geïnduceerd etsen. In EBID (EBIE) wordt de elektronenbundel gescand in de aanwezigheid van een voorlopergas dat in de vacuümkamer van de SEM ingebracht is. De geabsorbeerde voorlopermoleculen op het monsteroppervlakte zijn gedissocieerd door de elektronenbundel, en door de secundaire en door terug verstrooide elektronen die gegenereerd zijn op het oppervlak door de interactie van de elektronenbundel met het proefstuk. De niet volatiele gedissocieerde producten vormen een depositie (ets) op het oppervlak, terwijl de volatiele componenten weggepompt worden. Een patroon kan dus gedeponneerd (geëtsd) worden enkel door het scannen van de elektronenbundel in de aanwezigheid van voorlopergas. Aangezien de secundaire elektronen lager zijn in energie (≈ 50 eV), dragen zij significant meer bij aan de dissociatie dan de hoog energetische terug verstrooide en primaire elektronen. De resolutie van EBID is daarom gelimiteerd door de emissieradius van de secundaire elektronen, die beperkt kan zijn tot slechts een paar nanometer. De fabricage van lijnen van slechts 3 nm breed op bulk silicium bevestigt de hoge resolutie patroonvormings mogelijkheden van EBID, wat het aantrekkelijk maakt voor lithografie. De ontwikkeling van een laboratorium nanofabricatie techniek als een geschikt alternatief voor lithografie vereist echter dat aan een aantal criteria wordt voldaan.

In dit proefschrift onderzoeken we de mogelijkheid om EBID te gebruiken voor hoge resolutie (sub-20 nm) lithografie. De nieuwste lithografietechnieken zoals EUV en EBL zijn ver gekomen in termen van controle en betrouwbaarheid. Om die reden zijn we begonnen met het onderzoeken van de aspecten van EBID die noodzakelijk zijn voor een betrouwbare en controleerbare patroonvorming. In EBID literatuur, met uitzondering van

de versnellingspanning en stroom, word er weinig vermeld over de parameter ruimte betrokken in een experiment. Deze bevat stroom, gasstroom, kamerdruk, contaminatieniveau, oppervlakte diffusie, etc. en kan worden opgedeeld in elektronenbundel gerelateerde en gas gerelateerde parameters. Aangezien een standaard EBID systeem simpelweg bestaat uit een SEM uitgerust met een gas injectie spuitmond, zijn gas gerelateerde parameters zoals de lokale gasflux en voorlopergas diffusie lastig te meten. Patroonvorming is daarom uitgevoerd in een elektronenstroom gelimiteerd regime, door gebruik te maken van een lage stroom (100 pA of lager). Omdat de groei in dit regime onafhankelijk is van de lokale gasflux en alleen bepaald wordt door de elektronenstroom kan een hogere mate van controle en herhaalbaarheid verwacht worden. Inderdaad, is aangetoond dat verbreding door diffusie geïnduceerde nabijheidseffecten afwezig is, resulterend in dichtbij gelegen lijnen van sub-20 nm breedte.

Een groot deel van dit proefschrift is toegewijd aan de ontwikkeling van methodes voor de metrologie van EBID lijnen, wat uitdagend is voor een aantal redenen. In tegenstelling tot resist gebaseerde lijnen die verticale zijwanden hebben, hebben EBID lijnen typisch een gaussisch profiel met hellende wanden en een lang uiteinde. Dit introduceert een onzekerheid in het bepalen van de omvang van de lijnen door middel van SEM afbeeldingen en in het meten van de lijnbreedte. Bovendien, het profiel van de EBID lijnen zoals gemeten bij veel gebruikte SE afbeeldingen, ligt niet vast maar evolueert met de dosis. Dit maakt het lastig om een consistente karakterisatie techniek te ontwikkelen en, niet verbazingwekkend, zo'n methode bestaat niet in de literatuur. Een randdetectie methode is ontwikkeld voor de meting van de lijnbreedte van EBID lijnen. SE en BSE afbeeldingstechnieken, evenals de keuze van afbeeldingsparameters zijn in detail bestudeerd. De randdetectie techniek is geïmplementeerd op beide type afbeeldingen, op lijnen die een reeks breedtes hebben en daarmee vervolgens verschillende profielen hebben. BSE afbeeldingen blijken beter geschikt voor kwantitatieve karakterisatie aangezien het minder gevoelig is voor afbeeldingsartefacten zoals versterkte SE emissie van een helling. Voor heel ondiepe lijnen die een BSE afbeelding opleveren met veel ruis zodat geen randdetectie toegepast kan worden zijn SE afbeeldingen vereist. Terwijl de methode kwantitatieve metingen oplevert van de lijnbreedte moet de kwestie van evoluerende lijnprofielen nog steeds worden geadresseerd. Bij vergelijking van de simultaan verkregen SE en BSE afbeeldingen, bli-

jken de buigpunten van de geïntegreerde lijn profielen hetzelfde te zijn. Dit vormt de basis van een andere techniek dat een verband zou kunnen opleveren tussen de lijnbreedte gemeten met SE en BSE afbeeldingen, wat het mogelijk maakt om het te gebruiken over een reeks van lijnbreedtes en profielen. Een belangrijke maatstaf van de kwaliteit van hoge resolutie lijnen met hoge dichtheid is de lijnrandruwheid (LER). Deze is bepaald voor EBID lijnen door het gebruik van de randdetectie techniek en waarden voor de gevonden ruwheid zijn slechts 1.4 nm.

Vervolgens is de reproduceerbaarheid van hoge resolutie EBID lijnen gemeten over een interval van 1 jaar, bij het patroonvormen van verschillende series van lijnen met hoge dichtheid wat iedere keer gedaan is over een oppervlak van 1 mm². De variaties in lijnbreedte over lijnen gemaakt met identieke parameters zijn minder dan 1.2 nm. De techniek is om die reden in hoge mate reproduceerbaar, wat een veelbelovend resultaat is omdat het betekent dat het behoud van standaard werkmethodes voldoende is om reproduceerbaarheid te garanderen. Dit vermijdt de extra moeite en kosten die nodig zouden zijn als het monitoren en controleren van andere procesparameter nodig zou zijn. Daarnaast is het alleen vanwege de hoge reproduceerbaarheid dat “typische” metingen gerapporteerd van elk gegeven experiment uitgevoerd in dit regime betrouwbaar.

Met dit resultaat, zijn we doorgeshaan naar het gecontroleerd fabriceren van lijnen waar de verbreding vanwege SE en BSE generatie een significante rol speelt. Dit is gekwantificeerd door het bestuderen van de resulterende lijnbreedte als functie van de gedefinieerde breedte voor lijnen gemaakt bij een constante dosis. Voor een EBID dosis van 10000 C/m², een lijn van een pixel breed resulteerde in een 23 nm lijnbreedte. Vanuit dit experiment is een recept ontwikkeld voor de patroonvorming van lijnen met gewenste breedte en tussenruimte. De studie kan verlengd worden door het gebruik van verschillende dosis om een meer precieze selectie van lijnbreedte mogelijk te maken.

De kwestie van koolstofhoudend materiaal tussen de EBID lijnen is aangepakt door het ontwikkelen van twee reinigingsrecepten door het gebruik van Elektron Bundel Geïnduceerde Etsen met water. De verwijdering van materiaal is gedemonstreerd met AFM metingen en het in-situ monitoren van het proces door gebruik van SE afbeeldingen is succesvol in het bepalen

van de elektronen dosis benodigd voor het reinigen.

Tot slot, het afstemmen van de 3D vorm van EBID structuren is gedemonstreerd door het toepassen van EBIE op de hellende zijwanden van de al gedeponeerde structuur. TEM afbeeldingen van een experiment om de zijwand evolutie als functie van de ets positie te volgen laat de succesvolle creatie van verticale zijwanden duidelijk zien. Een analytisch model gebaseerd op fysische principes is ontwikkeld en de resultaten komen overeen met de experimentele observaties. Een belangrijke conclusie dat volgt uit de simulaties is dat onderetsen door elektronen geëmitteerd van het substraat kritisch is voor het creëren van de verticale zijwanden.

Appendix A

Fabrication of calibration standards for super-resolution microscopy

“ *Double, double toil and trouble;
Fire burn and cauldron bubble.*

”
Shakespeare,

ocused Electron Beam Induced Processing is a reproducible, well-controlled high resolution technique for nanofabrication, with dense lines and spaces as well as complex patterns shown to be possible. The ability to pattern practically any shape makes it an attractive technique for the fabrication of calibration standards for microscopy. High resolution optical microscopy [92] is a growing area with applications in cell biology, neuroscience, medicine and materials science, to name just a few. While the resolution in conventional optical techniques is limited by diffraction, superresolution techniques such as Structured Illumination Microscopy (SIM)[93], Photoactivated Localization Microscopy (PALM) [94] [95], Stimulated Emission Depletion Microscopy (STED)[96], Stochastic Optical Reconstruction Microscopy (STORM) [97] have been developed which can overcome the diffraction barrier and allow very high resolution imaging. These techniques require, in general, some kind of image reconstruction implemented using specifically developed complex algorithms. SIM is one such technique widely used for imaging biological specimens. It works on the principle of grid illumination together with rotation, following which a reconstruction algorithm is used to make an image, which has a theoretical resolution of $\lambda/4$ where λ is the wavelength of the incident light. However, the reconstruction can result in artifacts, which are hard to differentiate from the features of interest themselves,

owing to the structural complexity of biological samples. This can be subject of intense debate in biology ([98][99][100]), with the application of different algorithms potentially leading to different interpretations of the same image. This work proposes a technique to fabricate high resolution fluorescent samples of known size and shape by EBID, that can effectively test the performance of these algorithms prior to their application on complex features. Such calibration samples can also be used for comparing SIM systems provided by different manufacturers, offering a quantitative method to test the system performance and make an informed choice.

The performance of optical superresolution microscopes is commonly tested using fluorescent beads. By imaging beads of diameter much smaller than the optical wavelength, therefore ensuring that they can be treated as point sources, the point spread function of the system can be determined and used for the deconvolution of images. The measurement of resolution, however, requires the imaging of two light sources at a known distance from each other, which clearly cannot be fulfilled by this method. Imaging two beads would still not provide this information, unless the distance between them were known a priori. Bearing in mind that this must be in the range of 120 nm (resolution in SIM) or lower (for STED, PALM, STORM) and measured independently by a sufficiently high resolution technique, it becomes evident that the fabrication of such a calibration standard is very challenging. The only existing standard, to our knowledge, is manufactured by GATTAQuant, Germany. At the heart of this technique is the concept of DNA origami: DNA strands folded in a desired configuration, to which fluorescent dye molecules can be attached. This is an elaborate technique resulting in the well-controlled fabrication of strands of known length as measured between the fluorophores. "Nanorulers" fabricated in this manner are currently available in lengths of 120 nm, 140 nm and 160 nm. The main advantage of this method is that the distance between the dye molecules is known with high accuracy because the attachment is localised to specific positions on the DNA structure. Consequently, these rulers provide a very reliable measurement technique. The limitation is of course that only lines of certain lengths are produced. An accurate measurement of SIM resolution requires a system where fluorophores are separated by a range of distances, which would add complexity to this recipe. Due to the method of grid illumination used in SIM, it is also of interest to determine the resolution as a function of the orientation angle in the sample plane,



Figure A.1: Superresolution image of Gatta SIM-120B Nanoruler showing randomly oriented folded DNA origami structures tagged with pairs of fluorescent dye molecules (Alexa Fluor 488) at a distance of 120 nm. Image taken from www.gattaquant.com

for which controlled patterning of lines at different orientations and/or fabrication of two-dimensional patterns is needed. Here we present a versatile technique to fabricate high resolution calibration standards (test samples) that meet these requirements. Such a test sample should satisfy the following conditions:

1. Be transparent for use in light microscopy
2. Contain fluorescent line patterns, e.g., lines, of a range of lengths, widths, shapes, spacing, and orientations
3. Be reusable
4. Its dimensions should be determined independently by another method with higher resolution than that of SIM.

The following section presents a technique to fabricate such a standard using FEBIP.

A.1 Experimental details

A recipe for selective patterning of fluorescent nanostructures by FEBIP has been reported by Schlapak et al. ([101]) and was used as a starting

point to fabricate fluorescent patterns in this work. The materials used in this research were:

1. 3-[Methoxy(polyethyleneoxy)propyl]trimethoxysilane (or PEG silane), 90%, 6-9 PE-units (CAS 65994-07-2) from abcr GmbH, Germany
2. Anhydrous toluene, 99.8% (CAS 108-88-3) from Sigma Aldrich Co., The Netherlands
3. triethylamine, 99.5% (CAS 121-44-8) from Sigma Aldrich Co., The Netherlands
4. A 100 nM solution of 2 g/L Rabbit anti-Mouse IgG (H+L) Cross-Adsorbed Secondary Antibody tagged with Alexa Fluor 488 (or IgG-Alexa 488) from Life Technologies BV, The Netherlands, was prepared in 1X TE buffer.
5. Deionised water
6. A Thorlabs FELH0500 emission filter and a Semrock dichroic mirror (395/495/610 nm BrightLine triple-edge dichroic beamsplitter) were used for imaging.

The technique described in [101] was used by them to fabricate square patterns as small as 100 nm on an ITO surface coated with a layer of PEG-silane. Upon incubation in a solution of IgG-Cy3, an antibody tagged with a dye molecule, the patterned areas were found to selectively fluoresce. They attributed this to Electron Beam Induced Deposition (EBID) of carbon on the PEG-silane surface, which is known to be an anti-fouling material. Upon electron beam exposure, however, antibody molecules were found to selectively attach to the patterns. A higher electron dose was found to result in increased fluorescence, which is explained as resulting from enhanced binding along the height of the deposited structure. The recipe was modified to use a rabbit-anti mouse immunoglobulin antibody (IgG) tagged with Alexa 488 dye due to the availability of appropriate filters for fluorescence imaging. The sample preparation technique is described briefly here, with particular emphasis on additional precautions taken and modifications made to the original recipe.

1. The ITO/glass slides were cleaned by sonicating in acetone, followed by ethanol for 20 minutes each. They were then rinsed in deionised water and dried by wiping with lint free tissues.

2. The ITO surface was exposed to an oxygen plasma at 200 Watt for 15 minutes in order to activate the surface.
3. Meanwhile, 200 mL of a 20 mM solution of PEG silane was prepared by dissolving 2.36 g of PEG silane in 190 mL of toluene with 5% (10 mL) triethylamine as a catalyst.
4. Immediately after the plasma cleaning, the slides were immersed in the PEG-silane solution and then incubated for 18 hours at 60° Celcius to form a uniform PEG-silane monolayer on the ITO surface.
5. This was followed by a washing step to remove unbound PEG-silane. The slides were sonicated in toluene and then in acetone for 20 minutes each, rinsed in deionised water and dried as before. They were then stored in dust-free boxes sealed with parafilm, taking care to ensure that the PEG layer did not make contact with any surface, including the box itself.
6. Next, the slides were mounted in the SEM and the patterning procedure was begun when the chamber pressure had reached approximately 1×10^{-5} mbar.
7. First, the approximate centre position was located by noting down the positions of the edges. This was done to ensure that the patterns would be at a safe location, minimising the chances of damage due to handling of the sample with tweezers.
8. After navigating to the centre position, it was necessary to find some features there on which to focus the beam. This was quite challenging as the formation of a clean and uniform PEG silane layer meant that such features were scarce. Nevertheless, a few small dust particles could always be located and they served as markers for focussing.
9. Patterning was carried out using a home built Labview script which positioned the beam onto co-ordinates defined by the user in a script file. Patterning was carried out "blindly", ie, the field of view was not inspected prior to patterning as the surface there would then receive an extra electron dose.
10. Large markers (about 200 μm) in size were first patterned in HR mode, next to which the arrays of high resolution patterns were made. This was found to be very useful when trying to locate the patterns in

the fluorescence microscope or if they were to be imaged later in the SEM. Arrays consisting of several repetitions of each pattern were made, in case some of them turned out to be situated on top of dust particles or surface non-uniformities. This could not be ascertained prior to patterning due to the "blind" exposure strategy and would only become obvious at the very end, during the fluorescence imaging.

11. After patterning, the sample was removed from the SEM and tagging of the patterns with an antibody bound to a fluorophore was performed. A 100 nM solution was prepared by dissolving 375 μL IgG-Alexa 488 in 50 mL of 1X TE buffer and pipetted out onto the sample drop by drop to cover the surface entirely. The sample was left to incubate for 45 minutes, in which time it was shielded from ambient light by covering with aluminium foil.
12. Next, it was washed in TE buffer and rinsed with deionised water to remove non-specifically bound antibody molecules. It was allowed to dry as before, stored in a box and kept covered to prevent photobleaching of the dye molecules.
13. A quick inspection was performed in the Nikon Eclipse fluorescence microscope with a 40X dry (air) objective to locate the markers (The high resolution patterns could, of course, not be distinguished).

A.1.1 Control experiment

Before the selective binding process was initiated, two control experiments were performed to check the uniformity of the (background) fluorescence from the substrate. The ITO/glass slide coated with a PEG layer was found to be uniformly fluorescent, except at the edges. The sample was then tagged with IgG-Alexa 488 as described previously, and imaged. Once again, uniform fluorescence was observed.

A.1.2 Patterning and biofunctionalisation

The patterning was carried out at 5 keV and 25 pA in an FEI Nova Nano 650 Dual Beam system. Care was taken to minimise vibrations (typically < 5 nm) and a fast beam blanker was used to prevent spurious patterning while translating the beam. Square and line patterns of a range of sizes were fabricated and were found to have sufficient contrast to be imaged

in the SEM using the In-lens secondary electron detector. As seen in Fig. A.2, an SE image of a pattern consisting of a square and a line patterned with a dose of 10 C/m^2 , the exposed patterns were found to be darker than the background. As a first step towards creating a commercially

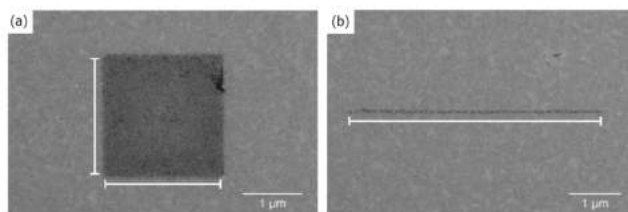


Figure A.2: SEM image of electron beam-exposed area showing the pattern that was used to check repeatability of the technique

viable technique, the reproducibility of the method was investigated. It was found by repeated patterning of this set, followed by incubation in the IgG-Alexa 488 solution, that the binding was often unsuccessful although the procedure followed was identical. This occurred in spite of using freshly prepared solutions of IgG-Alexa in TE buffer, storing the chemicals in sealed bottles and performing longer cleaning of the bare ITO slides to remove any contamination that might prevent the formation of a uniform PEG layer. Since EBID from hydrocarbons is likely to play a role in the patterning, care was also taken to maintain similar base vacuum levels (5×10^{-6} to 1×10^{-5} mbar) in the SEM. The failure of these steps to solve the problem indicated that it was not due to the electron beam exposure but more likely due to an inhomogeneous PEG layer. The possible role of the ITO substrate in the quality of the PEG layer formed is therefore relevant. Due to the wide use of Self Assembled Monolayers (SAM's) in research, there is a vast amount of literature available, and although to our knowledge no study addresses the combination of materials used here, a study by Chockalingam et al. ([102]) was found very relevant. An octadecylphosphonic acid (ODPA) SAM was grown on an ITO substrate and the relation between the homogeneity of the layer and the grain size of ITO was investigated. The results should also be applicable for the case of PEG-silane SAM's as they are both mostly made up of long carbohydrate chains. Using samples from different manufacturers, the amorphousness, grain structure and hydroxide content of the SAM's were examined and the quality of the monolayers was graded by their packing density and

stability. The study showed that the highest quality monolayers were formed on smooth amorphous ITO substrates having homogeneous grains and a high hydroxide content. Polycrystalline ITO surfaces resulted in lower quality SAM's with defects observed to occur at the grain boundaries. The more the defects, the higher the surface roughness. The quality of the monolayer formed was therefore shown to be strongly influenced by the characteristics of the underlying ITO. No information about the production technique of the ITO slides used in our experiment could be found and therefore three kinds of substrates were tested for use:

1. ITO-1: A glass slide with a 17 nm thick ITO layer (SPI supplies # 06494-AB: ITO coated cover slips, size: 22X40 mm, thickness # 1:0.13-0.17 mm, resistivity: 70-100 ohms/square, nominal transmittance: 88%)
2. ITO-2: A glass slide with a 17 nm thick ITO layer (Optics Balzers cover glass 22X22X0.17 mm with ITO, OBL P/N 208965)
3. ITO-3: ITO-2 coated with \approx 10 nm thick silicon oxide layer deposited by sputtering

ITO-1 and ITO-2 were commercially available options, the exact difference between which could not be ascertained, and ITO-3 was designed in this manner because based on the results of [102] the amorphous SiO₂ resulting from deposition by sputtering would be expected to lead to better PEG quality. The layer was kept very thin to prevent charging of the sample, although the value of 10 nm was chosen arbitrarily. Patterning on ITO-2 and ITO-3 showed highly reproducible results both over a large area of the sample as well as over different samples. ITO-2 was therefore selected for all subsequent experiments and ITO-3, while found satisfactory, was not used due to the additional manufacturing step.

A.1.3 Influence of electron dose on resolution

An experiment was performed to study the dimensions of the biofunctionalised structures as a function of dose. A series of lines/squares/dots was tagged with IgG-Alexa 488 after patterning with 5 keV and 25 pA. The dose was varied from 50 C/m² to 500 C/m² in steps of 50 C/m², by increasing the number of passes, using a fixed dwell time of 52.4 μ s. Based on the

results of [101], a straightforward increase in fluorescence intensity was expected. The results were, however, quite surprising. Fig. A.3(a) shows the image of two arrays of squares (indicated by the yellow rectangles and labelled Row 1 and Row 2) acquired using the Nikon Eclipse fluorescence microscope with a 100X oil immersion objective. They were patterned with increasing electron dose in the direction indicated by the arrow, i.e., Row 1 was patterned with doses 50 C/m^2 to 250 C/m^2 (left to right), and Row 2 with doses 300 C/m^2 to 500 C/m^2 (left to right). For low doses (50 C/m^2 , 100 C/m^2) the fluorescence appears homogeneous over the entire square, becoming more intense with dose. However, there comes a turning point (150 C/m^2) when the intensity in the centre of the square drops, appearing dark, and the edges begin to appear fluorescent. This is verified by taking integrated line scans for each row along the length of the yellow rectangles, and the corresponding plots shown in Fig. A.3(b) and (c), for Row 1 and Row 2 respectively, confirm this observation.

This result cannot be explained by the mechanism proposed in [101] involving a carbon EBID deposit that grows in height with electron dose, leading to increased binding at the sidewalls. Firstly, although the article states that the chamber hydrocarbons are the precursors for the deposition of carbon by EBID, it is also possible that the PEG-silane molecules are dissociated in the process, leading to carbon deposition. Secondly, the claim of increase in deposit height with dose is based on AFM measurements of contamination grown on a silicon substrate coated with PEG-silane which do in fact show an increase from 1 nm to 4 nm. But in the absence of a model describing the process, it is not clear whether this increase in height alone could be concluded as being responsible for the increased fluorescence. The EBID growth rate on silicon could also be different from that on ITO. It is also not described if the increase in height continues beyond 4 nm if the dose is increased further. One would expect that in a clean chamber, the contamination growth would stop increasing in height after a certain dose. It is unclear whether this was tested or how the binding was affected if the height did in fact reach a maximum.

A complete explanation must take into account electron beam induced modification of the PEG layer. This has been studied in detail by [103] and one of the main findings is that the manner of modification of PEG depends on the electron dose used. It is highly likely, therefore, that during

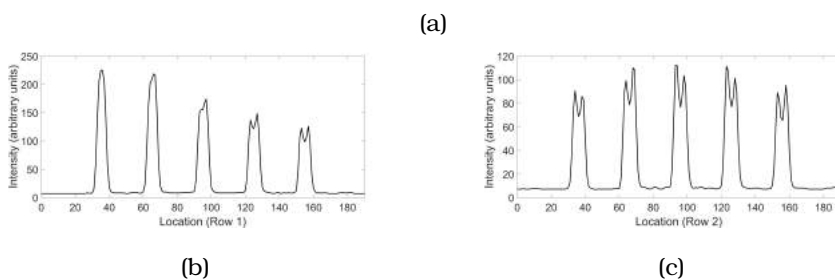
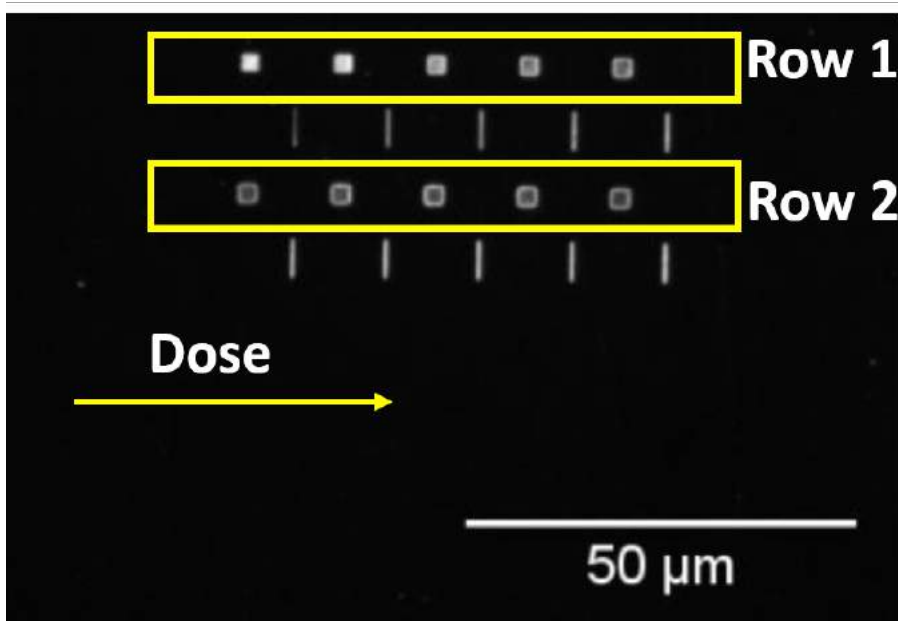


Figure A.3: Square patterns imaged in the Nikon Eclipse fluorescence microscope using a 100X oil immersion objective. (a) Two arrays of squares (Row 1 and Row 2) indicated by the yellow rectangles patterned with increasing dose as indicated by the arrow. The dose range used in Row 1 was 50 C/m² to 250 C/m² and in Row 2 was 300 C/m² to 500 C/m². Low doses (50 C/m², 100 C/m²) show uniformly fluorescent squares, but an increase in dose results in the fluorescence shifting to the edges of the square instead and the centre darkening. (b) Integrated intensity plot along Row 1 and (c) along Row 2, confirming the observation.

the experiment imaged in Fig. A.3, one or more transitions between dose ranges took place. A very simple explanation can be provided by dividing the electron dose into three regimes as follows:

Regime 1: Low dose (< 120 electrons/nm²)

The exposed area of PEG is modified by the total number of PE's and SE's.

The total dose is such that the PEG molecules there have been modified in a manner suitable for antibody binding. This results in a uniformly fluorescent square.

Regime 2: Intermediate dose (120 to 600 electrons/nm²)

The modification by electrons is such that the exposed area is further modified, increasing the probability of antibody attachment. This results in a square with higher fluorescence intensity. A literature review of PEG modification under electron beam exposure is not conclusive as to the mechanism responsible for the observed trend in antibody attachment. In general, low electron doses are known to cause cross-linking of adjacent polymer molecules, which appears to result in increased binding. It is therefore also perceivable that increasing the dose beyond a certain maximum value could cause damage to PEG, preventing molecules from attaching. This is in fact observed in Regime 3.

Regime 3: High dose (> 600 electrons/nm²)

The electron dose in the exposed region is now so high that the PEG is severely modified and binding is no longer possible. The intensity from the centre of the square therefore drops. The region just surrounding the patterned pixels has not been exposed to the high dose of PE's but only to the SE's generated there during patterning. This region is therefore modified suitably for antibody binding and fluorescence from the edges is observed, going up with dose as in Regime 2.

The dose ranges provided here refer to the dose of PE's only, and the use of different patterning parameters could change the values at which the trend is observed to change. Further, the values are approximate and variations were observed between samples. These values are merely to give a rough idea of the doses involved in this experiment. It should also be noted here that the lines visible alongside have not been included in this analysis as they were patterned with a different range of doses and are not relevant for this study.

An important conclusion of this study is that the choice of dose can be significant in obtaining patterns of not only the desired size, but also the desired intensity distribution over the pattern. For the fabrication of high

resolution, uniformly fluorescent structures, low doses ($< 100 \text{ C/m}^2$) must be used.

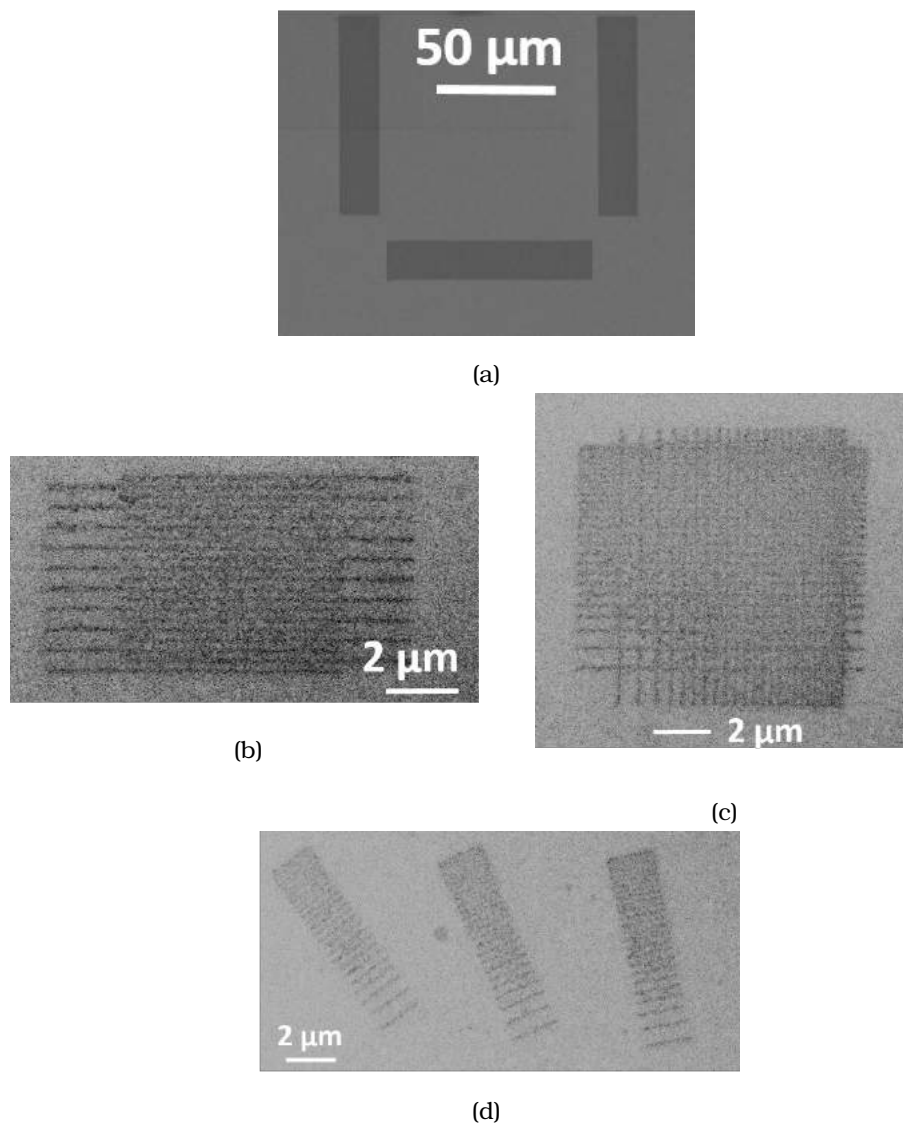


Figure A.4: SEM images of some example patterns fabricated to test the performance of a given SIM: (a) uniformly fluorescent structure/marker extending over a large area (b) array of interleaved dense lines with increasing line spacing (c) 2D checkerboard array with increasing line spacing in x and y (d) array of dense lines with increasing line spacing patterned at arbitrary rotation angles

A.2 Fabrication of high resolution dense fluorescent patterns

A range of patterns has been fabricated in the SEM to test the performance of a given Structured Illumination microscope: uniformly fluorescent structures/markers extending over a large area (Fig. A.4(a)) as well as high resolution patterns like interleaved dense lines with increasing line spacing (Fig. A.4(b)), 2D checkerboard arrays with increasing line spacing in x and y (Fig. A.4(c)), and arrays of dense lines with increasing line spacing patterned at arbitrary rotation angles (Fig. A.4(d)). A schematic of the layout of the test slide is shown in Fig. A.5. It comprises two large markers (Marker 1 and Marker 2) shown in Fig. A.5 (a) and (b) respectively, next to which several repetitions of the high resolution structures imaged in Fig. A.4 are patterned, comprising Blocks A, B and C. The test structures were defined to be:

1. Marker 1 and Marker 2: HR mode, Pitch = 200 nm, Dose = 1.4 C/m²

2. Block A: Interleaved dense lines with increasing line spacing

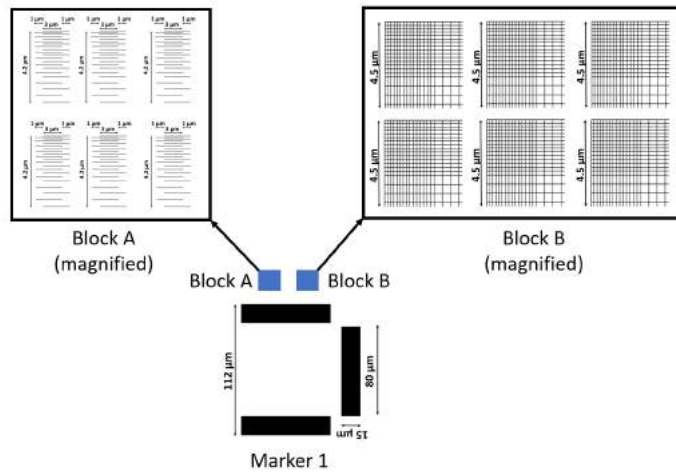
UHR mode, Line width = 50 nm, Line length = 4 μm, Line spacing = 80 nm to 200 nm in steps of 6 nm, Pitch = 2 nm, Dwell time = 100 ns, Number of passes = 4, Dose = 5 C/m². The pattern is so defined that the spacing at the ends of the lines is larger than in the middle.

3. Block B:

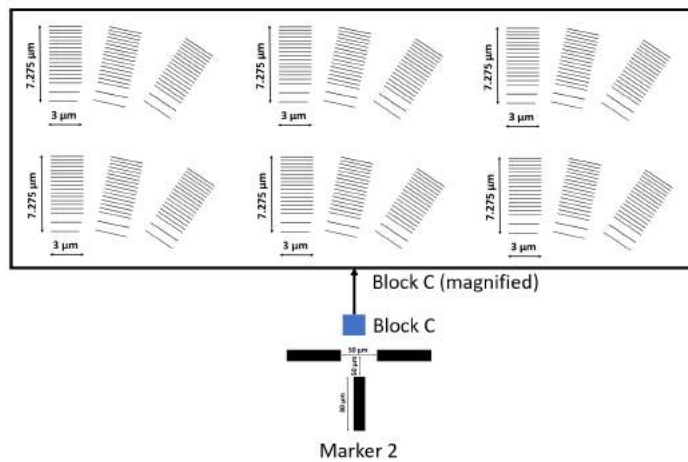
2D checkerboard array with increasing line spacing in x and y UHR mode, Line width = 50 nm, Line length = 4.5 μm, Line spacing = 80 nm to 200 nm in steps of 6 nm, Pitch = 2 nm, Dwell time = 100 ns, Number of passes = 4, Dose = 5 C/m².

4. Block C:

Arrays of dense lines with increasing line spacing patterned at arbitrary rotation angles: UHR mode, Line width = 50 nm, Line length = 1 μm, Rotation angle = 12°, 24°, 36°, Line spacing = 80 nm to 200 nm in steps of 6 nm, Pitch = 2 nm, Dwell time = 100 ns, Number of passes = 4, Dose = 5 C/m².



(a)



(b)

Figure A.5: Schematic of the layout of the test slide (a) Several repetitions of the array of dense lines (comprising Block A) and the 2D checkerboard array (comprising Block B) patterned alongside a large homogeneous structure (Marker 1) (b) Several repetitions of the array of dense lines at arbitrary angles (comprising Block C), patterned alongside Marker 2

The slides were then immunofunctionalised as described previously and transferred to the Zeiss Elyra Structured Illumination Microscope (Erasmus University Medical Centre, Rotterdam) for imaging, often several days later.

Experiments showed that the bleaching of the dye molecules (resulting in loss of fluorescence intensity) due to imaging once or due to storage over this period was negligible. A wide field image was first acquired, followed by confocal imaging and finally Structured Illumination Microscopy. A visual comparison of images, for example, of an array of dense lines from Block A (Fig. A.6(a)) clearly shows a qualitative improvement in resolution in SIM as compared to wide field and confocal techniques. Note: after confocal imaging, the patterns were found to have bleached heavily. A quantitative

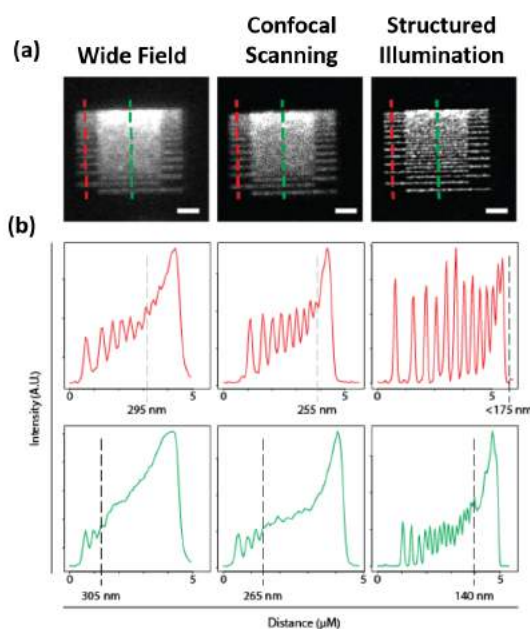


Figure A.6: Quantitative assessment of resolution using the calibration test slides patterned by electron beam exposure and functionalised with IgG-Alexa 488. (a) Comparative images of an array of dense lines from Block A taken using wide field, scanning confocal and structured illumination microscopy techniques. A qualitative improvement in resolution can be seen with SIM compared to the other two techniques. (b) Line scans taken across the red and green dashed lines in (a), providing a quantitative assessment of resolution with the three microscopy techniques. The black dashed line indicates the resolution limit, i.e., the minimum spacing at which two lines can be resolved and this has been determined to be 305 nm for wide field, 265 nm for scanning confocal and 140 nm for structured illumination microscopy.

assessment of the resolution is provided by the corresponding line scans in Fig. A.6(b). The green and red plots correspond to the line scans taken

along the respective dashed lines in (a). As the red line is located near the edges of the pattern, the red plot represents a measurement over lines spaced farther apart. The resolving power is determined from the green plot which represents a more precise measurement, taken over the denser (central) part of the array. The black dashed line indicates the minimum spacing at which two lines can be resolved and this has been determined to be 305 nm for wide field, 265 nm for confocal scanning and 140 nm for structured illumination microscopy. Thus this technique can be used to accurately control the spacing in dense lines, enabling an accurate measurement of resolution in SIM.

A.2.1 Quantitative dimensional analysis using SEM

The previous section dealt with the quantitative measurement of the resolving power of SIM, which was determined by the measurement of the centre to centre distance of dense lines at a range of spacings. In order to accurately interpret SIM images of biological specimens it is also important to have an independent measure of the "real" dimensions. Then, with prior knowledge of the pattern geometry at a resolution better than that of SIM, the data contained in the reconstructed images can be verified. The presence of artefacts can be ascertained and the algorithms can be improved to provide reliably reconstructed images. The question we address here is therefore: what are the widths and spacings of the dense lines patterned above? As mentioned before, the pattern exposed to the electron beam can be imaged in the SEM. However, it is the part of the pattern to which the IgG molecules bind that results in the width as imaged in SIM. This may or may not be simply related to the exposed area. As the IgG-Alexa 488 does not provide SEM contrast, this was performed by functionalising the test structures with IgG molecules bound to quantum dots instead. By comparing the SIM images of IgG-Alexa 488 labelled patterns with SEM images of IgG-QDots, it would be possible to achieve a one to one correlation between the dimensions as measured using SIM and SEM. This would be a very accurate measure as the SEM can be used to acquire images with very high resolution (of the order of a few nanometres).

A 1% solution of IgG-QDot in TE buffer was prepared by dissolving 20 μL of F(ab')₂-Rabbit anti-Goat IgG (H+L) Secondary Antibody, Qdot 655 (Life Technologies BV, The Netherlands) in 200 μL of 1X TE buffer. The test sam-

ple was incubated in this solution, leading to selective functionalisation of the patterns with IgG as before, while the conjugated CdSe/ZnS quantum dots provided SEM contrast as well as being fluorescent. It should be noted that while the selectivity was verified by SIM imaging in this case as well, the images are not of high quality (Fig. A.7) as the SIM was not optimally configured for imaging fluorescence emission in the range of 655 nm. These images were therefore not used for any quantitative analysis, but merely as a confirmation of successful labelling.

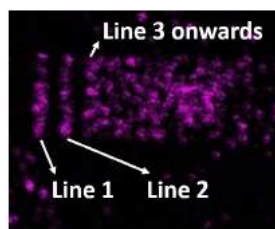


Figure A.7: An array of dense lines from Block C tagged with IgG-QDots 655 nm, imaged using the Zeiss Elyra SIM. Although some selectivity can be seen, the image is not of high quality as the microscope was not optimally configured for the detection of fluorescence emission in the range of 655 nm.

The samples were then imaged in the SEM using the In-lens SE detector (TLD) and some typical images of the test patterns are shown in Fig. A.8. The quantum dots appear brighter than the substrate in the SE image, which is expected due to the fact that they are composed of heavy metals, resulting in high SE yield. The high resolution SE images clearly show that the procedure led to successful functionalisation of the test structures with a high selectivity. This is particularly remarkable for the case of high resolution lines as in Fig. A.8(a) where the lines can be distinguished by eye with the aid of contrast from quantum dots, down to very dense lines. The lines can also be distinguished by eye due to the SE contrast from the exposed area itself, which appears darker than the substrate. The use of a higher electron dose (while remaining in Regime 1) for patterning results in increased SE contrast from the patterned area and, of course, wider lines, as seen from Fig. A.8(b). The patterned lines are expected to be broader than defined, as discussed elsewhere in this thesis, but it is also interesting to note from such images the extent of the exposed area which permits quantum dot labelling. The SE contrast in (b) is maximum at the centre of the line and falls off towards the edges on either side.

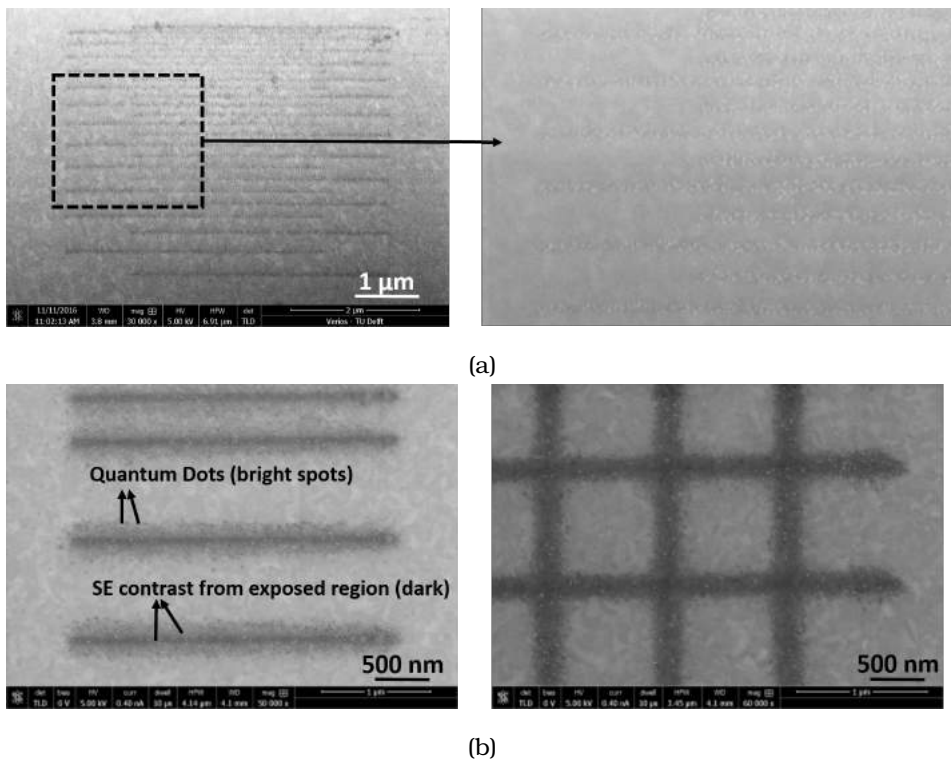


Figure A.8: SE image of test structures labelled with quantum dots conjugated to IgG. (a) Dense lines of Block A. Inset shows a high magnification image of the part of the array indicated by the black dashed square, where homogeneous and selective labelling of the patterns can be seen. The quantum dots are visible as bright spots. (b) Patterns fabricated with a higher electron dose. The SE contrast from the exposed region (dark) can be seen to have increased overall, with the intensity falling off on moving away from the centre of the line. The high resolution image shows the quantum dot attachment to be limited to the patterned area. In fact, the binding appears to be within the region showing SE contrast.

This is consistent with the expected distribution of SE's due to exposure with the primary beam. The labelling is also clearly a function of dose, as the quantum dots do not appear to extend beyond the region showing SE contrast. Further, if the SE contrast is a measure of height, an increase in which leads to more binding ([101]), the labelling density should be higher in the centre of the lines. But neither the lines in (a) patterned at a low dose nor in (b) patterned at a high dose, appear to have such a profile. This suggests that while the binding is a function of dose, the physical model is not straightforward. On the other hand, these observations do lend support to the explanation proposed in A.1.3. If the increased SE contrast

in (b) is a measure of some other form of modification of the PEG-silane layer or a more complex process involving carbon deposition in addition to surface activation or modification, it could explain why it does not result in increased binding. However, this explanation is also largely conjecture and it is not possible to quantify it, mainly because the SE dose received by the surface as a function of distance from the exposed pixels in the experiment is not known. The absence of darkening at some distance from the line cannot be taken to mean that it the surface there did not receive a dose of SE's. It can only be concluded that the region showing SE contrast seems to be the same as that of IgG (or quantum dot) attachment. A model based on physical principles, taking into account such factors as surface chemistry, the composition of gases in the chamber, and electron beam induced processes in PEG-silane would be needed to determine a relation between the applied electron dose and labelling.

Nevertheless, this work demonstrates that the technique can be used for versatile patterning at the nanoscale, with quantum dot labelling creating the possibility of high resolution nanopattern characterisation as well, most importantly in the sub-diffraction limit for SIM. From Fig. A.8(a), it can be seen that the labelling is quite homogeneous, in addition to being specific. This is very promising for the purpose of testing SIM algorithms as non-uniformities in the pattern would complicate the interpretation of reconstructed images. Next, the determination of resolving power from quantum dot labelling followed by SEM imaging is presented here. The dense lines in the inset of Fig. A.8(a) were analysed and the number of quantum dots per pixel line was plotted as a function of position (Fig. A.9(a)). A Gaussian fit was performed to each line profile in (a) and the peaks (line centre positions) were detected. The line spacings were measured (Fig. A.9(b)) and a resolution of 134 nm was determined. As the quantum dots appeared to be present only where the SE contrast due to exposure was visible, a measurement of resolution based on SE contrast in the image is very relevant as well.

The analysis of SE contrast in Fig. A.10(c) and (d) shows that all the lines in the array can be resolved, down to 80 nm. Next, the ultimate resolution of the technique was achieved by patterning lines of a single quantum dot-width. The line profile plotted using the contrast of quantum dots from the SEM image (Fig. A.11(a)) is shown in (b), with values of approximately

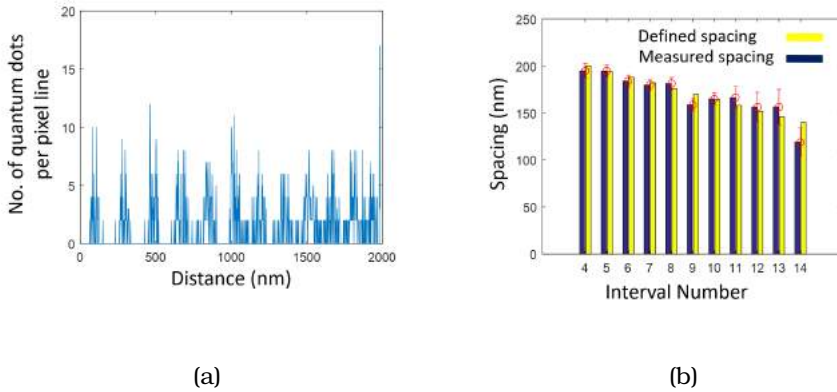


Figure A.9: Quantitative analysis of lines based on quantum dot counting from the SEM image in the inset of Fig. A.8(a). (a) Plot of the number of quantum dots per pixel line as a function of position (b) Line spacings measured by peak detection following Gaussian fits to the line profiles in (a). The resolution from this image is determined to be 134 nm.

90 nm determined from the Gaussian fit to the data.

The ultimate goal would be to find the correlation between the quantum dot contrast and SE contrast, so that the real pattern dimensions can be measured without quantum dot labelling; SE imaging of the patterns would suffice. This could be compared with SIM imaging of the patterns with a dye conjugated to IgG, which is much simpler and less expensive to perform than quantum dot labelling, to relate the fluorescence image to the real pattern dimensions. From Fig. A.11(a), there appears to be a good correspondence between the two regions. However, in order to quantify this result, an identical pattern should be exposed. Instead of functionalising with quantum dots, it should be used as a reference from which line widths can be measured using SE contrast alone. A comparison of the two would provide a quantitative measure of the positions of binding with respect to the electron beam modified area. Finally, as the main application of SIM is in biomedical imaging where the features being imaged rarely contain lines, this technique has been applied to the fabrication of some biologically relevant shapes. The ability to control the pattern dimensions by controlling the dose, and to pattern virtually any shape by using FEBIP are the biggest advantages of this method. A pattern resembling a DNA double helix was fabricated and imaged with SEM (Fig. A.12(a)) and SIM (Fig. A.12(b)) after the necessary labelling procedure in both cases. A

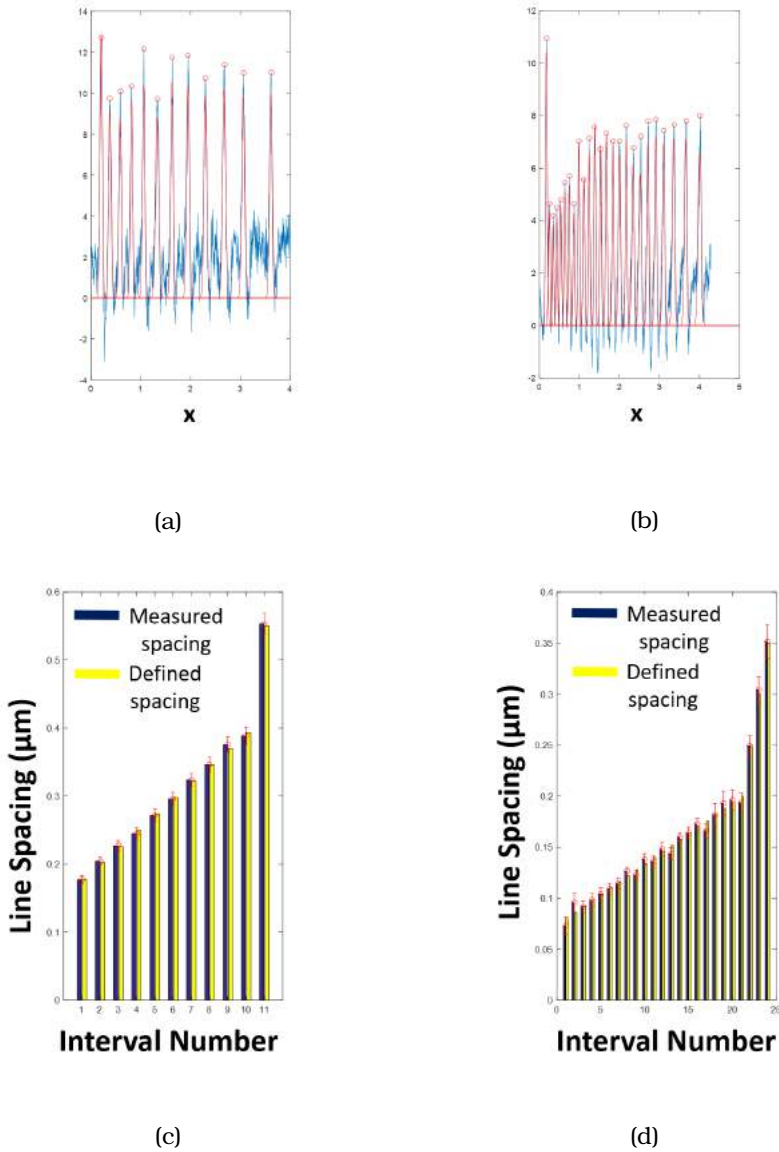


Figure A.10: Quantitative analysis of lines based on SE contrast from the (complete) SEM image in Fig. A.8(a). (a) Integrated line scan taken over the left part of the image, containing widely spaced lines (b) Integrated line scan taken over the central part of the image, containing dense lines. The blue and red plots indicate the measured data and the Gaussian fits respectively. (c) Line spacings measured from (a) (d) Line spacings measured from (b)

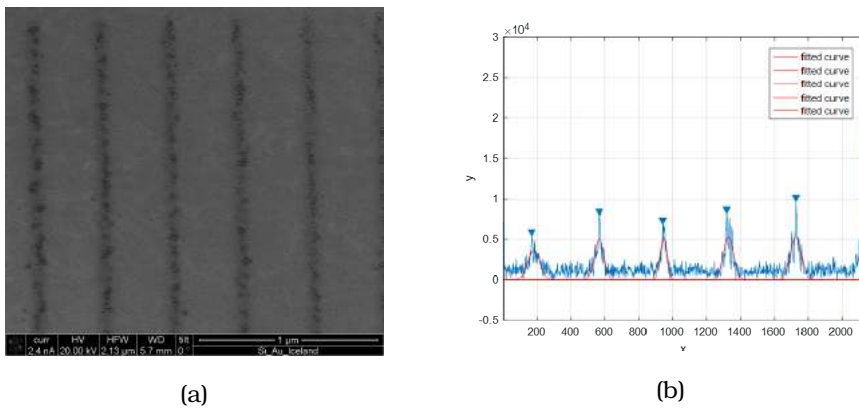


Figure A.11: (a) SE image of single quantum dot-wide dense lines, demonstrating the ultimate resolution of the technique (b) Plot of line profile using contrast from quantum dots, showing line widths of approximately 90 nm.

smooth well-defined shape with uniform labelling can be seen, even at critical positions where the curves cross each other.

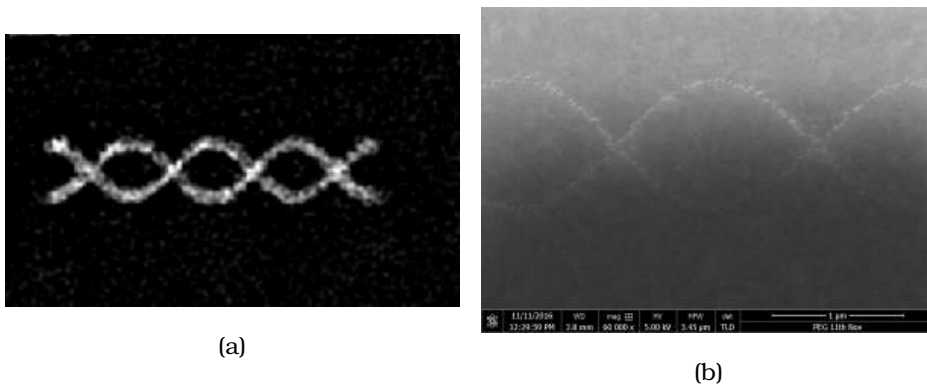


Figure A.12: Demonstration of the versatility of the test slide fabrication technique. Controlled patterning of not only straight lines, but virtually any shape including one that resembles a DNA double helix has been shown. (a) SEM image of pattern labelled with quantum dots and (b) SIM image of pattern labelled with Alexa 488, showing a smooth well-defined pattern with homogeneous labelling including at locations where the curves cross each other.

Complex patterns can also be fabricated with relative ease, either by loading a bitmap or by specifying the beam positions and pixel dwell times. A miniature "Sky and Water I" by M. C. Escher patterned in the SEM and labelled with Alexa 488 was imaged in the SIM as shown in Fig. A.13 and serves to point out the potential of this technique for well controlled

fabrication of complex patterns.

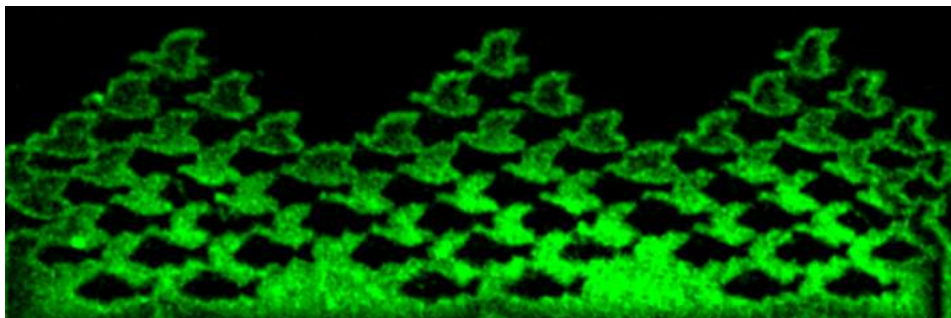


Figure A.13: SIM image of a miniature "Sky and Water I" by M. C. Escher patterned using this technique and labelled with Alexa 488 conjugated to IgG

A.3 Discussion

In the initial stages of this work, inhomogeneities/stains on the sample were invariably found. These interfere with the imaging as they are also fluorescent and are often present on the patterns. They were also found to exist on parts of the sample unexposed to the electron beam, ruling out electron exposure of the PEG as the cause. One possibility is that the PEG layer itself was wrinkled, either due to inhomogeneities on the substrate or due to the process. To avoid clustering of the PEG, the solution was placed in an ultrasound bath for several minutes, before incubating the sample. However, this was found to be ineffective in preventing clustering. Subsequently, the recipe was revisited and other sources of contamination were considered. On two occasions while PEG-coating the sample, nitrogen flow was used for drying it. Since the marks on the sample appeared to have a directionality, this could have been the process responsible for it. Subsequently, this step was excluded and the drying was performed instead by allowing the water droplets remaining on the surface to drain to the edge of the sample and wiping it off with lint-free paper. This succeeded in completely removing the clustering, resulting in very homogeneous patterns.

The patterns fabricated in this work were specifically for the purpose of measuring SIM resolution, and the smallest line spacings patterned were in the range of 140 nm. However, the technique has the potential to pattern

still smaller spacings by a different choice of parameters, for example, using a lower dose.

This method is very versatile in the conjugation of several different antibodies ([101]). As demonstrated by [101], it is also not restricted to IgG, a variety of proteins and even DNA origami have been patterned on electron beam modified PEG. In addition to Alexa 488 and quantum dots, gold conjugated labelling was also performed (not shown). Different fluorophores can therefore be used for labelling, in principle, any dye that can be bound to IgG could be used. So labelling can also be performed for STED, STORM and PALM.

The patterns fabricated here also lend allow a more elaborate analysis of SIM algorithm performance, using, for example, the lines of different orientations (A.5(b)). Also performance is tested under real experimental conditions (noise, aberrations, etc) as opposed to simulated data. Importantly, imaging such patterns and how they reproduce allows comparison of different microscopes, or monitoring the microscope performance/alignment over time.

A.4 Conclusions

1. The fabrication of test samples for the calibration of SIM is of prime importance in testing the performance of the reconstruction algorithms to obtain reliable and quantitative information, particularly for biological samples containing complex features. In the absence of such a calibration technique, different algorithms could result in the observation of different artefacts or features in the final image. It is easy to see that hotly contested debates regarding features of interest in biological samples can only be settled if prior information about the sample is available from a higher resolution method.

A multitude of dyes and antibodies can be used to fabricate test samples using this technique, making it applicable not only to SIM, but potentially also to the other types of superresolution microscopy.

2. The resolution of wide field, confocal scanning and structured illumination microscopy modes of the Zeiss Elyra microscope used in this study have been measured using test slides labelled with Alexa 488,

and determined to be 305 nm, 265 nm and 140 nm respectively.

3. The determination of pattern dimensions from high resolution SEM makes the calibration of SIM images very reliable as it gives nanometre-scale resolution. This has been performed by SE imaging of the pattern labelled with quantum dots that provide SEM contrast. Homogeneous and specific binding was obtained and it was demonstrated that high resolution lines could be fabricated and their dimensions accurately measured using this method. By performing quantum dot labelling of patterns identical to the ones imaged with SIM, it could be verified that the lines patterned at a spacing less than 134 nm were in fact no longer well-separated. The method used for the measurement of SIM resolution is therefore reliable, as is the value of 140 nm obtained.
4. The patterned areas show SE contrast - they appear darker than the surrounding substrate and a correspondence was observed between this SE contrast and quantum dot contrast. Performing experiments to quantify this would enable the calibration of SIM images by simply comparing them with SE images of the patterned area, without the need for quantum dot labelling.
5. Single quantum dot wide lines have been patterned and labelled in a successful demonstration of the high resolution capabilities of the technique. Unlike other techniques that may be limited to patterning straight lines of fixed length, FEBIP can also be used, for eg., to fabricate patterns customised for testing specific algorithms. Even complex structures resembling biological features can be patterned with ease, either using a bitmap or by specifying the necessary set of beam positions.
6. The dose dependence observed for the labelling does not seem to comply with the explanation provided in [101]. Instead there seem to be three regimes of sequential PEG modification, classified on the basis of electron dose, and more research is needed to determine the precise nature of the electron beam induced changes to PEG resulting in the observed fluorescence trend.

Appendix B

EBID simulator including the effect of vibrations

The following code simulates an EBID line by pixel exposure. Single pass or multiple pass patterning may be implemented. The amplitude and frequency of vibrations can be input by the user and the fluctuations are generated with a random phase.

```
clear;

X = linspace(-50,50,1024);
Y = linspace(-500,500,1024);
P = zeros(numel(X),numel(Y));

[GX,GY] = meshgrid(X,Y);

spotSize = 4; % effective deposition one-sigma radius [nm]
pitch = 10; % pitch between two exposures [nm]

beamVelocity = 1/10e-6; % [nm/s]

Fx = 50; % vibration frequency dx [Hz]
Fy = 50; % vibration frequency dy [Hz]
Ax = 0; % amplitude dx [nm]
Ay = 0; % amplitude dy [nm]

exposureFun = @(x,y)exp(-0.5*((GX-x).^2+(GY-y).^2)/spotSize^2);
for i = 1:10
    phi_x = 2*pi*rand;
    phi_y = 2*pi*rand;
    disp(i);
    for y = (1.5*min(Y)):pitch:(1.5*max(Y))
        dx = Ax*sin(2*pi*y/(beamVelocity/Fx)+phi_x);
        dy = Ay*sin(2*pi*y/(beamVelocity/Fy)+phi_y);
        P = P+exposureFun(dx,y+dy);
    end
end

P = random('Poisson',200*P); % The statistics/fluctuations on every point of the image M are 1/sqrt(n)
P = 1*P/(max(max(P))); % normalise in order to convert to tif
imagesc(X,Y,P);
colormap gray;

imwrite(P,'errrr.png');
```

Bibliography

- [1] "[http://www.nobelprize.org/educational/physics/integrated %5fcircuit/history/.](http://www.nobelprize.org/educational/physics/integrated%5fcircuit/history/)"
- [2] "[http://www.computerhistory.org/atcm/who-invented-the-ic/.](http://www.computerhistory.org/atcm/who-invented-the-ic/)"
- [3] "[http://www.research.ibm.com/topics/popups/serious/nano/html/sfuture.html.](http://www.research.ibm.com/topics/popups/serious/nano/html/sfuture.html)"
- [4] Doi:10.1038/nnano.2016.131, "Otte,"
- [5] I. Utke, P. Hoffmann, and J. Melngailis, "Gas-assisted focused electron beam and ion beam processing and fabrication," *Journal of Vacuum Science & Technology B: Microelectronics and Nanometer Structures*, vol. 26, no. 4, p. 1197, 2008.
- [6] W. F. van Dorp and C. W. Hagen, "A critical literature review of focused electron beam induced deposition," *Journal of Applied Physics*, vol. 104, no. 8, p. 081301, 2008.
- [7] S. J. Randolph, J. D. Fowlkes, and P. D. Rack, "Focused, Nanoscale Electron-Beam-Induced Deposition and Etching," *Critical Reviews in Solid State and Materials Sciences*, vol. 31, pp. 55–89, sep 2006.
- [8] N. Silvis-Cividjian and C. W. Hagen, "Electron Beam-Induced Nanometer Scale Deposition," *Advances in Imaging and Electron Physics*, vol. 143, no. 06, pp. 1–235, 2006.
- [9] S. Sengupta, C. Li, C. Baumier, A. Kasumov, S. Guéron, H. Bouchiat, and F. Fortuna, "Superconducting nanowires by electron-beam-induced deposition," *Applied Physics Letters*, vol. 106, no. 4, p. 042601, 2015.
- [10] M. Winhold, P. M. Weirich, C. H. Schwalb, and M. Huth, "Superconductivity and metallic behavior in $\text{PbxCyO}\delta$ structures prepared by focused electron beam induced deposition," *Applied Physics Letters*, vol. 105, no. 16, p. 162603, 2014.
- [11] M. G. Lassiter, T. Liang, and P. D. Rack, "Inhibiting spontaneous etching of nanoscale electron beam induced etching features: Solutions for nanoscale repair of extreme ultraviolet lithography masks,"

- Journal of Vacuum Science & Technology B*, vol. 26, no. 3, pp. 963–967, 2008.
- [12] T. D. Yuzvinsky, A. M. Fennimore, W. Mickelson, C. Esquivias, and A. Zettl, “Precision cutting of nanotubes with a low-energy electron beam,” *Applied Physics Letters*, vol. 86, no. 5, p. 053109, 2005.
- [13] R. W. Christy, “Formation of Thin Polymer Films by Electron Bombardment Formation of Thin Polymer Films by Electron Bombardment,” *J. Appl. Phys.*, vol. 31, no. 9, 1983.
- [14] H. W. P. Koops, “High-resolution electron-beam induced deposition,” *Journal of Vacuum Science & Technology B: Microelectronics and Nanometer Structures*, vol. 6, p. 477, jan 1988.
- [15] A. N. Broers, W. W. Molzen, J. J. Cuomo, and N. D. Wittels, “Electron-beam fabrication of 80-A metal structures,” *Applied Physics Letters*, vol. 29, no. 9, p. 596, 1976.
- [16] N. Silvis-Cividjian, C. W. Hagen, and P. Kruit, “Spatial resolution limits in electron-beam-induced deposition,” *Journal of Applied Physics*, vol. 98, no. 8, p. 084905, 2005.
- [17] W. F. van Dorp, B. van Someren, C. W. Hagen, P. Kruit, and P. A. Crozier, “Approaching the resolution limit of nanometer-scale electron beam-induced deposition.,” *Nano letters*, vol. 5, pp. 1303–7, jul 2005.
- [18] W. F. van Dorp, B. van Someren, C. W. Hagen, P. Kruit, and P. A. Crozier, “Statistical variation analysis of sub-5-nm-sized electron-beam-induced deposits,” *Journal of Vacuum Science & Technology B*, vol. 24, no. 2, pp. 618–622, 2006.
- [19] L. van Kouwen, A. Botman, and C. W. Hagen, “Focused electron-beam-induced deposition of 3 nm dots in a scanning electron microscope.,” *Nano letters*, vol. 9, pp. 2149–52, may 2009.
- [20] J. C. van Oven, F. Berwald, K. K. Berggren, P. Kruit, and C. W. Hagen, “Electron-beam-induced deposition of 3-nm-half-pitch patterns on bulk Si,” *Journal of Vacuum Science & Technology B: Microelectronics and Nanometer Structures*, vol. 29, no. 6, p. 06F305, 2011.

- [21] R. M. Thorman, R. Kumar T. P., D. H. Fairbrother, and O. Ingólfsson, "The role of low-energy electrons in focused electron beam induced deposition: four case studies of representative precursors," *Beilstein Journal of Nanotechnology*, vol. 6, pp. 1904–1926, 2015.
- [22] A. Szkudlarek, W. Szmyt, C. Kapusta, and I. Utke, "Lateral resolution in focused electron beam-induced deposition: scaling laws for pulsed and static exposure," *Applied Physics A*, vol. 117, no. 4, pp. 1715–1726, 2014.
- [23] R. Winkler, J. Fowlkes, A. Szkudlarek, I. Utke, P. D. Rack, and H. Plank, "The Nanoscale Implications of a Molecular Gas Beam during Electron Beam Induced Deposition," 2014.
- [24] H. Plank, D. A. Smith, T. Haber, P. D. Rack, and F. Hofer, "Fundamental proximity effects in focused electron beam induced deposition," *ACS Nano*, vol. 6, no. 1, pp. 286–294, 2012.
- [25] Jason D Fowlkes, "Fundamental Electron-Precursor-Solid Deposition Simulations and Experiments," vol. 4, no. 3, pp. 1619–1629, 2010.
- [26] E. C. S. Transactions and T. E. Society, "Effects of Adsorbate Surface Diffusion in Focused-Electron-Beam-Induced- Deposition A. Szkudlarek," vol. 50, no. 12, pp. 495–498, 2012.
- [27] R. Winkler, A. Szkudlarek, J. D. Fowlkes, P. D. Rack, I. Utke, and H. Plank, "Toward Ultraflat Surface Morphologies During Focused Electron Beam Induced Nanosynthesis: Disruption Origins and Compensation.," *ACS applied materials & interfaces*, jan 2015.
- [28] M. Winhold, P. M. Weirich, C. H. Schwalb, and M. Huth, "Identifying the crossover between growth regimes via in-situ conductance measurements in focused electron beam induced deposition," *Nanofabrication*, vol. 1, no. 1, pp. 86–95, 2014.
- [29] J. D. Fowlkes, S. J. Randolph, and P. D. Rack, "Growth and simulation of high-aspect ratio nanopillars by primary and secondary electron-induced deposition," *Journal of Vacuum Science & Technology B: Microelectronics and Nanometer Structures*, vol. 23, no. 6, p. 2825, 2005.

- [30] D. a. Smith, J. D. Fowlkes, and P. D. Rack, "A nanoscale three-dimensional Monte Carlo simulation of electron-beam-induced deposition with gas dynamics.," *Nanotechnology*, vol. 18, no. 26, p. 265308, 2007.
- [31] K. Rykaczewski, W. B. White, and A. G. Fedorov, "Analysis of electron beam induced deposition (EBID) of residual hydrocarbons in electron microscopy," *Journal of Applied Physics*, vol. 101, no. 5, p. 054307, 2007.
- [32] D. a. Smith, J. D. Fowlkes, and P. D. Rack, "Simulating the effects of surface diffusion on electron beam induced deposition via a three-dimensional Monte Carlo simulation.," *Nanotechnology*, vol. 19, p. 415704, oct 2008.
- [33] D. A. Smith, J. D. Fowlkes, and P. D. Rack, "Understanding the kinetics and nanoscale morphology of electron-beam- induced deposition via a three-dimensional monte carlo simulation: the effects of the precursor molecule and the deposited material," *Small*, vol. 4, no. 9, pp. 1382–1389, 2008.
- [34] I. Utke, V. Friedli, M. Purrucker, and J. Michler, "Resolution in focused electron- and ion-beam induced processing," *Journal of Vacuum Science & Technology B: Microelectronics and Nanometer Structures*, vol. 25, no. 6, p. 2219, 2007.
- [35] A. Szkudlarek, M. Gabureac, and I. Utke, "Determination of the Surface Diffusion Coefficient and the Residence Time of Adsorbates via Local Focused Electron Beam Induced Chemical Vapour Deposition," *Journal of Nanoscience and Nanotechnology*, vol. 11, no. 9, pp. 8074–8078, 2011.
- [36] S. Hari, A. M. Goossens, L. M. K. Vandersypen, and C. W. Hagen, "Electron Beam Induced Deposition on graphene on silicon oxide and hexagonal boron nitride: A comparison of substrates," *Microelectronic Engineering*, vol. 121, pp. 122–126, 2014.
- [37] M. Toth, C. Lobo, V. Friedli, A. Szkudlarek, and I. Utke, "Continuum models of focused electron beam induced processing," *Beilstein Journal of Nanotechnology*, vol. 6, pp. 1518–1540, 2015.

- [38] W. F. van Dorp, J. D. Wnuk, J. M. Gorham, D. H. Fairbrother, T. E. Madey, and C. W. Hagen, "Electron induced dissociation of trimethyl (methylcyclopentadienyl) platinum (IV): Total cross section as a function of incident electron energy," *Journal of Applied Physics*, vol. 106, no. 7, p. 074903, 2009.
- [39] W. F. van Dorp, I. Lazić, A. Beyer, A. Gölzhäuser, J. B. Wagner, T. W. Hansen, and C. W. Hagen, "Ultrahigh resolution focused electron beam induced processing: the effect of substrate thickness.," *Nanotechnology*, vol. 22, no. 11, p. 115303, 2011.
- [40] T. Verduin, P. Kruit, and C. W. Hagen, "Determination of line edge roughness in low-dose top-down scanning electron microscopy images," *Journal of Micro/Nanolithography, MEMS, and MOEMS*, vol. 13, no. 3, p. 033009, 2014.
- [41] J. C. van Oven, F. Berwald, K. K. Berggren, P. Kruit, and C. W. Hagen, "Electron-beam-induced deposition of 3-nm-half-pitch patterns on bulk Si," *Journal of Vacuum Science & Technology B: Microelectronics and Nanometer Structures*, vol. 29, no. 6, p. 06F305, 2011.
- [42] N. Silvis-Cividjian, C. W. Hagen, P. Kruit, M. A. J. V. D. Stam, and H. B. Groen, "Direct fabrication of nanowires in an electron microscope," *Applied Physics Letters*, vol. 82, no. 20, pp. 3514–3516, 2003.
- [43] C. Heerkens, M. Kamerbeek, W. van Dorp, C. Hagen, and J. Hoekstra, "Electron beam induced deposited etch masks," *Microelectronic Engineering*, vol. 86, pp. 961–964, apr 2009.
- [44] A. Bezryadin, "Nanofabrication of electrodes with sub-5 nm spacing for transport experiments on single molecules and metal clusters," *Journal of Vacuum Science & Technology B: Microelectronics and Nanometer Structures*, vol. 15, no. 4, p. 793, 1997.
- [45] I. G. C. Weppelman, P. C. Post, C. T. H. Heerkens, C. W. Hagen, and J. P. Hoogenboom, "Fabrication of narrow-gap nanostructures using electron-beam induced deposition etch masks," *Microelectronic Engineering*, vol. 153, pp. 77–82, 2016.
- [46] L. Reimer, *Scanning Electron Microscopy*, vol. 45. Berlin, Heidelberg: Springer, 1998.

- [47] H. Hiroshima, "Fabrication of conductive wires by electron-beam-induced deposition," *Nanotechnology*, vol. 9, pp. 108–112, 1998.
- [48] S. Hari, C. W. Hagen, T. Verduin, and P. Kruit, "Size and shape control of sub-20 nm patterns fabricated using focused electron beam-induced processing," *Journal of Micro/Nanolithography, MEMS, and MOEMS*, vol. 13, p. 033002, jul 2014.
- [49] P. Rack, D. Smith, and J. Fowlkes, "Understanding Electron-Beam-Induced Deposition and Etching via a Monte - Carlo Based, 3D Growth Simulation with Gas Dynamics," *Microscopy and Microanalysis*, vol. 13, no. S02, pp. 1468–1469, 2007.
- [50] M. G. Lassiter, P. D. Rack, H. Search, C. Journals, A. Contact, M. Iopscience, I. P. Address, M. G. Lassiter, and P. D. Rack, "Nanoscale electron beam induced etching: a continuum model that correlates the etch profile to the experimental parameters.," *Nanotechnology*, vol. 19, no. 45, p. 455306, 2008.
- [51] D. A. Smith, J. D. Fowlkes, and P. D. Rack, "A nanoscale three-dimensional Monte Carlo simulation of electron-beam-induced deposition with gas dynamics," *Nanotechnology*, vol. 265308, no. 18, p. 265308, 2007.
- [52] W. F. van Dorp, A. Beyer, M. Mainka, A. Gölzhäuser, T. W. Hansen, J. B. Wagner, C. W. Hagen, and J. T. M. De Hosson, "Focused electron beam induced processing and the effect of substrate thickness revisited.," *Nanotechnology*, vol. 24, p. 345301, aug 2013.
- [53] T. Bret, I. Utke, a. Bachmann, and P. Hoffmann, "In situ control of the focused-electron-beam-induced deposition process," *Applied Physics Letters*, vol. 83, no. 19, p. 4005, 2003.
- [54] I. Utke, V. Friedli, J. Michler, T. Bret, X. Multone, and P. Hoffmann, "Density determination of focused-electron-beam-induced deposits with simple cantilever-based method," *Applied Physics Letters*, vol. 88, no. 3, p. 031906, 2006.
- [55] "EBID Simulator."
- [56] R. Schmied, J. D. Fowlkes, R. Winkler, P. D. Rack, and H. Plank, "Fundamental edge broadening effects during focused electron beam

- induced nanosynthesis,” *Beilstein Journal of Nanotechnology*, vol. 6, pp. 462–471, 2015.
- [57] T. Verduin, S. R. Lokhorst, and C. W. Hagen, “GPU accelerated Monte-Carlo simulation of SEM images for metrology,” *Proc. SPIE 9778, Metrology, Inspection, and Process Control for Microlithography XXX*, vol. 9778, p. 97780D, 2016.
- [58] W. F. van Dorp, S. Lazar, C. W. Hagen, and P. Kruit, “Solutions to a proximity effect in high resolution electron beam induced deposition,” *Journal of Vacuum Science & Technology B: Microelectronics and Nanometer Structures*, vol. 25, no. 5, p. 1603, 2007.
- [59] M. T. Postek, A. E. Vladár, J. S. Villarrubia, and A. Muto, “Comparison of Electron Imaging Modes for Dimensional Measurements in the Scanning Electron Microscope,” *Microscopy and Microanalysis*, vol. 22, no. 04, pp. 768–777, 2016.
- [60] a. Botman, C. W. Hagen, J. Li, B. L. Thiel, K. a. Dunn, J. J. L. Mulders, S. Randolph, and M. Toth, “Electron postgrowth irradiation of platinum-containing nanostructures grown by electron-beam-induced deposition from Pt(PF₃)₄,” *Journal of Vacuum Science & Technology B: Microelectronics and Nanometer Structures*, vol. 27, no. 6, p. 2759, 2009.
- [61] a. Botman, J. J. L. Mulders, and C. W. Hagen, “Creating pure nanostructures from electron-beam-induced deposition using purification techniques: a technology perspective.,” *Nanotechnology*, vol. 20, p. 372001, sep 2009.
- [62] S. Mehendale, J. J. L. Mulders, and P. H. F. Trompenaars, “A new sequential EBID process for the creation of pure Pt structures from MeCpPtMe₃,” *Nanotechnology*, vol. 24, p. 145303, apr 2013.
- [63] F. Porrati, R. Sachser, C. H. Schwalb, a. S. Frangakis, and M. Huth, “Tuning the electrical conductivity of Pt-containing granular metals by postgrowth electron irradiation,” *Journal of Applied Physics*, vol. 109, no. 6, p. 063715, 2011.
- [64] H. Plank, G. Kothleitner, F. Hofer, S. G. Michelitsch, C. Gspan, A. Hohenau, and J. Krenn, “Optimization of postgrowth electron-beam curing for focused electron-beam-induced Pt deposits,” *Journal*

of Vacuum Science & Technology B: Microelectronics and Nanometer Structures, vol. 29, no. 5, p. 051801, 2011.

- [65] F. Nanostructures, H. Plank, J. H. Noh, J. D. Fowlkes, K. Lester, B. B. Lewis, and P. D. Rack, "Electron-Beam-Assisted Oxygen Purification at Low Temperatures for Electron-Beam-Induced Pt Deposits: Towards Pure and High-Fidelity Nanostructures," *ACS Applied Materials & Interfaces*, vol. 6, p. 1018, 2014.
- [66] V. Gopal, E. a. Stach, V. R. Radmilovic, and I. a. Mowat, "Metal delocalization and surface decoration in direct-write nanolithography by electron beam induced deposition," *Applied Physics Letters*, vol. 85, no. 1, p. 49, 2004.
- [67] J. W. Coburn and H. F. Winters, "Ion- and electron-assisted gas-surface chemistry—An important effect in plasma etching," *Journal of Applied Physics*, vol. 50, no. 5, p. 3189, 1979.
- [68] H. Miyazoe, I. Utke, J. Michler, and K. Terashima, "Controlled focused electron beam-induced etching for the fabrication of sub-beam-size nanoholes," *Applied Physics Letters*, vol. 92, no. 4, p. 043124, 2008.
- [69] M. Yemini, B. Hadad, Y. Liebes, A. Goldner, and N. Ashkenasy, "The controlled fabrication of nanopores by focused electron-beam-induced etching.," *Nanotechnology*, vol. 20, no. 24, p. 245302, 2009.
- [70] A. Ganczarczyk, M. Geller, and A. Lorke, "XeF(2) gas-assisted focused-electron-beam-induced etching of GaAs with 30 nm resolution.," *Nanotechnology*, vol. 22, p. 045301, jan 2011.
- [71] A. A. Martin, M. R. Phillips, and M. Toth, "Dynamic Surface Site Activation: A Rate Limiting Process in Electron Beam Induced Etching," *ACS Applied Materials & Interfaces*, vol. 5, pp. 8002–8007, 2013.
- [72] S. J. Randolph, J. D. Fowlkes, and P. D. Rack, "Focused electron-beam-induced etching of silicon dioxide," *Journal of Applied Physics*, vol. 98, no. 2005, p. 34902, 2005.
- [73] A. A. Martin and M. Toth, "Cryogenic Electron Beam Induced Chemical Etching," *ACS Applied Materials & Interfaces*, vol. 6, pp. 18457–18460, 2014.

- [74] S. Randolph, M. Toth, J. Cullen, C. Chandler, and C. Lobo, "Kinetics of gas mediated electron beam induced etching," *Applied Physics Letters*, vol. 99, no. 21, p. 213103, 2011.
- [75] V. Friedli and I. Utke, "Optimized molecule supply from nozzle-based gas injection systems for focused electron- and ion-beam induced deposition and etching: simulation and experiment," *Journal of Physics D: Applied Physics*, vol. 42, no. 12, p. 125305, 2009.
- [76] M. Toth, C. J. Lobo, W. R. Knowles, M. R. Phillips, M. T. Postek, and E. Vlada, "Nanostructure Fabrication by Ultra-High-Resolution Environmental Scanning Electron Microscopy," 2007.
- [77] C. J. Lobo, A. Martin, M. R. Phillips, and M. Toth, "Electron beam induced chemical dry etching and imaging in gaseous NH₃ environments.," *Nanotechnology*, vol. 23, p. 375302, sep 2012.
- [78] Y. M. Lau, P. C. Chee, J. T. L. Thong, and V. Ng, "Properties and applications of cobalt-based material produced by electron-beam-induced deposition," *Journal of Vacuum Science & Technology A: Vacuum, Surfaces, and Films*, vol. 20, no. 4, p. 1295, 2002.
- [79] M. Shimojo, K. Mitsuishi, A. Tameike, and K. Furuya, "Electron induced nanodeposition of tungsten using field emission scanning and transmission electron microscopes," *Journal of Vacuum Science & Technology B: Microelectronics and Nanometer Structures*, vol. 22, no. 2, p. 742, 2004.
- [80] D. Wang, P. C. Hoyle, J. R. A. Cleaver, G. A. Porkolab, and N. C. MacDonald, "Lithography using electron beam induced etching of a carbon film," *Journal of Vacuum Science & Technology B*, vol. 13, no. 5, p. 1984, 1995.
- [81] M. G. Lassiter, "Electron Beam Induced Etching," 2009.
- [82] M. Xu, D. Fujita, and N. Hanagata, "Monitoring electron-beam irradiation effects on graphenes by temporal Auger electron spectroscopy.," *Nanotechnology*, vol. 21, no. 26, p. 265705, 2010.
- [83] G. Arnold, R. Timilsina, J. Fowlkes, A. Orthacker, G. Kothleitner, P. D. Rack, and H. Plank, "Fundamental resolution limits during electron-induced direct-write synthesis.," *ACS applied materials & interfaces*, vol. 6, no. 10, pp. 7380–7, 2014.

- [84] N. Silvis-Cividjian, C. Hagen, L. Leunissen, and P. Kruit, "The role of secondary electrons in electron-beam-induced-deposition spatial resolution," *Microelectronic Engineering*, vol. 61-62, pp. 693-699, 2002.
- [85] M. G. Lassiter and P. D. Rack, "Nanoscale electron beam induced etching: a continuum model that correlates the etch profile to the experimental parameters.," *Nanotechnology*, vol. 19, p. 455306, nov 2008.
- [86] P. S. Spinney, D. G. Howitt, S. D. Collins, and R. L. Smith, "Electron beam stimulated oxidation of carbon.," *Nanotechnology*, vol. 20, p. 465301, nov 2009.
- [87] M. Henderson, "The interaction of water with solid surfaces: fundamental aspects revisited," *Surface Science Reports*, vol. 46, no. 1-8, pp. 1-308, 2002.
- [88] P. A. Thiel and T. E. Madey, "The interaction of water with solid surfaces: Fundamental aspects," *Surface Science Reports*, vol. 7, no. 6-8, pp. 211-385, 1987.
- [89] D. Menzel, "Water on a Metal Surface," *Science*, vol. 295, no. 2002, p. 58, 2002.
- [90] B. C. Garrett, C. W. McCurdy, A. R. Nilsson, S. Mukamel, T. S. Zwieter, J. A. Franz, D. Meisel, N. G. Petrik, S. M. Pimblott, M. S. Gutowski, T. M. Orlando, T. E. Madey, L.-S. Wang, J. A. LaVerne, D. A. Dixon, D. M. Camaioni, D. M. Chipman, M. A. Johnson, C. D. Jonah, G. A. Kimmel, J. H. Miller, T. N. Rescigno, P. J. Rossky, S. S. Xantheas, S. D. Colson, A. H. Laufer, D. Ray, P. F. Barbara, D. M. Bartels, K. H. Becker, K. H. Bowen, S. E. Bradforth, I. Carmichael, J. V. Coe, L. R. Corrales, J. P. Cowin, M. Dupuis, M. Dupuis, K. B. Eisenthal, K. D. Jordan, B. D. Kay, S. V. Lyman, J. R. Rustad, G. K. Schenter, S. J. Singer, A. Tokmakoff, K. B. Eisenthal, and C. Wittig, "Role of Water in Electron-Initiated Processes and Radical Chemistry: Issues and Scientific Advances," *Chemical Reviews*, vol. 105, no. 1, pp. 355-390, 2005.
- [91] M. Toth, C. J. Lobo, G. Hartigan, and W. Ralph Knowles, "Electron flux controlled switching between electron beam induced etching and

- deposition,” *Journal of Applied Physics*, vol. 101, no. 5, p. 054309, 2007.
- [92] S. W. Hell, “Far-Field Optical Nanoscopy,” *Science*, vol. 2, no. May, pp. 1153–1158, 2007.
- [93] M. G. L. Gustafsson, “Nonlinear structured-illumination microscopy: Wide-field fluorescence imaging with theoretically unlimited resolution,” *Proceedings of the National Academy of Sciences*, vol. 102, no. 37, pp. 13081–13086, 2005.
- [94] E. Betzig, G. H. Patterson, R. Sougrat, O. W. Lindwasser, S. Olenych, J. S. Bonifacino, M. W. Davidson, J. Lippincott-Schwartz, and H. F. Hess, “Imaging intracellular fluorescent proteins at nanometer resolution,” *Science*, vol. 313, no. 5793, pp. 1642–5, 2006.
- [95] S. T. Hess, T. P. Girirajan, and M. D. Mason, “Ultra-High Resolution Imaging by Fluorescence Photoactivation Localization Microscopy,” *Biophysical Journal*, vol. 91, no. 11, pp. 4258–4272, 2006.
- [96] S. W. Hell and J. Wichmann, “Breaking the diffraction resolution limit by stimulated emission: stimulated-emission-depletion fluorescence microscopy,” *Optics Letters*, vol. 19, no. 11, p. 780, 1994.
- [97] M. J. Rust, M. Bates, and X. Zhuang, “Sub-diffraction-limit imaging by stochastic optical reconstruction microscopy (STORM),” *Nature Methods*, vol. 3, no. 10, pp. 793–796, 2006.
- [98] D. Li, L. Shao, B.-C. Chen, X. Zhang, M. Zhang, B. Moses, D. E. Milkie, J. R. Beach, J. A. Hammer, M. Pasham, T. Kirchhausen, M. A. Baird, M. W. Davidson, P. Xu, and E. Betzig, “Extended-resolution structured illumination imaging of endocytic and cytoskeletal dynamics,” *Science*, vol. 349, no. 6251, pp. aab3500–aab3500, 2015.
- [99] S. Sahl, J. E., Balzarotti, F., Keller-Findeisen, J., Leutenegger, M., Westphal, V., Egner, A., Lavoie-Cardinal, F., Chymrov, A., Grotjohann, T., Jakobs, “Comment on “Extended-resolution structured illumination imaging of endocytic and cytoskeletal dynamics”,” *Science*, vol. 352, no. 6285, pp. aab3500–aab3500, 2016.
- [100] D. Li and E. Betzig, “Response to Comment on “Extended-resolution structured illumination imaging of endocytic and cytoskeletal dynamics”,” *Science*, vol. 352, no. 6285, p. 527, 2016.

- [101] R. Schlapak, J. Danzberger, T. Haselgrübler, P. Hinterdorfer, F. Schäffler, and S. Howorka, "Painting with biomolecules at the nanoscale: Biofunctionalization with tunable surface densities," *Nano Letters*, vol. 12, no. 4, pp. 1983–1989, 2012.
- [102] M. Chockalingam, N. Darwish, G. L. Saux, and J. J. Gooding, "Importance of the Indium Tin Oxide Substrate on the Quality of Self-Assembled Monolayers Formed from Organophosphonic Acids," *Langmuir*, vol. 27, pp. 2545–2552, 2011.
- [103] J. Rundqvist, J. H. Hoh, and D. B. Haviland, "Directed Immobilization of Protein-Coated Nanospheres to Nanometer-Scale Patterns Fabricated by Electron Beam Lithography of Poly (ethylene glycol) Self-Assembled Monolayers," *Langmuir*, vol. 22, no. 11, pp. 5100–5107, 2006.

Acknowledgements



would like to thank Pieter for the opportunity to do a PhD in the Charged Particle Optics group. The friendly and open atmosphere with easy access to people and equipment made working in CPO a very enjoyable experience, and I appreciate having the freedom to make my own choices for my project.

I would like to thank Kees for the opportunity to work on this project and for his enthusiasm for all things high resolution. I benefited a lot from lengthy discussions that so often went on past his regular working hours, and from the interest he took in me - my work and life. I would also like to thank him for being organised, so he could make time to review my abstracts and manuscripts invariably submitted before the stroke of the midnight hour. And finally, for the freedom to attend any meetings or workshops that seemed interesting, to steer clear of those that didn't, and for his company at all the conferences.

My office was a place of fun and comfort throughout my stay. It was great to spend time with Gerward, whose unique personality and willingness to be taken aboard any and all plans resulted in some very memorable moments. I will always remember with warmth the time spent in the lab and office, travelling, our visits to Leonidas, and help of all kinds offered in typical uncalculating style. I had a great time with Marijke - doing EBID, troubleshooting the Nova, attending conferences and learning to plan even shopping trips ages in advance. She is a positive influence and I'm glad we somehow managed to spend time together in spite of our vastly different notions of morning and night! I want to thank Robert for always helping out, especially with optical imaging, even after leaving CPO. It was so nice to have company during the evenings spent at the university! We had a lot of fun times in Delft with coffee, conversation and squash. I met Angela and Nalan when I first came to Delft, and I really enjoyed being tourists together over the years, celebrating Koninginnedag, visiting Keukenhof and the 'big cities'. It was also helpful to work with Nalan in the initial stages of functionalising PEG with antibodies, and she helped me grasp the sample preparation in a very biological project! I was grateful to have Angela's

Acknowledgements

company in arriving 'late' to work and last minute dinner plans with her were often the highlight of a rainy weekend.

I would like to thank the people with whom I collaborated during my PhD: Hans Mulders and Piet Trompenaars, who were kind enough to give us an SEM, and together with Remco Geurts, also arranged for me to do experiments at FEI, Eindhoven; Jacob, for his suggestions and support in bringing the biofunctionalisation project to a successful conclusion. I really appreciate his encouragement and sitting down together for discussions; Thomas, for working together on developing the edge detection technique, and the many lengthy discussions on line profiles and metrology; Willem, for his work on the analytical model of sidewall etching and for TEM imaging; Ragesh, for visiting Delft to work on the silacyclohexane project, and Oddur for his valuable inputs in interpreting the results; Stijn, for introducing me to the V-I measurement setup at QT and for fabricating graphene samples for my very first EBID project; the group at Erasmus MC, Rotterdam, particularly Johan, for SIM measurements and feedback that helped improve the sample preparation protocol. I was lucky to work on the biofunctionalisation project with Yoram, Christian and Miranda, and I would like to thank them for all the work they put in. Thanks also to Niels for his work on characterising EBID lines.

This work wouldn't have been possible without the help of many skilled technicians. I would like to thank Jan de Loeff for the time we spent working in the lab and for his efforts in the workshop. He was always on hand to help and his warmth and friendliness made me feel immediately welcome in the group. Coffee time was particularly enjoyable because of his presence and animated storytelling. Bedankt voor alles! I would also like to thank Frans, Jacques, Han, Carel, Paul and Ruud for their help and support on various projects as well as on daily tasks revolving around the microscope and the chemicals lab. I am grateful to Marc Zuiddam for frequently taking time out of his busy schedule to help me with the AFM, and to Martin Kamerbeek for fabricating chips for patterning.

I am very grateful to Margaret for her enthusiastic involvement in arranging a lot of my travel to conferences, and for her help with paperwork. She was always ready with suggestions for interesting places to visit, and I really enjoyed our conversations in her office! I would like to thank Anjella for

going out of her way to make administrative procedures easier, and for helping in a million ways with the arrangements for my defence. She made my stay in CPO very comfortable, and it was a lot of fun to celebrate our birthday together!

Everyone in the group contributed to the great atmosphere there. So thanks to Vincenzo, Ali, Ben, David, Christiaan, Chris, Daan, Leon, Takashi, Minoru, Mauricio, Jayson, Dusan, Wilco, Mathijs, Dustin, Kerim, Maurice, Aya, Laura and Neda for being there. It was a lot of fun getting to know Yan and Ting and I am grateful for the many invitations home. It was so nice to have a mini-Indian community at work, and I would like to thank Shammi, Aditi and Gaudham, for the time we spent together.

I am happy to have worked with EK during the time I was at TIFR. I learnt a lot about molecular physics and experimental design from our interactions. I would also like to thank my physics teacher Mr. Sanjay Yadav for getting me interested in the subject.

My time in Europe was made enjoyable by Aditya, Himani, Madhurima and Samrith, with whom I visited some beautiful places and always had a relaxing time.

I would like to thank my family and friends - my parents, my brother, Naren, and my close friends - Pyoli, Manisha, Himani, Vaishnavi and Snigdha, for their support and encouragement throughout.